# Nuclear reactions of high energy protons, photons, and leptons

Inaugural-Dissertation
zur
Erlangung des Doktorgrades
der Naturwissenschaftlichen Fakultät
der Justus-Liebig-Universität Gießen
Fachbereich 7 – Mathematik, Physik, Geographie

vorgelegt von
Thomas Falter
aus Gießen

Gießen, 2004

Dekan: Prof. Dr. Volker Metag
I. Berichterstatter: Prof. Dr. Ulrich Mosel
II. Berichterstatter: Prof. Dr. Werner Scheid
Tag der mündlichen Prüfung: 23.07.2004

# Contents

# Chapter 1

# Introduction

As far as we know today, the luminous matter in the universe, i.e. any matter that directly or indirectly emits electromagnetic radiation, is almost completely composed of nucleons (=protons, neutrons) and electrons. According to the big bang model the universe began in a state of infinite density and temperature which was followed by a rapid expansion and cooling [Mis73]. About $10^{-30}$ seconds after its birth, quarks, leptons and gauge bosons were created; an overview is given in Tabs. 1.1 and 1.2. Only a few microseconds later the quarks were bound together and formed the nucleons. This process is called *hadronization*.

In addition to the nucleons, hundreds of unstable bound states of quarks (and antiquarks) have been discovered in various cosmic ray and accelerator experiments within the last 60 years. These strongly interacting particles are called hadrons and can be grouped into two types of quark combinations [Gel64]: *baryons* (three quark fermion states $qqq$) and *mesons* (quark-antiquark boson states $q\bar{q}$). Since the quarks themselves are fermions, the existence of a spin-3/2 bound state of three identical quarks is forbidden by Fermi statistics. However, in 1951 Fermi and collaborators discovered the $\Delta^{++}$ which is a baryon made up of three $u$ quarks with aligned spins. It is therefore necessary to introduce a new quantum number for quarks: *color*. One usually supposes that quarks come in three colors[1]: red $r$, green $g$ and blue $b$, and that every free particle must be color neutral. The latter assumption is supported by the experimental fact that one does not observe several color combinations for hadrons, e.g. a red, a green and a blue proton. The existence of exactly three colors is indicated by experiments like electron-positron annihilation into hadrons or the two-photon decay of the neutral pion [Per87].

The requirement that all free particles have to be color neutral also explains why one does not observe free (colored) quarks but only the color singlet combinations $qqq$ and $q\bar{q}$, i.e. the hadrons[2]. This phenomenon is called *confinement* and implies that the potential energy of two colored objects strongly increases with their separation. In fact the spectroscopy of charmonium ($c\bar{c}$) points towards a potential which is Coulomb-like at small distances and increases linearly for larger separations. The field configuration that corresponds to the linear potential has a cylindric shape and is concentrated between the two color charges. It is usually called *flux tube* or *string*. If one tries to

---

[1]The antiquarks carry anticolor.

[2]Recently, evidence for a color neutral *pentaquark* state has been discovered experimentally [Nak03].

| fermions | generation | | | el. charge | color |
|----------|:---:|:---:|:---:|:---:|:---:|
|          | 1 | 2 | 3 |            |       |
| leptons  | $\nu_e$ | $\nu_\mu$ | $\nu_\tau$ | 0 | – |
|          | $e$ | $\mu$ | $\tau$ | -1 |  |
| quarks   | $u$ | $c$ | $t$ | +2/3 | $r, g, b$ |
|          | $d$ | $s$ | $b$ | -1/3 |  |

Table 1.1: Elementary spin-1/2 fermions of the standard model [Pov97].

stretch the string by more than 1–2 fm the field energy becomes large enough to create a quark-antiquark pair from the vacuum which combines with the endpoint particles to form two color neutral hadrons.

The quark substructure of hadrons suggests a dynamical understanding of the strong force in terms of color interactions between the quarks: *quantum chromodynamics* (QCD). In contrast to quantum electrodynamics (QED), QCD is a *non-Abelian* gauge theory. As a result the gauge bosons that mediate the color interactions, i.e. the *gluons*, themselves carry (color) charge and can therefore interact with each other. This leads to an anti-shielding of color charges which has two remarkable consequences that do not exist in an Abelian gauge theory like QED. At short distances, or correspondingly large momentum transfers, the coupling becomes small and the quarks inside the hadrons behave essentially as free noninteracting particles (*asymptotic freedom*). In this kinematic regime one can thus apply perturbative techniques to calculate the interaction between quarks and gluons. On the other hand, the anti-shielding of QCD is analogous to a color-dielectric medium with a dielectric constant $\epsilon \ll 1$ [Mos98]. An isolated color charge in such a medium would correspond to a state of infinite (or very large) energy (*confinement*).

Since the coupling increases with decreasing momentum transfer, perturbative methods cannot be used to describe the low-energy phenomena of QCD. Therefore, a thorough proof that QCD indeed leads to color confinement is yet missing. For the same reason, also the properties of hadrons like masses and excitation spectra cannot be calculated within perturbative QCD (pQCD). The only possibility is to numerically solve a discretized version of QCD on a lattice. However, this is connected with a lot of computational effort and conceptional problems and one is still far away from a complete lattice description of both the hadronic spectra and low-energy hadronic interactions. We are therefore left with a purely phenomenological treatment of low-energy QCD.

One of the greatest achievements of high-energy physics over the last 30 years has been the quantitative verification of QCD in very hard collisions. Because of asymptotic freedom the constituents of the hadrons, i.e. the quarks and gluons, behave like free particles in such collisions. As pointed out, this behavior vanishes for small momentum transfers and the quarks and gluons are confined into hadrons by the strong force that does not allow for the observation of any free colored object. This phase transition from partonic degrees of freedom (quarks and gluons) to interacting hadrons – as encountered in the early universe shortly after the big bang – is a central topic of modern hadron physics. In order to understand the dynamics and relevant scales of this

| interaction | couples to | exchange boson |
|---|---|---|
| strong | color | 8 gluons $(g)$ |
| electromagnetic | el. charge | photon $(\gamma)$ |
| weak | weak charge | $W^{\pm}$, $Z^0$ |

Table 1.2: Elementary interactions of the standard model [Pov97].

transition, laboratory experiments under controlled conditions are presently performed at the SPS and RHIC with ultra-relativistic nucleus-nucleus collisions that are being thought of as repeated 'tiny bangs'. However, the complexity of a heavy-ion collision that passes through various density and temperature phases makes it hard to draw any comprehensive conclusion about the space-time picture of the hadronization process.

In the early 1970s, the quark structure of the nucleon has been verified by deep inelastic electron-proton scattering at SLAC. In such a reaction the electron emits a virtual photon with large energy and momentum which is absorbed by a quark inside the proton. The four-momentum transfer readily determines the fraction of the proton momentum that is carried by the struck quark. By varying the energy and momentum of the virtual photon, one can therefore measure the quark distributions inside the nucleon. Since this pioneering work, a lot has been learned about the quark and gluon structure of hadronic matter through deep inelastic scattering experiments at CERN, DESY, FNAL and SLAC.

By deep inelastic lepton scattering on nuclear targets the modifications of the quark and gluon distributions inside the nuclear medium are accessible. However, the use of nuclear targets has an additional advantage. If the quark that is struck by the virtual photon separates from the rest of the residual system it takes a finite time until the reaction products hadronize. Due to time dilatation the corresponding hadron formation length at high energies is comparable to nuclear radii. In lepton-nucleus interactions the reaction products can, therefore, interact with the surrounding nuclear medium during the formation time. Here the nuclear target can be viewed as a micro-laboratory that provides an intrinsic (variable) time scale due to the size of the target nucleus, which can be exploited to get information on the actual time scale of the hadronization itself. By using different nuclear targets and varying the kinematics of the virtual photon, one can therefore study the propagation of the quark and how the color field of the hadron is restored.

First studies of high-energy hadron electroproduction off nuclei have been carried out in the late seventies at SLAC [Osb78]. In the early nineties the European Muon Collaboration (EMC) [Ash91] and E665 [Ada94] have looked into the attenuation of fast hadrons in the scattering of high-energy muons on nuclear targets at CERN and FNAL. Recently, the HERMES collaboration at DESY has put a lot of effort into the detailed experimental investigation of hadron attenuation in deep inelastic scattering of 27.7 GeV positrons on complex nuclei [Air01, Air03b]. A similar experiment is currently performed at Jefferson Lab using the available 6 GeV electron beam [WBr02, KWa04] and an additional one is anticipated to run after the 12 GeV upgrade [Arr03, WBr03]. Furthermore, the investigation of hadronization in nucleons and nuclei is part of the
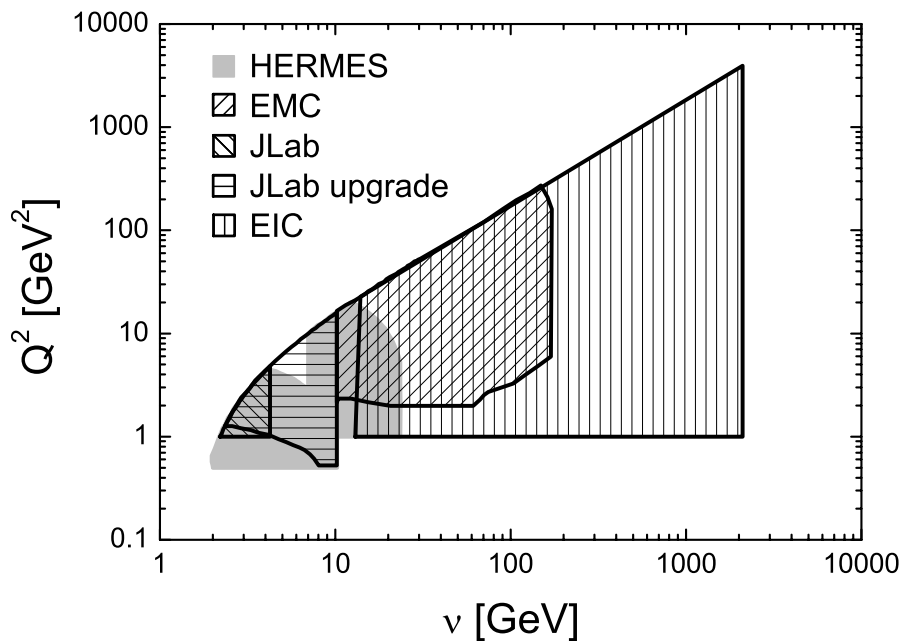
Figure 1.1: Kinematic regime covered by the electron-nucleus scattering experiments at CERN, DESY, Jefferson Lab and the planned EIC. The photon energy in the rest frame of the nucleus is denoted by $\nu$ and the virtuality of the photon by $Q^2$.

physics program at the planned electron-ion collider (EIC) [Des02] which will collide 5-10 GeV electrons/positrons and a 100 $A$GeV nuclear beam. In Fig. 1.1 we give an overview of the different kinematic regimes covered by the various experiments. The energy of the photon in the rest frame of the nuclear target is denoted by $\nu$ and $-Q^2$ is the four-momentum of the virtual photon squared. The theoretical understanding of the observed hadron attenuation is a subject of high current interest [Guo00, Wan01, Wan02, Wan03, Acc03, Arl03, Kop03].

Closely related to hadron production in deep inelastic scattering is the phenomenon of *color transparency* [Mue82, Bro82]. In a deep inelastic scattering event the photon transfers all of its energy and momentum to one single quark inside the target nucleon. As a result the target nucleon is in general destroyed. However, at high energies the (virtual) photon can also fluctuate into a vector meson or perturbatively branch into a quark-antiquark pair before the actual interaction with the nucleon takes place. In the subsequent scattering the momentum transfer may be soft. A prominent example is diffractive vector meson production where a hadronic fluctuation of the photon is put on its mass shell by a small momentum exchange with the nucleon. The nucleon stays intact and the two final states, i.e. the vector meson and the nucleon, are separated by a large gap in rapidity. The geometric size of the initial quark-antiquark fluctuation is expected to decrease with increasing photon virtuality $Q^2$. For large $Q^2$ the colorless quark-antiquark pair is thus in a small sized configuration during the early stage of the evolution and mainly reacts via its color dipole moment. Its cross section is therefore quadratic in the transverse size of the pair. Because of time dilatation the high-energy quark-antiquark pair can travel a large distance while being 'frozen' in this small sized

configuration. If this distance exceeds the diameter of a nucleus color transparency leads to a large nuclear transparency for vector meson production at large photon energy and virtuality.

The HERMES collaboration has studied the nuclear transparency ratio of exclusive $\rho^0$ electroproduction on a nitrogen target [Ack99, Air03] and a similar experiment is currently performed at Jefferson Lab [Haf02]. It is hard to extract a clear signal for color transparency from such a reaction since the effect is superposed by coherent multiple scattering of the photon's vector meson fluctuation in the nuclear target. The latter leads to nuclear shadowing, i.e. a reduction of the nuclear production cross section by 'initial state interactions' of the photon. This effect is also observed in the nuclear photoabsorption cross section [Bau78] and gives rise to the EMC effect [EMC83, Arn94] at small values of the Bjorken scaling variable $x$.

A clear separation between the direct photon interactions and the ones mediated by the hadronic fluctuations of the photon, is not possible in the kinematic regimes of the EMC, HERMES and Jefferson Lab experiments. Therefore, both aspects of high-energy photon interactions have to be taken into account if one wants to extract the space-time behavior of hadronization from these experiments.

Besides being a fascinating topic on its own, a detailed space-time picture of hadronization should also help to clarify to what extent the jet suppression, recently observed in heavy-ion collisions at RHIC [PH03, PH04, ST03, ST03b], is due to (pre-) hadronic final state interactions (FSI) [Gal03, Kop03, Cas04] or partonic energy loss [Wan92, Wan98, Bai00, Gyu03]. The suppression of high $p_T$ hadrons in Au+Au reactions relative to $p + p$ collisions is often thought to be due to jet quenching in a quark gluon plasma, i.e. a state where the relevant degrees of freedom are no longer hadrons but free quarks and gluons. However, the attenuation of high $p_T$ hadrons might at least partly be due to hadronic rescattering processes.

Electron-nucleus interactions have the advantage that the nucleus remains more or less in its ground state throughout the reaction. Contrary to nucleus-nucleus collisions, where the created 'fireball' is rapidly expanding, lepton-nucleus reactions therefore provide rather clear geometrical constraints, which are well under control experimentally. In addition the system is closer to equilibrium than in a heavy-ion collision.

The standard theoretical approach to high-energy nuclear reactions is Glauber theory [Gla59, Gla70] which reduces the nuclear reaction to more elementary interactions with individual nucleons. It allows for a full quantum-mechanical description of the scattering process by a coherent summation of the various multiple scattering amplitudes. Such a quantum-mechanical treatment is of course only feasible under many approximations. Therefore, one usually neglects all coupled-channel effects in the calculation and restricts oneself to a purely absorptive description of the FSI of the reaction products.

A more sophisticated, although probabilistic, coupled-channel treatment of the FSI can be realized in the framework of semi-classical transport models. During the past 20 years transport models based on the Boltzmann-Uehling-Uhlenbeck (BUU) equation [Brt84] have been successfully applied to describe particle production in heavy-ion collisions. One major drawback of these models is obviously the vast number of free parameters. It is therefore mandatory to test the results of the model against as many experimental observables as possible, thereby using the same set of param-

eters and physics assumptions. Our transport model has been originally developed to describe heavy-ion collisions at SIS energies [Tei96, Tei97, Hom99]. Later on it has been extended in Refs. [Wei99, Eff99b] and [Eff99a, Eff96, Leh99, Leh00] to describe pion-induced as well as photon- and electron-induced reactions in the nucleon resonance region. Based on the earlier work on high-energy photon-nucleus reactions in Refs. [Eff99c, Eff00] we have extended the model to simulate nuclear interactions of high-energy photons and electrons in the kinematic regime of the Jefferson Lab, HERMES and EMC experiments.

We begin our studies with a discussion of the different event classes of elementary hadron-hadron interactions in Chap. 2. It turns out that the high-energy cross sections of hadrons are dominated by diffractive excitation which can be addressed within Regge theory. For this reason we included a brief introduction to the Regge picture of high-energy collisions.

We then turn to the interactions of high-energy photons and electrons with hadrons. In the one-photon exchange approximation the electron-nucleon scattering can be decomposed into the emission and absorption of a virtual photon. In certain kinematic regimes the contributions from the hadronic fluctuations of the (virtual) photon dominate the photon-nucleon interaction. In that case we expect strong similarities between photon- and hadron-induced reactions. In Chap. 3 we outline the possible event classes and discuss their importance in different kinematic regimes.

In Chap. 4 we give an overview on the actual event generation in our model. The event generators PYTHIA [Sjö01a, Sjö01b] and FRITIOF [And87, Pi92, And93] that determine the final state of a scattering event above the resonance region are based on the Lund model [And83, And98]. In Sec. 4.3 we use the Lund model to extract the production and formation times of the hadrons. While the production times of the color neutral prehadrons are essentially the times of the string fragmentation, the formation time corresponds to the time when the hadronic wave function has built up.

In Chap. 5 we turn to hadron-induced nuclear reactions. Since we often compare our results from the transport model with those of Glauber theory we start this chapter with an introduction to the Glauber model. The BUU transport model is described in Sec. 5.2. We give a complete description of all model aspects that we consider relevant for the high energy reactions addressed in this work. In Sec. 5.3 we compare the predictions of the Glauber and the BUU model for reactions of 100 GeV protons incident on various nuclear targets. Here, we also discuss the concept of leading hadrons which is generally used in transport models for high-energy nuclear reactions.

The central part of this work – the description of high energy photon- and electron-induced nuclear reactions – is presented in Chap. 6. Like before we discuss both the Glauber and the BUU approach. As already pointed out, the high-energy interactions of photons are shadowed in nuclei. While this shadowing can be in principle understood within Glauber theory, it is not straight forward to account for this quantum mechanic interference effect within a semi-classical transport model. A first attempt has been made in Ref. [Eff99a] but still disregarded the fact that the various photon components are modified differently in the nuclear medium. In Sec. 6.1.2 we present a method to correctly account for shadowing in transport theory.

In Sec. 6.2 we test whether our implementation of shadowing correctly reproduces the coherence length effects observed in exclusive $\rho^0$ electroproduction at HERMES

[Ack99, Air03]. In addition we focus on the impact of the coherence length and the coupled channel FSI on the nuclear transparency ratio of $\rho^0$ production. In Sec. 6.3 we study semi-inclusive photoproduction of pions, kaons and open charm at photon energies in the range 1–30 GeV. The attenuation of charged hadrons in deep inelastic lepton scattering off complex nuclei is discussed in Sec. 6.4 using different hadronization scenarios. We split this section into three parts according to the different kinematic regimes of the HERMES, the EMC and the Jefferson Lab experiments. Besides the attenuation of pions, kaons, protons and antiprotons as a function of the photon energy and the energy and transverse momentum of the hadrons, we also consider the double hadron attenuation which has recently been measured at HERMES. We also demonstrate how the detector acceptance and kinematic cuts affect the observed multiplicity ratio.

We end this work with a summary and outlook in Chap. 7.

# Chapter 2

# Hadron-hadron interactions

In this work we investigate interactions of high-energy protons, photons and electrons with nuclei. In such reactions the projectile and the reaction products scatter off the bound nucleons inside the nucleus. Unlike in heavy-ion collisions, interactions between the reaction products themselves such as meson-meson collisions are very unlikely.

As we show in Chap. 3 reactions of high-energy photons show some striking similarities to those of hadronic projectiles. The reason for this is the hadronic structure of the photon as explained in Sec. 3.1.1. Also electron scattering can be reduced to the exchange of a (virtual) photon with the target nucleon (see Sec. 3.2.1). We therefore need at first a way to model the interactions of high-energy hadrons with nucleons before we turn to electromagnetic probes. A comprehensive introduction to hadron interactions at high energies can be found in Ref. [Col84].

At low energies interactions between hadrons and nucleons mainly proceed via the excitation and decay of nucleon resonances. At high energies the possible reactions can be divided into four different classes: elastic scattering (which is of course also possible at low energies), diffractive excitation, hard scattering between the constituents (quarks and gluons) of the colliding partners and soft non-diffractive interactions (e.g. soft gluon exchange). The first task is to determine the probability for each reaction type to occur, i.e. the size of the cross sections for the different event classes. This problem is tackled within this chapter using Regge theory and perturbative QCD (pQCD). The second task, namely the determination of the final-state particles emerging from an inelastic collision, is postponed to Chap. 4 where we provide a description of the Lund string model.

We start this chapter with a short introduction to Regge theory and address the four different event classes in Secs. 2.2.2 – 2.2.5. At the end of this chapter we try to link Regge theory to the string model that is later on used to determine the fragmentation of the reaction products into the final-state hadrons.

## 2.1 $\mathcal{S}$ matrix and Regge theory

In the resonance region, i.e. at center-of-mass energies below approximately 2 GeV the scattering of hadrons can be described using effective field theories with meson and baryon resonance degrees of freedom. Some detailed studies in this field have been made in Refs. [Pen02a, Pen02b] which simultaneously investigate pion-nucleon

and photon-nucleon scattering within the framework of a coupled-channel model by solving the Bethe-Salpeter equation in the so-called $K$-matrix approximation. The model parameters are the masses and coupling constants of the resonances. They are extracted by comparing the model predictions with the experimental cross sections on meson production ($\pi N$, $2\pi N$, $\eta N$, $K\Lambda$, $\omega N$, $\gamma N$).

At higher energies the resonant structure in the cross sections vanishes and interactions lead to more complicated final states with large particle multiplicities. Thus resonance models seem not to be the right tool to describe high-energy reactions.

With increasing center-of-mass energy the scattering of single hadron constituents at large momentum transfer becomes possible. Therefore, pQCD can be applied to calculate the cross section for the elementary hard parton-parton scattering. If the parton distributions in the hadrons are known one can also deduce the size of the hard hadron-hadron scattering cross section. However, it is not possible within pQCD to determine the final state of a hard reaction since the hadronization of the reaction products involves small momentum transfers of only a few hundred MeV. The strong coupling constant becomes large at these low energies and perturbation theory breaks down.

Furthermore, hard interactions make up only for a small fraction of the total hadronic cross section because of the smallness of the strong coupling constant at large momentum transfers (asymptotic freedom).

Regge theory [Reg59, Reg60] provides us with a framework to describe the interaction of hadrons at large energies and momentum transfer of the order of a hadronic mass scale without the assumption of an underlying field theory, solely by making use of Lorentz invariance, unitarity and analyticity of the scattering matrix. A profound discussion of Regge theory and its applications can be found in Ref. [Col77].

### 2.1.1 Scattering Matrix

Consider a set of free particles which are described by the physical state vector $|i\rangle$ and scatter into a set of outgoing particles characterized by the state vector $|f\rangle$. In our studies the initial state always consists of only two particles whereas the final state can in principle contain an arbitrarily large number of ejectiles which is only constrained by the conservation of energy, momentum and quantum numbers. The $(fi)$-th element of the scattering matrix $\mathcal{S}$ is defined as the overlap of the asymptotic initial and final state in the scattering process:

$$\mathcal{S}_{fi} = \langle f|i\rangle.$$

One can separate the trivial part of the scattering matrix by introducing the $T$ matrix:

$$\mathcal{S} = \mathbb{1} + iT \tag{2.1}$$

whose elements can be expressed in terms of the invariant amplitude $\mathcal{M}$:

$$\langle\{\vec{p}_f\}|iT|\vec{p}_a, \vec{p}_b\rangle = (2\pi)^4 \delta^{(4)}\left(p_a + p_b - \sum_f p_f\right) i\mathcal{M}\left(p_a, p_b \to \{p_f\}\right). \tag{2.2}$$

Here $\vec{p}_a$ ($p_a$) and $\vec{p}_b$ ($p_b$) denote the (four-)momenta of the incoming collision partners and $\{\vec{p}_f\}$ ($\{p_f\}$) are the (four-)momenta of the final-state particles. The delta function
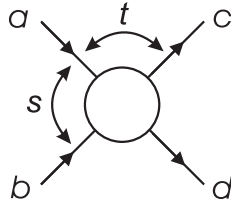
Figure 2.1: Mandelstam variables $s$ and $t$ in the scattering process $ab \to cd$.

in Eq. (2.2) reflects energy and momentum conservation. All particles are assumed to be on their mass shell ($p^0 = E = \sqrt{m^2 + \vec{p}^2}$) and the normalization is chosen to be the same as in Ref. [Pes95]:

$$\langle \vec{p}' | \vec{p} \rangle = 2E(2\pi)^3 \delta^{(3)} \left( \vec{p} - \vec{p}' \right).$$

In the following three sections we postulate three properties of the scattering matrix and discuss their consequences.

### 2.1.2 Lorentz invariance

**Postulate 1:** The $\mathcal{S}$ matrix is Lorentz invariant, i.e. it can be expressed as a function of Lorentz-invariant Mandelstam variables.

This postulate seems quite reasonable since the outcome of a scattering process should not depend on the reference frame one is using for the description. Lorentz invariant quantities can be obtained by squaring the sums and differences of the four-momenta of the colliding particles and the reaction products. The Mandelstam variables for a $2 \to 2$ scattering process (see Fig. 2.1) for example are defined as:

$$
\begin{aligned}
s &= (p_a + p_b)^2 \\
t &= (p_c - p_a)^2 \\
u &= (p_d - p_a)^2.
\end{aligned}
$$

Hence, $s$ is just the center-of-mass energy squared, $t$ is the square of transfered four-momentum and $u$ is related to $s$ and $t$ via the relation:

$$s + t + u = m_a^2 + m_b^2 + m_c^2 + m_d^2. \tag{2.3}$$

In the case that the initial or final state consists of more than two particles one can define additional invariants in an analogous way [Byk73].

### 2.1.3 Unitarity

**Postulate 2:** The $\mathcal{S}$ matrix is unitary: $\mathcal{S}^\dagger \mathcal{S} = \mathbb{1}$.

Postulate 2 is equivalent to the conservation of probability, i.e. the probability for an initial state to end up in a particular final state, summed over all possible final states,
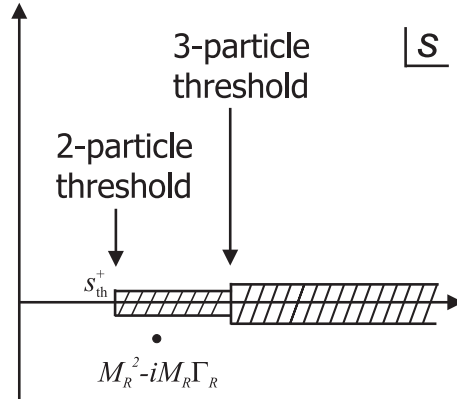
Figure 2.2: Singularities of the scattering amplitude $\mathcal{M}$ in the (right) complex $s$ plane.

must be unity. As a consequence this leads to the optical theorem which relates the imaginary part of the forward-scattering amplitude to the total cross section:

$$\mathrm{Im}\mathcal{M}(p_a, p_b \to p_a, p_b) = 2p_{\mathrm{cm}}\sqrt{s}\,\sigma_{\mathrm{tot}}(ab \to X). \tag{2.4}$$

Here $p_{\mathrm{cm}}$ denotes the center-of-mass momentum of the incoming particles:

$$p_{\mathrm{cm}} = \sqrt{\frac{(s - m_a^2 - m_b^2)^2 - 4m_a^2 m_b^2}{4s}}.$$

The derivation of Eq. (2.4) as well as further forms of the optical theorem for different scattering amplitudes can be found in Appx. A.

### 2.1.4  Analyticity

**Postulate 3:** The $\mathcal{S}$ matrix is an analytic function of Lorentz invariants with only those singularities required by unitarity.

It can be shown [Col77] that this analyticity property follows from causality, i.e. that two spacelike separated regions do not influence each other.

The analyticity structure of the amplitude $\mathcal{M}$ in the complex $s$ plane can be determined using the optical theorem (2.4). Two particles can either scatter into a bound state with mass $M_R$ and width $\Gamma_R$ or, at large enough energies, into a final state that consists of two or more particles. For massive scatterers the cross section $\sigma_{\mathrm{tot}}$ is zero below a minimum energy $s_{\mathrm{th}}^+$ and $\mathcal{M}$ is real on the positive real $s$ axis for $s < s_{\mathrm{th}}^+$ because of relation (2.4). The latter allows the application of the Schwarz reflection principle [Br95]

$$\mathcal{M}(s^*, t) = \mathcal{M}(s, t)^*$$

throughout the domain of analyticity. Hence, we obtain for real $s$ and $\epsilon$ the so-called $s$-channel discontinuity

$$
\begin{aligned}
\lim_{\epsilon \to 0} \mathrm{Im}\mathcal{M}(s + i\epsilon, t) &= \frac{1}{2i} \lim_{\epsilon \to 0} \left( \mathcal{M}(s + i\epsilon, t) - \mathcal{M}(s + i\epsilon, t)^* \right) \\
&= \frac{1}{2i} \lim_{\epsilon \to 0} \left( \mathcal{M}(s + i\epsilon, t) - \mathcal{M}(s - i\epsilon, t) \right) \\
&\equiv \mathrm{Disc}_s \mathcal{M}(s, t).
\end{aligned}
\tag{2.5}
$$
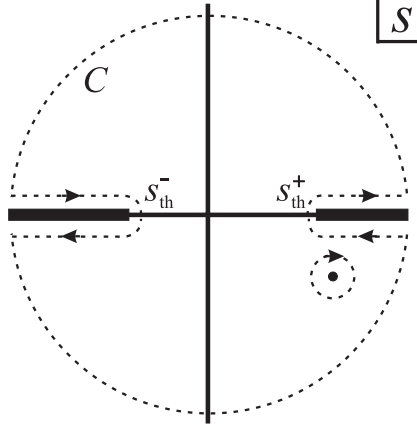
Figure 2.3: Contour of the integral in Eq. (2.8).

The amplitude $\mathcal{M}$ thus has a branch cut along the real $s$ axis above the two-particle threshold $s_{\mathrm{th}}^+$. The bound states lead to poles in the complex $s$ plane at positions $M_R^2 - iM_R\Gamma_R$ (see also Ref. [Col77]) as depicted in Fig. 2.2.

**Crossing symmetry**

One of the consequences of analyticity is crossing symmetry. For example one gets from the amplitude $\mathcal{M}_{ab\to cd}$ by analytical continuation from the physical region $s > 0$ and $t, u < 0$ to the region $t > 0$ and $s, u < 0$ the scattering amplitude for the $t$-channel process $a\bar{c} \to \bar{b}d$:

$$\mathcal{M}_{a\bar{c}\to\bar{b}d}(s,t,u) = \mathcal{M}_{ab\to cd}(t,s,u). \qquad (2.6)$$

In an analogous way one has for the $u$ channel

$$\mathcal{M}_{a\bar{d}\to\bar{b}c}(s,t,u) = \mathcal{M}_{ab\to cd}(u,t,s). \qquad (2.7)$$

Using Eq. (2.3) one finds from the physical threshold $u_{\mathrm{th}}^+$ of the $u$-channel process (2.7) that the $s$-channel amplitude must also have a cut along the negative real $s$ axis with a branch point at $s_{\mathrm{th}}^- = \sum_i m_i^2 - t - u_{\mathrm{th}}^+$.

**Dispersion relations**

Another useful consequence of analyticity is the so-called dispersion relation that makes it possible to reconstruct the real part of an amplitude from its imaginary part. Starting from the Cauchy integral formula [Br95]

$$\mathcal{M}(s,t) = \frac{1}{2\pi i} \oint_C \frac{\mathcal{M}(s',t)}{s'-s} ds', \qquad (2.8)$$

where $C$ is a contour that does not enclose any of the singularities of $\mathcal{M}$ (see Fig. 2.3) one ends up with the dispersion relation

$$
\begin{aligned}
\mathcal{M}(s,t) &= \frac{1}{2\pi i}\left( \int_{\infty}^{s_{\mathrm{th}}^{+}} \frac{\mathcal{M}(s'-i\epsilon,t)}{s'-s}ds' + \int_{s_{\mathrm{th}}^{+}}^{\infty} \frac{\mathcal{M}(s'+i\epsilon,t)}{s'-s}ds' \right. \\
&\quad \left. + \int_{-\infty}^{s_{\mathrm{th}}^{-}} \frac{\mathcal{M}(s'+i\epsilon,t)}{s'-s}ds' + \int_{s_{\mathrm{th}}^{-}}^{-\infty} \frac{\mathcal{M}(s'-i\epsilon,t)}{s'-s}ds' \right) \\
&= \frac{1}{\pi}\left( \int_{s_{\mathrm{th}}^{+}}^{\infty} \frac{\mathrm{Im}\mathcal{M}(s',t)}{s'-s}ds' + \int_{-\infty}^{s_{\mathrm{th}}^{-}} \frac{\mathrm{Im}\mathcal{M}(s',t)}{s'-s}ds' \right)
\end{aligned}
\tag{2.9}
$$

provided $\mathcal{M}(s,t)$ tends to zero as $|s|\to\infty$. In the last step we have used the discontinuity Eq. (2.5). In the dispersion relation (2.9) we have assumed no contributions from bound state poles which generally add extra contributions. In the second integral the imaginary part of the amplitude for $s < s_{\mathrm{th}}^{-}$ can be obtained by crossing from the discontinuity of the corresponding $u$ channel process.

In the case that the amplitude $\mathcal{M}(s,t)$ does not vanish for $|s|\to\infty$ one has to divide it by as many factors of $s - s_i$ as necessary to produce a vanishing contribution from the semi circles of $C$ at infinity. Making only one of these so-called subtractions at $s = s_0$ one ends up with the subtracted dispersion relation

$$
\begin{aligned}
\mathcal{M}(s,t) &= \mathcal{M}(s_0,t) + \frac{(s-s_0)}{\pi}\left( \int_{s_{\mathrm{th}}^{+}}^{\infty} \frac{\mathrm{Im}\mathcal{M}(s',t)}{(s'-s)(s'-s_0)}ds' + \right. \\
&\quad \left. \int_{-\infty}^{s_{\mathrm{th}}^{-}} \frac{\mathrm{Im}\mathcal{M}(s',t)}{(s'-s)(s'-s_0)}ds' \right).
\end{aligned}
\tag{2.10}
$$

Together with the optical theorem (2.4) we now have a tool at hand to deduce the imaginary and the real part of the forward-scattering amplitude $\mathcal{M}(s, t=0)$ from the total cross section.

### 2.1.5   Reggeon exchange

In 1959 Regge [Reg59] suggested to regard the angular momentum in non-relativistic potential scattering as a complex variable. This led to the foundation of a new concept for dealing with scattering amplitudes which in the following years became a very useful tool in high-energy particle physics. The interested reader can find a detailed introduction to Regge theory in the book of Collins [Col77]. In Appx. B we present the construction of the Regge amplitude, i.e. the scattering amplitude in the kinematic limit $s \gg t$, for the scattering process $ab \to cd$.

**Regge amplitude**

The Regge amplitude which is diagrammatically illustrated in Fig. 2.4 can be written in the factorized form

$$
\mathcal{M}_{ab\to cd}(s,t) = \frac{\gamma_{ac}(t)\gamma_{bd}(t)}{\Gamma(\alpha(t))} \frac{(\eta + e^{-i\pi\alpha(t)})}{\sin(\pi\alpha(t))}\left( \frac{s}{s_0} \right)^{\alpha(t)}.
\tag{2.11}
$$
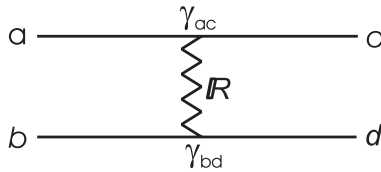
Figure 2.4: Regge exchange diagram (see Eq. (2.11)).

As discussed in Appx. B it can be viewed as the exchange of an object with 'angular momentum' $\alpha(t)$ which is called Reggeon. Since $\alpha(t)$ does not need to be integer (or half integer) and is a function of the Mandelstam variable $t$, the Reggeon is not a real particle. The Reggeon exchange amplitude can rather be seen as the superposition of all particle exchanges in the $t$ channel that are quantum mechanically allowed. The Sommerfeld-Watson transformation (B.3) includes all partial waves in the $t$ channel. The amplitude (2.11) is thus not restricted to the exchange of some isolated poles but includes a whole family of particles with the same internal quantum numbers (baryon number $B$, strangeness $S$, charge conjugation $C$, parity $P$, $G$ parity, charge $Q$, signature $\eta$, etc.) but with different spin. The factorization of the Regge amplitude into a coupling $\gamma_{ac}(t)$ of the Reggeon to particles $a$ and $c$, a similar coupling $\gamma_{bd}(t)$ between particles $b$ and $d$, and a universal contribution from the Reggeon exchange is verified by various experiments.

Using the Regge amplitude (2.11) one can immediately write down the ratio of the real to imaginary part of the scattering amplitude at large energies:

$$\rho = \frac{\mathrm{Re}\mathcal{M}}{\mathrm{Im}\mathcal{M}} = -\frac{\eta + \cos(\pi\alpha(t))}{\sin(\pi\alpha(t))}. \tag{2.12}$$

**Regge trajectories**

If $\alpha(t)$ passes through an integer the 'Reggeon propagator' $[\sin(\pi\alpha(t))]^{-1}$ in Eq. (2.11) produces a pole in the amplitude. For positive integers this can be understood as the $t$-channel exchange of a particle with integer spin $J_i$ and mass $m_i = \sqrt{t}$, where $\alpha(m_i^2) = J_i$. The nonsense poles at negative integer values of 'spin' are canceled by the factor $\Gamma(\alpha(t))^{-1}$. It has phenomenologically been observed by Chew and Frautschi [Che61, Che62] that the spins of a set of resonant states are linear functions of their masses squared (see Fig. 2.5), i.e.

$$\alpha(t) = \alpha(0) + \alpha' t,$$

for positive values of $t$. For all observed baryon and meson trajectories the slope turns out to be $\alpha'_{\mathbb{R}} \approx 0.9$ GeV$^{-2}$. We show in Sec. 2.3 how this linear behavior and the universal slope is related to the underlying partonic substructure and the confining potential of all hadrons. In addition, the trajectories of mesons that contain only light quarks (up $u$ and down $d$) have the same intercept $\alpha_{\mathbb{R}}(0) \approx 0.44$ as can be seen for example from the $\rho$-, $\omega$-, $f$- and the $a$-trajectory in Fig. 2.5. The intercepts of meson trajectories that involve heavier quarks are in general smaller. This has also a straight-forward interpretation in the parton model of Regge exchange as we show later.
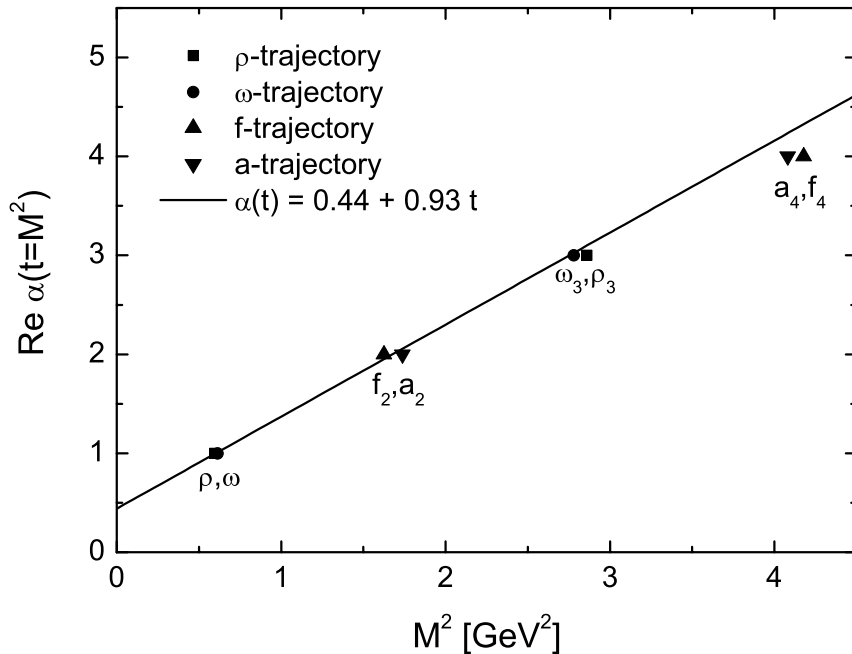
Figure 2.5: Chew-Frautschi plot of the $\rho$-, $\omega$-, $f$- and the $a$-trajectory. The linear fit is taken from Ref. [Don92]: $\alpha_{\mathbb{R}}(t) = 0.44 + 0.93t$. The masses of the particles are taken from Ref. [PDG02].

The functional form of the Regge trajectories for negative values of $t$, i.e. in the physical $t$ region, can be deduced from the asymptotic $s$ dependence of the differential cross section

$$\frac{d\sigma}{dt} \approx \frac{|\mathcal{M}(s,t)|^2}{16\pi s^2} \sim s^{2\alpha(0)-2\alpha' t-2} \tag{2.13}$$

of a scattering process with the $t$-channel exchange of the corresponding internal quantum numbers. For example, to extract the functional form of the $\rho$ trajectory for negative $t$ one has to consider a process in which isospin $I = 1$ is exchanged in the $t$ channel, such as

$$\pi^- p \to \pi^0 n.$$

It turns out that the linearity continues for negative values of $t$ with the same values for the slope and the intercept.

**Parton model of Reggeon exchange**

The resonances which lie on the Regge trajectories in Fig. 2.5 are quark-antiquark bound states. One can therefore try to understand Reggeon exchange in terms of the building blocks of hadrons namely quarks and gluons. Fig. 2.6 suggests a physical description [Col84, Col77] of the Reggeon exchange process in meson-baryon scattering. In the process depicted on the left-hand side of Fig. 2.6 two quarks $q_2$ and $q_3$ of the approaching hadrons attract each other and slow down by radiating many soft virtual gluons. By absorbing the gluons emitted from the other quark, each quark can reverse
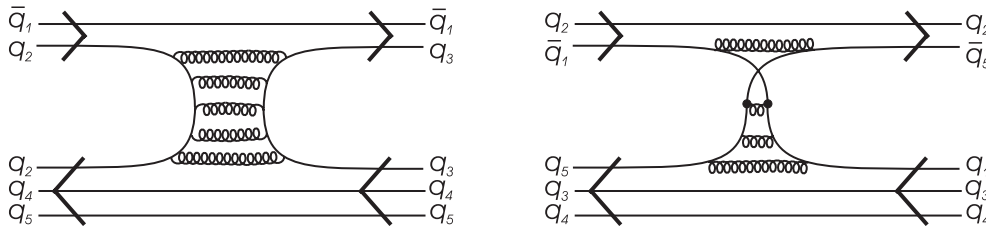
Figure 2.6: Parton description of Reggeon exchange. See text for details. *Left:* A meson ($\bar{q}_1 q_2$) and a baryon ($q_3 q_4 q_5$) exchange the quarks $q_2$ and $q_3$ in the scattering process. *Right:* The antiquark $\bar{q}_1$ from the meson ($\bar{q}_1 q_2$) and the quark $q_1$ from the incoming baryon ($q_1 q_3 q_4$) annihilate into a new quark-antiquark pair $q_5 \bar{q}_5$ and form the meson ($\bar{q}_5 q_2$) and baryon ($q_3 q_4 q_5$).

its direction of motion, and thus they can be exchanged between the hadrons. If a quark $q_1$ from the baryon and an antiquark $\bar{q}_1$ from the meson attract each other as shown on the right-hand side of Fig. 2.6, they can annihilate and subsequently form a new quark-antiquark pair $q_5 \bar{q}_5$ leaving again behind two colorless hadrons in the final state.

In contrast to the hard parton scattering which we discuss in Sec. 2.2.4 each gluon in the scattering processes of Fig. 2.6 carries only a momentum transfer of the order of the hadronic mass scale. Because of the running coupling constant of QCD the cross section for Reggeon exchange is therefore much larger than the direct annihilation of a quark and an antiquark of the projectiles into a single high-energy gluon.

Since heavier quarks (strange $s$, charm $c$, bottom $b$) are harder to 'turn around' one might expect a smaller cross section for a scattering process involving the exchange of a $S = 1$ trajectory. This is indeed the case, as the intercept of the $K$ trajectory is $\alpha(0) = -0.2$ and that of the $K^*$ trajectory is $\alpha(0) = 0.3$. These intercepts lead to a smaller cross section (2.13) than the exchange of the trajectories shown in Fig. 2.5 which have an intercept $\alpha(0) = 0.44$.

## 2.2 Hadronic cross sections

Following the procedure of the PYTHIA model [Sjö01a, Sjö01b] which we later use in our Monte Carlo simulation, we distinguish between four event classes that can occur in the scattering of two hadrons $a$ and $b$ at high energies. The first possibility is elastic scattering $ab \to ab$ which is discussed in Sec. 2.2.2. The second possibility is diffractive excitation ($ab \to Xb$, $ab \to aX$, $ab \to X_1 X_2$) in which one or both hadrons get excited via a small momentum transfer (small means of the order of the hadronic mass scale) but keep their intrinsic quantum numbers. The decay products of the two excited hadrons thus have a large rapidity gap. This event class is explained in Sec. 2.2.3. At large enough energies there is also the possibility of a hard scattering taking place between the partons, i.e. the quarks and gluons inside the hadrons. These hard non-diffractive processes can be described with the help of perturbative QCD as sketched in Sec. 2.2.4. Last but not least, there are the events which we refer to as soft non-diffractive that cannot be treated within perturbative QCD. How one has to deal
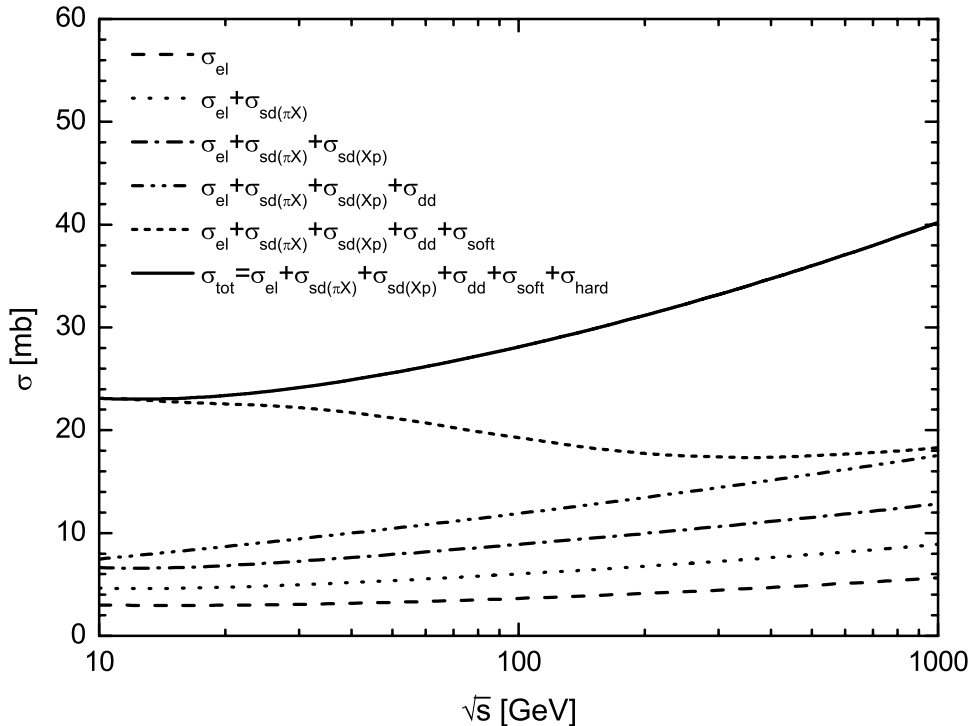
Figure 2.7: The composition of the total $\pi p$ cross section according to Ref. [Sch94].

with this last event class is explained in Sec. 2.2.5.

Hence, we subdivide the total cross section according to

$$\sigma_{\text{tot}}^{ab} = \sigma_{\text{el}}^{ab} + \sigma_{\text{sd(Xb)}}^{ab} + \sigma_{\text{sd(aX)}}^{ab} + \sigma_{\text{dd}}^{ab} + \sigma_{\text{nd}}^{ab},$$

where $\sigma_{\text{el}}$ is the elastic cross section, $\sigma_{\text{sd}}$ and $\sigma_{\text{dd}}$ are the single and double diffractive cross sections, respectively, and the non-diffractive cross section is split into a hard and a soft part: $\sigma_{\text{nd}} = \sigma_{\text{hard}} + \sigma_{\text{soft}}$. As an example we illustrate the contributions of the different event classes to the total pion-proton cross section in Fig. 2.7.

## 2.2.1 Total cross section

The total cross section is related to the forward-scattering amplitude via the optical theorem (2.4). If Reggeon exchange was the only process that contributes to forward scattering at large values of $s$ one would get from the Regge amplitude (2.11) the following asymptotic behavior of the total cross section:

$$\sigma_{\text{tot}} \approx \frac{1}{s} \text{Im} \mathcal{M}(s, t = 0) \sim s^{\alpha(0)-1} \tag{2.14}$$

with the intercept $\alpha(0)$ of the exchanged Reggeon. As discussed above the Regge trajectories in general have $\alpha(0) \lesssim 1/2$ and thus lead to a falling cross section with increasing $s$. One expects this behavior from the parton model of Reggeon exchange since the probability for two outgoing hadrons mopping up all the virtual glue in the way depicted in Fig. 2.6 is rather small at high energies.
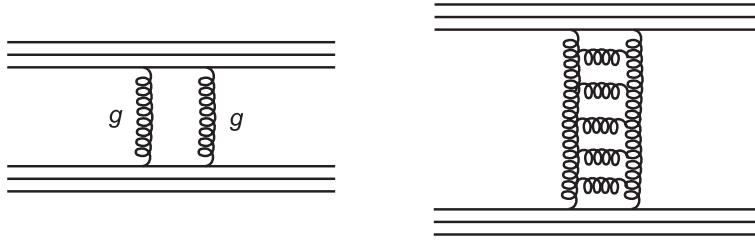
Figure 2.8: Parton description of Pomeron exchange in elastic scattering. *Left*: Fundamental two gluon exchange diagram. *Right*: Exchange of gluon ladders may sum up to produce a Pomeron trajectory.

However, it is observed experimentally that total cross sections rise slowly as $s$ increases (cf. Fig. 2.7). It has been shown in Ref. [Fol63] that if the cross section for a particular scattering process does not fall as $s$ increases, the process must be dominated by the exchange of vacuum quantum numbers ($I = 0$, $C = +$, $Q = 0$, ...). If one therefore attributes the increasing cross section to the exchange of a single Reggeon in the forward-scattering amplitude it must carry the quantum numbers of the vacuum and have an intercept $\alpha_{\mathbb{P}}(0)$ that is larger than 1. This object is called the Pomeron, named after its inventor I. Y. Pomeranchuk.

At high energies the experimental data for all total cross sections, e.g. $pp$, $p\bar{p}$, $pn$, $\pi^{\pm}p$, $K^{\pm}p$ but also $\gamma p$, can be fitted by the simple ansatz [Don92]

$$\sigma_{\text{tot}}^{ab} = X_{ab}s^{\epsilon} + Y_{ab}s^{-\eta} \tag{2.15}$$

with

$$\epsilon = 0.0808 \qquad \eta = 0.4525.$$

The fact that the photon-proton cross section also perfectly fits into the scheme of the hadronic cross sections can already be seen as a hint for the hadronic structure of the photon. The second term in Eq. (2.15) clearly arises from the exchange of the $\rho$-, $\omega$-, $f$- and the $a$-trajectory which have the intercept $\alpha_{\mathbb{R}}(0) = 0.44$ as can be seen from Fig. 2.5. The small deviation from the exponent 0.56 that one expects according to Eq. (2.14) arises from multi Reggeon exchange [Don92]. The first term in the expression (2.15) stems from Pomeron exchange and determines the intercept of the Pomeron trajectory $\alpha_{\mathbb{P}}(0) \approx 1.08$. Since the Pomeron is even under charge conjugation it couples with the same strength to particle and antiparticle. This is indeed seen in the experimentally observed coefficients: $X_{pp} = X_{p\bar{p}}$, $X_{\pi^+p} = X_{\pi^-p}$ and $X_{K^+p} = X_{K^-p}$. In addition, one finds $X_{pn} = X_{pp}$ which reflects the fact that the Pomeron has isospin $I = 0$.

The experimentally observed approximate flavor blindness of the Pomeron exchange, e.g. $X_{\pi^+p} \approx X_{K^+p}$, and the fact that the known trajectories involving quark exchange all have an intercept smaller that $1/2$ suggest that the Pomeron represents the exchange of gluons. The fundamental diagram for Pomeron exchange in the forward-scattering amplitude, or more general in elastic scattering, is shown on the left-hand side of Fig. 2.8. It represents the exchange of two gluons between the scatterers. Single-gluon exchange would lead to two color octets as we discuss in more detail in Sec. 2.2.5. The exchange of a second gluon is necessary to produce two outgoing color

singlets. Inserting gluons to make ladders like on the left-hand side of Fig. 2.8 may finally reproduce the Pomeron trajectory [For97]. The Pomeron that we have discussed so far cannot be calculated from QCD since it involves soft momentum transfers. It is purely phenomenological and its slope and intercept are extracted from experimental data. The Pomeron that one calculates in perturbative QCD [For97] is *hard* and has a different slope and intercept than the soft Pomeron. It is important for the description of scattering processes at larger $t$ and cannot be extrapolated to zero $t$.

The scattering process in Fig. 2.8 might be regarded as a Pomeron exchange between two quarks with the remaining quarks in the hadrons being simply spectators. From the different number of ways of pairing the valence quarks one gets for the total cross sections of meson-meson, meson-baryon and baryon-baryon scattering: $\sigma_{\text{tot}}^{mm} = 4\sigma_{\text{tot}}^{qq}$, $\sigma_{\text{tot}}^{mb} = 6\sigma_{\text{tot}}^{qq}$ and $\sigma_{\text{tot}}^{bb} = 9\sigma_{\text{tot}}^{qq}$. Hence, in this additive quark model the ratio of, e.g., the coefficients $X_{\pi p}$ and $X_{pp}$ should be 2/3 which is close to the experimental value 0.63. A further justification of the assumption that the Pomeron couples to a quark inside a hadron like a point particle comes from the $t$ dependence of elastic meson-baryon and baryon-baryon scattering. We postpone this discussion to the next Section.

### 2.2.2  Elastic scattering

Elastic scattering above the resonance region can be described by the sum of the Reggeon and the Pomeron exchange amplitudes. As discussed in the last Section the Reggeon amplitude falls off at large $s$ so that the elastic scattering amplitude at high energies is dominated by Pomeron exchange and can be written with the help of Eq. (2.11) and (2.12) as

$$
\begin{aligned}
\mathcal{M}_{ab \to ab}(s,t) &= \beta_{a\mathbb{P}}(t)\beta_{b\mathbb{P}}(t)(i + \rho)\left(\frac{s}{s_0}\right)^{\alpha_{\mathbb{P}}(t)} \\
&\approx i\beta_{a\mathbb{P}}(t)\beta_{b\mathbb{P}}(t)\left(\frac{s}{s_0}\right)^{\alpha_{\mathbb{P}}(t)}.
\end{aligned}
\tag{2.16}
$$

In the last step we have neglected the real part of the forward-scattering amplitude since inserting $\alpha_{\mathbb{P}}(0)$ into Eq. (2.12)[1] yields a ratio of only $\rho = 13\%$. The new vertex functions $\beta(t)$ denote the coupling of particle $a$ and $b$ to the Pomeron and are obviously related via the optical theorem to the fit parameter $X_{ab} = \beta_{a\mathbb{P}}(0)\beta_{b\mathbb{P}}(0)$ of Eq. (2.15).

The slope of the Pomeron trajectory can therefore be determined from the large $s$ dependence of the differential elastic cross section at different values of $t$, cf. Eq. (2.13). A fit to the experimental data on elastic $pp$ and $p\bar{p}$ scattering at large energy gives $\alpha'_{\mathbb{P}} = 0.25$ GeV$^{-2}$. Using this slope one sees that $\alpha_{\mathbb{P}}(t)$ reaches the value 2 at $t = 3.7$ GeV$^2$ which means that there should exist a spin 2 particle with the quantum numbers of the vacuum and a mass of $\sqrt{3.7\,\text{GeV}^2} = 1.9$ GeV. A glueball candidate with this mass has been found at CERN [Aba94] meaning that the right-hand side of Fig. 2.8 can be interpreted as the exchange of a flavorless particle made solely from gluons just as the particles on the Regge trajectories in Sec. 2.1.5 arose from the binding of quarks.

From the differential elastic cross section one can also determine the $t$ dependence of the vertex functions $\gamma(t)$ in Eq. (2.11). They turn out to be proportional to the

---

[1]The Pomeron has even signature $\eta = +1$.

electromagnetic form factor which supports the assumption that the Pomeron couples to hadrons like the photon, namely as a point particle.

At not too large momentum transfer the $t$ dependence of the experimental differential cross section can be approximated by a simple exponential fall-off. Neglecting again the ratio $\rho$ of real to imaginary part of the forward-scattering amplitude one gets with the help of the optical theorem (2.4):

$$\begin{aligned} \frac{d\sigma_{\mathrm{el}}}{dt} &= \frac{\sigma_{\mathrm{tot}}^2}{16\pi}(1+\rho^2)e^{B_{\mathrm{el}}t} \\ &\approx \frac{\sigma_{\mathrm{tot}}^2}{16\pi}e^{B_{\mathrm{el}}t}. \end{aligned} \quad (2.17)$$

Unless we state something different, the elastic slope $B_{\mathrm{el}}$ is parametrized in the same way as in the PYTHIA model [Sjö01b]:

$$B_{\mathrm{el}} = 2b_a + 2b_b + 4s^\epsilon - 4.2$$

with $s$ given in units of GeV$^2$ and $B_{\mathrm{el}}$ in GeV$^{-2}$. The constants $b_x$ arise from the form factors of the particles involved in the scattering process: $\beta_{x\mathbb{P}}(t) = \beta_{x\mathbb{P}}(0)\exp(b_x t)$. The values are taken from Ref. [Sjö01b]: $b_p = 2.3$, $b_{\pi,\rho,\omega,\phi} = 1.4$ and $b_{J/\psi} = 0.23$. The $s$ dependence of the slope parameter reproduces the experimentally observed ratio $\sigma_{\mathrm{el}}/\sigma_{\mathrm{tot}}$. In the following we use the slope parameter $b_p$ for all baryons and $b_{\pi,\rho,\omega,\phi}$ for all mesons except for the $J/\psi$.

There is a second relation between $\sigma_{\mathrm{el}}$ and $\sigma_{\mathrm{tot}}$ besides Eq. (2.17) which can be derived using the finite mass sum rule [Gou83] of diffractive interactions. The latter relates the high mass and the low mass diffractive cross sections (including elastic scattering) and is an extension of the finite energy sum rule which states that the description of the total cross section via $s$-channel resonance production and decay (which works best at low energies) and the description via $t-$channel Reggeon exchanges (which works at high energies) are equivalent. As a result the average behavior of the total cross section in the resonance region is well described by the extrapolation of the smooth high-energy behavior into low energies. This phenomenon is usually referred to as duality. From the finite mass sum rule one can obtain the relation [Gou83]:

$$\sigma_{\mathrm{tot}} \sim \int_0^{-\infty} t\left(\frac{d\sigma_{\mathrm{el}}}{dt}\right)dt. \quad (2.18)$$

If one again assumes that the differential elastic cross section is of the form $d\sigma_{\mathrm{el}}/dt = A\exp[B_{\mathrm{el}}t]$ the right-hand side of Eq. (2.18) can be integrated by parts and one gets

$$\sigma_{\mathrm{tot}} \sim \frac{\sigma_{\mathrm{el}}}{B_{\mathrm{el}}}. \quad (2.19)$$

On the other hand the integration of Eq. (2.17) leads to the relation

$$\sigma_{\mathrm{el}} \sim \frac{\sigma_{\mathrm{tot}}^2}{B_{\mathrm{el}}}. \quad (2.20)$$

Combining Eqs. (2.19) and (2.20) and eliminating $B_{\mathrm{el}}$ one finally has

$$\sigma_{\mathrm{el}} = c\,\sigma_{\mathrm{tot}}^{3/2} \quad (2.21)$$

where the constant $c$ is the same for all hadrons. Relationship (2.21) has been compared to high-energy data in Ref. [Gou83] and was found to hold remarkably well.

$$E_c \frac{d^3\sigma}{d^3p_c} = \frac{1}{2s} \sum_X \left| \vcenter{\hbox{}} \right|^2 = \frac{1}{2s} \sum_X \vcenter{\hbox{}} = \frac{1}{2s} \sum_X \vcenter{\hbox{}} = \frac{1}{s} \operatorname{Disc}_{M_X^2} \vcenter{\hbox{}}$$

Figure 2.9: Pictorial representation of Mueller's optical theorem. In the first step the definition of the differential cross section for the inclusive process $ab \rightarrow cX$ has been used. In the second step we use the completeness relation, then cross $c \rightarrow \bar{c}$ and in the last step use the unitarity relation for the $3 \rightarrow 3$ amplitude.

### 2.2.3 Diffractive excitation

In addition to elastic scattering the Pomeron exchange depicted in Fig. 2.8 can lead to the excitation of quarks so that the outgoing particles have the same flavor content but higher masses than the incoming hadrons. In the process of single diffractive dissociation $ab \rightarrow aX$ one of the incident particles remains unchanged and just scatters through a small angle by emitting a Pomeron. By absorbing the Pomeron the other incident particle $b$ receives enough energy to break up into its constituent partons which then hadronize to produce a cluster of hadrons $X$. In the case that both incident particles break up, $ab \rightarrow X_1 X_2$ one talks about double diffractive excitation.

Diffractive events are characterized by a large rapidity gap between the parent hadron $a$ and the hadronic system $X$ (between $X_1$ and $X_2$ in case of double diffractive scattering). Since the scattering angle is small ($|t| \ll s$) the rapidity

$$y = \frac{1}{2} \ln \left( \frac{E + p_z}{E - p_z} \right)$$

of the parent hadron is large and positive (provided the $z$ direction is chosen as the incident direction of particle $a$) while the particles in the hadronic subsystem $X$ are moving almost parallel to the negative $z$ axis and therefore have large negative rapidities. The subsystem $X$ is therefore often called the beam jet of particle $b$ while in double diffractive events $X_1$ and $X_2$ are the beam remnants of $a$ and $b$ respectively.

The terminology 'diffractive' arises from the angular distribution of diffractively (but also elastically) scattered hadrons at high energies which shows a zero-degree peak followed by a dip and a secondary maximum very much like the diffraction of light through a hole.

One can make use of Mueller's generalized optical theorem [Mue70] to relate the differential cross section of the inclusive reaction $ab \rightarrow cX$ to the elastic forward amplitude of the three-body process $ab\bar{c} \rightarrow ab\bar{c}$:

$$E_c \frac{d^3\sigma}{d^3p_c}(ab \rightarrow cX) \approx \frac{1}{s} \operatorname{Disc}_{M_X^2} \mathcal{M}(ab\bar{c} \rightarrow ab\bar{c})$$

where the discontinuity has to be taken across the $M_X^2 = (p_a + p_b + p_{\bar{c}})^2 = (p_a + p_b - p_c)^2$ cut of the elastic $3 \rightarrow 3$ amplitude. The pictorial derivation of Mueller's theorem is given in Fig. 2.9 and can directly be compared with the representation of the optical theorem in Fig. A.1.

Using Mueller's theorem one can directly read off the form of the single diffractive cross section for the process $ab \rightarrow aX$ from the factorized Pomeron interaction shown
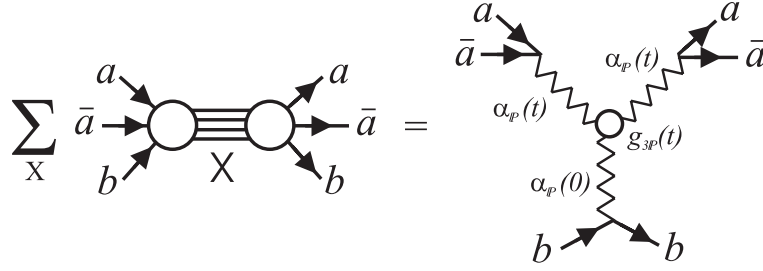
Figure 2.10: Triple Pomeron amplitude for the single diffraction reaction $ab \to aX$.

in Fig. 2.10:

$$\frac{d^2\sigma_{\text{sd}}}{dt\,dM_X^2} = \frac{g_{3\mathbb{P}}(t)}{16\pi M_X^2}\beta_{a\mathbb{P}}(t)^2\beta_{b\mathbb{P}}(0)\left(\frac{s}{M_X^2}\right)^{2(\alpha_\mathbb{P}(t)-1)}\left(\frac{M_X^2}{s_0}\right)^{\alpha_\mathbb{P}(0)-1} \tag{2.22}$$

where $s = (p_a + p_b)^2$ is the total center-of-mass energy squared and $t = (p_a - p_a')^2 = (p_a+p_{\bar{a}})^2$ denotes the four-momentum transfer between the parent hadron $a$ and hadron $b$. The vertex functions are the same as in elastic scattering and take the form $\beta_{a\mathbb{P}}(t) = \beta_{a\mathbb{P}}(0)\exp(b_a t)$ for small values of $t$. Strictly speaking Eq. (2.22) is only valid for intermediate $M_X$, i.e. in the so-called triple Regge limit ($M_X^2 \to \infty, s/M_X^2 \to \infty$). However, for lack of better alternatives it is usually used over a wider range of masses.

The form of the double diffractive cross section can be derived in a similar way [Sch94]:

$$\frac{d^3\sigma_{\text{dd}}}{dt\,dM_1^2\,dM_2^2} = \frac{g_{3\mathbb{P}}^2(t)}{16\pi M_1^2 M_2^2}\beta_{a\mathbb{P}}(0)\beta_{b\mathbb{P}}(0)$$
$$\times \left(\frac{ss_0}{M_1^2 M_2^2}\right)^{2(\alpha_\mathbb{P}(t)-1)}\left(\frac{M_1^2}{s_0}\right)^{\alpha_\mathbb{P}(0)-1}\left(\frac{M_2^2}{s_0}\right)^{\alpha_\mathbb{P}(0)-1}.$$

In summary it may be said that Regge theory relates total, elastic and diffractive cross sections and allows for a consistent parametrization of all three quantities. However, elastic and diffractive scattering do not sum up to yield the total cross section as can be seen from Fig. 2.7. The difference $\sigma_{\text{nd}} = \sigma_{\text{tot}} - \sigma_{\text{el}} - \sigma_{\text{sd}} - \sigma_{\text{dd}}$ can be attributed to non-diffractive interactions between the incident hadrons. These remaining non-diffractive events are discussed within the next two sections.

### 2.2.4 Hard scattering

Instead of exchanging many soft gluons as in Reggeon exchange the quarks of the two projectiles can also interact by the exchange of one hard gluon which caries a large momentum as depicted in Fig. 2.11. The struck quarks then change their flight direction with respect to the original axis and fly apart with a considerable large transverse momentum $p_T$. Due to confinement the colored quarks cannot separate over macroscopic distances but hadronize due to the creation of several quark-antiquark pairs from the vacuum. This hadronization process involves only soft momentum transfers
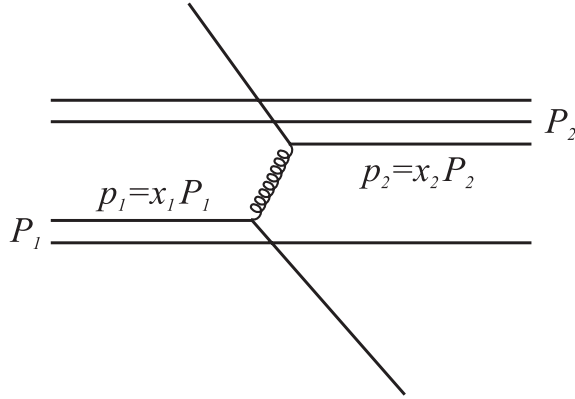
Figure 2.11: Example for a hard scattering process. A quark carrying the fraction $x_1$ of the incoming meson momentum $P_1$ scatters from a quark with momentum $x_2 P_2$ inside the baryon. Initial transverse momenta have been neglected. At large transverse momentum transfers the elementary interaction takes place very rapidly compared to the internal time scale of the hadron wave functions. The scattering cross section is therefore given by the cross section of the leading order QCD subprocess folded with the parton distribution functions $f(x, Q^2)$ (see Eq. (2.23)).

and therefore does not strongly affect the momentum of the leading hadrons, i.e. those involving the quarks of the hard interaction. Therefore, a hard scattering leads to the creation of hadron jets with large $p_T > p_{T \min} \approx 1.5 - 2$ GeV which can be seen in collider experiments at large energies $s$.

From Fig. 2.7 it can be seen that the cross sections for hard interactions between one or several parton pairs (quarks $q$ as well as gluons $g$) of the projectiles such as

$$
\begin{aligned}
q + q' &\rightarrow q + q' \\
q + g &\rightarrow q + g \\
g + g &\rightarrow g + g
\end{aligned}
$$

are small over a large range of $s$. The reason for this is that hard processes by definition involve a large momentum scale $p_T$ at which the QCD coupling constant is small. On the other side, this is what makes the cross sections in principle calculable using perturbative QCD (see for example [Mut87]). To lowest order the differential cross section for hard hadron-hadron scattering is given by

$$
\frac{d\sigma}{dp_T^2} = \sum_{i,j,k} \int dx_1 \int dx_2 \int d\hat{t} f_i(x_1, Q^2 = p_T^2) f_j(x_2, Q^2 = p_T^2) \frac{d\hat{\sigma}_{ij}^k}{d\hat{t}} \delta(p_T^2 - \frac{\hat{t}\,\hat{u}}{\hat{s}}) \quad (2.23)
$$

where $i$ and $j$ label possible incoming partons from the incoming hadrons and $k$ different allowed final-state flavor contents. Eq. (2.23) expresses the hadronic cross section $\sigma$ in terms of the partonic cross section $\hat{\sigma}$ for the underlying QCD subprocess $i + j \rightarrow k$. The Mandelstam variables $\hat{s}$, $\hat{t}$ and $\hat{u}$ of the partons involved in the $2 \rightarrow 2$ scattering are explained in Appx. C. At large enough $p_T^2$ the parton-parton scattering cross section $d\hat{\sigma}/d\hat{t}$ can be calculated within perturbative QCD using Feynman diagram techniques [Owe78].
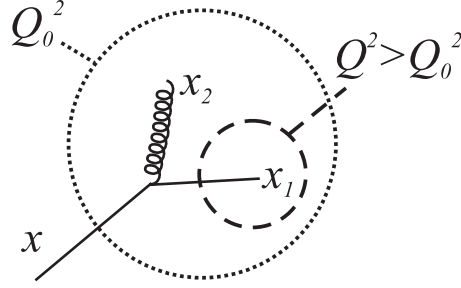
Figure 2.12: Physical origin of scaling violation. A quark with momentum fraction $x$ can radiate a gluon with momentum fraction $x_2 < x$. After the emission of the gluon the quark carries a smaller momentum fraction $x_1 < x$ than before. At low resolution $Q_0^2$ the probe sees the quark and the gluon as a whole. When increasing the resolution from $Q_0^2$ to $Q^2 > Q_0^2$ the probe can see the quark (or the gluon) separately and therefore always probes a smaller momentum fraction.

The parton distribution functions $f_i(x, Q^2)$ in Eq. (2.23) describe the probability that the struck parton $i$ carries a fraction $x$ of the hadron's light-cone momentum $p^+ = E + p_z$ where $E$ and $p_z$ denote energy and momentum of the hadron respectively. The $x$ dependence of the $f_i$ cannot be derived from QCD and has to be taken from experimental measurements. Since the $f_i$ are closely related to the structure functions that are measured in deep inelastic lepton-hadron scattering (cf. Eq. (3.22)) a large number of parton distribution sets for the proton is on the market [Plo93, Plo95]. The up and down quark distributions for the neutron can be related by isospin symmetry to those of the proton measured in deep inelastic scattering: $f_d^n = f_u^p$, $f_u^n = f_d^p$. For the hyperons $\Lambda$, $\Sigma$, $\Xi$ and $\Omega$ one can make a simple ansatz [Sjö01b] and construct an average valence quark distribution $f_{\text{val}} = \frac{1}{3}(f_{u,\text{val}}^p + f_{d,\text{val}}^p)$, assuming that the sea quark and gluon distributions are the same as in the proton. Data on meson parton distributions are only available for the $\pi^{\pm}$ [Glü92]. One therefore has again to make simple assumptions for the parton distributions of the other mesons, e.g., $f_i^{\rho^0} = f_i^{\pi^0} = \frac{1}{2}(f_i^{\pi^+} + f_i^{\pi^-})$ which is motivated by the additive quark model, or $f_{\text{val}} = \frac{1}{2}(f_{u,\text{val}}^{\pi^+} + f_{d,\text{val}}^{\pi^-})$ similar to the case of baryons.

Due to QCD processes like for example gluon bremsstrahlung the parton distributions are scale dependent [Mut87] as is illustrated in Fig. 2.12. The resolution of the probe, i.e. the virtual photon in case of deep inelastic scattering or the gluon in hard hadron-hadron scattering, is determined by its wave length which again depends on the momentum transfer $Q^2$. Increasing the momentum transfer and, hence, the resolution one gets an increased probability of finding a parton at small $x$ and a decreased chance of finding one at high $x$ because high momentum quarks lose momentum by radiating gluons. In the case of parton-parton scattering one usually fixes the scale by the transverse momentum transfer: $Q^2 = p_T^2$. Once the $x$ dependence of the parton distributions are known for one scale $Q_0^2$, e.g. from deep inelastic scattering experiments, they can be evolved to different scales $Q^2$ using the Altarelli-Parisi Equation [Mut87].

To avoid regions where pQCD is not applicable one has to introduce a lower cut-off $p_{T\,\text{min}}$ below which the wavelength of the exchanged gluon is not large enough to resolve
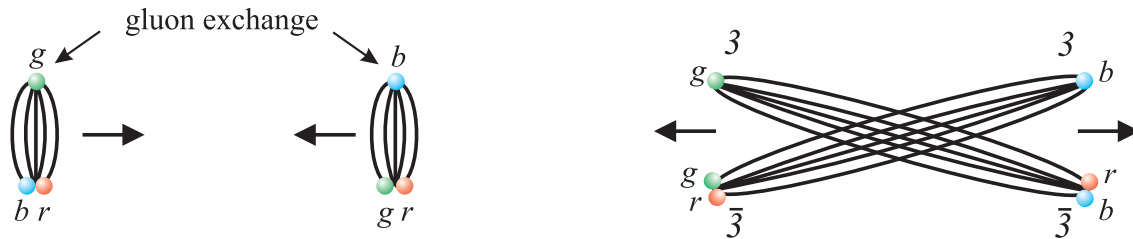
Figure 2.13: Soft non-diffractive interaction of two baryons. While the two baryons pass each other a soft gluon exchange between the blue and the green quark of the incoming baryons leads to the two-string configuration shown on the right-hand side: Each of the two color strings is stretched between the quark in one baryon and the diquark in the other, i.e. between a color triplet 3 and antitriplet $\bar{3}$.

individual color charges. The integrated cross section for hard scattering above this cut-off is given by

$$\sigma_{\mathrm{hard}}(p_{T\min}) = \int_{p_{T\min}}^{s/4} \frac{d\sigma}{dp_T^2} dp_T^2. \qquad (2.24)$$

Note that since each hard scattering event described by Eq. (2.24) contains two jets the inclusive jet rate measured in experiment is a factor two larger.

For a reasonable large $p_{T\min}$, such that $\sigma_{\mathrm{hard}} \ll \sigma_{\mathrm{nd}}$, the partonic cross section (2.24) can be roughly equated with the cross section for a hard hadron-hadron interaction. One can then subdivide the non-diffractive events into a part of events with hard jets and a part of low-$p_T$ events with a cross section $\sigma_{\mathrm{soft}}(p_{T\min}) = \sigma_{\mathrm{nd}}(s) - \sigma_{\mathrm{hard}}(p_{T\min})$. However, the differential jet cross section diverges with increasing $s$ and can exceed $\sigma_{\mathrm{nd}}(s)$. This is not a contradiction since $\sigma_{\mathrm{hard}}$ gives the parton-parton cross section and each of the incoming hadrons may be viewed as a beam of partons with the possibility of having several parton-parton interactions when the hadrons pass through each other. Therefore, $\langle n \rangle = \sigma_{\mathrm{hard}}(p_{T\min})/\sigma_{\mathrm{nd}}(s)$ is simply the average number of parton-parton scatterings above $p_{T\min}$ in an event, and can be larger than unity. Unitarization corrections are applied by distributing a varying number of interactions per event [Dur88] to ensure $\sigma_{\mathrm{soft}} \geq 0$.

At the end of this section we want to point out that hard interactions are in general accompanied by initial and final-state showers ($q \rightarrow qg$, $g \rightarrow q\bar{q}$ and $g \rightarrow gg$) which smear the kinematics of the naive hard process described above and can be viewed as higher order corrections in the strong coupling $\alpha_S$. In principle the partons in the actual hard reaction might also stem from initial-state showers.

## 2.2.5   Soft non-diffractive scattering

At the end of this section we want to discuss the remaining event class, namely the soft non-diffractive scattering. As can be seen from Fig. 2.7 the hard processes make up only for a very small fraction of the total cross sections at low energies. The other class of non-diffractive events which does not contain high-$p_T$ jets in the final states can be handled [Sjö01a, Sjö01b] as if originating from a single soft gluon exchange between the incoming hadrons. In contrast to the two gluon or Pomeron exchange in
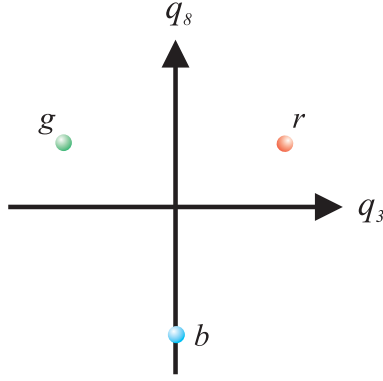
Figure 2.14: Color charges in the chromodielectric model. A green and a red quark are sources for both the $D_3$ and the $D_8$ field, while the blue quark is only a source of the $D_8$ field.

diffractive interactions and elastic scattering the two outgoing hadron remnants are now color octets, i.e. they are connected by color fields. Because of the strong color interactions these fields are pulled together into the form of a tube or string. If one decomposes each remnant into a color triplet and one antitriplet, e.g., a quark and a diquark in the case of baryons or a quark and an antiquark in the case of mesons, one ends up with two strings per event. Each of the strings stretches between a triplet in one remnant and an antitriplet in the other as illustrated in Fig. 2.13 for the case of soft non-diffractive baryon-baryon scattering. The two strings are then assumed to fragment independently of each other.

The simplified string configuration of Fig. 2.13 is not very different from what can be extracted from the chromodielectric model [Fri77a, Fri77b, Tra99, Mar04]. In this model the nonabelian part of the gluon sector is accounted for by a scalar $\sigma$ field. This field acts like a medium with dielectric constant $\epsilon < 1$ in which the color charges are embedded. These color charges are sources of two fields, the $D_3$ and the $D_8$ field (corresponding to the commuting Gell-Mann matrices $\lambda_3$ and $\lambda_8$ in QCD) which can only interact indirectly with each other via a scalar $\sigma$ field. In this abelian approach the colored quarks carry electric charges according to Fig. 2.14. The green and the red quark are sources for both the $D_3$ and the $D_8$ field, while the blue quark provides only a source for the $D_8$ field.

The quark configuration on the right-hand side of Fig. 2.13 thus leads to the field configurations [Mar] illustrated in Fig. 2.15. The solid lines represent the contour lines of the electric energy density

$$W = \frac{1}{2} \sum_{a=3,8} \vec{D}_a \cdot \vec{E}_a \tag{2.25}$$

where $\vec{E} = \vec{D}/\epsilon$ as in usual Maxwell theory. The shape of the energy density looks pretty much like in the simplified string configuration of Fig. 2.13. However, one sees that in contrast to the situation described above the $D_8$ field now connects all four string ends. The assumption that the two strings decay independently of each other might therefore be questionable.
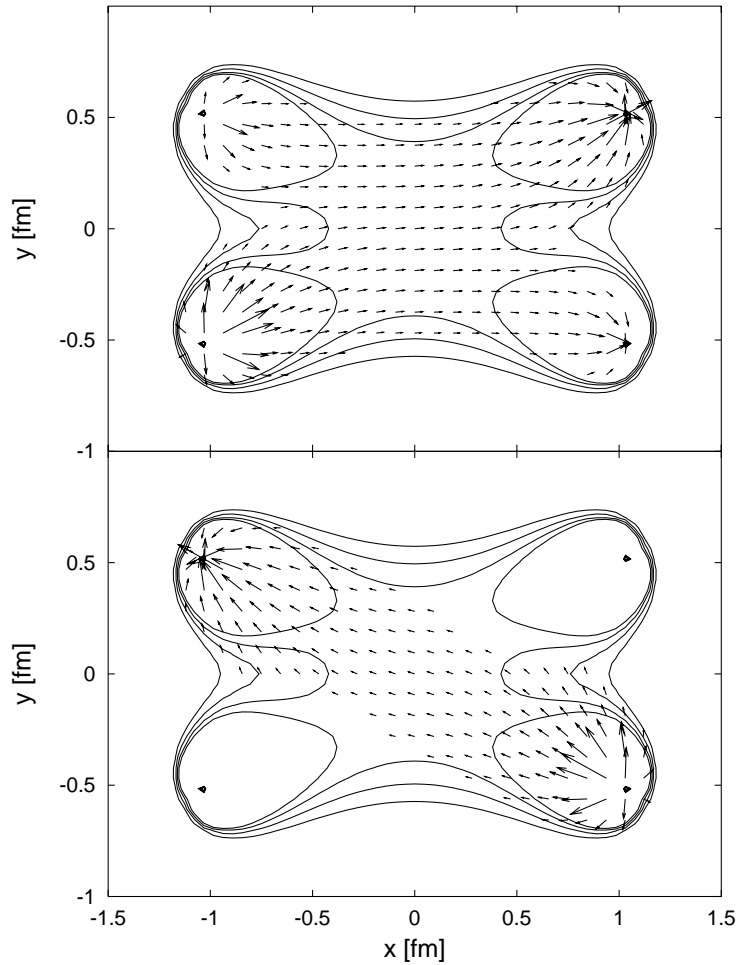
Figure 2.15: Field configuration of the $D_8$ (*upper panel*) and the $D_3$ (*lower panel*) field in the chromodielectric model [Mar]. The color configuration of the quarks corresponds to that after the soft gluon exchange, i.e. the situation depicted on the right-hand side of Fig. 2.13. The contour lines represent the electric energy density (2.25) for the values 3, 4, 5 and 6 fm$^{-4}$ (increasing towards the locations of the charges).

## 2.3   String model of Regge trajectories

At the end of this chapter we give a classical explanation [Per87] for the linearity of Regge trajectories and the universal slope parameter $\alpha'_{\mathbb{R}}$ of Sec. 2.1.5. Since the mediators of the color force, i.e. the gluons, themselves carry color charges they are subject to strong self interactions. If the sources are separated more than $\approx 0.3$ fm these strong color interactions confine the field lines to a narrow flux tube with constant energy density $\kappa$ per unit length. This leads to the linear increase of the quark potential at large distances which is seen for example in charmonium and bottonium spectroscopy, i.e. the energy levels of bound $c\bar{c}$ pairs.

   If one considers a hadron as two (massless) quarks which are connected by a string as in Fig. 2.16 the angular momentum of this object will be equal to the total orbital
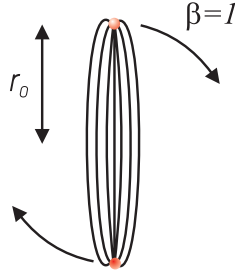
Figure 2.16: Simple string model for hadron. Neglecting the masses of the quarks the angular momentum of the hadron is given by the orbital angular momentum of the flux tube.

momentum of the flux tube. Assume that the ends of the tube rotate with the velocity of light. Then the local velocity at radius $r$ will be

$$\beta(r) = \frac{r}{r_0} \tag{2.26}$$

where $r_0$ is half the length of the string. The total mass is then

$$M = 2 \int_0^{r_0} \frac{\kappa \, dr}{\sqrt{1 - \beta(r)^2}} = \kappa r_0 \pi,$$

and the orbital momentum of the hadron is given as

$$J = 2 \int_0^{r_0} \frac{\kappa r \beta \, dr}{\sqrt{1 - \beta(r)^2}} = \frac{\kappa r_0^2 \pi}{2}.$$

Eliminating $r_0$ between these equations yields the linear relation between the angular momentum and mass of a hadron which we know from the Chew-Frautschi plot in Fig. 2.5:

$$J = \alpha' M^2 + \text{const}$$

with $\alpha' = (2\pi\kappa)^{-1}$. The string tension $\kappa$ can be estimated via the typical hadronic mass 1 GeV and the hadronic diameter which is known from electron scattering to be about 1 fm. The linear energy density then yields $\kappa \approx 1 \text{ GeVfm}^{-1}$ and $\alpha' \approx 0.8 \text{ GeV}^{-2}$ which has to be compared to $\alpha'_{\mathbb{R}} \approx 0.9 \text{ GeV}^{-2}$ of the Regge trajectories. One can say that despite of its simplicity the string model yields an astonishing good estimate for the Regge slope $\alpha'_{\mathbb{R}}$.

# Chapter 3

# Photon-hadron and electron-hadron interactions

The interactions of high-energy photons with hadrons show some striking similarities to hadronic reactions. Since the scattering of leptons off nucleons can be reduced to the interaction of a virtual photon $\gamma^*$ in the so-called one-photon exchange approximation these similarities also show up in electron-induced reactions. An extensive discussion of the hadronic properties of the (virtual) photon in high-energy reactions as well as a theoretical interpretation in terms of generalized vector meson dominance can be found in Refs. [Bau78, Don78].

This chapter is organized as follows. In Sec. 3.1 we discuss the hadronic structure of real photons and their interaction with nucleons. We show that instead of coupling directly to a quark inside the nucleon the photon can also fluctuate into a quantum mechanically allowed hadronic state which subsequently scatters off the nucleon. This picture is generalized in Sec. 3.2 for the description of virtual photons. The probability whether the photon interacts directly or as a resolved hadronic state will strongly depend on its kinematics, i.e. the photon's energy and in case of lepton scattering also on the four-momentum transfer squared. We adopt the theoretical approach of Sjöstrand et al. [Sch93a, Sch93b, Sch95, Sch96, Fr00a, Fr00b, Fr00c] which has been developed during the past 20 years and which has been successfully implemented into the PYTHIA model [Sjö01a, Sjö01b] to describe $\gamma N$, $\gamma^* N$ and $\gamma^* \gamma^*$ reactions at large energies.

In what follows we mainly focus on the description of resolved photon events since the direct photon interactions are completely taken care of by the PYTHIA Monte Carlo generator.

## 3.1  Real photons

There are many experiments, performed e.g. at DESY, ELSA, MAMI, Jefferson Lab, SLAC and SPring8 with beam energies ranging from a few hundred MeV up to several hundred GeV, that investigate the hadronic interactions of real photons. Most of them use a tagged photon beam, i.e. they produce high-energy photons via bremsstrahlung by bombarding a thin radiator with a monochromatic electron or positron beam. The energy of the photon is determined by measuring the momentum of the incoming and

outgoing electron.

In most of the experiments one uses hydrogen or deuterium targets. In the low energy regime, i.e. at center-of-mass energies below $\sqrt{s} \approx 2$ GeV, the main goal of these experiments is to investigate the structure of nucleons via resonance excitation. At larger energies one can study the production mechanism of vector mesons as well as strange and charmed baryons and mesons.

By using nuclear targets one can examine the in-medium properties of hadrons such as a possible modification of masses and widths at finite nuclear density. For an overview see [Fal03a] and references therein. In addition, the determination of mean free paths allows to extract the cross sections of unstable particles. The nucleus can also serve as a kind of 'micro-detector' for the study of hadron formation times in photonuclear reactions as we discuss in detail in Chap. 6.

There is also the possibility to use polarized photon beams and/or targets to investigate the spin structure of the nucleon. In this work, however, we only consider spin averaged cross sections mainly due to technical reasons.

### 3.1.1 Hadronic structure of the photon

The total photon-nucleon cross section shows a clear resonant structure at low energies which vanishes for center-of-mass energies above approximately 2 GeV. For high energies the cross section becomes more or less constant with only a logarithmic energy dependence. The same behavior is observed in pion-proton scattering. Above the resonance region the two cross sections differ only by a constant factor of the order of the fine structure constant $\alpha_{em}$ [Gre73]. In addition, one observes that the photoabsorption cross sections for protons and neutrons become approximately equal at high energies which shows that high-energy photons do not couple primarily to the charge of the target.

Above the baryon resonance region also the $t$ dependence of the cross section for Compton scattering ($\gamma N \rightarrow \gamma N$) does not differ qualitatively from that of hadronic cross sections like elastic $\pi N$ scattering or vector meson photoproduction despite a rescaling with the appropriate powers of $\alpha_{em}$. All differential cross sections show a fast exponential decrease with increasing momentum transfer $|t|$.

Concerning the phase of the Compton amplitude dispersion relations (cf. Eq. (2.10)) for the forward amplitude [Dam70] as well as direct measurements [Alv73] show that the forward amplitude is almost purely imaginary for high values of $s$. This is also the case for elastic $\pi N$ and $N N$ amplitudes.

All of these observations can be understood within Regge theory if one assumes that the photon can couple to the Pomeron. We have already mentioned in Sec. 2.2.1 that the Regge parametrization of total cross sections also works for photon-induced reactions which means that the Compton forward amplitude is dominated by Reggeon and Pomeron exchange. In addition, we have seen in Sec. 2.2.2 that the leading contribution to elastic scattering at high energies arises from the $t$-channel exchange of a Pomeron which would give a natural explanation for the similarity of the elastic scattering amplitudes. A further hint to a a photon-Pomeron coupling is provided by the phase of the Compton amplitude. Inserting the Pomeron intercept $\alpha_{\mathbb{P}}(0)$ into Eq. (2.12) yields a very small value for the ratio of real to imaginary part of the forward-scattering am-

plitude. The parton model of the last chapter, which explains Reggeon and Pomeron exchange in terms of quarks and gluons therefore suggests a hadronic substructure of the photon.

Besides the above mentioned similarities, there is also an important difference between photon and hadron-induced reactions at high energies. In purely hadronic reactions the elastic cross section $\sigma_{\text{el}}$ typically makes up for about 15-20% of the total cross section $\sigma_{\text{tot}}$ (see also Fig. 2.7). This is not the case for electromagnetic processes since the cross section for Compton scattering is smaller by a factor $\alpha_{\text{em}}$ in order of magnitude. However, the fraction of the total cross section that stems from exclusive vector meson production ($\gamma N \to V N$) approximately equals the ratio $\sigma_{\text{sd}}/\sigma_{\text{tot}}$ in hadronic scattering. If one in addition accounts for the similar $s$ and $t$ dependence of $d\sigma/dt(\gamma N \to V N)$ and diffractive hadron-hadron scattering, vector meson photoproduction at large energies can be viewed as the photon analogon to diffractive excitation in hadron scattering.

Last but not least one observes a striking similarity between photon and hadron-induced reactions in nuclear reactions. In both cases the total nuclear cross section $\sigma_A$ is considerably reduced compared to $A$ times the nucleonic cross section $\sigma_N$:

$$\sigma_A < A\sigma_N,$$

where $A$ denotes the atomic mass number. At large energies the nuclear absorption cross section scales approximately with $A^{2/3}$ for both photon and hadron-induced reactions[1]. In case of hadronic projectiles this can easily be understood since the mean free path of the hadron inside the nuclear medium is short compared to the nuclear diameter and the first interaction of the projectile already takes place on the front side of the nucleus. This leads to an absorption cross section that is proportional to the nuclear surface. The fact that this so-called shadowing effect also occurs in $\gamma A$ reactions has been considered for a long time as the perhaps strongest confirmation of the photon's hadronic structure. However, as we show in Sec. 6.1.1 one can in principle understand this effect within Glauber theory without the need of a hadronic component of the photon.

## 3.1.2 Resolved interactions

If one uses time-ordered perturbation theory to describe the interaction of a (virtual) photon with a hadron one will encounter two time-ordered contributions to the scattering amplitude [Pil95]. The two amplitudes are shown in Fig. 3.1. In the left diagram the photon is absorbed by a quark from the target. In the right diagram the photon dissociates into a quark-antiquark pair before the interaction with the target takes place. In the rest frame of the target the photon has energy $\nu$ and momentum $\vec{q}$. We assume that its energy is large compared to the average momentum of a quark inside the hadron $\langle \vec{p}_q^2 \rangle^{1/2}$ and the photon virtuality

$$Q^2 = -(\nu^2 - \vec{q}^2),$$

---

[1]Note that in contrast to the total $\gamma A$ and $hA$ cross sections the inclusive production cross sections can show a different $A$ dependence. For example one expects the inclusive production cross section $\sigma(aA \to bX)$ to scale with the nuclear mass number $A$ at high energies (AGK cancellation) as we discuss at the end of Sec. 5.1.2.
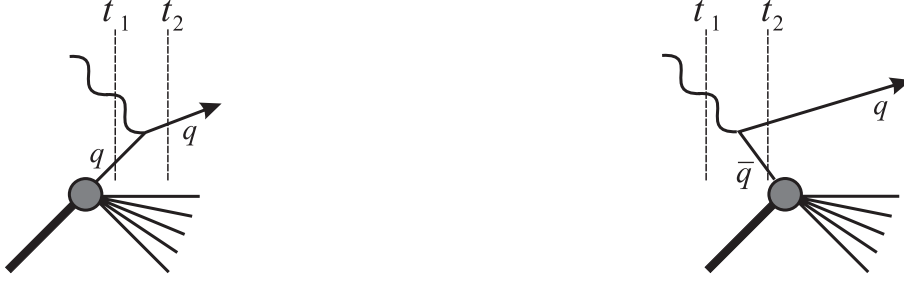
Figure 3.1: Time-ordered amplitudes for photon-hadron scattering ($t_2 > t_1$). *Left:* The photon interacts with a quark inside the target (amplitude $\mathcal{A}_a$). *Right:* The photon fluctuates into a quark-antiquark pair which subsequently scatters off the target (amplitude $\mathcal{A}_b$).

i.e. $\nu^2 \gg \langle \vec{p}_q^2 \rangle$ and $\nu^2 \gg Q^2$.

The weight of each time-ordered amplitude can be estimated via the energy difference that occurs if one puts the quarks on their mass shell and postulates only three momentum conservation at each vertex [Hal84]. Neglecting the masses of the quarks the energy difference for the left diagram (amplitude $\mathcal{A}_a$) in Fig. 3.1 is then given by

$$
\begin{aligned}
\Delta E_a &= E_a(t_2) - E_a(t_1) \\
&= \sqrt{\langle ((\vec{p}_q + \vec{q})^2) \rangle} - (\nu + \langle \vec{p}_q^2 \rangle^{1/2}) \\
&= \sqrt{\langle \vec{p}_q^2 \rangle + \vec{q}^2} - (\nu + \langle \vec{p}_q^2 \rangle^{1/2}) \\
&\approx \frac{\langle \vec{p}_q^2 \rangle + Q^2}{2\nu} - \langle \vec{p}_q^2 \rangle^{1/2}
\end{aligned}
$$

and that of the right diagram (amplitude $\mathcal{A}_b$) is

$$
\begin{aligned}
\Delta E_b &= E_b(t_2) - E_b(t_1) \\
&= E(q\bar{q}) - \nu \\
&= \sqrt{m_{q\bar{q}}^2 + \vec{q}^2} - \nu \\
&\approx \frac{m_{q\bar{q}}^2 + Q^2}{2\nu}
\end{aligned}
$$

where $m_{q\bar{q}}$ denotes the mass of the quark-antiquark pair. In the case of large photon energies the ratio of the two amplitudes can then be estimated as

$$
\begin{aligned}
\frac{|\mathcal{A}_b|}{|\mathcal{A}_a|} \sim \left| \frac{\Delta E_a}{\Delta E_b} \right| &= \left| \frac{\langle \vec{p}_q^2 \rangle + Q^2 - 2\nu \langle \vec{p}_q^2 \rangle^{1/2}}{m_{q\bar{q}}^2 + Q^2} \right| \\
&\approx \frac{2\nu \langle \vec{p}_q^2 \rangle^{1/2}}{m_{q\bar{q}}^2 + Q^2}.
\end{aligned}
\tag{3.1}
$$

Of course only the sum of the two time-ordered amplitudes is gauge invariant. However, if one assumes that only $q\bar{q}$ pairs with $m_{q\bar{q}}^2 \lesssim Q^2$ contribute to amplitude $\mathcal{A}_b$, Eq. (3.1)
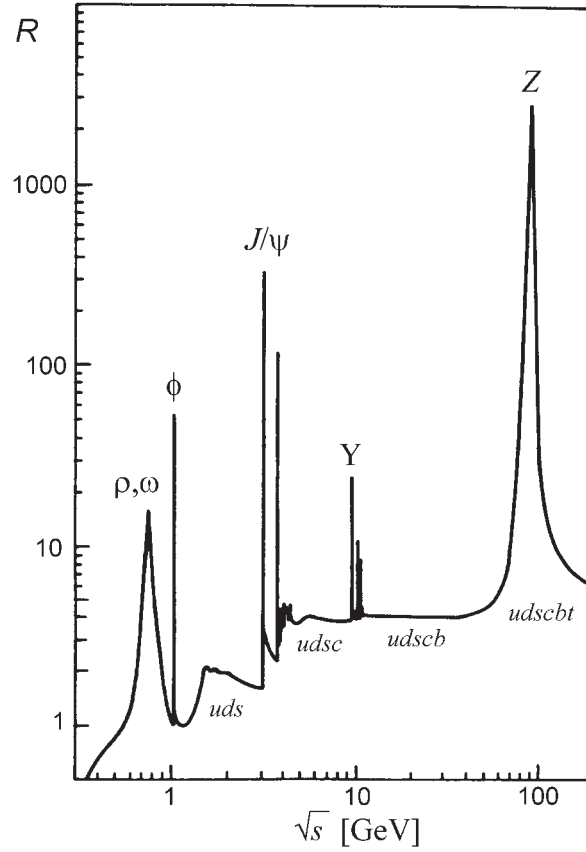
Figure 3.2: Ratio $R = \frac{\sigma(e^+e^- \to \text{hadrons})}{\sigma(e^+e^- \to \mu^+\mu^-)}$ as function of the center-of-mass energy $\sqrt{s}$.

shows that amplitude $\mathcal{A}_b$ dominates for very high photon energies. In this kinematic regime the photon therefore fluctuates into a hadronic state with quantum numbers of the photon (spin, parity and charge conjugation $J^{PC} = 1^{--}$) which subsequently scatters from the target.

For real photons, i.e. $Q^2 = 0$, the requirement $m_{q\bar{q}}^2 \lesssim Q^2$ constrains the fluctuations to the lightest hadronic states with the appropriate quantum numbers. Looking into the hadronic spectrum of the reaction $e^+e^- \to \gamma^* \to$ hadrons in which a timelike photon dissociates into hadrons (see Fig. 3.2), one can identify the four lowest resonant states: the vector mesons $\rho^0$, $\omega$, $\phi$ and $J/\psi$ with masses $m_\rho = 771$ MeV, $m_\omega = 783$ MeV, $m_\phi = 1019$ MeV and $m_{J/\psi} = 3097$ MeV. They can be viewed as bound quark-antiquark systems where the first two contain the light up and down quarks and the latter two are made of strange and charm quarks, respectively. In addition, one observes a non-resonant background with thresholds at energies where $q\bar{q}$ pairs of new flavors can be produced.

The physical photon can therefore be decomposed as illustrated in Fig. 3.3 into a bare photon that interacts directly with a parton from the target, the vector meson fluctuations $V = \rho^0, \omega, \phi, J/\psi$, some non-resonant $q\bar{q}$ fluctuation of larger virtuality as

Figure 3.3: Physical photon. The physical photon can be thought of as a superposition of a bare photon, vector mesons as well as fluctuations into $q\bar{q}$ and dilepton pairs.

well as fluctuations into dileptons:

$$|\gamma\rangle = \sqrt{Z_3}|\gamma_0\rangle + \sum_V \frac{e}{g_V}|V\rangle + \sum_q \frac{e}{g_{q\bar{q}}}|q\bar{q}\rangle + \sum_l \frac{e}{g_{ll}}|l^+l^-\rangle \qquad (3.2)$$

with the wave function renormalization

$$Z_3 = 1 - \sum_V \left(\frac{e}{g_V}\right)^2 - \sum_q \left(\frac{e}{g_{q\bar{q}}}\right)^2 - \sum_l \left(\frac{e}{g_{ll}}\right)^2. \qquad (3.3)$$

Since the leptonic component of the photon can only interact strongly at higher orders in $\alpha_{\mathrm{em}}$ its contributions to hadronic interactions can be neglected.

**Vector meson dominance**

The strict vector meson dominance (VMD) model [Sak60, Gel61] neglects any contribution from the bare photon and the $q\bar{q}$ continuum in photon-hadron interactions. The invariant amplitude for the process $\gamma^* h \to X$ can therefore be expressed in terms of the on-shell vector meson scattering amplitudes:

$$\mathcal{M}_{\gamma^* h \to X}(Q^2, s, t, \ldots) = \sum_V \frac{e}{g_V} \frac{m_V^2}{Q^2 + m_V^2} \mathcal{M}_{Vh \to X}(s, t, \ldots). \qquad (3.4)$$

Here $m_V$ denotes the mass of the vector meson $V$ and $(e/g_V)^2$ gives the probability for the transition $\gamma^* \to V$. Any dependence of the amplitude on the virtuality $Q^2$ is taken care of by the vector meson propagator. In Sec. 3.2.1 we show that for $Q^2 \neq 0$ also a contribution from longitudinally polarized photons exists. This issue is not addressed by (3.4) which only describes the $Q^2$ dependence of the transverse part. The photon-vector meson coupling constants $e/g_V$ can either be extracted directly from $e^+e^- \to$ hadrons or via Eq. (3.8) from photoproduction of vector mesons on nucleons. Throughout this work we use the values from Ref. [Bau78] which are the geometrical mean of the two possible extractions and coincide with the values used in the PYTHIA model (see Tab. 3.1). Inserting these values into Eq. (3.3) one sees that the real photon can be found in a VMD state about 0.5% of the time. Although this sounds tiny, one has to be aware that the vector meson component interacts with a hadronic cross section that is a factor $\alpha_{\mathrm{em}}^{-1}$ larger in order of magnitude than that of the bare photon.

As discussed in Sec. 2.2.1 one can use Regge theory to parametrize total hadronic cross sections. Assuming an additive quark model the total $Vp$ cross sections can be

| $V$ | $\rho^0$ | $\omega$ | $\phi$ | $J/\psi$ |
|---|---|---|---|---|
| $g_V^2/4\pi$ | 2.20 | 23.6 | 18.4 | 11.5 |

Table 3.1: VMD coupling constants $g_V$ [Bau78].

parametrized as [Sch95, Sch96]

$$\sigma_{\text{tot}}^{\rho^0 p}(s) \approx \sigma_{\text{tot}}^{\omega p}(s) \approx \frac{1}{2}(\sigma_{\text{tot}}^{\pi^+ p} + \sigma_{\text{tot}}^{\pi^- p}) \approx 13.63 s^\epsilon + 31.79 s^{-\eta}\,[\text{mb}],$$

$$\sigma_{\text{tot}}^{\phi p}(s) \approx \sigma_{\text{tot}}^{K^+ p} + \sigma_{\text{tot}}^{K^- p} - \sigma_{\text{tot}}^{\pi^+ p} \approx 10.01 s^\epsilon - 1.52 s^{-\eta}\,[\text{mb}],$$

$$\sigma_{\text{tot}}^{J/\psi p}(s) \approx \frac{m_\phi^2}{m_{J/\psi}^2}\sigma_{\text{tot}}^{\phi p}(s) \approx \frac{1}{10}\sigma_{\text{tot}}^{\phi p}(s), \tag{3.5}$$

with $s$ in GeV$^2$ and $\epsilon$, $\eta$ as in Eq. (2.15). The cross sections on a neutron are the same because of isospin symmetry.

Using the VMD amplitude (3.4) in the optical theorem (2.4) one gets in the 'diagonal approximation', i.e. neglecting off-diagonal scattering $VN \to V'N$ with $V' \neq V$:

$$\sigma_{\text{VMD}}^{\gamma p}(s) = \sum_V \frac{e^2}{g_V^2}\sigma_{\text{tot}}^{V p}(s). \tag{3.6}$$

This has to be compared with the empirical parametrization [Don92] for the total $\gamma p$ cross section:

$$\sigma_{\text{tot}}^{\gamma p}(s) = 67.7 s^\epsilon + 129 s^{-\eta}\,[\mu\text{b}]. \tag{3.7}$$

The two cross sections are plotted in Fig. 3.4. One sees that the vector meson components (dashed line) alone already make up for about 80% of the real photoabsorption cross section which explains the Regge form of the total $\gamma N$ cross section. The remaining 20% are shared among the direct and $q\bar{q}$ interactions. Fig. 3.4 also shows the $\rho^0$ contribution to the total photoabsorption cross section (dotted line). Obviously, the VMD contribution is dominated by the $\rho^0$ component of the photon.

In case that the photon interacts via a vector meson fluctuation all processes that are allowed in hadron physics and that are described in Chap. 2 may occur. This includes elastic and diffractive as well as soft and hard non-diffractive events. In case of elastic scattering one ends up with exclusive $V$ production $\gamma N \to VN$. Exclusive vector meson production at large energies can therefore be understood as a process where a preformed vector meson fluctuation is put on its mass shell by a small momentum transfer to the proton. This explains the observed exponential fall-off of the differential exclusive vector meson production cross section:

$$\frac{d\sigma}{dt}(\gamma N \to VN) \approx \left(\frac{e}{g_V}\right)^2 \frac{(\sigma_{\text{tot}}^{VN})^2}{16\pi}\,(1+\rho^2)e^{B_{\text{el}}t}, \tag{3.8}$$

which simply arises from the exchange of a Pomeron (cf. Eq. (2.17)).
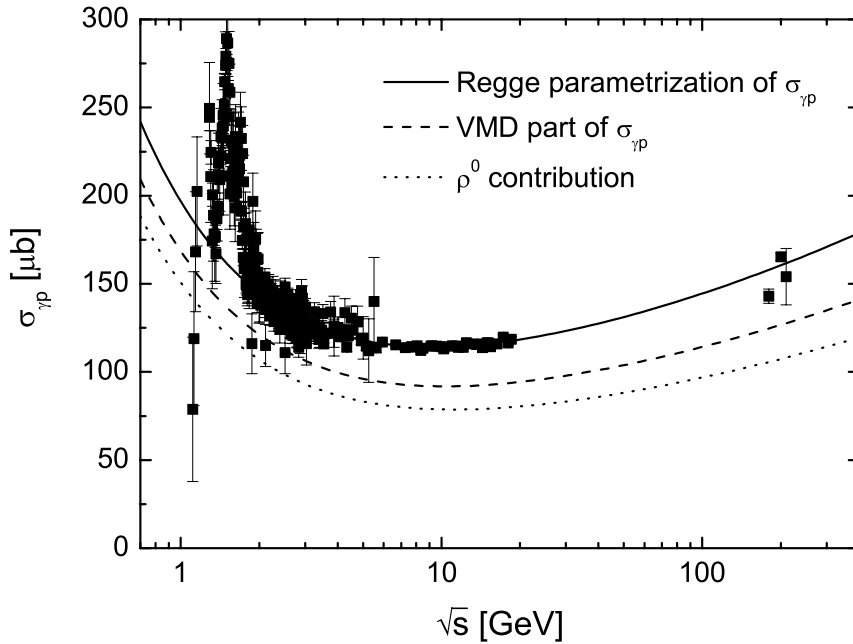
Figure 3.4: Photoabsorption cross section on the nucleon. The solid line represents the fit (3.7) to the proton data [Don92], the dashed line shows the VMD contribution according to Eq. (3.6) and the dotted line is the part that arises from the fluctuation into $\rho^0$. The data are taken from Ref. [PDG02].

## Generalized vector meson dominance

As can be seen from Fig. 3.4 the VMD events do not sum up to the full photoabsorption cross section. The major fraction of what remains stems from interactions of the $q\bar{q}$ fluctuations. Since one may view these states as excited higher resonances ($\rho'$ etc.) one calls this event class 'generalized vector meson dominance' (GVMD). Their contribution to the photoabsorption cross section can be written similarly to the VMD part (3.6) as [Fr00c]

$$\sigma_{\text{GVMD}}^{\gamma p}(s) = \frac{\alpha_{\text{em}}}{\pi} \sum_q z_q^2 \int_{k_0^2}^{k_1^2} \frac{dk_T^2}{k_T^2} \sigma^{q\bar{q}p}(s; k_T), \qquad (3.9)$$

where $z_q$ is the charge of a quark with flavor $q$ in units of $e$ and $k_1$ can be identified with the $p_{T\,\text{min}}$ cut-off of the perturbative hard hadron-hadron scattering on Sec. 2.2.4. The prefactor and integral over $dk_T^2/k_T^2$ gives the probability for the photon to split into a $q\bar{q}$ pair of transverse momenta $\pm k_T$ and $\sigma^{q\bar{q}p}$ denotes the cross section for this pair to interact with the proton. The $k_T$ dependence of this cross section can be modeled using color transparency arguments. As we discuss in Sec. 6.2 the cross section of small-sized color singlet object scales with its transverse radius squared. The uncertainty relation yields a maximal size $k_T^{-1}$ for a state of virtuality $k_T$. If the $q\bar{q}$ had formed a virtual vector meson state $V$ it would have the size $k_{V(q\bar{q})}^{-1} \approx 2/m_V$. This suggests the rescaling
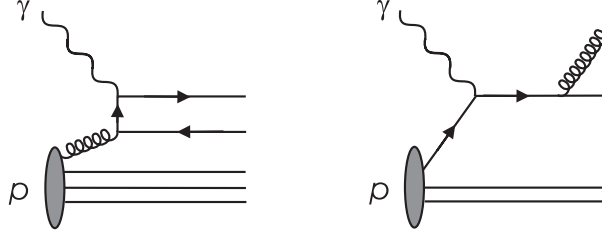
Figure 3.5: Direct photon interaction in lowest order of $\alpha_s$. *Left:* Photon-gluon fusion $\gamma g \to q\bar{q}$. *Right:* QCD Compton $\gamma q \to qg$.

ansatz:

$$\sigma^{q\bar{q}p}(s; k_T) = \frac{k_{V(q\bar{q})}^2}{k_T^2}\sigma^{V(q\bar{q})p}(s),$$

where $\sigma^{V(q\bar{q})p}$ is the cross section of a vector meson with quark content $q\bar{q}$ (cf. Eq. (3.5)). We adopt the values from the PYTHIA model [Sjö01b] $k_0 = 0.5$ GeV, $k_{V(q\bar{q})} = 0.4$ GeV and $k_1 = p_{T\min} = (1.9\,\text{GeV})(s/\text{TeV}^2)^\epsilon$.

After the photon has branched into a $q\bar{q}$ pair one of the quarks or a daughter parton thereof interacts with a parton from the target. This is not different from the usual hard hadron-hadron scattering discussed in Sec. 2.2.4 besides the fact that the initial parton distribution and its subsequent QCD evolution is now perturbatively calculable [Sjö01b]. It is important to note that the higher Fock components of the photon such as $|q\bar{q}g\rangle$, $|q\bar{q}gg\rangle$, $|q\bar{q}q\bar{q}\rangle$, etc. are effectively taken into account by the possibility of initial-state radiation in the hard scattering process.

### 3.1.3 Direct interactions

As can be seen from the wave function renormalization (3.3) the physical photon is still a pointlike particle most of the time, $1 - Z_3 \ll 1$. The reason why most $\gamma p$ reactions are dominated by the VMD and GVMD contributions is because the hadronic $\rho^0 p$ cross section is so much larger than that of the direct photon.

To leading order in the strong coupling $\alpha_s$ the direct photon processes are the photon-gluon fusion $\gamma g \to q\bar{q}$ and the QCD Compton process $\gamma q \to qg$, both shown in Fig. 3.5. The latter can be viewed as the higher-order correction to deep inelastic scattering of virtual photons $\gamma^* q \to q$ which is discussed in the next section and is illustrated in Fig. 3.7. The absorption of a real photon on a single quark without the emission of a hard gluon is not possible because it requires a quark far off its mass shell either in the entrance or in the outgoing channel. Since the bound quarks in the proton are in general only slightly off-shell[2] and the hadronization of the outgoing quark involves only soft momentum transfers this process cannot contribute for real photons. The cross sections for the photon-gluon fusion and the QCD Compton process become calculable within pQCD by introducing a lower cut-off on the transverse momenta $k_T > p_{T\min}(= k_1)$ of the outgoing quark pair (see [Sjö01b] and references therein). The

---

[2]Note that the interactions with other quarks inside the nucleon may lead to a finite quark width, e.g. the on-shell width of constituent quarks ($m_q = 300$ MeV) in infinite quark matter is 0.1–10 MeV [Frö03].

parton distributions of the nucleon that enter the calculations are the same as for hard hadron-hadron scattering.

The events that correspond to the different cross sections in the incoherent sum

$$\sigma_{\text{tot}}^{\gamma N}(s) = \sigma_{\text{VMD}}^{\gamma N}(s) + \sigma_{\text{GVMD}}^{\gamma N}(s) + \sigma_{\text{dir}}^{\gamma N}(s)$$

lead by construction to experimentally distinguishable final states: The typical event structure of a direct photon-proton interaction is two high $p_T > k_1$ jets and a proton remnant. In contrast to resolved events where the photon also leaves behind a beam remnant which in case of VMD events is smeared with a typical primordial $k_T \lesssim k_0$, i.e. a few hundred MeV and in case of GVMD events has $k_T \gtrsim k_0$. The direct events do not involve a beam remnant of the photon. Interference effects between the three different event classes can therefore be neglected.

## 3.2 Electron-nucleon interactions

In this section we give a brief introduction to electron-nucleon interactions. A detailed review on electron-induced reactions can be found in Refs. [Hal84, Bof96a]. In Sec. 3.2.1 we show how to relate electron-nucleon scattering to the interaction of a virtual photon with a nucleon. After that we generalize the theoretical framework of Sec. 3.1 to virtual photons.

### 3.2.1 One-photon exchange approximation

Let us consider the inelastic scattering of an electron with four-momentum $k$ on a nucleon with four-momentum $p$. The four-momentum transfer

$$q = k - k'$$

is always spacelike as can be easily seen in the rest frame of the projectile:

$$q^2 = 2m_e^2 - 2kk' = 2m_e^2 - 2m_e\sqrt{m_e^2 + \vec{k}^2} < 0. \qquad (3.10)$$

One therefore usually introduces the photon virtuality $Q^2 := -q^2$ as a positive quantity. For large values of $Q^2$ the target nucleon is destroyed and in addition to the scattered electron one observes a ensemble of hadrons with invariant mass squared $W^2 = (p+q)^2$ (see Fig. 3.6).

If one detects only the scattered electron one ends up with the inclusive scattering cross section which in the rest frame of the target nucleon takes on the form

$$\frac{d^2\sigma}{d\Omega dE'} = \frac{\alpha_{\text{em}}^2}{Q^4}\frac{E'}{E}L^{\mu\nu}W_{\mu\nu}. \qquad (3.11)$$

Here $E$ and $E'$ denote the energy of the electron before and after the collision. The leptonic tensor has the simple form

$$L^{\mu\nu} = 2\left(k^\mu k'^\nu + k'^\mu k^\nu + \frac{q^2}{2}g^{\mu\nu}\right).$$
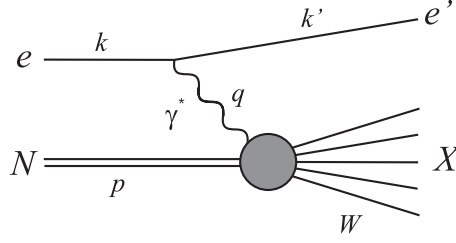
Figure 3.6: Electron-nucleon scattering in first order of $\alpha_{em}$: One-photon exchange approximation.

The hadronic tensor $W^{\mu\nu}$ describes the coupling of the photon to the nucleon. Since the nucleon is not a pointlike particle, two structure functions $W_1(\nu, Q^2)$ and $W_2(\nu, Q^2)$ enter the hadronic tensor ($\nu = E - E'$):

$$W^{\mu\nu} = W_1(\nu, Q^2)\left(\frac{q^\mu q^\nu}{q^2} - g^{\mu\nu}\right) + \frac{1}{m_N^2}W_2(\nu, Q^2)\left(p^\mu - \frac{p \cdot q}{q^2}q^\mu\right)\left(p^\nu - \frac{p \cdot q}{q^2}q^\nu\right).$$

We have omitted the antisymmetric part of $W^{\mu\nu}$, since it does not contribute to the cross section when contracted with the symmetric tensor $L^{\mu\nu}$ in (3.11).

The lower part of the diagram in Fig. 3.6 solely represents the absorption of the virtual photon $\gamma^*$ which has been emitted by the electron. By defining a virtual photon flux $\Gamma$ one can therefore rewrite the inclusive electrons scattering cross section (3.11) in the factorized form

$$\frac{d^2\sigma}{d\Omega dE'} = \Gamma(\sigma_T^{\gamma^*N} + \epsilon\sigma_L^{\gamma^*N}) \equiv \Gamma\sigma_{tot}^{\gamma^*N}.$$

Here $\sigma_T^{\gamma^*N}$ and $\sigma_L^{\gamma^*N}$ denote the photoabsorption cross sections for transversal and longitudinal photons and the polarization parameter $\epsilon$ gives the ratio of the longitudinal and transversal photon flux:

$$\epsilon = \frac{\Gamma_L}{\Gamma_T} \equiv \frac{\Gamma_L}{\Gamma}.$$

Of course there is an ambiguity in the definition of the virtual photon flux. We use the Hand convention [Han63]:

$$\Gamma = \frac{\alpha_{em}K}{2\pi^2Q^2}\frac{E'}{E}\frac{1}{1-\epsilon}, \tag{3.12}$$

$$\epsilon = \left[1 + 2\left(1 + \frac{\nu^2}{Q^2}\right)\tan^2\frac{\theta}{2}\right]^{-1} \tag{3.13}$$

where

$$K = \frac{W^2 - m_N^2}{2m_N} \tag{3.14}$$

is the equivalent photon energy, i.e. the energy that a real photon must have in the rest frame of the nucleon to produce the same invariant mass $W$ in the photon-nucleon system as the virtual photon. The electron scattering angle $\theta$ is is also taken in the

nucleon rest frame. With these definitions the photoabsorption cross sections become [Hal84]

$$
\sigma_T^{\gamma^*N} = \frac{4\pi^2\alpha_{em}}{K}W_1(\nu,Q^2),
$$

$$
\sigma_L^{\gamma^*N} = \frac{4\pi^2\alpha_{em}}{K}\left(\left(1+\frac{\nu^2}{Q^2}\right)W_2(\nu,Q^2)-W_1(\nu,Q^2)\right).
$$

In case of electron-induced reactions on nuclei the lab frame, i.e. the frame where the nucleus is at rest, does not coincide with the rest frame of the nucleon because of Fermi motion. It is therefore useful to define the Lorentz-invariant cross section

$$
\frac{d^2\sigma}{dydQ^2} = \frac{\pi}{E'}\frac{d^2\sigma}{dE'd\Omega}
$$

with all quantities on the right-hand side given in the rest frame of the nucleon and $y = pq/pk$. We show in Appx. D that for large energies this invariant cross section takes on the form

$$
\frac{d^2\sigma}{dydQ^2} \approx \frac{\alpha_{em}}{2\pi}\frac{(1-x)}{Q^2}\left(\frac{1+(1-y)^2}{y}\right)(\sigma_T^{\gamma^*N}+\epsilon\sigma_L^{\gamma^*N}) \tag{3.15}
$$

with

$$
\epsilon \approx \frac{1-y}{1-y+y^2/2} \tag{3.16}
$$

and

$$
\sigma_T^{\gamma^*N} = \frac{4\pi\alpha_{em}}{Q^2(1-x)}2xF_1(x,Q^2), \tag{3.17}
$$

$$
\sigma_L^{\gamma^*N} = \frac{4\pi\alpha_{em}}{Q^2(1-x)}F_L(x,Q^2). \tag{3.18}
$$

In the last step we have expressed the virtual photoabsorption cross sections in terms of the dimensionless structure functions

$$
F_1(x,Q^2) = m_N W_1(\nu,Q^2), \tag{3.19}
$$

$$
F_2(x,Q^2) = \nu W_2(\nu,Q^2), \tag{3.20}
$$

$$
F_L(x,Q^2) = \frac{4m_N^2x^2+Q^2}{Q^2}F_2(x,Q^2)-2xF_1(x,Q^2) \tag{3.21}
$$

which scale in the so-called Bjorken limit

$$
\nu, Q^2 \to \infty \quad \text{for fixed} \quad x = \frac{Q^2}{2m_N\nu},
$$

i.e. they only show a weak logarithmic dependence on $Q^2$. The variable $x$ is usually called Bjorken scaling variable. In the Breit frame the energy transfer vanishes and the spacial resolution of the virtual photon is given by $\sqrt{Q^2}$. If the photon scattered from non-interacting pointlike partons inside the nucleon the structure functions would be independent of $Q^2$. The observed scaling violation of the structure functions is directly

connected to the $Q^2$ dependence of the quark distribution functions $f_q(x, Q^2)$ which we discussed in Sec. 2.2.4. If one considers the $eN$ scattering process in a frame that is moving very fast, i.e. where the nucleon is moving with a very large momentum $|\vec{p}| \rightarrow \infty$, one can neglect the masses and the transverse momenta of the partons and the inner structure of the nucleon is given by their longitudinal momentum distribution only. Because of time dilatation the interactions of the partons among each other is frozen during the scattering process. In this infinite momentum frame the Bjorken variable $x$ simply yields the fraction of the nucleon's four-momentum carried by the struck quark. Using the parton distribution functions $f_q$ of Sec. 2.2.4 one can express the structure function $F_2$ as a weighted sum over the quark momentum distributions

$$F_2(x, Q^2) = x \sum_q z_q^2 f_q(x, Q^2).$$
(3.22)

Here the sum runs over both quarks and antiquarks inside the nucleon. Since quarks are spin-1/2 fermions one obtains in addition the so-called Callan-Gross relation [Hal84]

$$F_2(x, Q^2) = 2x F_1(x, Q^2).$$
(3.23)

From Eq. (3.21) one sees that the Callan-Gross relation leads to a vanishing of the longitudinal photoabsorption cross section (3.18) in the Bjorken limit and gives

$$\sigma_{\text{tot}}^{\gamma^* N} \xrightarrow{\text{Bjorken}} \sigma_T^{\gamma^* N} = \frac{4\pi^2 \alpha_{\text{em}}}{Q^2} F_2(x, Q^2)$$
(3.24)

for the total virtual photoabsorption cross section.

To summarize we expect that the virtual photon in the limit of very large $Q^2$ couples directly to the quarks inside the nucleon. However, Eq. (3.1) tells us that also for virtual photons a kinematic regime exists where the photon interacts via a hadronic fluctuation.

### 3.2.2 Resolved interactions

The resolved event classes of real photons can easily be extended to those of virtual photons. For the transverse part of the photon one can account for the virtuality $Q^2$ via a dipole factor as in strict VMD (cf. (3.4)) which ensures a smooth transition to real photons ($Q^2 = 0$). However, measurements of the structure functions $F_1$ and $F_2$ [Ben89, Adl97, Ack00] show a non-negligible contribution to $\sigma_{\text{tot}}^{\gamma^* N}$ arising from longitudinal photons (cf. Eq. (3.18)). A common approach is to attribute the longitudinal cross section with an extra factor of $r_V \sim Q^2/m_V^2$ relative to the transverse one [Sak69] which guarantees that $\sigma_L^{\gamma^* N}$ vanishes for $Q^2 \rightarrow 0$. Since such an ansatz seems only reasonable for moderately small $Q^2$ we adopt the alternative parametrization from Ref. [Fr00c]:

$$r(m_V^2, Q^2) = a \frac{4 m_V^2 Q^2}{(m_V^2 + Q^2)^2},$$
(3.25)

with $a$=0.5 as in the PYTHIA model [Sjö01b]. Now the longitudinal contribution vanishes for both low ($Q^2 \rightarrow 0$) and very high virtualities ($Q^2 \rightarrow \infty$).
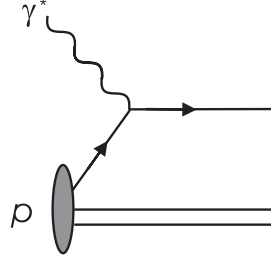
Figure 3.7: Lowest-order deep inelastic scattering $\gamma^* q \to q$. The photon-gluon fusion and QCD Compton process of Fig. 3.5 can be viewed as higher-order $\alpha_s$ corrections of this process.

**Vector meson dominance**

Using Eq. (3.25) to account for longitudinal photons and replacing the squared center-of-mass energy $s$ of the real photon interaction by the corresponding invariant mass squared $W^2$ of the virtual photon-nucleon interaction, the VMD contribution (3.6) to the total cross section becomes:

$$\sigma_{\text{VMD}}^{\gamma^* p}(W^2, Q^2) = \sum_V \frac{e^2}{g_V^2}[1 + \epsilon\, r(m_V^2, Q^2)] \left(\frac{m_V^2}{m_V^2 + Q^2}\right)^2 \sigma_{\text{tot}}^{Vp}(W^2). \qquad (3.26)$$

From Eq. (3.26) one sees that with increasing $Q^2$ also the heavier vector mesons become important. In the limit of very large $Q^2$, however, the VMD contribution vanishes as it should since for high virtualities $Q^2$ and finite $\nu$ the photon behaves like a pointlike particle according to Eq. (3.1).

**Generalized vector meson dominance**

The GVMD part (3.9) of the total photon cross section generalizes in a completely analogous way if one recalls that now $m_V$ has to be replaced by $2k_T$:

$$\sigma_{\text{GVMD}}^{\gamma^* p}(W^2, Q^2) = \frac{\alpha_{\text{em}}}{\pi} \sum_q z_q^2 \int_{k_0^2}^{k_1^2} \frac{dk_T^2}{k_T^2}[1 + \epsilon\, r(4k_T^2, Q^2)] \left(\frac{4k_T^2}{4k_T^2 + Q^2}\right)^2 \sigma^{q\bar{q}p}(W^2; k_T).$$
$$(3.27)$$

As can be seen from Eq. (3.27) also the GVMD contribution to $\sigma_{\text{tot}}^{\gamma^* N}$ vanishes for asymptotically large $Q^2$.

### 3.2.3 Direct interactions

As discussed in Sec. 3.2.1 electron-nucleon scattering at large values of $Q^2$ is dominated by deep inelastic scattering of the virtual photon on a quark inside the nucleon. The process is depicted in Fig. 3.7. To lowest order in $\alpha_s$, i.e. at very high $Q^2$, the deep inelastic scattering cross section is given via Eqs. (3.24) and (3.22) as

$$\sigma_{\text{DIS}}^{\gamma^* N} \approx \frac{4\pi^2 \alpha_{\text{em}}}{Q^2} x \sum_q z_q^2 f_q(x, Q^2) \qquad (3.28)$$
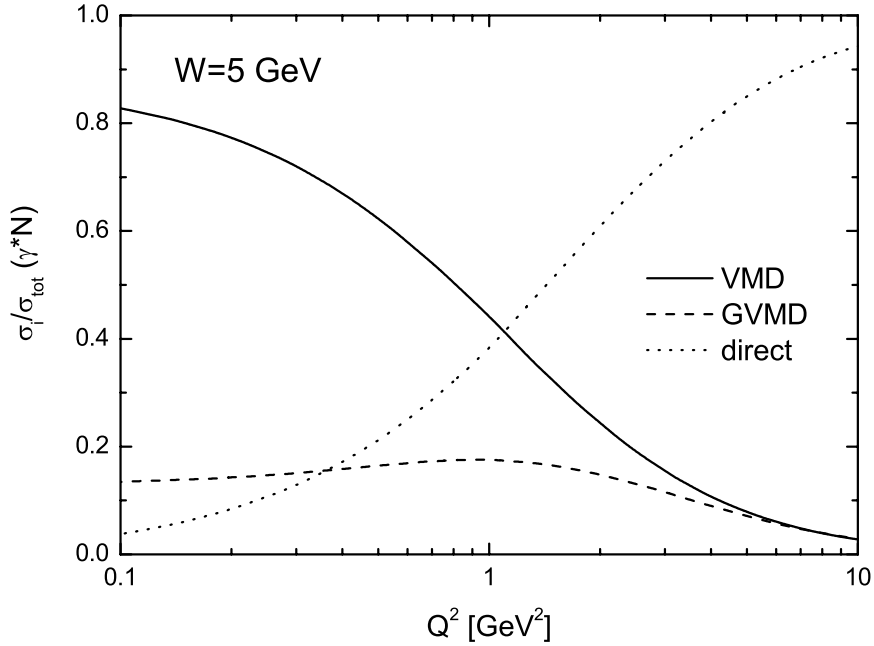
Figure 3.8: PYTHIA result for the fraction of the total $\gamma^*N$ cross section that is contributed by the VMD (solid line), GVMD (dashed) and direct (dotted) part of the photon as a function of $Q^2$ for fixed invariant mass $W$=5 GeV. Note that in contrast to the authors of Ref. [Fr00c] we call every pointlike interaction of the photon a direct process.

where the sum runs again over quarks and antiquarks inside the nucleon. In addition, one has the higher-order corrections whose matrix elements smoothly approach those of QCD Compton scattering and photon-gluon fusion of real photons as $Q^2 \to 0$. In the PYTHIA model [Sjö01b] the contribution of the lowest-order deep inelastic scattering to the direct processes is damped by a further factor of $Q^4/(Q^2 + m_\rho^2))^2$ to obtain a well-behaved deep inelastic scattering cross section for $Q^2 \to 0$ and to simultaneously retain (3.28) in the limit of very high $Q^2$.

Furthermore the resolved events in the PYTHIA model are suppressed by a factor $(W^2/(Q^2 + W^2))^3$ to avoid double counting with the lowest-order DIS events in the region of intermediate $Q^2$ and small $W^2$ [Fr00c]. The total virtual photon-nucleon cross section is therefore given by

$$\sigma_{\text{tot}}^{\gamma^*N}(W^2, Q^2) = \sigma_{\text{dir}}^{\gamma^*N}(W^2, Q^2) + \left( \frac{W^2}{Q^2 + W^2} \right)^3 \left( \sigma_{\text{VMD}}^{\gamma^*N}(W^2, Q^2) + \sigma_{\text{GVMD}}^{\gamma^*N}(W^2, Q^2) \right)$$

(3.29)

where $\sigma_{\text{dir}}^{\gamma^*p}$ now contains the lowest-order deep inelastic scattering plus the two higher-order corrections that reproduce the QCD Compton and photon-gluon fusion in the limit $Q^2 \to 0$. Speaking of resolved photon cross sections in the following we always

implicitly include the damping factor $(W^2/(Q^2 + W^2))^3$, i.e.

$$\sigma_{\text{VMD}}^{\gamma^* N}(W^2, Q^2) = \left(\frac{W^2}{Q^2 + W^2}\right)^3 \sum_V \frac{e^2}{g_V^2}[1 + \epsilon\, r(m_V^2, Q^2)] \left(\frac{m_V^2}{m_V^2 + Q^2}\right)^2 \sigma_{\text{tot}}^{VN}(W^2)$$

(3.30)

and

$$\sigma_{\text{GVMD}}^{\gamma^* N}(W^2, Q^2) = \frac{\alpha_{\text{em}}}{\pi} \left(\frac{W^2}{Q^2 + W^2}\right)^3 \sum_q z_q^2 \int_{k_0^2}^{k_1^2} \frac{dk_T^2}{k_T^2}[1 + \epsilon\, r(4k_T^2, Q^2)]$$
$$\times \left(\frac{4k_T^2}{4k_T^2 + Q^2}\right)^2 \frac{k_{V(q\bar{q})}^2}{k_T^2} \sigma^{V(q\bar{q})N}(W).$$

(3.31)

Fig. 3.8 shows the contributions of the three event classes to the total photon-nucleon cross section as a function of $Q^2$ for a fixed invariant mass $W$=5 GeV. This is approximately the kinematic regime of the HERMES experiment which we mainly focus on in our discussion of electroproduction in Sec. 6. One clearly sees that for $Q^2 \to 0$ one retains the situation we encountered for real photons, namely that the VMD class (solid line) contributes to about 80% to the real photon cross section while the rest is dominated by the GVMD class (dashed line). The situation changes with increasing $Q^2$. At $Q^2 \approx 1$ GeV$^2$ about half of the total cross section can be attributed to pointlike photon interactions (dotted line) with the rest shared among the VMD and GVMD events. Already at $Q^2 \gtrsim 10$ GeV$^2$ the cross section is mainly due to the direct photon interactions. In the whole kinematic regime that we are interested in throughout this work the GVMD component of the photon only contributes with less than 15 % to the total photon-nucleon cross section.

# Chapter 4

# The Lund model

In the preceding chapters we have focused on the different event classes in high-energy hadron-hadron and photon-hadron scattering. We have shown in Sec. 2.2.5 how in the case of soft non-diffractive scattering the single-gluon exchange leads to the creation of two hadronic strings, i.e. the properties of the QCD vacuum confine the energy density to narrow flux tubes connecting the colored string ends. One can imagine that also shortly after a hard non-diffractive event the various colored objects that emerge from the hard scattering and the final-state radiation[1] are connected by such strings. In addition, the excited hadronic states of the diffractive scattering events can be viewed as hadronic strings – however with a lower invariant mass than in the other event classes. The final particle spectrum of a high-energy reaction therefore strongly depends on the decay mechanism of the hadronic string.

The Monte Carlo simulation programs PYTHIA [Sjö01a, Sjö01b] and FRITIOF [And87, Pi92, And93] which determine the outcome of high-energy photon-nucleon and hadron-hadron interactions in our model use the Lund formalism to describe the breakup of the strings into hadrons in form of the JETSET package. This chapter should serve as a brief introduction into the basic ideas of the Lund model [And83, And98]. In Sec. 4.1 the concept of the massless relativistic string is introduced as a simple model for hadrons. In Sec. 4.2 we describe how an excited string fragments into hadrons due to the creation of quark-antiquark pairs from the vacuum. Within the Lund model it is also possible to give a quantitative estimate of the hadron-formation times. This is done in Sec. 4.3. We end this chapter with a brief discussion of the Monte Carlo methods that we use for the event generation in high-energy reactions.

## 4.1   Yoyo hadrons

As discussed in Sec. 2.3 the Regge spectrum of hadrons can be explained by assuming that the quark and antiquark (diquark) are connected by a color field which is compressed into a flux tube that contains a constant amount of energy per unit length. This constant force field leads to a linearly rising potential which is also seen in charmonium and bottonium spectroscopy as well as lattice QCD results. Phenomenologically, the string tension is known to be $\kappa \approx 1$ GeV/fm $\approx 0.2$ GeV$^2$, cf. Sec. 2.3.

---

[1]In case of hadron-hadron scattering or resolved photon interactions there might be also color charges arising from the initial-state radiation.
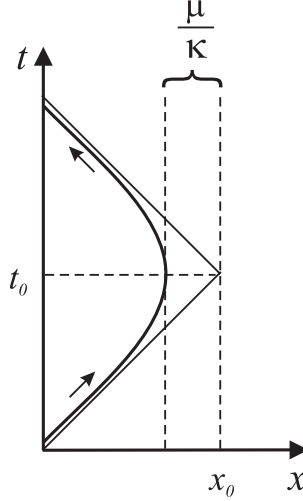
Figure 4.1: Space-time trajectory of a particle with mass $\mu$ moving in positive $x$-direction at $t = 0$ under the influence of a constant force $-\kappa$.

In this section we introduce a simple model which describes hadrons as a charge and an anticharge connected by a massless relativistic string that plays the role of the constant force field. The momentum of the state is located in the endpoint particles and its total energy can be decomposed into the potential energy in the force field and the kinetic energy of the endpoint particles.

The solution of the equation of motion

$$\frac{dp}{dt} = -\kappa \tag{4.1}$$

of a relativistic particle under the influence of a constant force $-\kappa$ is

$$p(t) = \kappa(t_0 - t). \tag{4.2}$$

The Hamilton equations of motion yield the velocity of this particle as

$$\frac{dx}{dt} = \frac{\partial H}{\partial p} = \frac{\partial}{\partial p} \left[ \sqrt{p^2 + \mu^2} + \kappa(x - x_0) \right] = \frac{p}{E}, \tag{4.3}$$

where

$$E = \sqrt{p^2 + \mu^2} \tag{4.4}$$

denotes the relativistic energy of a (free) particle with mass $\mu$. Combining Eqs. (4.1) and (4.3), one gets

$$\frac{dE}{dx} = \frac{dE}{dp}\frac{dp}{dt}\frac{dt}{dx} = -\kappa \tag{4.5}$$

and, hence, the energy

$$E(x(t)) = \kappa(x_0 - x(t)). \tag{4.6}$$

depends on the space coordinate of the particle. By taking the square of Eq. (4.4):

$$\mu^2 = E^2 - p^2 = \kappa^2 \left[ (x_0 - x)^2 - (t_0 - t)^2 \right] ,$$
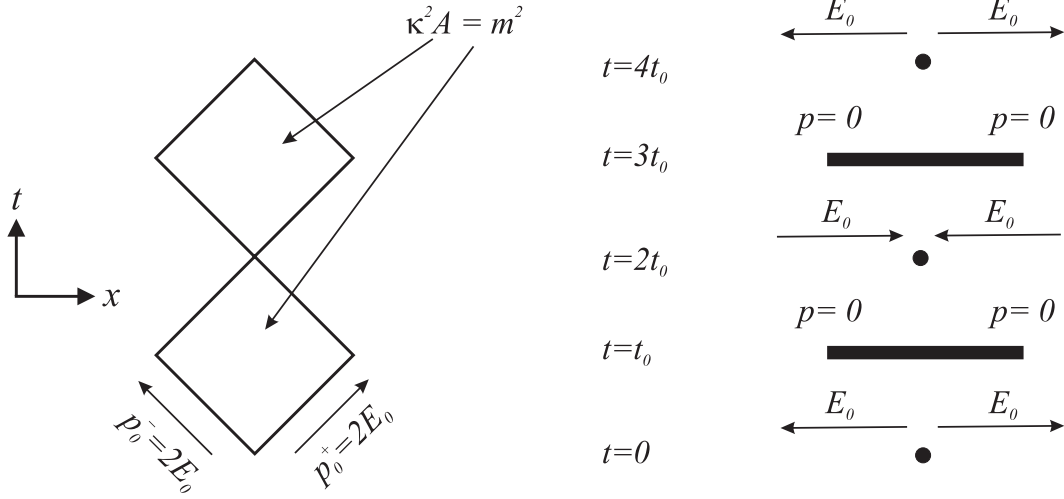
Figure 4.2: *Left:* Space-time diagram of a yoyo hadron with mass $m$ at rest. *Right:* Snap shots of the yoyo hadron at different times. At time $t = 0$ the two endpoint charges move apart with the same energy $E_0$ but opposite direction. During the following separation each particle looses the energy $\kappa t$ due to the force field while the force field has gained the energy $2\kappa t$. At time $t_0 = E_0/\kappa$ they have lost all their energy and turn back towards each other. While approaching each endpoint particle obtains the energy $\kappa(t - t_0)$ from the force field until they meet again at time $2t_0$. Obviously, the period of motion is $T = 4t_0 = 2E_{\text{tot}}/\kappa$.

one sees that the particle moves on a hyperbola in space time which is centered at $(t_0, x_0)$ and has the size parameter $\mu/\kappa$ (see Fig. 4.1). A massless particle ($\mu = 0$) would move on the lightcones $|t - t_0| = |x - x_0|$, i.e. the asymptotes in Fig. 4.1. At the turning point $(t_0, x_0)$ it would have vanishing momentum and energy and would change its velocity instantaneously from $+c$ to $-c$.

We will treat a meson as a system of two massless particles, a quark and an anti-quark, which interact with each other by an attractive constant force. Replacing the antiquark by a diquark one ends up with a model for a baryon. The space-time picture of such a yoyo hadron at rest is depicted in Fig. 4.2. If the two constituents of the hadron move apart with the same energy $E_0$ from a common origin but in opposite direction, the total momentum of the system vanishes and its total energy

$$E_{\text{tot}} = 2E_0$$

equals the hadron mass $m$. The two particles then move along the two different light-cones and loose energy and momentum $\kappa$ per unit length and time to the force field according to Eqs. (4.2) and (4.6). At time $t_0 = E_0/\kappa$ they turn around and after that they head towards each other and now gain energy and momentum from the force field. The period of the motion is

$$T = 4t_0 = \frac{2E_{\text{tot}}}{\kappa}, \tag{4.7}$$

where the latter equality is also true for a moving yoyo hadron as we will show in a moment.
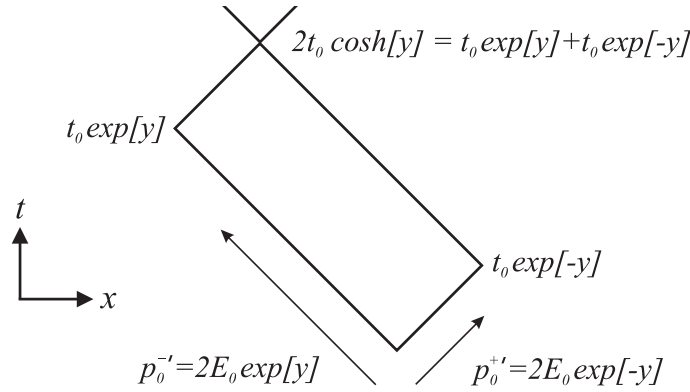
Figure 4.3: yoyo hadron that moves with rapidity $y$ along the negative $x$-direction.

Another general property of the massless relativistic string model is the so-called area law: The total area spanned by the force field in space-time during one period is related to the squared mass of the system. For the yoyo hadron at rest this area can directly be read off from the left-hand side of Fig. 4.2. It is given by the sum of the two squares with diagonal $2t_0 = E_{\text{tot}}/\kappa$:

$$\kappa^2 A = \kappa^2 2 \frac{t_0^2}{2} = E_{\text{tot}}^2 = m^2. \tag{4.8}$$

Fig. 4.3 now shows a yoyo hadron that moves with rapidity

$$y = \frac{1}{2} \ln \left[ \frac{E_h + p_h}{E_h - p_h} \right] \tag{4.9}$$

along the negative $x$-direction. The energy $E_h$ and momentum $p_h$ of the hadron is given by the sum of the quark energies and momenta. Boosting from the rest frame of the yoyo hadron to the moving system one gets for the particle which initially moves to the right the new turn-over time

$$t \cosh y - x \sinh y = t(\cosh y - \sinh y) = t_0 \exp[-y]$$

and for the particle moving to the left

$$t \cosh y - x \sinh y = t(\cosh y + \sinh y) = t_0 \exp[+y]$$

where we have used the fact that massless particles move on the lightcone ($x = \pm t$). Fig. 4.3 shows that by adding these two times one gets the new meeting time $2t_0 \cosh y$. The period of the moving hadron is therefore time dilated

$$T' = 4t_0 \cosh y > T.$$

Using Eq. (4.7), one can rewrite this as

$$T' = \frac{2E_{\text{tot}} \cosh y}{\kappa} = \frac{2E'_{\text{tot}}}{\kappa}$$
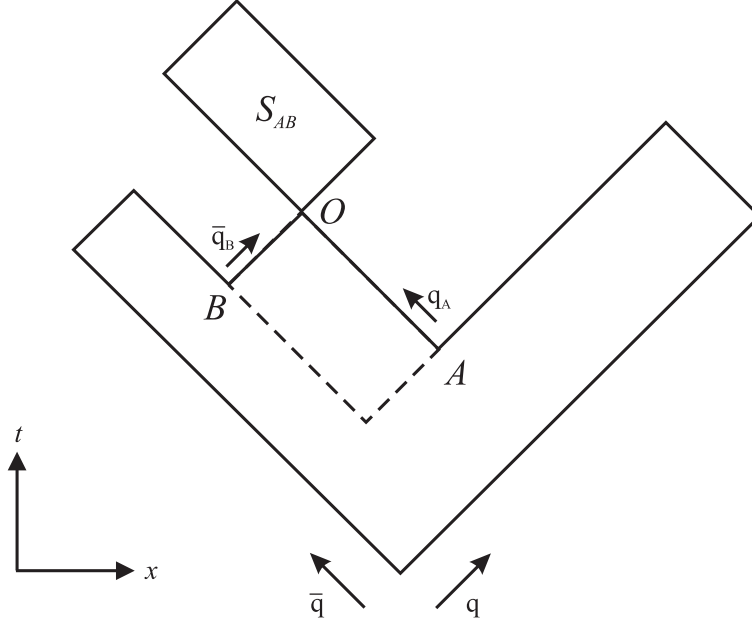
Figure 4.4: The string fragments due to the creation of two $q\bar{q}$ pairs at vertices $A$ and $B$. The quark $q_A$ and the antiquark $\bar{q}_B$ meet at space-time point $O$ to form a yoyo hadron $S_{AB}$.

and the yoyo period of a moving hadron is again determined by its total energy $E'_{\text{tot}} = E_h$.

The space-time area covered by the force field can once more be directly read off from Fig. 4.3. It is two times the size of the shown rectangle, i.e.

$$A' = 4t_0^2 = \frac{m^2}{\kappa^2} = A.$$

## 4.2 Decay of an excited string

The strings that are formed after a high-energy collision have an invariant mass that is in general larger than that of stable hadrons or low lying excited states. Therefore, they decay into lower mass fragments due to the creation of new quark-antiquark pairs out of the vacuum along the force field. At each vertex where a new $q\bar{q}$ pair is produced one has to require local conservation of energy, momentum and internal quantum numbers, e.g. charge, strangeness, etc. As a consequence the newly created $q$ and $\bar{q}$ have zero momenta and start to separate because of the two attached string pieces. During the separation they gain energy and momentum by 'eating up' the force field between them and the other string end.

Fig. 4.4 shows how a quark from vertex $A = (x_A, t_A)$ and an antiquark from vertex $B = (x_B, t_B)$ form a state $S_{AB}$ which consists of the quark $q_A$, the antiquark $\bar{q}_B$ and the field in between them. From Eqs. (4.2) and (4.6) one sees that at the meeting point $O$ the two constituents of $S_{AB}$ have gained momentum

$$p_A = \kappa(t_A - t_O), \qquad p_B = \kappa(t_O - t_B)$$
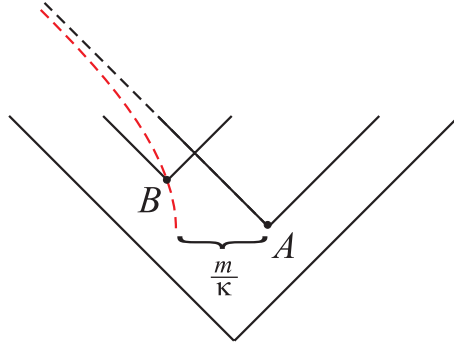
Figure 4.5: The on-shell condition for meson $S_{AB}$ forces vertex $B$ to lie on a hyperbola with size parameter $m/\kappa$ centered around vertex $A$.

and energy
$$E_A = \kappa(x_A - x_O), \qquad E_B = \kappa(x_O - x_B).$$
The total energy and momentum of the system $S_{AB}$ therefore only depend on the space-time difference of the production vertices $A$ and $B$
$$
\begin{aligned}
p_{AB} &= p_A + p_B = \kappa(t_A - t_B), \\
E_{AB} &= E_A + E_B = \kappa(x_A - x_B).
\end{aligned}
$$
If $S_{AB}$ is supposed to be a hadron with invariant mass $m$ the on-shell condition yields
$$\frac{m^2}{\kappa^2} = \frac{E_{AB}^2 - p_{AB}^2}{\kappa^2} = (x_A - x_B)^2 - (t_A - t_B)^2, \tag{4.10}$$
i.e. for a given vertex $A$ vertex $B$ has to lie on a hyperbola with size parameter $m/\kappa$ (cf. Fig. 4.5).

From Eq. (4.10) one sees that the distance of the two vertices $A$ and $B$ has to be spacelike. Hence, the two production points are not causally related and the (ordinary) time ordering of the break up vertices is not Lorentz invariant. One therefore usually orders the produced hadrons along one of the two lightcones, which is unique. The choice of the positive lightcone, i.e. starting from the right is illustrated in Fig. 4.6. The $j$-th hadron, i.e. the one that consists of the quark $q_{j-1}$ and the antiquark $\bar{q}_j$ has energy and momentum
$$
\begin{aligned}
E_j &= \kappa(x_{j-1} - x_j) \equiv \kappa\Delta x_j \\
p_j &= \kappa(t_{j-1} - t_j) \equiv \kappa\Delta t_j
\end{aligned}
$$
where $(x_j, t_j)$ denotes the production vertex of the pair $q_j\bar{q}_j$. The index $j$ is also called the *rank* of the hadron. For meson $j$ the lightcone momenta $p_j^+ = E_j + p_j$ and $p_j^- = E_j - p_j$ are given by the space-time distance passed by $\bar{q}_j$ and $q_{j-1}$ respectively before they meet. Thus the $\bar{q}_j$ can be considered as the carrier of the $p^+$ component of meson $j$ while $q_{j-1}$ carries the $p^-$ component.

Introducing the lightcone coordinates $x_i^{\pm} = t_i \pm x_i$ of the production vertices as well as the lightcone distances
$$\Delta x_j^{\pm} = \Delta t_j \pm \Delta x_j = x_{j-1}^{\pm} - x_j^{\pm},$$
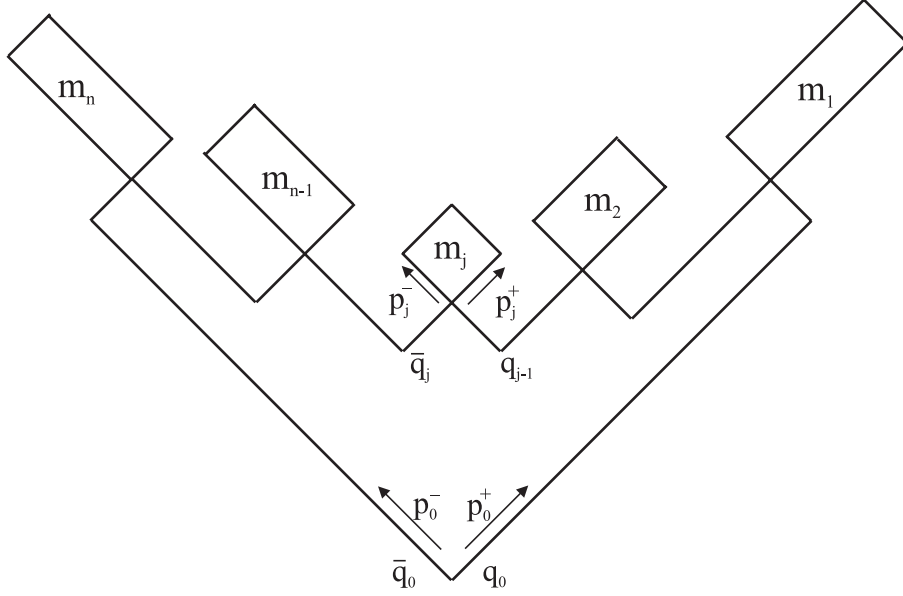
Figure 4.6: Numbering of the produced hadrons along the positive lightcone.

one can write the on-shell condition (4.10) for meson $j$ as

$$\frac{m_j^2}{\kappa^2} = \Delta x_j^2 - \Delta t_j^2 = -\Delta x_j^+ \Delta x_j^- . \tag{4.11}$$

Therefore, the production process of mesons in the fragmentation of a hadronic string can be viewed as a series of steps along the (positive) lightcone (cf. Fig. 4.7). Starting at the turning point of the original quark $q_0$ in the excited string

$$x_0^+ = \frac{p_0^+}{\kappa} , \qquad x_0^- = 0 ,$$

where $p_0^+$ denotes the lightcone momentum of $q_0$ at time zero, one takes random steps along the positive lightcone

$$\Delta x_j^+ = z_j x_{j-1}^+ , \qquad z_j \in [0, 1]. \tag{4.12}$$

The fragmentation function $f(z)$ which gives the probability distribution of the random variable $z_j$ is discussed at the end of this section. A step along the negative lightcone is fixed by the mass constraint (4.11):

$$\Delta x_j^- = -\frac{m_j^2}{\kappa^2 \Delta x_j^+} . \tag{4.13}$$

Thus we have the recursion formulae

$$x_j^+ = x_{j-1}^+ - \Delta x_j^+ = (1 - z_j) x_{j-1}^+ \tag{4.14}$$

$$x_j^- = x_{j-1}^- - \Delta x_j^- = x_{j-1}^- + \frac{1 - z_j}{z_j x_j^+} \frac{m_j^2}{\kappa^2} \tag{4.15}$$
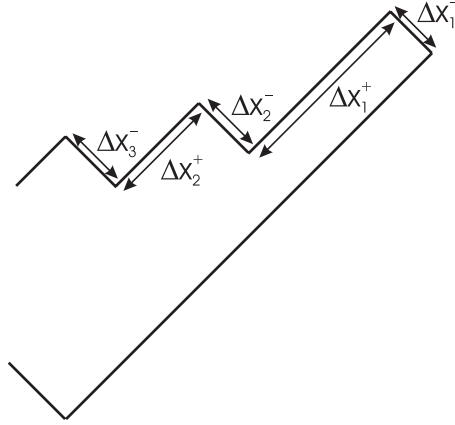
Figure 4.7: The fragmentation of the string viewed as a series of steps along the positive lightcone. The on-shell condition fixes the steps along the negative lightcone. See text for details.

together with the constraint that the path must end at the turning point of $\bar{q}_0$:

$$x_n^+ = 0\,, \qquad\qquad x_n^- = \frac{p_0^-}{\kappa}\,. \tag{4.16}$$

Each step divides the fragmenting system into a meson $(q_{j-1}\bar{q}_j)$ and a remainder string $(\bar{q}_0 q_j)$ with reduced energy and momentum (cf. Fig. 4.8).

The requirement that the last fragmentation step has to end at the turning point of $\bar{q}_0$ assures energy and momentum conservation

$$\sum_{j=1}^{n} p_j^{\pm} = p_0^{\pm}\,.$$

The fragmentation process is uniquely determined by the set of Lorentz-invariant scaling variables $\{z_i\}$ and therefore only depends on the fragmentation function $f(z)$. As shown in Appx. E, the requirement that taking the fragmentation steps along the negative and positive lightcone should lead to the same result in the limit $n \to \infty$ restricts the fragmentation function to the following functional form

$$f(z) = N\frac{(1-z)^a}{z}\exp(-b\frac{m^2}{z})\,, \tag{4.17}$$

which is called *Lund fragmentation function*. Here $a$ and $b$ are parameters which have to be fitted to experiment while $N$ is a normalization constant and $m$ denotes the mass of the produced hadron. For details see Appx. E.

The Lund fragmentation function $f(z)$ is plotted in Fig. 4.9 for $m = 0.5$ GeV and different choices of the parameters $a$ and $b$ (cf. Tab. 4.1). The parameters determine the behavior of $f(z)$ as $z$ approaches 0 or 1. The factor $(1/z)\exp(-bm^2/z)$ peaks at $z = bm^2$ (for $bm^2 < 1$) and rapidly vanishes for smaller $z$. The factor $(1-z)^a$ vanishes as $z \to 1$. One sees that as long as the mass $m$ of the produced hadron is small
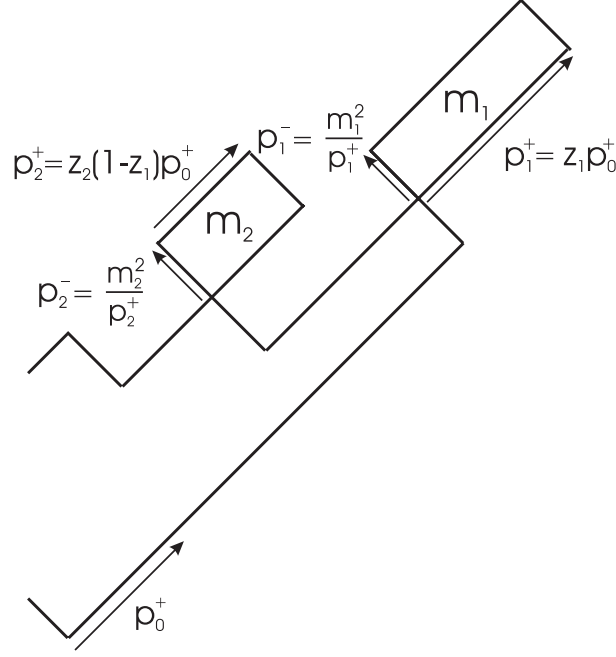
Figure 4.8: Every creation of a new $q\bar{q}$ pair splits the system into a meson and a remainder string with down-scaled lightcone momentum.

|   |                       | $a$  | $b\,[\text{GeV}^{-2}]$ |
|---|-----------------------|------|------------------------|
| 1 | Lund [And83]          | 1.   | 0.44                   |
| 2 | PYTHIA 6.208 [Sjö01b] | 0.3  | 0.58                   |
| 3 | HSD [Gei98a, Gei98b]  | 0.23 | 0.34                   |
| 4 | FRITIOF 7.02 [Pi92]   | 0.44 | 0.37                   |
| 5 | JETSET 7.3 [Sjö04]    | 0.5  | 0.9                    |

Table 4.1: Different parameter sets for the Lund fragmentation function (4.17).

compared to $1/\sqrt{b} \approx$ 1.0–1.7 GeV it is very unlikely that the fragment carries a large fraction of the available string energy. The average fraction

$$\langle z \rangle = \int\limits_0^1 dz\, z f(z)$$

that the hadron takes from the (positive) lightcone momentum of the (remainder) string lies between 0.18 (for $m = 0.14\,\text{GeV} \approx m_\pi$) and 0.5 (for $m = 1\,\text{GeV} \approx m_N$). The ultimate number of string fragments depends on the invariant mass of the initial string.

In principle, a set of independently chosen random numbers $\{z_i\}$ can solve the problem of fragmenting a high energetic string. However, it is very unlikely that the iteration process ends at the turning point of the $\bar{q}_0$ which is required by energy
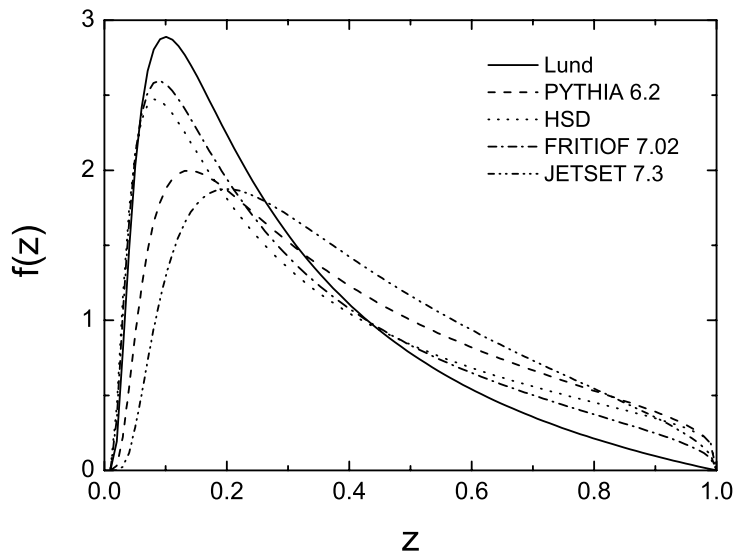
Figure 4.9: Lund fragmentation function (4.17) for $m$=0.5 GeV and different parameter sets $(a,b)$. See Tab. 4.1 for details.

and momentum conservation. There are some ways to cure this problem [Ede00] but which show up to be unsuitable for Monte Carlo implementation. In the JETSET package the following way was chosen: Fragmentation happens randomly at both ends of the string, until the remaining invariant mass drops below a certain threshold. In the final step the kinematics of two hadrons are chosen simultaneously and energy and momentum conservation is guaranteed. The choice of some parameters, e.g. the threshold invariant mass, ensure that the $z$ distribution of the final particles agrees with the default distribution (4.17).

As we have already discussed, Eq. (4.10) states that the different production vertices are not causally connected. The fact that the string nevertheless fragments into on-shell hadrons cannot be understood in purely classical terms. It can be argued on a quantum mechanical level that all breakup configurations that give unphysical masses simply cannot be projected onto a physical state. Note that in the nuclear medium the interactions with the surrounding nucleons may modify the masses of the fragments compared to the situation in vacuum.

**Transverse momentum and massive quarks**

Up to now we have neglected the transverse momenta $p_T$ and the masses $\mu$ of the quarks. The $q$ and the $\bar{q}$ that are created in the string fragmentation have transverse momentum $p_T(q) = -p_T(\bar{q})$ and instead of the hadron mass $m$ the transverse mass

$$m_T = \sqrt{m^2 + p_T^2}$$

enters Eqs. (4.13) and (4.17). Furthermore, if the quarks have a finite mass they do not move on the lightcones anymore but their trajectories in space-time will be the hyperbolae discussed in Sec. 4.1. The asymptotes of such a yoyo mode are again
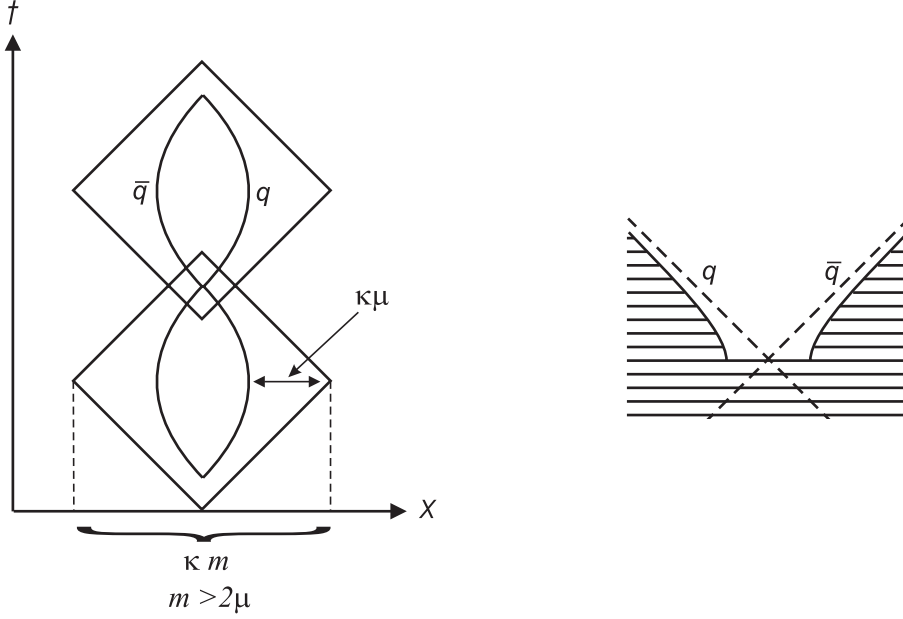
Figure 4.10: *Left:* Motion of a massive $q$ and $\bar{q}$ in a yoyo hadron. *Right:* A pair of massive quarks is created in the force field and moves apart on different branches of the same hyperbola.

rectangles, cf. left-hand side of Fig. 4.10, but in contrast to the situation of massless constituents the oscillation time now also depends on the constituent mass $\mu$. However, this only influences the internal motion of the hadron after the production and is of no importance for the fragmentation process itself. Note, however, that the constituent masses $\mu$ might influence the hadron-formation times, i.e. the times when the world lines of the quark and antiquark of a yoyo hadron cross. By interpreting the straight lines of the previous fragmentation diagrams as the asymptotes for the hyperbolic world lines of massive quarks, the fragmentation model can be developed in exactly the same way as before [And98].

There is nevertheless a physical difference between the production of massless and massive quarks (see right-hand side of Fig. 4.10). Because of local energy conservation a real massive $q\bar{q}$ pair cannot be created at one single space-time point. This is only possible for virtual quark pairs which then tunnel to real quark pairs. The connected tunneling probability has been calculated in Ref. [Gle83] and leads to an additional suppression of heavy quark production in the string fragmentation. Consider a newly created virtual $q\bar{q}$ pair at time $t = 0$. Due to local energy conservation the energy of the quark (or antiquark) must be zero:

$$t = 0: \quad E_q^2 = E_{\bar{q}}^2 = 0 = p_L^2 + p_T^2 + \mu^2,$$

where $p_T$ denotes the transverse momentum of the quark $(p_T(\bar{q}) = -p_T(q))$ and $\mu$ its constituent mass. They therefore both have (imaginary) longitudinal momenta:

$$t = 0: \quad p_L = \pm i\mu_T = \pm i\sqrt{p_T^2 + \mu^2}.$$

At time $t > 0$ the quark and antiquark have separated a distance $2r$ and thereby gained the energy $2\kappa r$ from the flux tube:

$$t > 0: \qquad E_q + E_{\bar{q}} = 2\sqrt{p_L(r)^2 + \mu_T^2} = 2\kappa r$$

$$\Rightarrow p_L(r) = \pm i\sqrt{\mu_T^2 - (\kappa r)^2}.$$

The quarks have tunneled to real quarks when $p_L(r) = 0$, i.e. when $r = \mu_T/\kappa$. Hence, the tunneling probability is given as [Sak94]:

$$P = |e^{-S}|^2 \quad \text{with} \quad S = 2\int_0^{\mu_T/\kappa} |p_L(r)|dr = \frac{\pi\mu_T^2}{2\kappa}. \tag{4.18}$$

Eq. (4.18) leads to a Gaussian distribution of transverse momentum and suppresses high $p_T$. Furthermore, the production of quarks with large constituent mass $\mu$ is strongly reduced by the tunneling probability. This leads to a suppression of strange and charm particle production in the string fragmentation.

Since the tunneling amplitude is very sensitive to the size of the constituent quark masses which are not well-defined quantities, one usually extracts the suppression factors from experiment. As we show in Sec. 4.4.1, one experimentally observes that strangeness production in $pp$ collisions is suppressed by about a factor of 0.3. If one inserts the constituent mass [Sjö01b] of the light quark flavors $u$ and $d$ ($\mu_u \approx \mu_d \approx 0.325$ GeV) into Eq. (4.18), one ends up with a realistic value for the constituent strange quark mass of $\mu_s \approx 0.425$ GeV for this suppression factor. Furthermore, a constituent charm quark mass $\mu_c \approx 1.3$ GeV leads to a relative suppression

$$P(u\bar{u}, d\bar{d}) : P(s\bar{s}) : P(c\bar{c}) \approx 1 : 0.3 : 10^{-11}. \tag{4.19}$$

This means that $c\bar{c}$ pair creation essentially never occurs during a soft hadronization process but only in hard processes like $q\bar{q} \rightarrow c\bar{c}$ or $gg \rightarrow c\bar{c}$. The tunneling probability also suppresses the production of antibaryons via diquark-antidiquark creation in the string fragmentation. Assuming a mass of about 0.5 GeV for the diquark leads to a suppression factor of about 0.1 compared to $u\bar{u}$ or $d\bar{d}$ creation. However, there are other possibilities for baryon creation in a fragmentation process as we discuss in Sec. 4.4.2.

Note that the above suppression factors are extracted from experiments using elementary targets and projectiles, i.e. they correspond to the string tension and quark masses in vacuum. If the string fragmentation takes place inside (a dense) nuclear medium, the quark masses as well as the value of $\kappa$ might change and could lead to different tunneling amplitudes.

### Degeneracies

So far we have not considered the spin degree of freedom in the fragmentation process. If one takes the degeneracy $(2J+1)$ of the final-state hadrons in spin space into account, one recognizes that, e.g. the production of $\rho$ mesons ($J = 1$) should be about a factor three times larger than that of the pseudoscalar $\pi$ meson ($J = 0$). This naive factor of three is then modified by some wave-function normalization factor which disfavors

the production of heavier states. This has to be kept in mind when determining the hadron species from the quark content.

At the end of this chapter we want to summarize how the decay of an excited string can be realized schematically. First the flavor and transverse momentum of the $q\bar{q}$ pair at the first vertex is chosen using the suppression factors and Gaussian $p_T$ distribution given by Eq. (4.18). Now, knowing the quark content of the first-rank hadron, its isospin and spin can be determined, hence, fixing the identity of the particle[2]. If the particle is unstable a mass is chosen according to its spectral function. After the mass has been fixed the fragmentation function (4.17) is used to determine the energy and momentum fraction carried away by the hadron. After that the whole process is repeated until the invariant mass of the remainder string drops below a certain threshold and the kinematics of the two final hadrons are chosen to fulfill energy and momentum conservation.

## 4.3   Formation time

One of our main goals is the investigation of the hadronization time, i.e. the time that passes between the photon-nucleon interaction and the time when the reaction products have evolved to physical hadrons. We now use the Lund model to extract some quantitative estimates and show that these formation times are indeed smaller than those usually quoted in connection with the Lund model, i.e. 2 fm/$c$. The reason for this is essentially the finite energy of the primarily excited string in contrast to the infinite-mass formulae used in literature. Before we start our discussion we point out that the Lund model might correctly describe the experimentally observed particle spectra. However, it is not clear whether the underlying space-time picture of hadronization is realistic. Therefore, we will use later on the output of the fragmentation model (i.e. the exclusive particle spectra) which is verified by experiment and investigate in addition different hadronization scenarios.

Within the Lund model Lorentz-invariant statements can only be made about the $q\bar{q}$ production vertices and the space-time points where $q$ and $\bar{q}$ world lines cross. If one defines the first ones as the production points of the prehadrons and the latter as the space-time points where the yoyo hadrons form, it is evident that for any Lorentz frame the particles with lowest momentum are always produced first in time[3] (cf. Fig. 4.11).

For the fragmentation of a string with a very large invariant mass $W$ into a large number of yoyo hadrons the proper times $\tau_V$ of the vertices $V$ are distributed according to Eq. (E.11) as

$$H(\Gamma_V) = C\Gamma_V^a \exp(-b\Gamma_V),$$

where $\Gamma_V$ and $\tau_V$ are connected via relation (E.1):

$$\tau_V^2 = \frac{\Gamma_V}{\kappa^2}.$$

---

[2]In FRITIOF and PYTHIA only the mesons and baryons with $L = 0$ are considered as possible fragments.

[3]This is only true if one does not consider the fragmentation into different mass hadrons. Here the vertices move along different hyperbolae during a Lorentz boost.
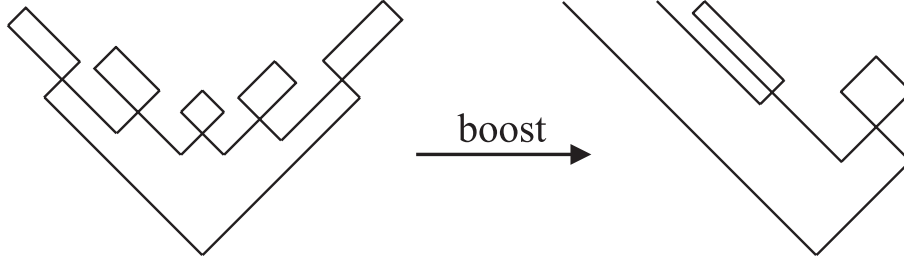
Figure 4.11: Before the Lorentz boost the third-rank particle is at rest and produced first in time. After boosting into the rest frame of the first-rank particle, the latter is produced first in time. The reason is that all the (spacelike separated) vertices move on hyperbolae during the Lorentz boost.

According to Eq. (E.11), the average production proper time of the prehadrons

$$\tau_{V\infty} = \sqrt{\langle \tau_V^2 \rangle_{W \to \infty}} = \left( \frac{1}{\kappa^2} \int\limits_0^\infty d\Gamma \, \Gamma H(\Gamma) \right)^{\frac{1}{2}} \tag{4.20}$$

lies in the range $\tau_{V\infty} \approx 1.3 - 2.1$ fm/$c$ for a string tension $\kappa \approx 1$ GeV$^2$ and the parameters given in Tab. 4.1. These times are quite large indeed.

**Production and formation times averaged over all ranks**

In Ref. [Bia87] Bialas and Gyulassy have examined the $z$ dependence of the vertices $V$ and the meeting points $O$ (cf. Fig. 4.4) using a somewhat simpler fragmentation function

$$f(z) = (1 + C)(1 - z)^C \tag{4.21}$$

which obviously does not depend on the mass of the produced hadrons. They have again considered the fragmentation of a very massive string into a large number of hadrons but now in a frame where hadronization occurs very near the lightcone, i.e. $p_j^+ \gg m_j$ so that the steps along the negative lightcone (4.13) can be neglected. In a scattering process where a large positive lightcone momentum is transfered to a constituent $q_0$ of the original yoyo hadron this frame coincides with the laboratory frame, i.e. the frame in which the yoyo hadron was initially at rest. By averaging over infinitely many ranks, they derived for $C = 1$ the analytic expressions

$$t_{V\infty}(z_h) = \left( \frac{\ln(1/z_h^2) - 1 + z_h^2}{1 - z_h^2} \right) z_h \frac{p_0^+}{2\kappa} \tag{4.22}$$

$$t_{O\infty}(z_h) = \left( \frac{\ln(1/z_h^2)}{1 - z_h^2} \right) z_h \frac{p_0^+}{2\kappa}. \tag{4.23}$$

for the average production and formation times of a hadron that carries the fraction $z_h$ of the original quark's lightcone momentum $p_0^+$. The $z_h$ dependence of both times is illustrated in Fig. 4.12. An increase of the yoyo formation time $t_O$ with rising $z_h$ might have already been expected from time-dilatation arguments even though
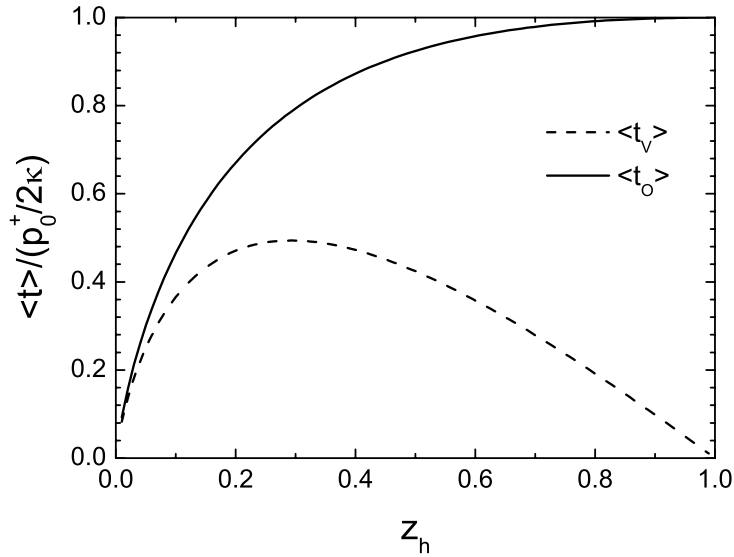
Figure 4.12: The dashed line represents the average time when the $q\bar{q}$ pairs are produced in the string fragmentation (Eq. (4.22)) and the solid line shows when the yoyo hadrons have formed according to Eq. (4.23).

such arguments (assuming a constant formation proper time) would predict a linear growth with $z_h$. The much more interesting aspect of Fig. 4.12 is that if one identifies $t_V$ with a prehadron-production time these prehadrons are created very early in the string fragmentation if they carry a very small or very *large* fraction of the lightcone momentum.

A similar behavior is also expected for the leading hadron, i.e. the first-rank hadron, from models where the struck quark $q_0$ looses energy through gluon bremsstrahlung (see e.g. Ref. [Kop03]). The radiated gluons then split into $q\bar{q}$ pairs and finally combine to produce the colorless prehadrons. In such a scenario the leading quark $q_0$ looses more energy by radiation the longer the hadronization process lasts. If it is not allowed to loose any energy at all, i.e. if $z_h = 1$, the colorless prehadron has to be created instantaneously.

**Production and formation times for different ranks**

Up to now we have only considered the production and formation times averaged over infinitely many hadrons. However, within the scope of this work the invariant mass of the hadronic string is only around $W \approx 5$ GeV which limits the average number of fragments to around 4–5. Hence, we now examine explicitly the average formation times of the first-, second- and third-rank hadrons in the Lund decay scheme. Let us first define the averaged rescaled fragmentation functions $\overline{f}_i(\zeta_i)$ that give the probability that the $i^{\text{th}}$ hadron carries away a fraction $z_h = \zeta_i$ of the original lightcone momentum. Obviously, this is given by

$$\zeta_i = z_i \prod_{j=1}^{i-1}(1 - z_j) \tag{4.24}$$
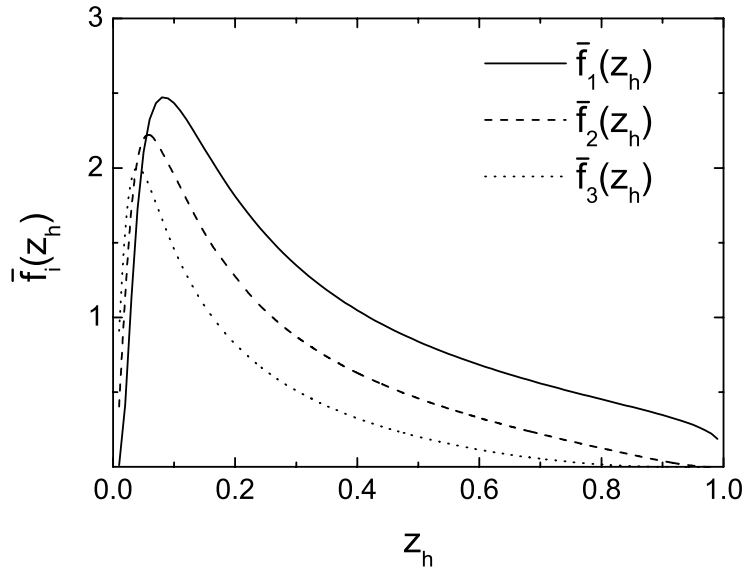
Figure 4.13: Averaged rescaled fragmentation functions $\overline{f}_i$ as defined in Eq. (4.25). We have used the parameter set (3) from Tab. 4.1 as well as an average hadron mass $m = 0.5$ GeV.

and the first three averaged rescaled fragmentation functions $\overline{f}_i$ are

$$\overline{f}_1(z_h) = f(z_h)$$

$$\overline{f}_2(z_h) = \int\limits_0^{1-z_h} dz_1 \, f(\frac{z_h}{1-z_1})f(z_1)$$

$$\overline{f}_3(z_h) = \int\limits_0^{1-z_h} dz_1 \int\limits_0^{\frac{1-z_1-z_h}{1-z_1}} dz_2 \, f(\frac{z_h}{(1-z_1)(1-z_2)})f(z_1)f(z_2). \qquad (4.25)$$

They are plotted in Fig. 4.13 for an average hadron mass $m = 0.5$ GeV using the parameter set (3) from Tab. 4.1. As expected, the higher-rank hadrons in average carry a smaller fraction $z_h$ of the original lightcone momentum, namely $\langle z_h \rangle_1 \approx 0.34$, $\langle z_h \rangle_2 \approx 0.17$ and $\langle z_h \rangle_3 \approx 0.08$.

We have already shown that the proper times of the vertices $V_i$ are connected to the areas $\Gamma_i$ illustrated in Fig. E.1 as

$$\tau_{V_i}^2 = x_i^+ x_i^-. \qquad (4.26)$$

Similarly, the proper times of the prehadron-formation points are given by the space-time areas under the meeting points $O_i$

$$\tau_{O_i}^2 = x_{i-1}^+ x_i^-. \qquad (4.27)$$

We can now use the recursion formulae (4.14) and (4.15) to express these times by the lightcone momentum fractions $\{z_i\}$. Replacing all hadron masses $m_i$ by an average
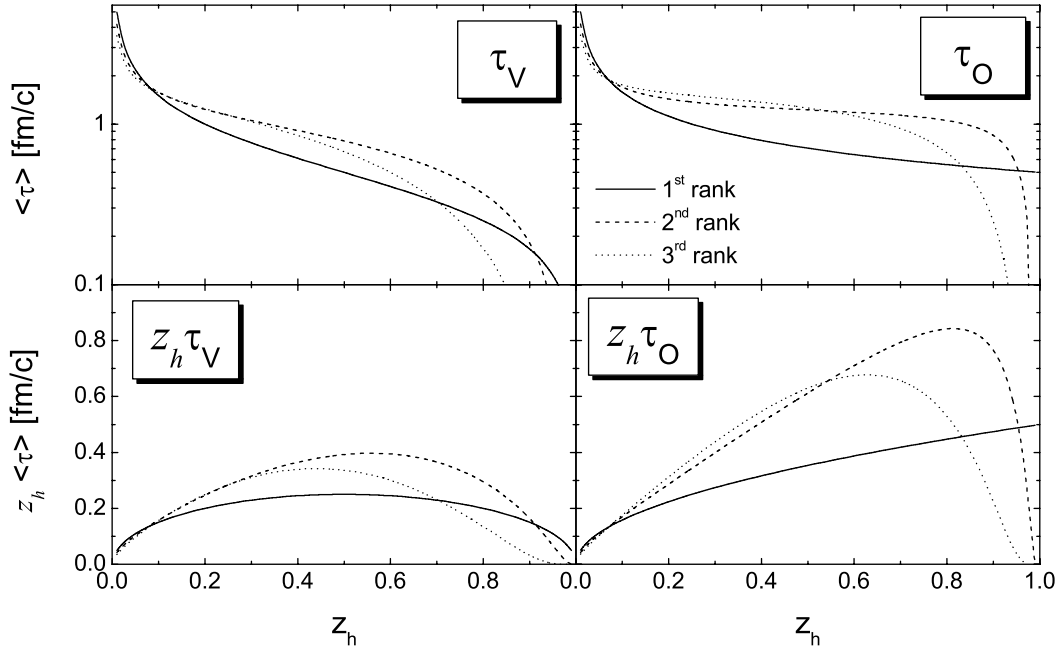
Figure 4.14: Average proper times for the production and formation of a hadron with lightcone momentum fraction $z_h$. The lower two plots show the product of the proper times and $z_h$ which is proportional to the dilated times in the laboratory frame. The parameter set (3) from Tab. 4.1 with an average hadron mass $m = 0.5$ GeV was used.

mass $m$, we get for the first three production times:

$$
\begin{align}
\tau_{V_1}^2(z_1) &= \frac{m^2}{\kappa^2}\frac{1 - z_1}{z_1} \\
\tau_{V_2}^2(z_1, z_2) &= \frac{m^2}{\kappa^2}(1 - z_2)(1 - z_1)\left(\frac{1}{z_1} + \frac{1}{z_2(1 - z_1)}\right) \\
\tau_{V_3}^2(z_1, z_2, z_3) &= \frac{m^2}{\kappa^2}(1 - z_3)(1 - z_2)(1 - z_1)\left(\frac{1}{z_1} + \frac{1}{z_2(1 - z_1)} + \frac{1}{z_3(1 - z_2)(1 - z_1)}\right)
\end{align}
\tag{4.28}
$$

and for the prehadron-formation times

$$
\tau_{O_j}^2(\{z_i\}) = \frac{\tau_{V_j}^2(\{z_i\})}{1 - z_j}.
\tag{4.29}
$$

These expressions can now be used to calculate the average proper times for production and formation of a hadron with mass $m$ that carries the fraction $z_h$ of the original

| $m$ [GeV] | $\overline{\tau}_{V_1}$ [fm/$c$] | $\overline{\tau}_{V_2}$ [fm/$c$] | $\overline{\tau}_{V_3}$ [fm/$c$] | $\overline{\tau}_{O_1}$ [fm/$c$] | $\overline{\tau}_{O_2}$ [fm/$c$] | $\overline{\tau}_{O_3}$ [fm/$c$] |
|-----------|-----------|-----------|-----------|-----------|-----------|-----------|
| 0.14 | 0.59–0.83 | 0.78–1.11 | 0.91–1.30 | 0.60–0.84 | 0.84–1.18 | 0.99–1.40 |
| 0.5 | 0.82–1.14 | 1.04–1.49 | 1.15–1.70 | 0.96–1.25 | 1.27–1.69 | 1.42–1.94 |
| 1.0 | 0.99–1.40 | 1.18–1.76 | 1.24–1.93 | 1.18–1.72 | 1.72–2.22 | 1.83–2.46 |

Table 4.2: Average proper times (4.30) for the production and formation of hadrons with different rank and mass $m$.

lightcone momentum:

$$
\begin{aligned}
\overline{\tau}^2_{V_1,O_1}(z_h) &= \tau^2_{V_1,O_1}(z_h) \\
\overline{\tau}^2_{V_2,O_2}(z_h) &= \int_0^{1-z_h} dz_1\, \tau^2_{V_2,O_2}(z_1, \frac{z_h}{1-z_1}) f(z_1) \\
\overline{\tau}^2_{V_3,O_3}(z_h) &= \int_0^{1-z_h} dz_1 \int_0^{\frac{1-z_1-z_h}{1-z_1}} dz_2\, \tau^2_{V_3,O_3}(z_1, z_2, \frac{z_h}{(1-z_1)(1-z_2)}) f(z_1) f(z_2)
\end{aligned}
$$

which are shown in Fig. 4.14 again for $m = 0.5$ GeV and the parameter set (3).

If one compares Fig. 4.14 with the averaged fragmentation functions shown in Fig. 4.13 one sees that the higher-rank hadrons are in general produced and formed later in time. Fig. 4.14 also shows the product of $z_h$ and $\overline{\tau}_{V_j,O_j}(z_h)$ which is proportional to the production and formation time in the lab frame, i.e. their shapes have to be compared with those shown in Fig. 4.12. One sees that Eqs. (4.22) and (4.23) oversimplify the physical picture. For large values of $z_h$ the production and formation times of higher-rank hadrons are smaller than those of the first-rank hadron. However, most of the higher-rank hadrons carry only small momentum fractions $z_h$ for which the production and formation times are larger. Furthermore, one sees that the behavior of the yoyo formation time (solid line in Fig. 4.12) at large $z_h$ is generated completely by the first-rank hadron. This is reasonable since $z_h = 1$ means that the string can only fragment into one hadron. We note that these findings are still in the framework of a toy model. Realistic production and formation times as given by JETSET are depicted in Figs. 4.16 and 4.17.

The average formation times can be calculated from Eqs. (4.28) and (4.29):

$$
\overline{\tau}^2_{V_j,O_j} = \left[ \prod_{i=1}^{j} \int_0^1 f(z_i) dz_i \right] \tau^2_{V_j,O_j}(\{z_i\}). \tag{4.30}
$$

Depending on which parameter set of Tab. 4.1 one uses, one gets the values listed in Tab. 4.2. Hereby, the parameter set (5) always gives the smallest values while the parameter set (1) in general gives the largest. One clearly sees how the average proper time of the vertices increases with rank which explains the large asymptotic value $\tau_{V\infty} \approx 1.3 - 2.1$ fm/$c$ for the vertex proper time averaged over infinitely many hadrons (4.20). Also the proper times of the meeting points grows with rank. In addition, one
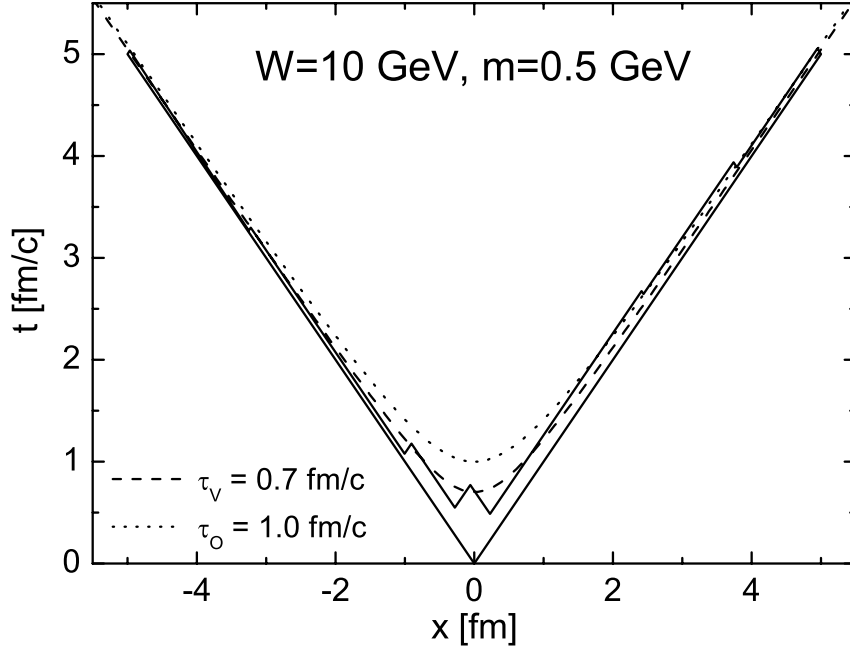
Figure 4.15: Example for a space-time picture of a real Lund fragmentation of a string with mass $W = 10$ GeV into hadrons with mass $m$. The dashed and dotted lines show the hyperbolae of the average production and formation time respectively. We have again used the parameter set (3) from Tab. 4.1 as well as an average hadron mass $m = 0.5$ GeV.

observes larger proper times for the heavier hadrons which could have been expected because of the factor $m^2/\kappa^2$ in Eq. (4.28). However, the production and formation proper times are not simply proportional to the hadron mass $m$ since the mass also enters the Lund fragmentation function (4.17). In the full Lund model one has to replace $m$ with the transverse mass $m_T$ in the equations given above. This implies that the differences between the production and formation times for different mass hadrons become smaller since they are smeared out by the transverse momentum $p_T$.

**Strings with finite invariant mass**

Up to now we always neglected the mass of the fragmenting system. For a finite mass $W = \sqrt{p_0^+ p_0^-}$, the boundary condition (4.16) that the last iteration step has to end on the turning point of the $\bar{q}_0$ leads to a change of the average proper times for vertices and meeting points. We have therefore investigated the decay of a string with invariant mass $W = 10$ GeV into hadrons of mass $m$ within a simple Lund fragmentation scheme. In our model simulation we assumed massless quarks and neglected the widths and transverse momenta of the produced hadrons. As above, Fig. 4.15 shows an example for such a fragmentation process. The production vertices and meeting points are distributed around hyperbolae which correspond to the average proper times deduced from many string fragmentations. The average production and formation times are

| $m$ [GeV] | $\overline{\tau}_V$ [fm/$c$] | $\overline{\tau}_O$ [fm/$c$] |
|:---:|:---:|:---:|
| 0.14 | 0.4–0.6 | 0.5–0.7 |
| 0.5 | 0.7–0.8 | 1.0–1.1 |
| 1.0 | 0.9–1.1 | 1.4–1.7 |

Table 4.3: Average proper times for the production and formation of hadrons with different mass $m$ in the fragmentation of a string with invariant mass $W = 10$ GeV.

listed in Tab. 4.3. Again, one observes an increase of the proper times with rising hadron mass $m$. However, the values are smaller than those shown in Tab. 4.2 which were derived for an infinitely large mass $W$ of the fragmenting system. These results make models relying on assumptions as indicated in Fig. 4.12 questionable.

**Production and formation times from JETSET**

The event generators implemented in our simulations (FRITIOF, PYTHIA) are based on the Lund fragmentation scheme. In the first place, they provide us with the reaction products and their four-momenta. Knowing that the fragmentation happens according to the Lund model, it is in principle possible to reconstruct the prehadron production and formation times from the kinematics of the string fragments (see Appx. F). However, it is much more reliable to extract the times directly form the fragmentation routines implemented in JETSET.

As described above there are in principle three time scales involved in the Lund fragmentation process: i) The production proper time $\tau_{p1}$ of the hadron's first constituent, which is obviously zero if the hadron contains a constituent from a string end, ii) the production proper time $\tau_{p2}$ when the second constituent is produced and a color neutral object is formed, and iii) the formation proper time $\tau_f$ where the two world lines of the constituents cross for the first time.

We now investigate how these times depend on the fractional hadron energy $z_h = E_h/\nu$ in deep inelastic scattering of 27.6 GeV positrons on nucleons[4]. This kinematic situation corresponds to the one in the HERMES experiment which we extensively study when investigating hadron attenuation in DIS off complex nuclei in Sec. 6.4.

In the upper panel of Fig. 4.16 we show the $z_h$ dependence of the extracted average production proper times $\tau_{p1}$ and $\tau_{p2}$ of the two hadron constituents as well as the hadron-formation proper time $\tau_f$. We always label the smaller production time $\tau_{p1}$ and the larger $\tau_{p2}$. Note that, if more than one string is produced in the electron-nucleon interaction, the observed $z_h = E_h/\nu$ is in general different from the quantity $\zeta$ of Eq. (4.24). The difference is most significant for $z_h \lesssim 0.5$. However, one also has to be careful with the interpretation of $z_h$ in the limit $z_h \to 1$. In this kinematic regime the hadron spectrum is dominated by diffractively produced vector mesons (cf. Fig. 4.29) whose production times $\tau_{p1}$ and $\tau_{p2}$ for the constituents are both zero. Furthermore, we show in our theoretical study of incoherent $\rho^0$ electroproduction in Sec. 6.2 that also the formation time $\tau_f$ of a diffractively produced vector meson is compatible with

---

[4]By 'nucleon' we mean the isospin average over proton and neutron
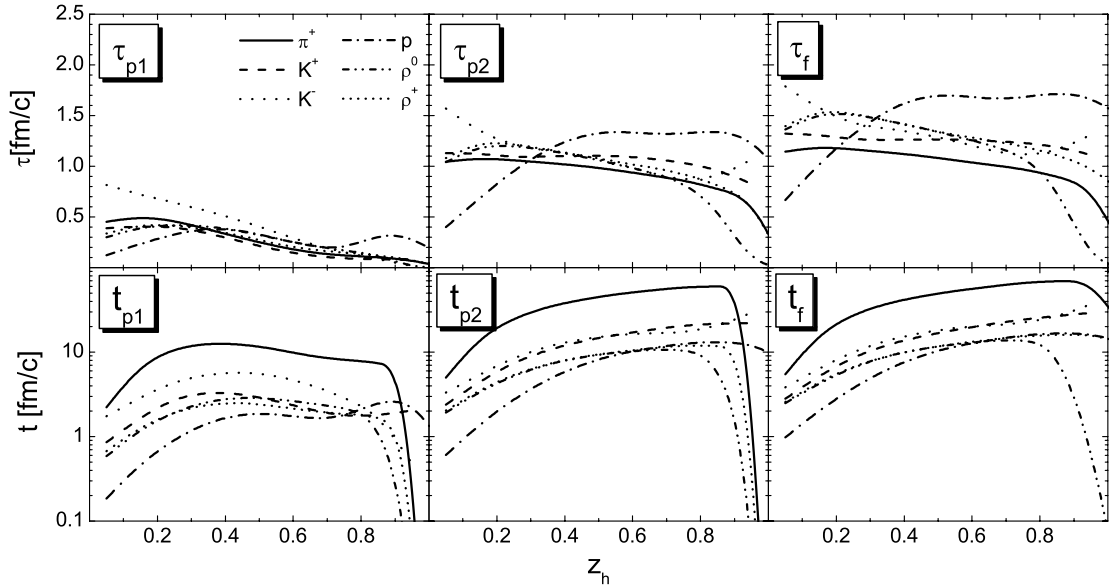
Figure 4.16: Average (proper) times for hadron formation and the production of the first and second constituent as a function of $z_h = E_h/\nu$ in the kinematic regime of the HERMES experiment. All times have been extracted directly from the JETSET routines which describes the string fragmentation in PYTHIA.

zero in the HERMES kinematic regime. Consequently, the proper times $\tau_{p1}$, $\tau_{p2}$ and $\tau_f$ for the $\rho^0$ (dash-dot-dotted line) vanish as $z_{\rho^0} \to 1$.

In a direct photon-nucleon interaction the probability, that a meson contains the struck quark from the string end, increases with $z_h$ and, consequently, $\tau_{p1}$ vanishes for larger $z_h$. On the other hand, the diquark that is left behind, i.e. the second string end, will most likely form a proton with small $z_h$ which leads to a vanishing of $\tau_{p1}$ for low-$z_h$ protons (dash-dotted line). In case of diffractive photon-nucleon interactions the proton stays intact and $\tau_{p1}$, $\tau_{p2}$ and $\tau_f$ are zero which leads to a decrease of $\tau_{p2}$ and $\tau_f$ for low-$z_h$ protons. The Lund model predicts a vanishing of the production time $\tau_{p2}$ for $z \to 1$ which can be seen from Eq. (4.28). However, because of the finite bin-size the production time $\tau_{p2}$ in Fig. 4.16 stays finite in the last $z_h$ bin for all hadrons except for the diffractively produced vector mesons.

In fact, one observes the general tendency that more massive hadrons like protons and $\rho$ mesons are formed later in proper time than lighter hadrons like pions (solid line) which is in line with our previous findings. Again the diffractively produced vector mesons are the exception.

In the lower panel of Fig. 4.16 we also show the corresponding production and formation times in the laboratory frame, i.e. the rest frame of the target nucleon. Because of time dilatation the light pions now have average production and formation times as large as 10–70 fm/$c$. However, as we discuss in the next section (and as can be seen from Fig. 4.29) pion production receives a large contribution from string fragmentation into $\rho$ mesons that – due to their larger mass – have a considerably smaller average production time 0.5–3 fm/$c$ in the laboratory frame. Therefore attenuation of pions in
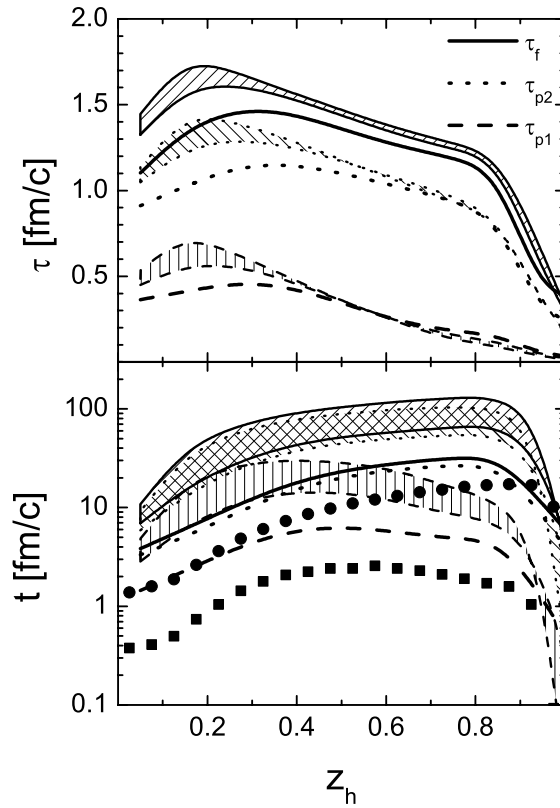
Figure 4.17: Average (proper) time for hadron formation (solid line) and the production of the first (dashed line) and second (dotted line) constituent as a function of $z_h = E_h/\nu$ in the kinematic regime of the HERMES and EMC experiments. The shaded areas are bounded by simulations using a 100 GeV (lower boundary) and 200 GeV (upper boundary) muon beam. All times have been extracted directly from the JETSET routines and averaged over all hadron species. The solid symbols indicate the average starting times of the prehadronic (squares) and hadronic (circles) interactions in the constituent quark concept (5.35) using a formation time $\tau_f = 0.5$ fm/$c$.

the nuclear medium is partly due to the absorption of $\rho$ mesons prior to their decay into pions.

In Fig. 4.17 we show the production and formation (proper) times averaged over all hadron species. For HERMES energies we find that the average production proper time $\tau_{p1}$ of the first hadron constituent (dashed line) lies between 0.04 fm/$c$ at $z_h \approx 0.95$ and 0.4 fm/$c$ at $z_h \approx 0.35$. The production proper time $\tau_{p2}$ of the second constituent (dotted line) is somewhat larger. It ranges from 0.3 fm/$c$ at $z_h \approx 0.95$ to about 1.2 fm/$c$ at $z_h \approx 0.35$. The average hadron-formation proper time $\tau_f$ (solid line) is of the order $1.1 - 1.5$ fm/$c$ except for the very large-$z_h$ hadrons which are dominated by diffractively produced $\rho^0$ mesons and, hence, have again a very small formation time around 0.4 fm/$c$ at $z_h \approx 0.95$.

In Fig. 4.17 we also show the production and formation (proper) times averaged over all hadron species at EMC energies. The muon-beam energy $E_{\mathrm{beam}} = 100 - 200$ GeV in the EMC experiment is considerably larger than the positron-beam energy at

HERMES. Hence, the invariant mass of the excited strings as well as time dilatation effects are in general increased. While the first leads only to a small increase of the production and formation proper times, the latter increases the production and formation times in the lab frame tremendously.

Note that the production and formation times in Fig. 4.16 and Fig. 4.17 are *averaged* times. In our actual simulations of nuclear reactions we assign in each scattering event the *individual* production and formation time from JETSET for each hadron.

In summary one can say that the large formation times that are usually quoted in connection with the Lund model are only valid for the fragmentation of an infinitely heavy system. The reason for this is that the proper times of vertices and yoyo formation points increase with rank and that in reality the number of fragments is limited, whereas Eqs. (E.11), (4.22) and (4.23) require an infinite number of $q\bar{q}$ production vertices. The boundary condition (4.16), which was dictated by energy and momentum conservation, leads to an additional reduction of the proper times. Furthermore, one observes that the production and formation times depend on the hadron masses. This is already the case for the decay of the infinitely heavy string. As a tendency, the average production and formation proper times of more massive particles are larger than those of lighter fragments.

## 4.4 Monte Carlo generators

In this last section we briefly discuss the event generators that are used in our transport simulation. In general the outcome of a (virtual) photon-nucleon interaction above the nucleon resonance region is determined by the event generator PYTHIA 6.208 which allows for the description of $\gamma N$, $\gamma^* N$ and $\gamma^* \gamma^*$ interactions. For technical reasons, resolved $\gamma^* N$ events can only be generated by PYTHIA if the invariant mass of the photon-nucleon system is larger than a threshold energy $W_{\mathrm{PY}}$ which depends on the PYTHIA parameters and takes on the value $W_{\mathrm{PY}} = 4$ GeV for the default parameter set. For invariant masses $2\,\mathrm{GeV} \leq W \leq W_{\mathrm{PY}}$ we employ the event generator FRITIOF 7.02 to simulate the resolved photon interactions since FRITIOF can be applied down to invariant masses of $W = 2$ GeV without any technical problems. FRITIOF is also used to model high-energy hadronic final-state interactions in case of nuclear reactions. Below an invariant mass of $\sqrt{s} = 2.2$ GeV for meson-baryon and $\sqrt{s} = 2.6$ GeV for baryon-baryon collisions we apply the resonance model of Ref. [Eff99a].

In the following two subsections we want to stress some of the important features of FRITIOF and PYTHIA. For a extensive discussion of the two Monte Carlo generators we refer the reader to Refs. [And87, Pi92, And93] and [Sjö01a, Sjö01b].

### 4.4.1 Simulation of hadronic interactions with FRITIOF

In the simulation of a hadron-hadron collision with FRITIOF, the momentum transfer between projectile and target leads to the excitation of two hadronic strings that carry the quantum numbers of the incoming particles. Physically, this can be interpreted as diffractive excitation due to Pomeron exchange which we have discussed in Sec. 2.2.3. The kinematics of the two incoming hadrons can be expressed in terms of the lightcone

momenta

$$
\begin{aligned}
P_1^i &= \left(p_1^+, p_1^-, \vec{0}_T\right) = \left(p_1^+, \frac{m_1^2}{p_1^+}, \vec{0}_T\right) \\
P_2^i &= \left(p_2^+, p_2^-, \vec{0}_T\right) = \left(\frac{m_2^2}{p_2^-}, p_2^-, \vec{0}_T\right)
\end{aligned}
$$

where we have assumed that particle 1 moves along the positive and particle 2 along the negative $z$ axis and used the on-shell condition $p^+ p^- = m^2$ to express the small components $p_1^-$, $p_2^+$ in terms of the large components $p_1^+$, $p_2^-$. The momentum transfer $Q = (-Q^+, Q^-, \vec{Q}_T)$ leads to two highly excited objects with lightcone momenta

$$
\begin{aligned}
P_1^f &= \left(p_1^+ - Q^+, \frac{m_1^2}{p_1^+} + Q^-, \vec{Q}_T\right) = \left(p_1^+ + \frac{m_2^2}{p_2^-} - P_f^+, P_f^-, \vec{Q}_T\right) \\
P_2^f &= \left(\frac{m_2^2}{p_2^-} + Q^+, p_2^- - Q^-, -\vec{Q}_T\right) = \left(P_f^+, p_2^- + \frac{m_1^2}{p_1^+} - P_f^-, -\vec{Q}_T\right).
\end{aligned}
$$

In the FRITIOF model the longitudinal momentum transfer is chosen by Monte Carlo according to the probability distribution

$$
dP \sim \frac{dP_f^-}{P_f^-} \frac{dP_f^+}{P_f^+}
$$

and the transverse momentum transfer is distributed according to a Gaussian

$$
P(Q_T) \sim \frac{1}{\sqrt{\pi}\sigma} \exp\left(-\frac{Q_T^2}{\sigma^2}\right)
$$

with width $\sigma = 0.5$ GeV. The invariant masses of the two strings and thus the energy available for particle production is essentially determined by the longitudinal momentum transfer.

We have seen in Chap. 2 that hard processes become sizable with increasing energy. Therefore, FRITIOF also allows for elastic parton-parton scattering above an invariant energy $\sqrt{s} > 10$ GeV using an older version of PYTHIA. The accompanying final-state gluon radiation is taken care of by the ARIADNE program [Lön92, And93].

If not stated differently, we employ the same FRITIOF parameters as in the HSD model [Gei98a, Gei98b, Cas99] throughout the scope of this work. In Refs. [Gei98a, Gei98b] it was shown that this choice of parameters provides a good description of particle production over a broad energy range. The only exception is the strangeness suppression factor for $s\bar{s}$ creation in the string fragmentation (cf. Eq. (4.19)) which we reset to the FRITIOF default value 0.3 to improve the agreement with the latest strangeness production data [Wag04].

### Total cross sections

In contrast to PYTHIA, the FRITIOF event generator does not provide absolute cross sections but only determines the final state of a scattering event. Therefore, we have to explicitly parameterize the total cross sections at large energies. For all baryon-baryon

| | $A$ | $B$ | $n$ | $C$ | $D$ |
|---|---|---|---|---|---|
| $\sigma_{pp}^{\text{tot}}$ | 48.0 | 0. | – | 0.522 | -4.51 |
| $\sigma_{pp}^{\text{el}}$ | 11.9 | 26.9 | -1.12 | 0.169 | -1.85 |
| $\sigma_{\bar{p}p}^{\text{tot}}$ | 38.4 | 77.6 | -0.64 | 0.26 | -1.2 |
| $\sigma_{\bar{p}p}^{\text{el}}$ | 10.2 | 52.7 | -1.16 | 0.125 | -1.28 |
| $\sigma_{\pi^+p}^{\text{tot}}$ | 16.4 | 19.3 | -0.42 | 0.19 | 0. |
| $\sigma_{\pi^+p}^{\text{el}}$ | 0. | 11.4 | -0.4 | 0.079 | 0. |
| $\sigma_{\pi^-p}^{\text{tot}}$ | 33.0 | 14.0 | -1.36 | 0.456 | -4.03 |
| $\sigma_{\pi^-p}^{\text{el}}$ | 1.76 | 14.0 | -1.36 | 0.456 | -4.03 |
| $\sigma_{K^+p}^{\text{tot}}$ | 18.1 | 0. | – | 0.26 | -1. |
| $\sigma_{K^+p}^{\text{el}}$ | 5. | 8.1 | -1.8 | 0.16 | -1.3 |
| $\sigma_{K^+n}^{\text{tot}}$ | 18.7 | 0. | – | 0.21 | -1.3 |
| $\sigma_{K^-p}^{\text{tot}}$ | 32.1 | 0. | – | 0.66 | -5.6 |
| $\sigma_{K^-p}^{\text{el}}$ | 7.3 | 0. | – | 0.29 | -2.4 |
| $\sigma_{K^-n}^{\text{tot}}$ | 25.2 | 0. | – | 0.38 | -2.9 |

Table 4.4: Parameters for the cross section parametrization (4.31). The parameters for are taken from Ref. [PDG94].

collisions – that solely involve non-strange baryons in the entrance channel – we use the cross section parametrization [PDG94]

$$\sigma = \left[ A + Bp^n + C \ln^2 p + D \ln p \right] \text{ mb} \tag{4.31}$$

with the parameters for proton-proton collisions listed in Tab. 4.4. In Eq. (4.31) $p$ denotes the laboratory momentum in GeV. As shown in Ref. [PDG94], this parametrization yields a good description of the cross sections down to the resonance region. In the current version of our transport simulation we neglect collisions of strange and charmed baryons.

For the meson-nucleon interactions, that can be addressed experimentally like $\pi^\pm p$, $K^\pm p$ and $K^\pm n$ (from $K^\pm d$), we use Eq. (4.31) with the parameters listed in Tab. 4.4. The cross sections for the other isospin channels are given by isospin symmetry

$$\begin{aligned}
\sigma_{\pi^0 N} &= \frac{1}{2}(\sigma_{\pi^+p} + \sigma_{\pi^-p}), \\
\sigma_{\pi^+n} &= \sigma_{\pi^-p}, \\
\sigma_{\pi^-n} &= \sigma_{\pi^+p}, \\
\sigma_{K^0p} &= \sigma_{K^+n}, \\
\sigma_{\bar{K}^0p} &= \sigma_{K^-n}, \qquad \text{etc.}
\end{aligned}$$

The cross sections for the $K^*$ and $\bar{K}^*$ mesons are assumed to be the same as for $K$ and $\bar{K}$.

As we have pointed out in Sec. 3.1.2, vector meson dominance relates the neutral vector meson-nucleon scattering cross sections to vector meson photoproduction via
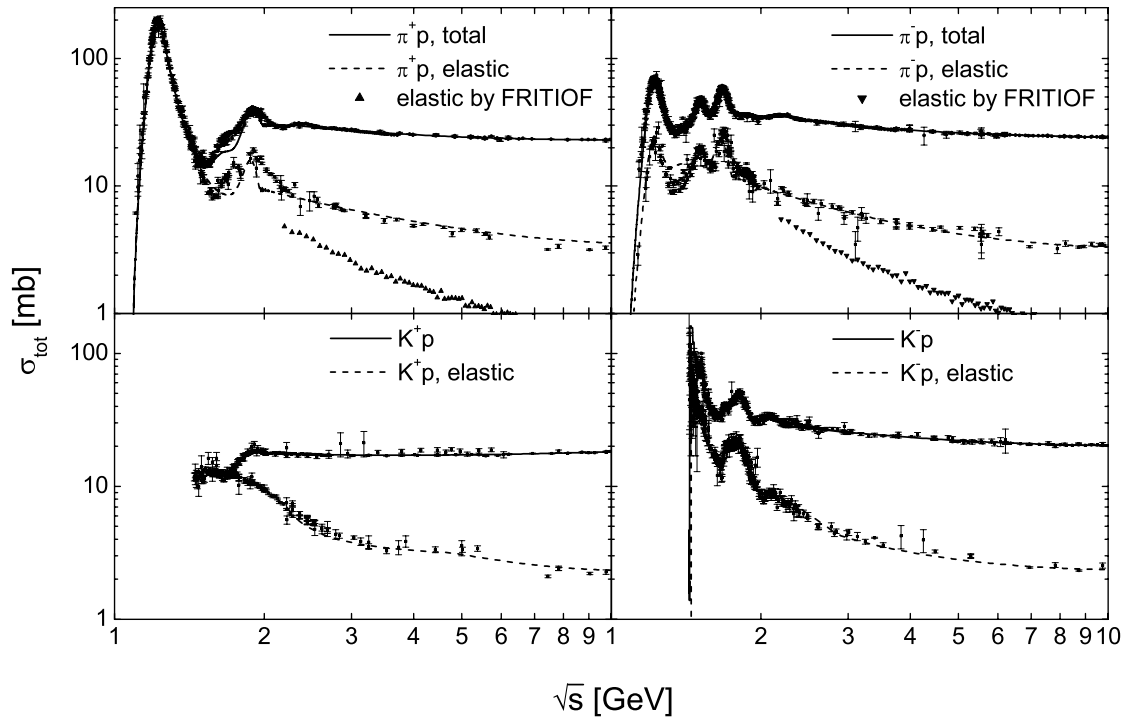
Figure 4.18:  Cross sections for $\pi^{\pm}p$ and $K^{\pm}p$ scattering.  The solid lines represent the total cross sections.  The dashed lines show the cross sections for elastic scattering.  The high-energy part given by Eq. (4.31) is continuously connected to the cross sections of the resonance model [Eff99a] below $\sqrt{s} = 2.2$ GeV.  The solid triangles show the FRITIOF result for elastic pion-proton scattering.  The data are taken from Ref. [PDG02].

Eq. (3.8).  We therefore use the same (total and elastic) $VN$ cross section as for the photon-induced reactions, i.e. the PYTHIA parameterizations (3.5) and (2.17).

For all other high-energy meson-baryon collisions we make an ansatz similar to that of the UrQMD model [Bas98]:

$$\sigma_{mb}^{\text{tot}}(s) = \sigma_{\pi N}^{\text{tot}}(s)\left(1 - 0.4x_S^m - 0.5x_C^m\right)\left(1 - 0.4x_S^b - 0.5x_C^b\right)$$

where $x_{S,C}^m$ and $x_{S,C}^b$ represents the strangeness and charm content of the meson $m$ and baryon $b$:

$$x_S^m = \frac{|S(m)|}{2}, \qquad x_C^m = \frac{|C(m)|}{2},$$
$$x_S^b = \frac{|S(b)|}{3}, \qquad x_C^b = \frac{|C(b)|}{3}.$$

Here $S$ and $C$ denote the strangeness and the charm quantum numbers of the meson and baryon, respectively.

Since the cross sections for baryon-baryon collisions below $\sqrt{s} = 2.6$ GeV and meson-baryon collisions below $\sqrt{s} = 2.2$ GeV are given by the resonance model of

Ref. [Eff99a], we continuously connect the high-energy parametrization to the resonance part. As an example, Fig. 4.18 shows our parametrization of the total and elastic $\pi^{\pm}p$ and $K^{\pm}p$ cross section in comparison with the experimental data.

### Elastic scattering

There are two problems connected with the FRITIOF model. The first is that it does not generate enough elastic scattering events as can be seen by the solid triangles in Fig. 4.18. We cure this deficiency by also parameterizing the elastic cross section and simulating elastic scattering externally; FRITIOF is then only called for inelastic collisions (cf. Ref. [Cas99]).

For all elastic baryon-baryon collisions, that solely involve non-strange baryons in the entrance channel, we use the same parametrization as for elastic $pp$ scattering (see Tab. 4.4).

The cross sections for elastic $\pi^{\pm}p$ and $K^{\pm}p$ scattering are again taken from experiment (see Tab. 4.4) and those for elastic $VN$ scattering are given by VMD, cf. Eq. (3.8):

$$\sigma^{\mathrm{el}}_{VN} \approx \left(\frac{g_V}{e}\right)^2 \sigma_{\gamma N \rightarrow VN}.$$

For the remaining particles we use Eq. (2.21) which relates elastic and total cross sections. The value $c = 0.039$ mb$^{-1/2}$ is taken from the UrQMD model [Bas98].

Above the resonance region the angular distribution for all elastic scatterings is given by Eq. (2.17).

### Quark-antiquark annihilation

A second problem with FRITIOF is that it does not account for quark-antiquark annihilation in meson-baryon scattering in correspondence to the $t$-channel Reggeon exchange depicted in Fig. 2.6. This process, however, gives a finite contribution to the total cross section for low $\sqrt{s}$ as we have pointed out in the discussion of Eq. (2.15). We therefore keep the option to simulate its contribution to the inelastic collisions independently of FRITIOF using the method of Ref. [Wag04] where the antiquark from the meson and a constituent of the baryon with the same flavor may annihilate. We assume that the momenta of the two annihilating quarks are very small so that we do not need to treat the final gluon explicitly. The final state of such an annihilation process is modeled by an excited string with the invariant mass of the colliding system. The decay of the string into hadrons is taken into account using the Lund fragmentation routine JETSET 7.3 as also used by FRITIOF. In contrast to the two excited strings of a FRITIOF event, the string – emerging after $q\bar{q}$ annihilation – has a larger invariant mass and therefore has more energy available for $s\bar{s}$ creation. Hence, the annihilation process has a strong effect on strangeness production in meson-baryon scattering and the energy dependence of its cross section. Above $\sqrt{s} = 2.2$ GeV the annihilation cross section relative to strangeness production in pion-nucleon scattering [Wag04] can be fitted by:

$$\frac{\sigma^{\mathrm{anni}}_{mb}}{\sigma^{\mathrm{inel}}_{mb}} = \max\left[1.2 - 0.2\frac{\sqrt{s}}{\mathrm{GeV}}, 0\right].$$
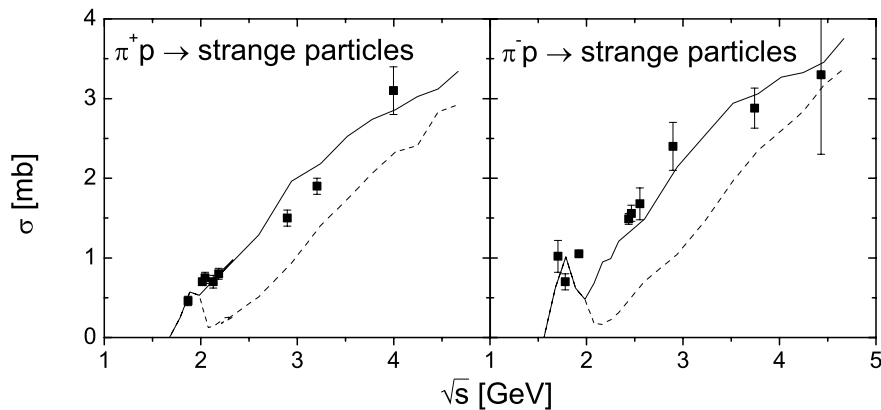
Figure 4.19: Cross sections for $\pi^{\pm}p \rightarrow$ *strange particles* in comparison with experimental data [Bal88]. The dashed line represents a simulation without quark-antiquark annihilation the solid line shows the full result. The figure is taken from Ref. [Wag04].

Fig. 4.19 shows the resulting cross section for strangeness production in $\pi^{\pm}p$ with (solid line) and without (dashed line) the quark-antiquark annihilation contribution. One clearly sees that the incorporation of the annihilation part leads to a much better agreement with data.

**Antibaryons**

Finally, there is the possibility of elastic and inelastic baryon-antibaryon ($b\bar{b}$) interactions in photon and hadron-induced nuclear reactions. The total and elastic cross sections for $p\bar{p}$ scattering are again taken from experiment, i.e. Eq. (4.31) and Tab. 4.4. For the rest of the non-strange antibaryons we use the same cross sections as for antiprotons. Elastic $b\bar{b}$ scattering is simulated in the same way as in all other elastic channels. The inelastic fraction of the total cross section is experimentally known to be dominated by annihilation. We therefore reduce the inelastic cross section of (anti-)baryons that involve $(\bar{s})s$ quarks according to the simple valence quark picture:

$$\sigma_{Y\bar{N}}^{\mathrm{anni}} = \sigma_{\bar{Y}N}^{\mathrm{anni}} = \frac{3 - |S|}{3}(\sigma_{p\bar{p}}^{\mathrm{tot}} - \sigma_{p\bar{p}}^{\mathrm{el}})$$

where $S$ denotes the strangeness of the (anti-)hyperons. The annihilation in collisions that involve charmed (anti-)baryons is neglected here. The annihilation process is modeled in the same way as in Ref. [Gei98a, Gei98b]: After annihilation of a quark and an antiquark with the same flavor the remaining (anti-)quarks form two orthogonal $q\bar{q}$ jets which equally share the invariant mass of the colliding system. This is of course a simplification of the real angular distribution. As in the case of $q\bar{q}$ annihilation in meson-baryon scattering the strings are fragmented using JETSET 7.3.

Throughout this work we neglect the possibility of meson-meson, meson-antibaryon as well as antibaryon-antibaryon interactions. They are very unlikely in reactions induced by elementary projectiles like protons, photons and electrons since they require interactions between the few reaction products among each other. However, we point

out that meson-meson interactions might become important for heavy-ion collisions that involve large meson densities.

## 4.4.2 Simulation of $\gamma^*N$ events with PYTHIA and FRITIOF

We use PYTHIA 6.208 to describe high-energy $\gamma^*N$ reactions. Normally, PYTHIA determines the kinematics of the virtual photon randomly by simulating the lepton-nucleon scattering event. However, for most of our purposes it is more convenient to initialize the reaction of a virtual photon with specific four-momentum and polarization. We therefore restrict the electron scattering kinematics in the PYTHIA simulation in such a way that the photon has the desired energy $\nu$, virtuality $Q^2$ and polarization $\epsilon$. After that we rotate the whole event until the photon momentum points into the $z$ direction of the lab frame. For real photons we simply take the limit $Q^2 \to 0$. In case that we need a realistic distribution of $\nu$, $Q^2$ and $\epsilon$ we choose the photon kinematics and polarization by Monte Carlo using the photon flux (D.6) and Eq. (D.4).

**Transition region** $W \leq W_{\mathrm{PY}}$

The physics of $\gamma^*N$ interactions that we have described in Sec. 3.2 is exactly what is implemented in PYTHIA 6.208. This means that there is the possibility of direct and resolved photon-nucleon interactions in PYTHIA. In case of VMD events the same processes as in hadron-hadron interactions (cf. Chap. 2) can occur including diffractive scattering. The major drawback of PYTHIA is that for technical reasons the resolved events can only be simulated down to $W = W_{\mathrm{PY}}$ where $W$ denotes the invariant mass of the photon-nucleon system. In the transition region from $W_{\mathrm{PY}}$ down to the resonance region ($W = 2$ GeV) we therefore generate the resolved events by FRITIOF. To simulate the VMD contribution we pass the photon as a massless vector meson $V$ with a probability

$$P_V(W^2,Q^2) = \frac{\left(\frac{W^2}{W^2+Q^2}\right)^3 \frac{e^2}{g_V^2}[1 + \epsilon\, r(m_V^2,Q^2)]\left(\frac{m_V^2}{m_V^2+Q^2}\right)^2 \sigma_{\mathrm{tot}}^{VN}(W^2)}{\sigma_{\mathrm{tot}}^{\gamma^*N}(W^2,Q^2)}, \qquad (4.32)$$

according to Eqs. (3.26) and (3.29).

   We have already pointed out in Sec. 4.4.1 that FRITIOF insufficiently describes elastic scattering, which directly affects the diffractive vector meson photoproduction $\gamma N \to VN$. In the transition region below $W_{\mathrm{PY}}$ we therefore parameterize the diffractive production cross section for $\rho^0$, $\omega$ and $\phi$ using the Regge prescription of Donnachie and Landshoff [Don00] which also provides us with the correct dependence on the four-momentum transfer squared $t$. The high-energy cross sections are continuously extrapolated to our parametrization in the resonance region [Eff99a]. For the description of $J/\psi$ production close to threshold we use the two- and three-gluon exchange model of Brodsky et al. [Bro00]. Fig. 4.20 shows our parameterizations in comparison with a collection of experimental data. For comparison we also show the result one obtains if one uses the PYTHIA parametrization of the total $VN$ cross sections (3.5) together with simple vector meson dominance (cf. (3.8) with $\rho = 0$). Both the Donnachie-Landshoff (solid line) as well as the PYTHIA parametrization (dashed line) are compatible with $\rho^0$, $\omega$ and $\phi$ photoproduction data but fail to describe diffractive
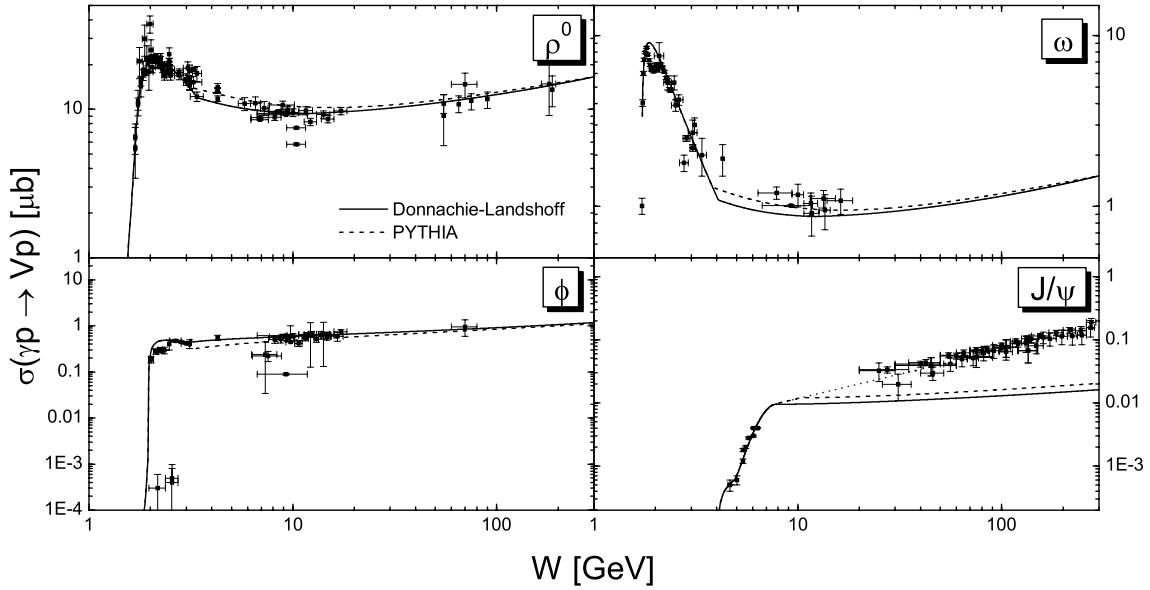
Figure 4.20: Cross sections for exclusive vector meson photoproduction $\gamma p \rightarrow V p$ as a function of the invariant energy $W$. Above the resonance region $W = 2$ GeV the solid lines represent our default parametrization taken from Refs. [Don00, Bro00]. The dashed lines illustrate the result that one obtains if one uses VMD and the total $VN$ cross sections (3.5). The dotted line in $J/\psi$ photoproduction represents our parametrization (4.33). The data are taken from Ref. [PDG02].

$J/\psi$ production. In case that we apply FRITIOF for $\gamma N$ reactions above $W_{\mathrm{PY}}$ (see discussion below) we therefore parameterize the high-energy $J/\psi$ photoproduction data as

$$\sigma_{\gamma N \rightarrow J/\psi N} = 0.002 \left( \frac{\sqrt{s}}{\mathrm{GeV}} \right)^{0.77} \mu\mathrm{b}. \qquad (4.33)$$

This parametrization is represented by the dotted line in Fig. 4.20.

In addition, we have found in [Müh03] and [Müh04] that it is better to also treat the process $\gamma N \rightarrow V\Delta$ independently of FRITIOF. We therefore parameterize the production cross section as

$$\sigma_{\gamma N \rightarrow V\Delta}(s) = \frac{1}{p_i s} \int d\mu_\Delta \int d\mu_V \mathcal{A}_\Delta(\mu_\Delta) \mathcal{A}_V(\mu_V) |\mathcal{M}_V(s)|^2 p_f(\mu_\Delta, \mu_V),$$

where $\mathcal{A}_{\Delta,V}$ denotes the spectral function of the $\Delta$ and $V$, $p_{i,f}$ the initial and final center-of-mass momentum and $\mathcal{M}_V$ the matrix element which is fitted to inclusive $\phi$ and $\omega$ production data:

$$
\begin{aligned}
|\mathcal{M}_\omega(s)|^2 &= \frac{A}{(\sqrt{s} - M)^2 + \Gamma^2/4} \\
|\mathcal{M}_\phi|^2 &= 7.45 \cdot 10^{-3}
\end{aligned}
$$

with $A = 0.122$ GeV$^2$, $M = 2.3$ GeV and $\Gamma = 1.8$ GeV. The spectral functions are
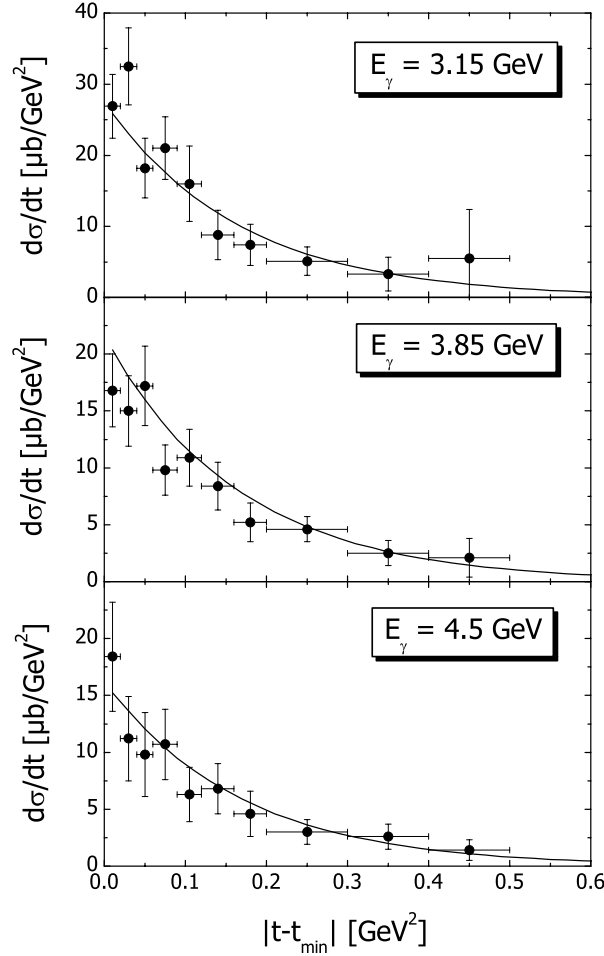
Figure 4.21: Differential cross section for the reaction $\gamma p \to \omega \Delta^+$. The experimental data is taken from Ref. [Bar84]. This figure is taken from Ref. [Müh04].

parameterized as in Ref. [Eff99a]:

$$\mathcal{A}_i(\mu) = \frac{2}{\pi} \frac{\mu^2 \Gamma_{\text{tot}}(\mu)}{(\mu^2 - M_i^2)^2 + \mu^2 \Gamma_{\text{tot}}^2(\mu)}. \tag{4.34}$$

where $M_i$ denotes the pole mass of particle $i$ and $\Gamma_{\text{tot}}$ its total width which in medium has an additional dependence on the particle momentum.

The angular dependence for the two channels is taken from the differential cross section

$$\frac{d\sigma_{\gamma N \to \omega \Delta}}{dt} \sim e^{B_\omega t}$$

$$\frac{d\sigma_{\gamma N \to \phi \Delta}}{dt} \sim e^{B_\phi t} \left( \frac{1}{t - m_\pi^2} \right)^2.$$

with $B_\omega = 6$ GeV$^{-2}$ and $B_\phi = 6.5$ GeV$^{-2}$. In Figs. 4.21 and 4.22 we compare the two parameterizations with experimental data. At the moment we use for $\gamma N \to \rho^0 \Delta$ the same matrix element and slope parameter $B$ as for the $\omega$ channel.
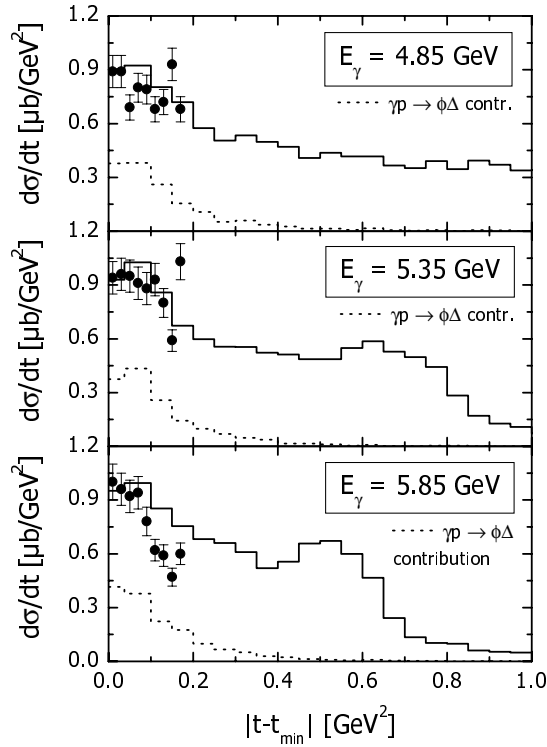
Figure 4.22: Differential cross section for the reaction $\gamma p \to \phi X$ with $1.2\,\text{GeV} \le M_X \le 2.1\,\text{GeV}$. The dashed line shows the contribution from $\gamma p \to \phi \Delta$. The experimental data is taken from Ref. [Beh78]. This figure is taken from Ref. [Müh03].

To account for the virtuality $Q^2$ of virtual photons we multiply the vector meson photoproduction cross sections with the VMD formfactor of Sec. 3.2:

$$F_V^2(Q^2) = \left( \frac{W^2}{Q^2 + W^2} \right)^3 [1 + \epsilon\, r(m_V^2, Q^2)] \left( \frac{m_V^2}{m_V^2 + Q^2} \right)^2 . \qquad (4.35)$$

Furthermore, the FRITIOF model has the tendency to simply flip the spin of the incoming vector meson to zero thereby creating a lot of events like $\gamma^* N \to \pi^0 N$ with vanishing momentum transfer, a problem not present in PYTHIA. These events would correspond to diffractive $\pi^0$ production. However, since the Pomeron carries the quantum numbers of the vacuum it cannot change the charge conjugation quantum number of the incoming $\rho^0$ ($C = -1$) to that of the outgoing $\pi^0$ ($C = +1$). We therefore simply remove these unphysical events from our simulation.

In Fig. 4.23 we compare the particle spectra of VMD events generated by FRITIOF and PYTHIA at the threshold energy $W = 4$ GeV. The virtuality of the photon was chosen to be $Q^2 = 1$ GeV$^2$. Since FRITIOF generates more $\Delta$ resonances than PYTHIA through diffractive excitation of the nucleon we compare the two model predictions after the $\Delta$ has decayed into $\pi N$. We thereby assume that the decay is isotropic in the rest frame of the $\Delta$ resonance. Note, however, that for nuclear reactions it is a
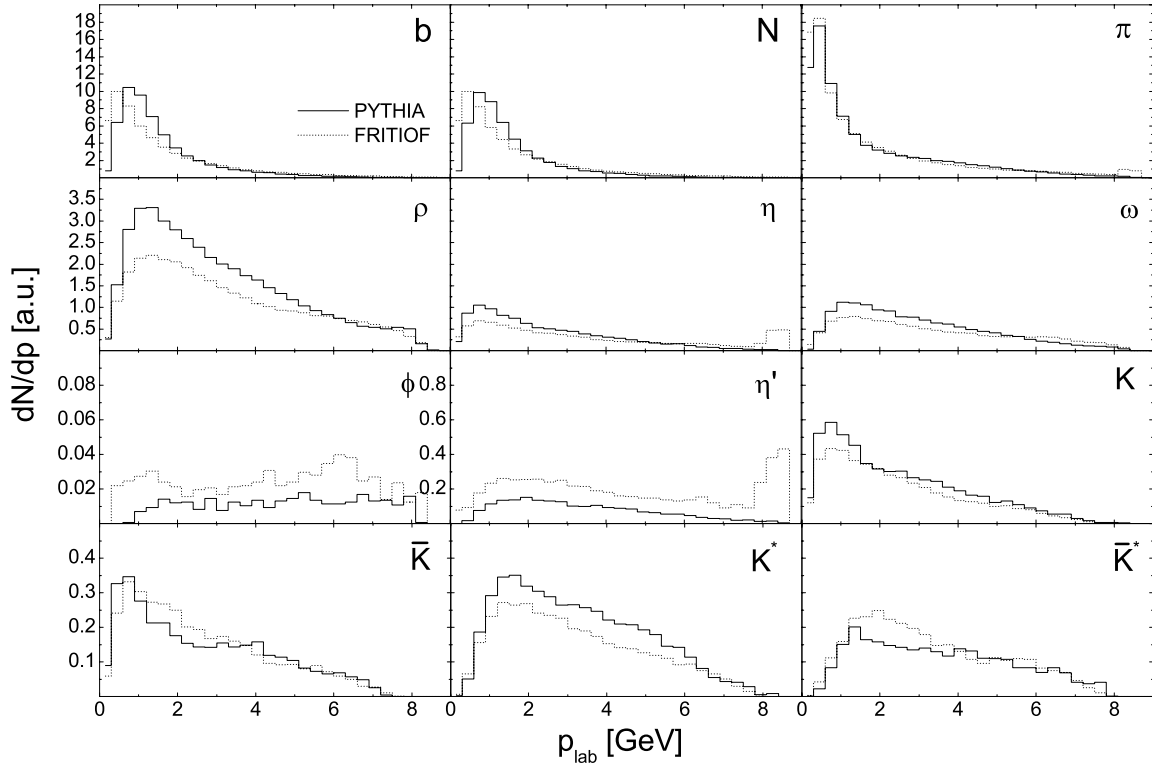
Figure 4.23: Momentum spectra of hadrons created in a VMD process. The invariant mass of the $\gamma^* N$ system is $W = 4$ GeV and the virtuality of the photon is $Q^2 = 1$ GeV$^2$. Diffractive vector meson production $\gamma^* N \to V N$ has been excluded. The solid line shows the result of PYTHIA 6.208, the dashed line shows the result of FRITIOF 7.02 together with our vector meson dominance recipe (4.32). To ease comparison we let all $\Delta$ resonances decay into $\pi N$.

priori not clear whether the explicit propagation of the $\Delta$ leaves the particle spectra unchanged. In the $\gamma^* A$ simulations we therefore include the possibility to switch between an instantaneous decay of the $\Delta$ and an explicit propagation. Throughout the results of this work we only found a negligible difference between the two methods.

Despite the two different natures of FRITIOF and PYTHIA the momentum spectra in Fig. 4.23 show an astonishingly strong similarity. The peaks at large $p_{\text{lab}}$ which are still visible in the $\eta$ and $\eta'$ spectra reflect the shortcoming of FRITIOF that we have already discussed above, namely that FRITIOF often does nothing else but simply changing the spin of the incoming vector meson to zero in the scattering event. Since the effect is not that pronounced as for $\rho^0 N \to \pi^0 N$ we decided to keep these events. Although the spectra are in satisfying agreement we keep the option to generate *all* VMD events by FRITIOF to ensure a continuous transition at invariant energies $W = W_{\text{PY}}$. For calculations that are clearly above the questionable energy regime, like at EMC energies, we use only the PYTHIA model. Note, however, that the VMD contribution vanishes with increasing $Q^2$ and already at $Q^2 = 1$ GeV$^2$ the VMD cross section $\sigma_{\text{VMD}}^{\gamma^* N}$ accounts for only 50% of the total photon-nucleon cross section at HERMES energies (see Fig. 3.8).

The GVMD part below $W_{\text{PY}}$ is modeled by passing a massless vector meson with
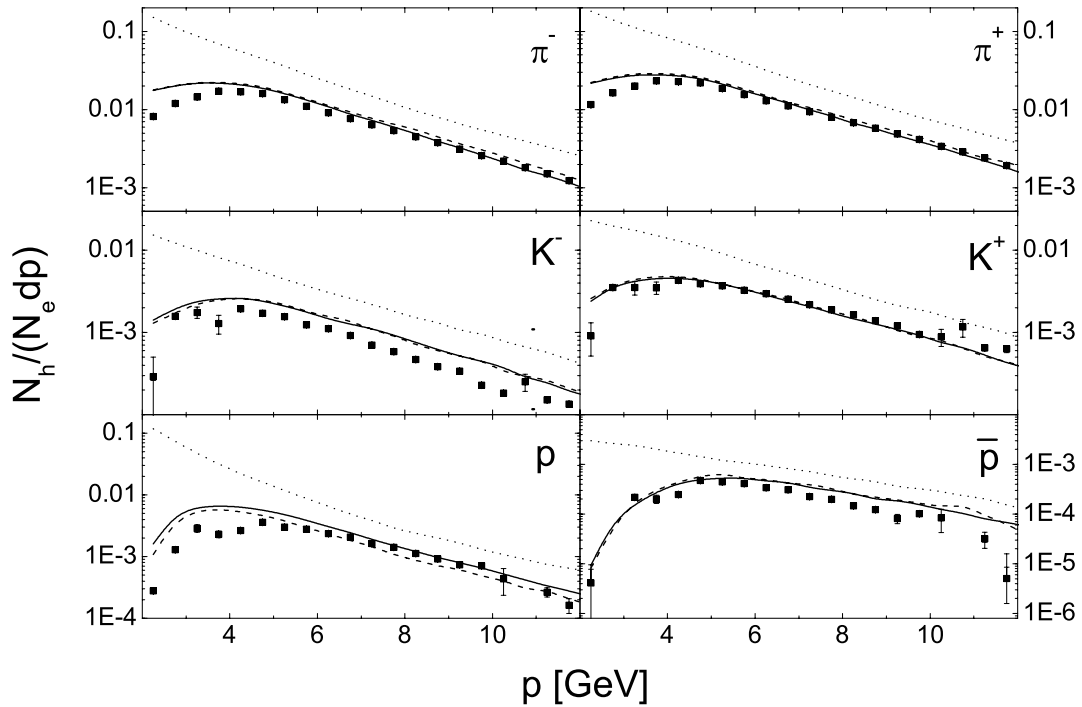
Figure 4.24: Momentum spectra of $\pi^{\pm}$, $K^{\pm}$, $p$ and $\bar{p}$ within the HERMES detector acceptance for a hydrogen target. The spectra are normalized to the number of deep inelastically scattered leptons. The solid lines represent the calculated results using our standard method of generating all resolved photon-nucleon events below $W_{\mathrm{PY}} = 4$ GeV and all VMD events above $W_{\mathrm{PY}}$ with FRITIOF. Generating all events with PYTHIA leads to the spectra shown in terms of the dashed lines. The dotted lines show the result of a simulation without employing any kinematic or detector cuts for the hadrons. The data (full squares) are taken from Ref. [Hil03].

the quark content of the $q\bar{q}$ fluctuation to FRITIOF. In analogy to Eq. (4.32) the probability is now given by the corresponding GVMD term in the sum (3.31) normalized to $\sigma_{\mathrm{tot}}^{\gamma^{*}N}$. As we have discussed in Section 3.1 the products of a GVMD and VMD event are different in nature since the VMD and GVMD components of the photon involve different intrinsic $k_T$. Therefore, we should not trust in this recipe too much. However, as one can see from Fig. 3.8 the GVMD part in the transition region only contributes by less than 15% to the total photon-nucleon cross section. Hence, one can postpone a more sophisticated treatment unless one looks at events that are especially triggered by the GVMD component of the photon.

**Comparison with *ep* data at HERMES**

An important aspect of this work is our investigation of hadron attenuation at HERMES energies in Sec. 6.4. For this reason we now compare our model for electroproduction on a proton target with the hydrogen data of the HERMES collaboration [Hil03] taken at a positron-beam energy $E_{\mathrm{beam}} = 27.6$ GeV. In our calculation we apply the same cuts on the event kinematics as in the experiment: For the positrons these are $Q^2 > 1$ GeV$^2$, $W^2 > 10$ GeV$^2$ and $0.1 < y = \nu/E_{\mathrm{beam}} < 0.85$. For the momenta of
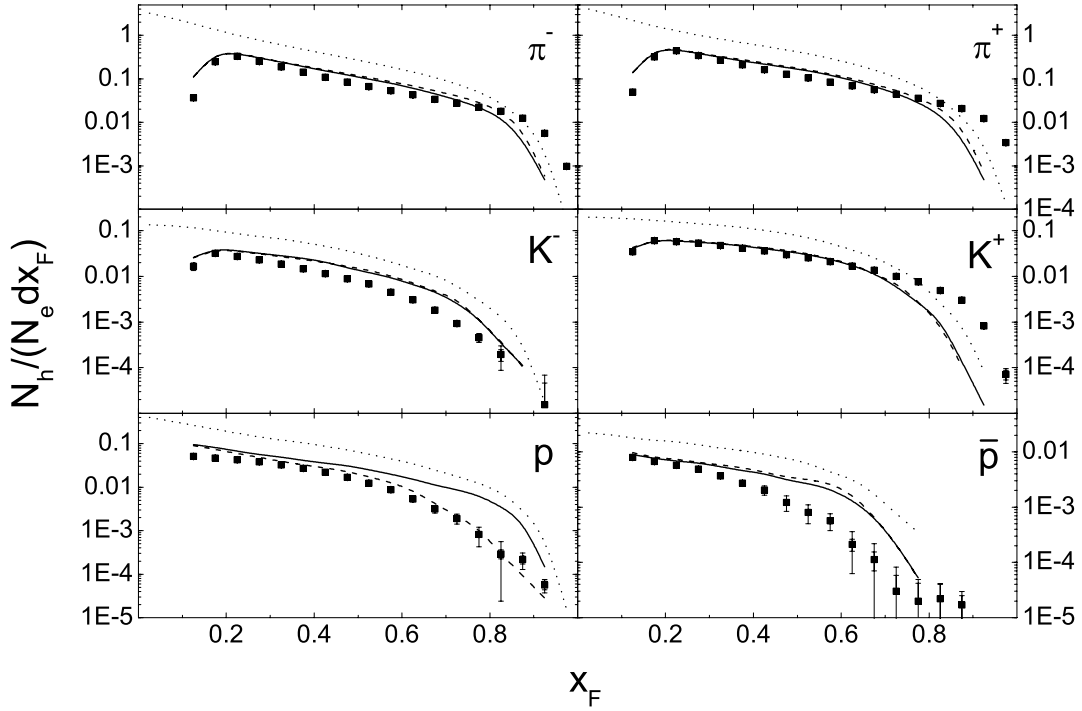
Figure 4.25: Feynman-$x_F$ spectra of $\pi^\pm$, $K^\pm$, $p$ and $\bar{p}$ within the HERMES detector acceptance for a hydrogen target. The meaning of the lines is the same as in Fig. 4.24. The data (full squares) are taken from Ref. [Hil03].

the produced hadrons we require 1 GeV/c $< p_\pi <$ 15 GeV/c, 2 GeV/c $< p_{K,p,\bar{p}} <$ 15 GeV/c as well as $x_F > 0.1$, where we define the Feynman variable $x_F$ as in experiment by

$$x_F = \frac{p_\parallel^{\mathrm{cm}}}{|\vec{q}_{\mathrm{cm}}|}. \tag{4.36}$$

Here $p_\parallel^{\mathrm{cm}}$ denotes the momentum of the hadron parallel to the momentum $\vec{q}_{\mathrm{cm}}$ of the virtual photon in the center-of-mass frame of the photon-nucleon system. Since the data are not acceptance and efficiency corrected we account for the angular acceptance of the HERMES detector [Ack98], i.e. $\pm 170$ mrad horizontally and $\pm(40 - 140)$ mrad vertically, for both the scattered positrons and the produced hadrons in our simulation.

In Figs. 4.24 through 4.27 we show the $p$, $x_F$, $z_h = E_h/\nu$ and $p_T$ spectra of $\pi^\pm$, $K^\pm$, $p$ and $\bar{p}$ normalized to the number $N_e$ of deep inelastically scattered positrons. The solid lines show our results using FRITIOF for the resolved events below $W_{\mathrm{PY}} = 4$ GeV as well as for all VMD events above $W_{\mathrm{PY}}$. The dashed lines represent calculations where we have changed the default parameters of PYTHIA 6.2 in such a way that it is applicable down to $W_{\mathrm{PY}} \approx 3$ GeV and, hence, simulate *all* events with PYTHIA. Except for a small deviation in the proton spectra both methods yield essentially the same result. In view of the fact, that we do not include the detector efficiency in our calculation, which is unknown to the author, but only account for its angular acceptance, our calculations are in satisfying agreement with the experimental data. One can see that without any further fine tuning our simulation including the kinematic cuts and detector acceptance reproduces the absolute size of the multiplicity spectra.
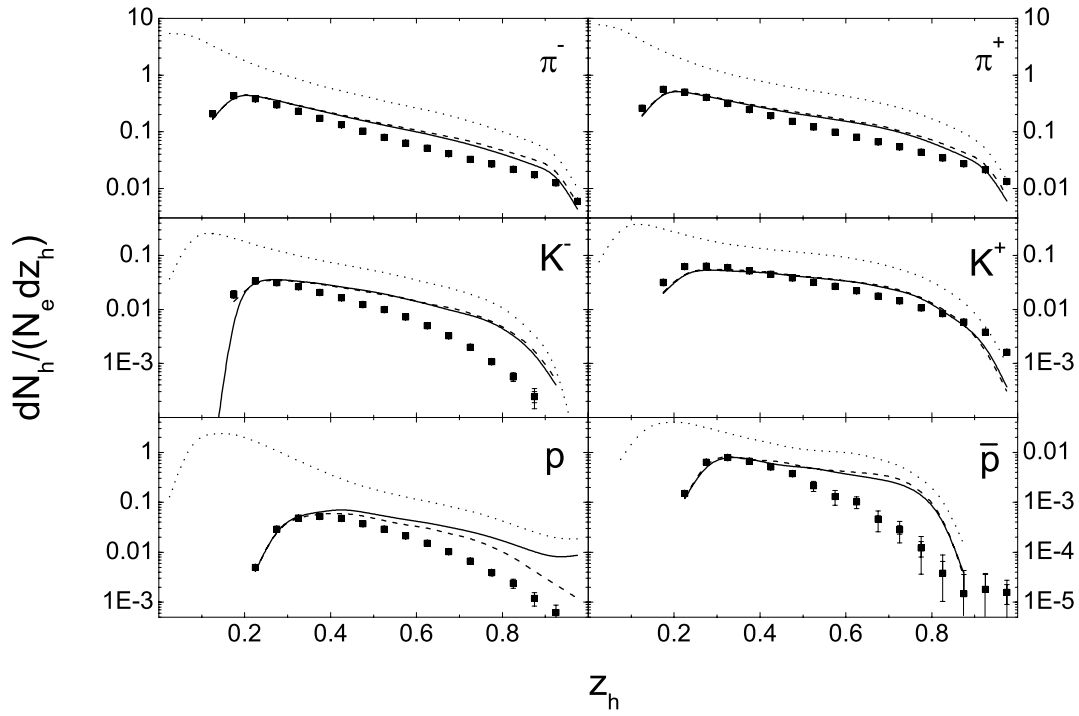
Figure 4.26: Fractional energy spectra of $\pi^{\pm}$, $K^{\pm}$, $p$ and $\bar{p}$ within the HERMES detector acceptance for a hydrogen target. The meaning of the lines is the same as in Fig. 4.24. The data (full squares) are taken from Ref. [Hil03].
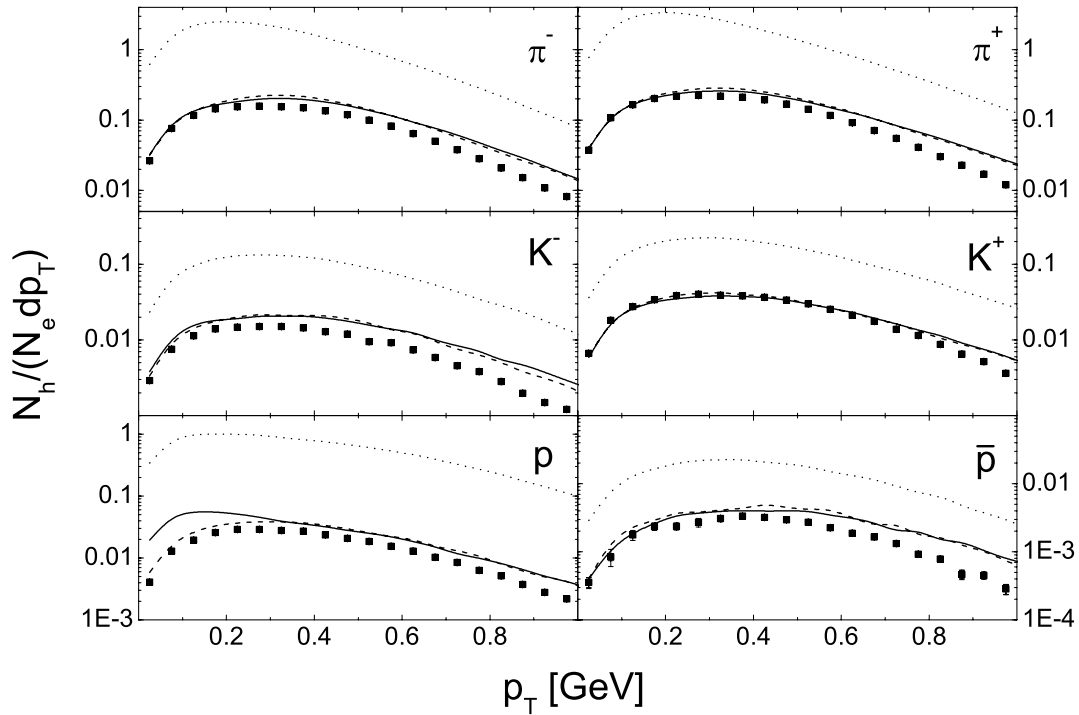


Figure 4.27: Transverse-momentum spectra of $\pi^{\pm}$, $K^{\pm}$, $p$ and $\bar{p}$ within the HERMES detector acceptance for a hydrogen target. The meaning of the lines is the same as in Fig. 4.24. The data (full squares) are taken from Ref. [Hil03].
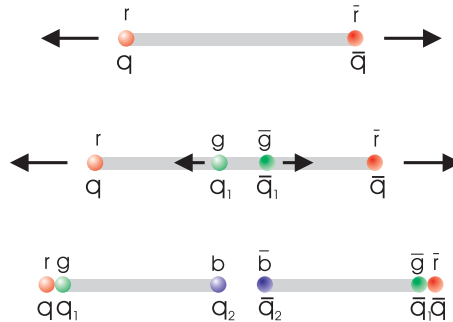
Figure 4.28: Production of a baryon-antibaryon pair via the popcorn mechanism. Instead of creating a diquark-antidiquark pair in the fragmentation of the mesonic string two quark-antiquark pairs $q_1\bar{q}_1$ and $q_2\bar{q}_2$ are subsequently created.

To demonstrate the effects of the kinematic cuts and the limited angular acceptance of the HERMES detector, the dotted lines in Figs. 4.24 through 4.27 show the results of a simulation where no cuts on the hadron kinematics have been applied and where we have assumed a $4\pi$-detector.

## Complications in the string fragmentation

We point out that particle production in PYTHIA (and also FRITIOF) is much more complicated than one might expect after having read the preceding sections. In addition to the complexity of initial and final-state radiation that come with most hard scattering events, string fragmentation in JETSET also includes more features than we can discuss within this work. As an example we mention the possibility of baryon-antibaryon production without diquark-antidiquark creation via the so-called popcorn mechanism. The process is depicted in Fig. 4.28. The first produced (green-antigreen) quark-antiquark pair $q_1\bar{q}_1$ combines with the original (red-antired) $q\bar{q}$ to produce an antiblue diquark $qq_1$ and a blue antidiquark $\bar{q}_1\bar{q}$. In a second step, a (blue-antiblue) quark-antiquark pair $q_2\bar{q}_2$ is created and separates in the color force field to produce a baryon $qq_1q_2$ an an antibaryon $\bar{q}\bar{q}_1\bar{q}_2$. Furthermore, JETSET can split the diquark and thereby create three target remnants from the fragmentation of a baryonic string. For a detailed discussion of all features of PYTHIA (and JETSET) we refer the reader to the PYTHIA manual [Sjö01b].

Furthermore, a string may contain one or several gluons, i.e. it might have the structure $qg\bar{q}$, $qgg\bar{q}$ etc. In general, the gluons have momenta transverse to the center-of-mass momentum of the quark and antiquark. This leads to more complicated topologies than just a linearly expanding string [And98] and has to be taken into account in the fragmentation.

## Beam and target remnants in $ep$ scattering at HERMES

It should have become clear that the modeling of particle production at high energies is very complicated. To make things worse, it turns out to be important for high-energy nuclear reactions that one identifies the target and beam remnants of a binary collision. To identify the target and beam remnants we trace the (anti-)quarks of the projectile
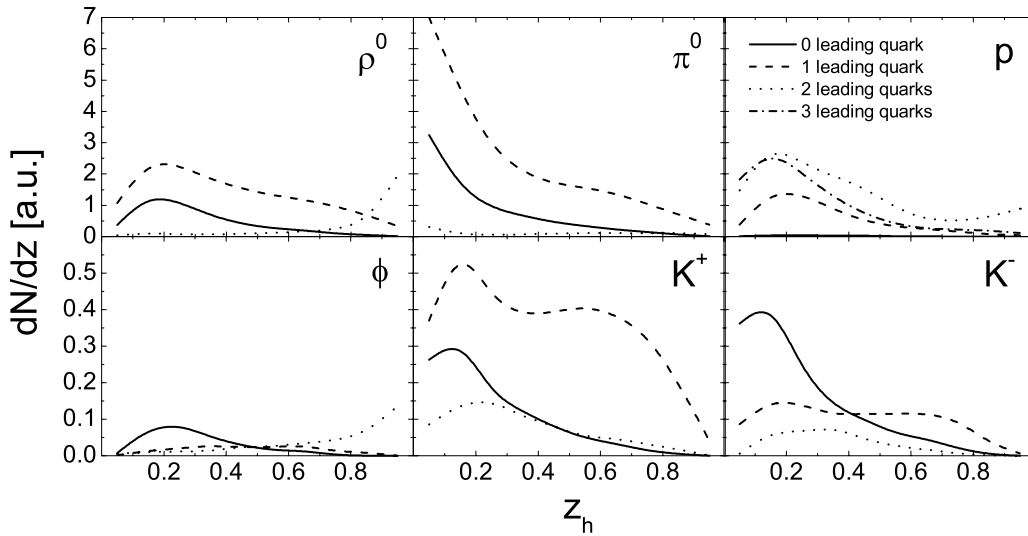
Figure 4.29: Energy spectra of hadrons produced in electron-nucleon interactions at HERMES. The different lines indicate the hadrons that contain zero (solid line), one (dashed line), two (dotted line) or three quarks (dash-dotted line) from the beam or target. For the proton the solid line nearly coincides with the $z_h$ axis, which implies that most protons contain at least one leading quark.

and target all the way through the fragmentation process in JETSET. At the end of the reaction we then know those hadrons that contain the original (anti-)quarks, i.e. the beam and target remnants. Correspondingly, also those hadrons exclusively made from (anti-)quarks created in the string fragmentation are known explicitly.

In Fig. 4.29 we show the fractional energy spectra of hadrons produced in electron-nucleon interactions at HERMES. The different lines indicate the hadrons that contain zero (solid line), one (dashed line), two (dotted line) or three quarks (dash-dotted line) from the beam or target. Obviously, only resolved photon interactions can lead to a beam remnant. In the dotted curves one can clearly identify the diffractive peak in the $\rho^0$ and $\phi$ spectra at $z_h \approx 1$, where the vector mesons contain the $q\bar{q}$ of the resolved photon. By comparing the $\rho^0$ and $\pi^0$ spectra one finds that the $\rho^0$ strongly contributes to the total pion yield by its subsequent decay into $\pi^+\pi^-$.

From the $K^+$ and $K^-$ spectra one sees (dashed lines) that due to their quark content ($\bar{u}s$) the $K^-$ mesons contain less quarks from the beam or target than the $K^+$ mesons. The $K^-$, that are not solely made of quarks and antiquarks created from the vacuum in the string fragmentation, carry (anti-)quarks from the resolved photon component or the nucleon sea.

Finally, one finds that there are only very few protons containing no quarks from the beam or target since diquark-antidiquark creation is strongly suppressed in the string fragmentation due to the relatively large diquark masses. This also explains why most protons at large $z_h$ contain two of the original quarks, i.e. the diquark from the target nucleon struck by the photon.

In our constituent quark ansatz (5.35) the number of quarks that originate from the beam or target determine the size of the prehadronic cross section during the formation

time. Because a diquark is counted as two quarks we expect a very large prehadronic cross section for the high-$z_h$-protons.

# Chapter 5

# Hadron-nucleus interactions

It is experimentally not possible to study elementary reactions of hadrons that are unstable with respect to the strong interaction. Due to their very short lifetimes these particles can neither be used as a beam or a target in experiment. In elementary hadronic reactions one is therefore limited to investigate the interactions of protons, pions and kaons. Furthermore, one cannot learn any details about the space-time picture of hadronization from elementary reactions since the reaction products hadronize long before they reach the detector.

This changes when using nuclear targets. If a collision takes place inside a nucleus the reaction products can interact with the surrounding nuclear medium. Hence, the nucleus serves as a kind of micro-detector for short-lived particles and in addition provides us with the possibility to explore the time scales of hadronization as well as prehadronic interactions.

In this chapter we focus on nuclear reactions of high-energy hadrons. Usually, these reactions are described within Glauber theory. We introduce the Glauber model in Sec. 5.1. The advantage of this model is the quantum mechanical treatment of the scattering process by a coherent summation of the multiple scattering amplitudes. This, however, is only possible under many approximations and restricts its applicability to a very limited number of observables. In Sec. 5.2 we introduce our BUU transport model which provides us with a probabilistic coupled-channel description of hadron-nucleus scattering. Within such a model the number of observables which can be investigated is almost unlimited. In Sec. 5.3 we compare the two models by looking at high-energy proton-nucleus scattering.

## 5.1   Glauber theory

Glauber theory [Gla59, Gla70] reduces the interaction of a high-energy particle with a nucleus to more fundamental interactions with the single nucleons in the nucleus. In the following section we give a brief introduction to the Glauber model. For a more detailed discussion of Glauber theory we refer the reader to Ref. [Fal00a]. At the end of this section we use the Glauber model to calculate the total, elastic and inelastic hadron-nucleus cross section.
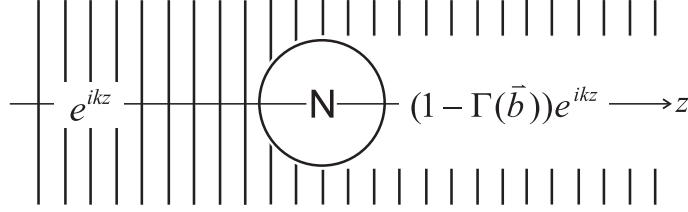
Figure 5.1: An incoming plane wave hits a nucleon which acts like an absorptive sphere. The result is a shadow region behind the nucleon which at high energies extends far beyond the nuclear radius.

### 5.1.1   Introduction to Glauber theory

The simple Glauber model treats the nucleus as an ensemble of nucleons whose Fermi motion and mutual interactions are neglected throughout the reaction with the projectile. The projectile always interacts with only one nucleon at a time and the possibility of scattering on virtual particles, i.e. exchange mesons that give rise to nuclear binding, is ignored.

At high energies one can assume that the reaction products of each single projectile-nucleon interaction are concentrated in the 'shadow region' immediately behind the nucleon. As we discuss in Ref. [Fal00a], the distance that it takes the shadow to 'heal' is very large compared to the nuclear radius. Fig. 5.1 illustrates the elastic scattering of an incoming plane wave with momentum $\vec{k} = k\vec{e}_z$,

$$\psi(\vec{r}) = \chi(\vec{b})e^{ikz}\,, \tag{5.1}$$

on a nucleon which is located at position $\vec{0}$. Behind the nucleon the wave can be considered a superposition of the original wave and a (negative) plane wave confined to the shadow region:

$$\psi(\vec{b}, z) = \chi(\vec{b})\left(e^{ikz} - \Gamma(\vec{b})e^{ikz}\right). \tag{5.2}$$

As shown in Ref. [Fal00a], the profile function $\Gamma$ is related to the elastic scattering amplitude $f$:

$$\Gamma(\vec{b}) = \frac{1}{2\pi ik}\int d^2q_T e^{-i\vec{q}_T\cdot\vec{b}}f(\vec{q}_T). \tag{5.3}$$

Here $\vec{q}_T$ denotes the transverse momentum transfer in the scattering process. The longitudinal momentum transfer can be neglected at high energies. Consequently, one obtains via Fourier transform in impact parameter space

$$f(\vec{q}_T) = \frac{ik}{2\pi}\int d^2b e^{i\vec{q}_T\cdot\vec{b}}\Gamma(\vec{b}) \tag{5.4}$$

and may express the elastic scattering cross section

$$\frac{d\sigma^{\text{el}}}{d\Omega} = |f(\vec{q}_T)|^2$$
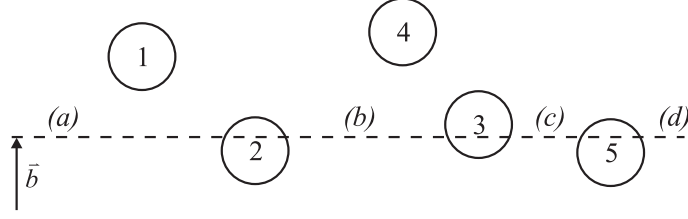
Figure 5.2: Wave path through the nucleus.

in terms of the profile function $\Gamma$

$$
\begin{aligned}
\sigma^{\text{el}} &= \int d\Omega |f(q_T)|^2 \\
&= \frac{k^2}{4\pi^2} \int d^2b \int d^2b' \int \frac{d^2q_T}{k^2} e^{i\vec{q}_T(\vec{b}-\vec{b}')} \Gamma(\vec{b})\Gamma^*(\vec{b}') \\
&= \int d^2b |\Gamma(\vec{b})|^2,
\end{aligned}
\tag{5.5}
$$

where in the second step we have used $d\Omega = d^2q_T/k^2$. Using the optical theorem (A.5) and (5.4) we obtain for the total cross section

$$
\begin{aligned}
\sigma^{\text{tot}} &= \frac{4\pi}{k}\text{Im}f(\vec{0}) \\
&= 2\int d^2b \, \text{Re}\Gamma(\vec{b}).
\end{aligned}
\tag{5.6}
$$

Finally, by combining Eqs. (5.5) and (5.6), the inelastic cross section is given as:

$$
\begin{aligned}
\sigma^{\text{inel}} &= \sigma^{\text{tot}} - \sigma^{\text{el}} \\
&= \int d^2b \left[ 2\text{Re}\Gamma(\vec{b}) - |\Gamma(\vec{b})|^2 \right].
\end{aligned}
\tag{5.7}
$$

Let us now consider the scattering of the incoming plane wave (5.1) on an ensemble of $A$ nucleons which are located at fixed positions $\{\vec{r}_i = (\vec{s}_i, z_i)\}$. According to Eq. (5.2), the plane wave is modified by a factor $1 - \Gamma(\vec{b} - \vec{s}_i)$ for each nucleon that is passed. The wave path through the nucleus is shown in Fig. 5.2 for a particular value of the impact parameter $\vec{b}$. The amplitude along the path is

(a) $1$

(b) $[1 - \Gamma(\vec{b} - \vec{s}_2)]$

(c) $[1 - \Gamma(\vec{b} - \vec{s}_2)][1 - \Gamma(\vec{b} - \vec{s}_3)]$

(d) $[1 - \Gamma(\vec{b} - \vec{s}_2)][1 - \Gamma(\vec{b} - \vec{s}_3)][1 - \Gamma(\vec{b} - \vec{s}_5)]$.

In total the collection of nucleons modifies the plane wave by a factor

$$
1 - \Gamma_A(\vec{b}, \vec{s}_i) = \prod_{i=1}^{A} [1 - \Gamma(\vec{b} - \vec{s}_i)],
$$
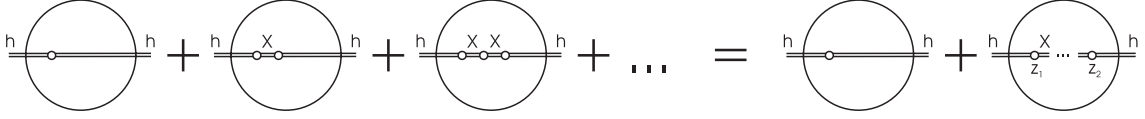
Figure 5.3: Multiple scattering series that corresponds to elastic $hA$ scattering. In Eq. (5.14) the intermediate state $X$ has been restricted to $h$. At very high energies, however, there are contributions from diagrams which include a diffractively excited intermediate state.

where we have also included those nucleons in the product that do not lie on the path with impact parameter $\vec{b}$. The latter is possible because the radius of the profile function $\Gamma$ approximately equals that of the nucleon and therefore the nucleons which do not lie on the trajectory lead to a factor $1 - \Gamma = 1$.

For a nucleus the nuclear profile function $\Gamma_A$ must be regarded as an operator which may induce transitions between the ground state $|0\rangle$ and an arbitrary final state $|f\rangle$ that consists of $A$ nucleons:

$$\Gamma_A^{f0}(\vec{b}) = \delta_{f0} - \langle f| \prod_{i=1}^{A} [1 - \Gamma(\vec{b} - \vec{s}_i)]|0\rangle. \tag{5.8}$$

The elastic scattering amplitude ($|f\rangle = |0\rangle$) on a nucleus is then given in analogy to Eq. (5.4):

$$F(\vec{q}_T) = \frac{ik}{2\pi} \int d^2 b\, e^{i\vec{q}_T \cdot \vec{b}} \Gamma_A^{00}(\vec{b}). \tag{5.9}$$

For the calculation of $\Gamma_A^{00}(\vec{b})$ one needs to know the nuclear ground state density

$$|\psi_0(\vec{r}_1, ..., \vec{r}_A)|^2 = \rho_A(\vec{r}_1, ..., \vec{r}_A).$$

For simplicity we treat the nucleons as independent particles and write the nuclear ground state density $\rho_A$ as a product of one-particle densities $\rho_1$:

$$\rho_A(\vec{r}_1, ..., \vec{r}_A) \cong \prod_{i=1}^{A} \rho_1(\vec{r}_i)$$

with the normalization

$$\int \rho_1(\vec{r}) d^3 r = 1.$$

One can improve this description by accounting for two-particle correlations as we discuss in Sec. 6.1.1.

Within the independent-particle model one obtains for the nuclear profile function

$$\Gamma_A^{00}(\vec{b}) \approx 1 - \prod_{i=1}^{A} \int d^2 s_i \int dz_i [1 - \Gamma(\vec{b} - \vec{s}_i)]\rho_1(\vec{s}_i, z_i)$$

$$= 1 - \left[1 - \int d^2 s \int dz \Gamma(\vec{b} - \vec{s})\rho_1(\vec{s}, z)\right]^A. \tag{5.10}$$

As already pointed out before, the nucleon profile function $\Gamma$ has typically a radius of the size of the nucleon. In Ref. [Fal00a] we have shown that one can therefore make the approximation

$$\rho_1(\vec{s}, z) \to \rho_1(\vec{b}, z)$$

in Eq. (5.10) to get

$$\Gamma_A^{00} \approx 1 - \left[ 1 - \int dz \rho_1(\vec{b}, z) \int d^2 s \Gamma(\vec{s}) \right]^A. \tag{5.11}$$

With the help of Eq. (5.4) it is possible to express the last integral in terms of the forward-scattering amplitude:

$$\int d^2 s \Gamma(\vec{s}) = \frac{2\pi}{ik} f(\vec{0}).$$

On the other hand, the forward-scattering amplitude is related to the total cross section via the optical theorem (A.5)

$$f(\vec{0}) = \frac{ik}{4\pi} \sigma^{\text{tot}} (1 - i\alpha)$$

with $\alpha = \mathrm{Re} f(\vec{0}) / \mathrm{Im} f(\vec{0})$. If one furthermore introduces the nucleon-number density

$$\rho(\vec{b}, z) := A \rho_1(\vec{b}, z),$$

one can write the nuclear profile function (5.11) as

$$\Gamma_A^{00} \approx 1 - \left[ 1 - \frac{1}{2} \sigma^{\text{tot}} (1 - i\alpha) \frac{\int_{-\infty}^{+\infty} dz \rho(\vec{b}, z)}{A} \right]^A. \tag{5.12}$$

With a relative error of order $A^{-1}$ one can approximate Eq. (5.12) as

$$\Gamma_A^{00} \approx 1 - \exp\left[ -\frac{1}{2} \sigma^{\text{tot}} (1 - i\alpha) \int_{-\infty}^{+\infty} dz \rho(\vec{b}, z) \right]. \tag{5.13}$$

Substituting Eq. (5.13) into Eq. (5.9) one ends up with the Glauber expression for the elastic scattering amplitude of a hadron $h$ on a nucleus

$$F(\vec{q}_T) = \frac{ik}{2\pi} \int d^2 b \, e^{i\vec{q}_T \cdot \vec{b}} \left\{ 1 - \exp\left[ -\frac{1}{2} \sigma^{\text{tot}} (1 - i\alpha) \int_{-\infty}^{+\infty} dz \rho(\vec{b}, z) \right] \right\}. \tag{5.14}$$

Graphically, this amplitude corresponds to the sum of multiple scattering diagrams shown in Fig. 5.3 with the intermediate state $X$ fixed to $X = h$. In each elementary scattering reaction $hN \to hN$ the nucleus is assumed to remain in its ground state. This guarantees that the nucleus is in the ground state after the last scattering as it has to be since we required $|f\rangle = |0\rangle$ in the beginning. In the independent-particle model it is not possible to excite the nucleus by scattering on one nucleon and return to the ground state by scattering on *another* nucleon. The latter would require two-particle correlations and is suppressed by the inelastic formfactor of the nucleus.

## 5.1.2   Nuclear cross sections

Using the optical theorem (A.5) and the Glauber amplitude (5.14) for elastic scattering on a nucleus, one can derive the total hadron-nucleus cross section

$$
\begin{aligned}
\sigma_{hA}^{\text{tot}} &= \frac{4\pi}{k}\text{Im}F(\vec{0}) \\
&= 2\int d^2b\,\text{Re}\left\{1-\exp\left[-\frac{1}{2}\sigma_{hN}^{\text{tot}}(1-i\alpha)\int_{-\infty}^{+\infty}dz\rho(\vec{b},z)\right]\right\}. \quad (5.15)
\end{aligned}
$$

Assuming a uniform density distribution with radius $R$:

$$
\rho(\vec{r}) = \rho_0\Theta(R-r)
$$

with

$$
\rho_0 = \frac{A}{\frac{4}{3}\pi R^3}
$$

and neglecting the imaginary part of the elementary $hN$ scattering amplitude ($\alpha = 0$), one can easily perform the integration in (5.15) and express the cross section in terms of the ratio of the nuclear radius $R$ and the mean free path $\lambda_h = 1/(\rho_0\sigma_{hN}^{\text{tot}})$:

$$
\sigma_{hA}^{\text{tot}} = \frac{3}{(R/\lambda_h)^3}\left[(1+R/\lambda_h)e^{-R/\lambda_h}-1+\frac{1}{2}(R/\lambda_h)^2\right]A\sigma_{hN}^{\text{tot}}. \quad (5.16)
$$

If the projectile has a very small nucleonic cross section $\sigma_{hN}^{\text{tot}}$, i.e. in the limit $\lambda_h \gg R$, one obtains by expanding the exponential function:

$$
\sigma_{hA}^{\text{tot}} = A\sigma_{hN}^{\text{tot}}.
$$

This result is trivial since a very large mean free path means that the interaction probability with the projectile is equal for all nucleons. The total cross section therefore scales with the total number of nucleons $A$ or in other words with the volume of the nucleus ($R \sim A^{1/3}$).

In the extreme case that the nucleonic cross section is very large ($\lambda_h \ll R$)) one gets from (5.16):

$$
\sigma_{hA}^{\text{tot}} = 2\pi R^2 \sim A^{2/3}. \quad (5.17)
$$

In this so-called black-disc limit the projectile always interacts with the nucleons on the front side of the nucleus and the nuclear cross section scales with the geometric cross section $\pi R^2$ of the nucleus. The factor two in Eq. (5.17) cannot be explained in classical terms. It arises because quantum mechanically the cross section consists of a real scattering term which exactly corresponds to the classical expectation and a diffractive term which only accounts for forward scattering of the incoming wave. The latter is necessary to interfere destructively with the original wave behind the target to assure unitarity. In principle, this just explains the optical theorem in terms of wave functions. In the black-disc limit, all of the original wave has to vanish behind the target and therefore the scattering and the diffractive term are of the same size, namely $\pi R^2$.

Finally, we want to note that even if the total cross section scales with $A^{2/3}$ the inclusive particle production cross section can behave quite differently. As discussed

for example in Ref. [Cap99] all rescattering terms that contribute to inclusive particle production in $hA$ collisions in the central rapidity region cancel with each other and one is left with

$$\sigma_{hA \to mX} = A\sigma_{hN \to mX} \qquad (5.18)$$

for the inclusive production of particles of type $m$. This is usually referred to as AGK[1] cancellation [AGK74] and at first sight seems to violate unitarity since $\sigma_{hA \to mX}$ can become larger than $\sigma_{hA}^{\text{tot}}$. This is, however, not a problem since the inclusive production cross section $\sigma_{hA \to mX}$ includes the multiplicity of particles $m$ as we show in the derivation of (5.18) in Appx. G.

## 5.2 BUU

In this section we give a brief introduction to our BUU transport model and sketch the basics of its numerical realization. Since we are only interested in its application at high energies we refer the reader to Refs. [Eff99a, Leh03] for a detailed description of the resonance part of the model, as well as medium modifications of resonances and off-shell transport. Refs. [Eff99a, Leh03] also contain an extensive discussion of the underlying theory as well as an explicit description of the numerical methods.

Our transport model is based on the Boltzmann-Uehling-Uhlenbeck (BUU) equation. It has been originally developed to model heavy-ion collisions at SIS energies [Tei96, Tei97, Hom99] and later been extended to describe pion-induced reactions [Wei99, Eff99b] as well as photo- [Eff99a, Eff96] and electroproduction [Leh99, Leh00] in the resonance region. In the more recent past we have extended the model to also simulate nuclear interactions of high-energy photons and electrons in the kinematic regime of the Jefferson Lab [Eff99c, Eff00, Fal02] and HERMES [Fal03b, Fal04, Fal04b] experiments. Obviously, one of the big advantages of the model is its applicability to many different kinds of nuclear reactions with basically the same set of parameters and physics assumptions. In addition, the coupled-channel treatment of the final-state interactions goes far beyond the standard Glauber approach since it allows for side-feeding of particles in the final-state interactions.

### 5.2.1 Theoretical basics

For each particle species $i$ in our model, there exists a generalized BUU equation

$$\left( \frac{\partial}{\partial t} + \vec{\nabla}_{\vec{p}} H \vec{\nabla}_{\vec{r}} - \vec{\nabla}_{\vec{r}} H \vec{\nabla}_{\vec{p}} \right) F_i(\vec{r}, \vec{p}, \mu; t) = I_{\text{coll}}(\{F_j\}) \qquad (5.19)$$

where

$$H = \sqrt{(\mu + U_S(\vec{r}, \vec{p}; t))^2 + \vec{p}^{\,2}} \qquad (5.20)$$

denotes the relativistic Hamilton function of a particle with mass $\mu$ in a scalar potential $U_S$. For vanishing collision term $I_{\text{coll}}$ Eq. (5.19) describes the time evolution of the spectral phase-space density

$$F_i(\vec{r}, \vec{p}, \mu; t) = f_i(\vec{r}, \vec{p}; t) \mathcal{A}_i(\mu, \vec{p}) \qquad (5.21)$$

[1] Abramovsky, Gribov, Kancheli

of non-interacting particles that move in a scalar mean-field potential $U_S$ which in general depends on the phase-space densities $\{f_j\}$ of all other particle species (including $i$). The spectral functions $\mathcal{A}_i$ are again of the form (4.34).

The collision term

$$I_{\text{coll}}(\{F_j\}) = -i\Sigma_i^>(\{F_j\})\mathcal{A}_i f_i - i\Sigma_i^<(\{F_j\})\mathcal{A}_i(1 \pm f_i) \tag{5.22}$$

in Eq. (5.19) accounts for changes in the spectral phase-space density of particle species $i = a_1$ due to multi-particle collisions of the type $a_1, \ldots, a_n \to b_1 \ldots b_m$ and $b_1 \ldots b_m \to a_1, \ldots, a_n$. The factor $(1 \pm f)$ has the plus sign for bosons (Bose enhancement) and the minus sign for fermions (Pauli blocking). The collision term consists of a loss term of particle species $a_1$

$$
\begin{aligned}
i\Sigma_{a_1}^> &= \frac{1}{2E_{a_1}} \int \left( \prod_{j=2}^n g_{a_j} \frac{d^3 p_{a_j}}{(2\pi)^3} \frac{d\mu_{a_j}}{2E_{a_j}} \mathcal{A}_{a_j}(\mu_{a_j}, \vec{p}_{a_j}) f_{a_j} \right) \\
&\times \left( \prod_{k=1}^m \frac{d^3 p_{b_k}}{(2\pi)^3} \frac{d\mu_{b_k}}{2E_{b_k}} \mathcal{A}_{b_k}(\mu_{b_k}, \vec{p}_{b_k})(1 \pm f_{b_k}) \right) \\
&\times (2\pi)^4 \delta^4 \left( \sum_{j=1}^n p_{a_j} - \sum_{k=1}^m p_{b_k} \right) S_{a_2,\ldots,a_n} S_{b_1,\ldots,b_m} \overline{|\mathcal{M}_{a_1,\ldots,a_n \to b_1 \ldots b_m}|^2}
\end{aligned}
$$

and a gain term

$$
\begin{aligned}
-i\Sigma_{a_1}^< &= \frac{1}{2E_{a_1}} \int \left( \prod_{j=1}^m g_{b_j} \frac{d^3 p_{b_j}}{(2\pi)^3} \frac{d\mu_{b_j}}{2E_{b_j}} \mathcal{A}_{b_j}(\mu_{b_j}, \vec{p}_{b_j}) f_{b_j} \right) \\
&\times \left( \prod_{k=2}^n \frac{d^3 p_{a_k}}{(2\pi)^3} \frac{d\mu_{a_k}}{2E_{a_k}} \mathcal{A}_{a_k}(\mu_{a_k}, \vec{p}_{a_k})(1 \pm f_{a_k}) \right) \\
&\times (2\pi)^4 \delta^4 \left( \sum_{j=1}^m p_{b_j} - \sum_{k=1}^n p_{a_j} \right) S_{b_1,\ldots,b_m} S_{a_2,\ldots,a_n} \overline{|\mathcal{M}_{b_1,\ldots,b_m \to a_1 \ldots a_n}|^2}
\end{aligned}
$$

where $g_j$ are degeneration factors that account for the spin of particle $j$ and $\overline{|\mathcal{M}|^2}$ is the squared scattering matrix element averaged over incoming and summed over outgoing spins. $S$ denotes symmetry factors that take into account the existence of identical particles in the incoming and outgoing channel, e.g.,

$$S_{b_1,\ldots,b_m} = \prod_{k=1}^m \frac{1}{M_{b_k}!}$$

with $M_{b_k}$ denoting the multiplicity of particle $b_k$.

### Potential

All BUU equations (5.19) are coupled by the collision term and the scalar potential $U_S$ in the Hamilton function (5.20) where in our model the latter is usually only incorporated in case of baryons. The scalar potential $U_S$ can be related to the effective

(non-relativistic) potential $U$ which accounts for the many-body interactions of the baryons among each other. The general expression for the relativistic energy of a particle under the influence of a scalar potential $S$ and a vector potential $V = (V_0, \vec{V})$ is

$$H = \sqrt{(\mu + S)^2 + (\vec{p} - \vec{V})^2} + V_0.$$

In the local rest frame (LRF), i.e. where the baryon current locally vanishes, the spatial components $\vec{V}$ vanish [Tei96]. We arbitrarily set $S = 0$ and interpret the effective potential $U$ as the zeroth component $V_0$ of the vector potential:

$$H_{\mathrm{LRF}} = \sqrt{\mu^2 + p_{\mathrm{LRF}}^2} + U(\vec{r}, \vec{p}_{\mathrm{LRF}}).$$

We can then define the scalar potential $U_S$ of Eq. (5.20) in any frame as

$$U_S := \sqrt{H_{\mathrm{LRF}}^2 - p_{\mathrm{LRF}}^2} - \mu.$$

Note that for photon- and electron-induced reactions the local rest frame coincides with the frame where the target nucleus is at rest, i.e. the laboratory frame in case of fixed target experiments.

For nucleons the effective potential $U$ is parameterized according to Refs. [Wel88, Ga90] as a sum of a Skyrme part, which only depends on the baryon density $\rho$, and a momentum-dependent part:

$$U(\vec{r}, \vec{p}) = A\frac{\rho(\vec{r})}{\rho_0} + B\left(\frac{\rho(\vec{r})}{\rho_0}\right)^\tau + \frac{2C}{\rho_0}g\int\frac{d^3p'}{(2\pi)^3}\frac{f(\vec{r}, \vec{p}')}{1 + \left(\frac{\vec{p}-\vec{p}'}{\Lambda}\right)^2}, \qquad (5.23)$$

where $\rho_0 = 0.168$ fm$^{-3}$ denotes the saturation density of nuclear matter. In the reactions considered in this work, the nucleus remains close to its ground state and the phase-space density $f$ in (5.23) can be approximated by the phase-space density of (uncorrelated) cold nuclear matter

$$f(\vec{r}, \vec{p}) = \Theta(p_F(\vec{r}) - |\vec{p}|) \qquad (5.24)$$

with the local Fermi momentum

$$p_F(\vec{r}) = \left(\frac{6\pi^2}{g}\rho(r)\right)^{1/3}.$$

Here $g = 4$ again denotes the factor of degeneracy. For the density distribution of complex nuclei we use the Woods-Saxon parametrization:

$$\rho(r) = \frac{\rho_0}{1 + \exp\left(\frac{r-R}{a}\right)} \qquad (5.25)$$

with the parameters of Tab. 5.1 that have been extracted from a Hartree-Fock calculation [Tei96] for stable nuclei. For light nuclei like $^{12}$C and $^{14}$N, however, we use in general a Gaussian shape:

$$\rho_g(r) = \frac{1}{\pi^{3/2}a_g^3}\exp\left(-\frac{r^2}{a_g^2 A^{2/3}}\right) \qquad (5.26)$$

|        | $R$ [fm] | $a$ [fm] | $\rho_0$ [fm$^{-3}$] |
|--------|----------|----------|---------------------|
| $^{12}$C  | 2.328 | 0.479 | 0.160 |
| $^{14}$N  | 2.476 | 0.479 | 0.161 |
| $^{20}$Ne | 2.851 | 0.479 | 0.161 |
| $^{27}$Al | 3.202 | 0.478 | 0.161 |
| $^{63}$Cu | 4.409 | 0.477 | 0.157 |
| $^{84}$Kr | 4.911 | 0.476 | 0.155 |
| $^{107}$Ag | 5.356 | 0.476 | 0.154 |
| $^{131}$Xe | 5.777 | 0.476 | 0.152 |
| $^{208}$Pb | 6.826 | 0.476 | 0.149 |

Table 5.1: Woods-Saxon parameters (5.25) for the nuclei investigated in this work.

| $A$ [MeV] | $B$ [MeV] | $C$ [MeV] | $\tau$ | $\Lambda$ [fm$^{-1}$] |
|-----------|-----------|-----------|--------|----------------------|
| $-29.3$ | 57.2 | -63.5 | 1.76 | 2.13 |

Table 5.2: Parameters of the nucleon potential (5.23) used in this work.

with $a_g A^{1/3} = \sqrt{\frac{2}{3}} r_{\mathrm{rms}}$ and $r_{\mathrm{rms}} = 1.21 A^{1/3}$ fm [Pov97].

The use of (5.24) allows us to employ an analytic expression for the momentum-dependent part of the potential (5.23)

$$
\frac{2C}{\rho_0} g \int \frac{d^3 p'}{(2\pi)^3} \frac{\Theta(p_F(\vec{r}) - |\vec{p}'|)}{1 + \left(\frac{\vec{p} - \vec{p}'}{\Lambda}\right)^2} = \frac{2C}{\rho_0} \frac{g}{(2\pi)^3} \pi \Lambda^3 \left\{ \frac{p_F^2(\vec{r}) + \Lambda^2 - p^2}{2p\Lambda} \ln \left[ \frac{(p + p_F(\vec{r}))^2 + \Lambda^2}{(p - p_F(\vec{r}))^2 + \Lambda^2} \right] \right.
$$

$$
\left. + \frac{2p_F(\vec{r})}{\Lambda} - 2 \left[ \arctan \left( \frac{p + p_F(\vec{r})}{\Lambda} \right) - \arctan \left( \frac{p - p_F(\vec{r})}{\Lambda} \right) \right] \right\}.
$$

The parameters of the mean-field potential (5.23) are fitted to the saturation properties of nuclear matter and the momentum dependence of the nucleon optical potential as measured in $pA$ collisions [Eff99a]. Throughout this work we employ the parameters given in Tab. 5.2. For nuclear matter density $\rho_0 = 0.168$ fm$^{-3}$ the effective potential $U$ increases monotonically from

$$
U(p = 0, \rho = \rho_0) = -75 \, \mathrm{MeV}
$$

to

$$
U(p \to \infty, \rho = \rho_0) = 30.5 \, \mathrm{MeV}. \tag{5.27}
$$

For the densities of nuclei listed in Tab. 5.1 the absolute value of the effective potential is even smaller.

We use the same mean-field potential for all baryons except for the $\Delta$ resonance for which we assume

$$
U_\Delta = \frac{2}{3} U.
$$

This choice is motivated by the phenomenological value of -30 MeV at density $\rho_0$ [Eri88]. As mentioned above, we neglect any hadronic potential for mesons as well as any influence of the Coulomb potential in our present investigations.

**Collision term**

According to Eq. (5.27) the coupling of the BUU equations (5.19) via the mean field is rather low in the multi-GeV range of interest. One is therefore left with the coupling through the collision term (5.22). For high-energy nuclear reactions of elementary probes like pions, protons and (virtual) photons binary collisions $a_1, a_2 \rightarrow b_1, \ldots b_m$ play the dominant role. Note, however, that in heavy-ion collisions due to the high densities involved, multi-particle collisions can become important. Since some of the particles in our simulation are unstable with respect to strong decays one has to keep in mind that also the decay of a particle into several other hadrons leads to changes in the phase-space densities.

In the mesonic sector we account for all particles listed in Tab. 5.3. Mesons that can only decay due to the weak interaction are considered stable within our model. The only exception is the $\eta$ whose decay is explicitly accounted for when looking into pion production.

Besides the nucleon ($m_N = 938$ MeV) and the Delta ($m_\Delta = 1232$ MeV, $\Gamma_\Delta = 118$ MeV) we account for 29 additional nucleon resonances [Eff99a] in the baryonic sector whose properties are taken from an analysis of $\pi N$ scattering [Man92]. In our model the $\Delta$ always decays to $N\pi$ whereas the other resonances can couple to the channels $N\pi$, $N\eta$, $\Lambda K$, $N\omega$, $\Delta\pi$, $N\rho$, $N\sigma$, $N(1440)\pi$ and $\Delta\rho$. In addition to the $\Lambda$ ($m_\Lambda = 1116$ MeV) and the $\Sigma$ ($m_\Sigma = 1189$ MeV), which are stable with respect to the strong decay, we also include 19 further $S = -1$ resonances that can decay into $\Lambda\pi$, $NK$, $\Sigma\pi$, $\Sigma^*\pi$, $\lambda\eta$, $NK^*$ and $\Lambda^*\pi$. Furthermore, we include the strange and charmed baryons of Tab. 5.4 in our model. Due to a lack of a complete analysis, the parameters for the strange and charmed baryons are taken from Ref. [PDG98]. For each baryon we also account for the corresponding antiparticle.

Since we explicitly consider the charge of the particles, each isospin state of a particle leads to a separate BUU equation. The spin is only accounted for as a statistical weight in the degeneracy factor $g$.

## 5.2.2 Numerical implementation

The set of coupled differential-integral equations (5.19) is solved via a test-particle ansatz for the spectral phase-space densities (5.21):

$$F(\vec{r}, \vec{p}, \mu; t) = \frac{1}{N} \frac{(2\pi)^3}{g} \sum_{i=1}^{N} \delta(\vec{r} - \vec{r}_i(t)) \delta(\vec{p} - \vec{p}_i(t)) \delta(\mu - \mu_i(t)) \qquad (5.28)$$

where $\vec{r}_i$, $\vec{p}_i$ and $\mu_i$ denote the position, momentum and mass of the test particle $i$ at time $t$ and $N$ is the number of test particles per physical particle. In this work we use the method of parallel ensembles, i.e. the test particles are divided into $N$ different

| | $m$ [MeV] | $\Gamma$ [MeV] | $J$ | $I$ | $S$ | $C$ | decay channel |
|---|---|---|---|---|---|---|---|
| $\pi$ | 138 | 0 | 0 | 1 | 0 | 0 | |
| $\eta$ | 547 | $1.2 \cdot 10^{-3}$ | 0 | 0 | 0 | 0 | $\gamma\gamma$ (40%), $\pi^+\pi^-\pi^0$ (28%), $3\pi^0$ (32%) |
| $\rho$ | 770 | 151 | 1 | 1 | 0 | 0 | $\pi\pi$ |
| $\sigma$ | 800 | 800 | 0 | 0 | 0 | 0 | $\pi\pi$ |
| $\omega$ | 782 | 8.4 | 1 | 0 | 0 | 0 | $\pi\pi$ (2%), $\pi^0\gamma$ (9%), $\pi^+\pi^-\pi^0$ (89%) |
| $\eta'$ | 958 | 0.2 | 0 | 0 | 0 | 0 | $\rho^0\gamma$ (31%), $\pi\pi\eta$ (69%) |
| $\phi$ | 1020 | 4.4 | 1 | 0 | 0 | 0 | $\rho\pi$ (13%), $K\bar{K}$ (84%), $\pi^+\pi^-\pi^0$ (3%) |
| $K$ | 496 | 0 | 0 | 1/2 | 1 | 0 | |
| $\bar{K}$ | 496 | 0 | 0 | 1/2 | -1 | 0 | |
| $K^*$ | 892 | 50 | 1 | 1/2 | 1 | 0 | $K\pi$ |
| $\bar{K}^*$ | 892 | 50 | 1 | 1/2 | -1 | 0 | $\bar{K}\pi$ |
| $\eta_c$ | 2980 | 0 | 0 | 0 | 0 | 0 | |
| $J/\psi$ | 3097 | 0 | 1 | 0 | 0 | 0 | |
| $D$ | 1869 | 0 | 0 | 1/2 | 0 | 1 | |
| $\bar{D}$ | 1869 | 0 | 0 | 1/2 | 0 | -1 | |
| $D^*$ | 2007 | 1 | 1 | 1/2 | 0 | 1 | $D\pi$ |
| $\bar{D}^*$ | 2007 | 1 | 1 | 1/2 | 0 | -1 | $\bar{D}\pi$ |
| $D_s$ | 1969 | 0 | 0 | 0 | 1 | 1 | |
| $\bar{D}_s$ | 1969 | 0 | 0 | 0 | -1 | -1 | |
| $D_s^*$ | 2112 | 1.9 | 1 | 0 | 1 | 1 | $D_s\gamma$ (94%), $D_s\pi$ (4%) |
| $\bar{D}_s^*$ | 2112 | 1.9 | 1 | 0 | -1 | -1 | $\bar{D}_s\gamma$ (94%), $\bar{D}_s\pi$ (4%) |

Table 5.3: List of mesons included in the BUU model, their quantum numbers (spin $J$, isospin $I$, strangeness $S$, charm $C$) and decay channels. The parameters are taken from Ref. [PDG98] except for the $\sigma$ meson [Man92].

ensembles which do not influence each other[2]. This is equivalent to simulating $N$ independent nuclear reactions in parallel and averaging the observables at the end. For a test-particle number $N \to \infty$ the test particles will give the time evolution of the spectral phase-space densities.

### Initialization

When initializing a nuclear reaction the test particles, that correspond to nucleons of the nucleus, are distributed in position space following the Woods-Saxon distribution

---

[2]Only the baryon density in $AA$ and $pA$ collisions which determines the mean-field potential and Pauli blocking is calculated from the distribution of *all* test-particles [Eff99a]. In case of photon- and electron-induced reactions one expects only minor changes in the nucleon density during the reaction. For these reactions we calculate the potential and Pauli blocking directly from the ground state density (5.25).

|        | $m$ [MeV] | $\Gamma$ [MeV] | $J$ | $I$ | $S$ | $C$ | decay channel |
|--------|-----------|----------------|-----|-----|-----|-----|---------------|
| $\Xi$      | 1315 | 0   | 1/2 | 1/2 | -2 | 0 |            |
| $\Xi^*$    | 1530 | 9.5 | 3/2 | 1/2 | -2 | 0 | $\Xi\pi$   |
| $\Omega$   | 1672 | 0   | 3/2 | 0   | -3 | 0 |            |
| $\Lambda_c$ | 2285 | 0   | 1/2 | 0   | 0  | 1 |            |
| $\Sigma_c$ | 2455 | 0   | 1/2 | 1   | 0  | 1 |            |
| $\Sigma_c^*$ | 2530 | 15 | 3/2 | 1   | 0  | 1 | $\Lambda_c\pi$ |
| $\Xi_c$    | 2466 | 0   | 1/2 | 1/2 | -1 | 1 |            |
| $\Xi_c^*$  | 2645 | 4   | 3/2 | 1/2 | -1 | 1 | $\Xi_c\pi$ |
| $\Omega_c$ | 2704 | 0   | 1/2 | 0   | -2 | 1 |            |

Table 5.4: List of baryons with $S < -1$ or $C > 0$ included in the BUU model, their quantum numbers (spin $J$, isospin $I$, strangeness $S$, charm $C$) and decay channels. The parameters are taken from Ref. [PDG98].

(5.25) or a Gauss distribution (5.26) for $^{12}$C and $^{14}$N, respectively. We here assume that the form of the density distribution is the same for protons and neutrons. For the initialization in momentum space we use the local Thomas-Fermi approximation (5.24).

**Propagation**

The calculation is performed on a discretized time grid with grid size $\Delta t = 0.5$ fm/$c$. A further reduction of the time step $\Delta t$ was found to have no influence on our results. However, as we discuss below, one has to use a smaller value for $\Delta t$ if one wants to describe reactions that involve high particle densities like heavy-ion collisions. During each time step the test particles are assumed to move as non-interacting particles in the mean field $U_S$. Substituting the test-particle ansatz (5.28) into the BUU Eq. (5.19) – with the collision term set to zero – yields the classical Hamilton equations of motion:

$$\begin{aligned}
\frac{d\vec{r}_i}{dt} &= \vec{\nabla}_{\vec{p}_i} H \\
\frac{d\vec{p}_i}{dt} &= -\vec{\nabla}_{\vec{r}_i} H \\
\frac{d\mu_i}{dt} &= 0
\end{aligned} \tag{5.29}$$

with $H$ being a functional of the phase-space density $f$.

The initializations according to Eqs. (5.25) and (5.26) do not correspond to the exact ground state of the nuclear potential. As discussed in Ref. [Eff99a] this leads to an oscillating density distribution of the nucleon test particles. For both initializations the density fluctuations are on the level of about 20% [Leh]. The period of the oscillation is about ten times larger than the time that a high-energy particle (with velocity close to the speed of light) needs to escape the nucleus, i.e. the reaction time. For photon and

electron induced reactions the density is frozen until the time of the primary photon-nucleon interaction. As a result, the mean squared radius has changed by less than 4% [Eff99a] by the time that the high-energy particles have left the nucleus.

## Collisions

Between the time steps the particles may collide. We do not assume any medium modification of the matrix elements $\mathcal{M}$ that enter the collision term (5.22). If one accounts for the energy shift caused by the scalar potential $U_S$, the transition rates can be directly taken from the corresponding vacuum cross sections. Note, however, that in the resonance region cross sections might be modified due to in-medium changes of the resonance properties as discussed in Refs. [Eff99a, Leh03].

Concerning the collision criteria we follow the method by Kodama et al. [Kod84]: Two particles collide in a time step $\Delta t$ if the impact parameter $b$, i.e. the minimum separation in their center-of-momentum system, is smaller than

$$b \leq \sqrt{\frac{\sigma^{\text{tot}}(s)}{\pi}}. \tag{5.30}$$

Furthermore, it is checked if both particles reach this minimal distance during the time step $\Delta t$. In Eq. (5.30) $\sigma^{\text{tot}}$ denotes the total cross section for the interaction of the two particles. For high-energy collisions these are the ones given in Sec. 4.4.1. Elastic interactions occur with a probability

$$P_{\text{el}} = \frac{\sigma^{\text{el}}(s)}{\sigma^{\text{tot}}(s)};$$

the scattering angle is determined according to Eq. (2.17). In case of a high-energy inelastic collision the reaction products are determined by FRITIOF (or JETSET for baryon-antibaryon annihilation). In the resonance region, i.e. below $\sqrt{s} = 2.2$ GeV for meson-baryon and $\sqrt{s} = 2.6$ for baryon-baryon scattering, the total cross section is an incoherent sum of the cross sections for the reactions

$$
\begin{array}{lllll}
mB \leftrightarrow R & \pi N \leftrightarrow \pi N & \pi N \rightarrow \pi\pi N & \pi N \leftrightarrow \eta\Delta & \pi N \leftrightarrow \omega N \\
\pi N \rightarrow \pi\omega N & \pi N \leftrightarrow \phi N & \omega N \leftrightarrow \omega N & \omega N \rightarrow \pi\pi N & \phi N \leftrightarrow \phi N \\
\phi N \rightarrow \pi\pi N & \pi B \leftrightarrow KY & \pi B \rightarrow K\bar{K}N & \bar{K}N \leftrightarrow \bar{K}N & \bar{K}N \leftrightarrow \pi Y \\
\bar{K}N \leftrightarrow \pi Y^* & KN \leftrightarrow KN & KN \rightarrow K\pi N
\end{array}
$$

in case of meson-baryon collisions and

$$
\begin{array}{lllll}
NN \leftrightarrow NN & NN \leftrightarrow NR & NN \leftrightarrow \Delta\Delta & NN \leftrightarrow NN\pi & NN \rightarrow NN\omega \\
NR \leftrightarrow NR' & BB \rightarrow NYK & BB \rightarrow NY^*K & BB \rightarrow NNK\bar{K}
\end{array}
$$

for baryon-baryon collisions. Here $m$ stands for a meson, $B = N, \Delta$; nucleon resonances are denoted by $R$ and $R'$, hyperon resonances by $Y^*$ and $Y = \Sigma, \Lambda$. The reactions involving antibaryons are obtained by charge conjugation. The reaction channel $ab \rightarrow X$ in the collision of two particles $a$ and $b$ is chosen by Monte Carlo with a probability

determined from its contribution to the summed total cross section (see Ref. [Eff99a] for details)

$$P_{ab \to X} = \frac{\sigma_{ab \to X}(s)}{\sigma_{ab}^{\text{tot}}(s)}. \tag{5.31}$$

Furthermore, our BUU model allows for meson-meson collisions of the kind $mm' \leftrightarrow m''$ as well as the reaction $\pi\pi \leftrightarrow K\bar{K}$. However, as we pointed out in Sec. 4.4.1, meson-meson collisions are only relevant at high meson densities as reached in heavy-ion collisions and can be neglected for photon- and electron-induced reactions.

Our model also includes the possibility to account for collisions with three particles in the initial state. If the matrix element is known from detailed balance, like for example in the process $NN \to \pi NN$, one can also include the three-particle collision $\pi NN \to NN$ following the method developed in Ref. [Eff99a]. However, these reactions turn out to be unimportant at higher energies and nuclear ground-state densities.

In the present realization of the collision term it is essential to forbid collisions among the products of a primary reaction before they have participated in another interaction [Eff99a]. Otherwise the same two particles would collide over and over again during the next time steps, since they do not separate far enough during $\Delta t$. However, this does not rule out the possibility that, during the same time step $\Delta t$, test particles created in one collision interact with test particles that emerge from another reaction. For large particle densities – as reached for example in heavy-ion collisions – this will lead to a vast number of collisions during one time step if one does not properly adjust $\Delta t$. This problem is absent for perturbative particles (see below) which are not allowed to interact with each other throughout the simulation.

**Decay**

An important feature of our model is the decay of unstable particles with mass $\mu$ and energy $E$ during a time step $\Delta t$. The corresponding decay probability is given by

$$P_{\text{dec}} = 1 - \exp\left(-\frac{\Gamma(\mu)}{\gamma}\Delta t\right)$$

where $\gamma = E/\mu$ is the Lorentz factor while $\Gamma$ denotes the width of the particle in its rest frame. The final state of the decay is again determined by Monte Carlo assuming the decay to be isotropic in the rest frame of the particle since we neglect the spin degree of freedom.

**Pauli blocking**

Due to the low densities of other baryons, Pauli blocking is only accounted for in collisions and decays that involve nucleons in the final state. The Pauli factors in the collision term (5.22) are in general calculated by averaging the phase-space density over a small volume around the phase-space point:

$$1 - f(\vec{r}, \vec{p}; t) = 1 - \int_{\Delta V_r} d^3r' \int_{\Delta V_p} d^3p'\, f(\vec{r}'\vec{p}'; t).$$

For $\gamma^* A$ reactions, where the nucleus approximately stays in its ground state, one can approximate the probability that an event at position $\vec{r}$ with an outgoing nucleon of momentum $\vec{p}$ is Pauli blocked via Eq. (5.24) as

$$P_{\text{Pauli}} = \Theta(p_F(\vec{r}) - |\vec{p}|). \qquad (5.32)$$

### Perturbative particles

Finally, we outline the method of perturbative particles which we employ for photon- and electron-induced reactions. Originally, this method has been developed to describe the production of particles which are created very rarely and which therefore have only very little influence on the time evolution of the spectral phase-space density [Wei99, Bra98]. The propagation and collisions of perturbative test particles are only effected by the real particles. On the other hand, the perturbative test particles have no influence on the real particles whatsoever.

As discussed above, the probability that the real final state $X$ is produced in a collision of two particles $a$ and $b$ is given by Eq. (5.31). Each real test particle in the final state $X$ can be assigned a statistical weight 1. Perturbative particles, however, are produced in every collision of $a$ and $b$ and therefore must be assigned a statistical weight $\sigma_{ab \to X}/\sigma_{ab}^{\text{tot}} < 1$. In any interaction of a perturbative particle with a real particle this statistical weight is transfered to the reaction products.

In case of high-energy $\gamma^* A$ interactions we initialize a $\gamma^* N$ reaction on each of the $A$ nucleons in one ensemble. The reaction products are then treated as perturbative particles, and each perturbative test particle gets a statistical weight $s(\vec{r})\sigma_{\gamma N}^{\text{tot}}/A$ where $s(\vec{r})$ denotes the shadowing factor which we introduce in Sec. 6.1.2. It accounts for the multiple scattering of the resolved photon components on the way through the nucleus to position $\vec{r}$ where the reaction takes place. In using the perturbative particle method for $\gamma^* A$ reactions one saves a tremendous amount of CPU time since one can now consider $A$ instead of one reaction per ensemble at a time.

The reaction products that are relevant for our investigations have momenta of the order of several GeV. We therefore neglect the effect of the effective potential $U_S$ for all perturbative particles. As a result, the equations of motions (5.29) for the perturbative particles simplify considerably:

$$\frac{d\vec{r}_i}{dt} = \frac{\vec{p}_i}{\sqrt{\mu_i^2 + \vec{p}_i^2}}$$
$$\frac{d\vec{p}_i}{dt} = 0$$
$$\frac{d\mu_i}{dt} = 0.$$

We have verified that this approximation does not affect the results of our model calculations in the kinematic regime of the HERMES experiment, and conclude that it is of no importance for the even higher EMC energies. However, it may play a role for the energy spectra of protons and neutrons observed at Jefferson Lab. However, since the latter are strongly contaminated by protons and neutrons that are knocked out of the nucleus in the FSI, they will most likely not be studied in experiment [WBr].
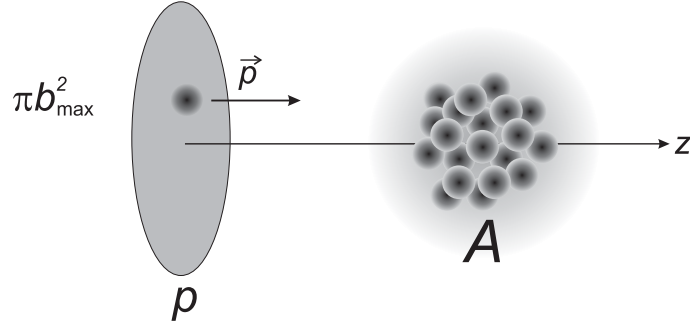
Figure 5.4: Initialization of a $pA$ collision in the BUU simulation.

## 5.3  Proton-nucleus reactions

In this section we want to compare the results of the Glauber and the BUU model for high-energy $pA$ collisions. To calculate the $pA$ cross section in the BUU model we randomly initialize the incoming protons in the lab frame with energy $E_p$ and momentum $\vec{p} = \sqrt{E^2 - m_N^2}\,\vec{e}_z$ inside a disc of radius

$$b_{\max} = 1.1\,\mathrm{fm} \cdot A^{1/3} + \sqrt{\frac{\sigma_{\max}}{\pi}}$$

which is located 4 fm away from the surface of the nucleus (cf. Fig. 5.4). The cross section $\sigma_{\max}$ must be larger than the total high-energy $pN$ cross section so that any proton with larger impact parameter would miss the nucleus in the simulation. We use the value $\sigma_{\max} = 55$ mb.

### 5.3.1  Total cross section

In the BUU model the incoherent $pA$ reaction cross section is given by the product of the area $\pi b_{\max}^2$ and the relative reaction frequency:

$$\sigma_{pA}^{\mathrm{reac}} = \pi b_{\max}^2 \left(\frac{N - N_0}{N}\right) \tag{5.33}$$

where $N$ denotes the numbers of initial protons[3] and $N_0$ is the number of protons from the incoming beam which pass the nucleus without any interaction. If one neglects coherent interactions where the proton scatters on the nucleus as a whole instead of individual nucleons the reaction cross section (5.33) equals the total $pA$ cross section $\sigma_{pA}^{\mathrm{tot}}$.

We have calculated the total cross section for the scattering of 100 GeV protons on $^{12}$C, $^{27}$Al, $^{63}$Cu, $^{107}$Ag and $^{208}$Pb targets. The BUU results are illustrated by the open circles in Fig. 5.5. From the $A$ dependence of the BUU cross section we extract a scaling with $A^{0.68}$ which perfectly agrees with the experimental result (solid crosses) of Ref. [Car79]. This is astonishing since our semi-classical approach disregards the quantum mechanic interference effects that led to the factor of two in Eq. (5.17). On

---

[3]In the parallel ensemble method this number equals the number of ensembles.
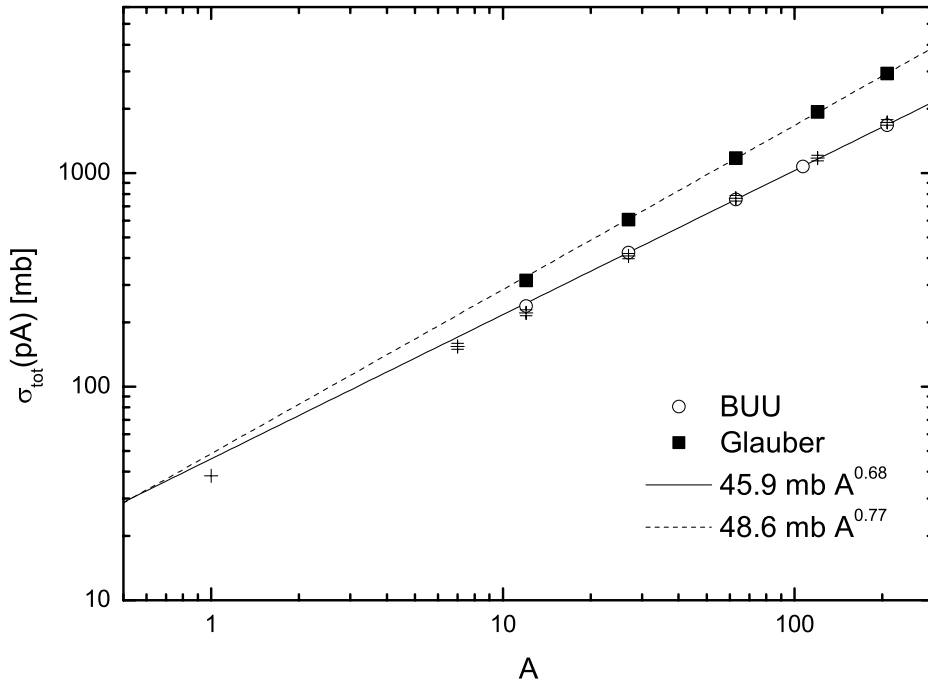
Figure 5.5: Total $pA$ cross section for a proton lab energy of 100 GeV. The open circles show the result (5.33) of the BUU simulation and show a scaling with $A^{0.68}$. The Glauber cross section (5.15) is represented by the solid squares. Its scaling with $A^{0.77}$ is clearly too large. The data (solid crosses) are taken from Ref. [Car79].

the other hand the total $pA$ cross section in the BUU model is not simply $\pi R^2$ but rather

$$\sigma_{pA}^{\text{tot}} \approx \pi \left( R + \sqrt{\frac{\sigma_{pN}}{\pi}} \right)^2,$$

which is further modified by the fact that a nucleus is not a sphere with a sharp radius $R = r_0 A^{1/3}$ (cf. Eqs. (5.25) and (5.26)).

We now discuss the prediction of Glauber theory for the total $pA$ cross section. In the discussion of Eq. (5.16) we have pointed out that – in the limit of a very small mean free path of the hadronic projectile in the nucleus – the cross section scales like $A^{2/3}$, i.e. the nucleons on the front side of the nucleus shadow the down stream nucleons from the interaction, a phenomenon called nuclear shadowing. For a high-energy proton ($\sigma_{pp} \approx 40$ mb) the mean free path in nuclear matter ($\rho_0 = 0.168$ fm$^{-3}$) is approximately $\lambda_p = 1.5$ fm. The average density of finite nuclei is somewhat smaller than $\rho_0$ and therefore $\lambda_p$ in nuclei is not much smaller than the nuclear radius (e.g. $R_{\text{Pb}} = 6.6$ fm) and we expect that the total $pA$ cross section scales like $A^\alpha$ with a scaling exponent $2/3 < \alpha < 1$ according to our Glauber investigations of Sec. 5.1.2. In Fig. 5.5 the solid squares represent the Glauber result (5.15) for the total cross section $\sigma_{pA}^{\text{tot}}$ for $^{12}$C, $^{27}$Al, $^{63}$Cu, $^{120}$Sn and $^{208}$Pb. Our calculations show that Glauber theory yields a scaling exponent $\alpha = 0.77$ for 100 GeV protons which is obviously too large compared to the experimental data. The reason for this deviation might be that at very high energies

expression (5.15) has to be corrected for single diffractive excitation $hN \to XN$. This means that an intermediate state $X$ with mass $m_X \geq m_h$ propagates in the multiple scattering series shown in Fig. 5.3. In addition, there might be off-diagonal transitions $X_1N \to X_2N$ in the single scattering events which complicate things furthermore. As Gribov has shown in Ref. [Gri69], such inelastic corrections guarantee that the non-relativistic Glauber approach that we have presented in Sec. 5.1 can be applied up to very high energies. In Appx. H we show how one has to modify the nuclear profile function (5.8) for $hA$ scattering to account for Gribov's inelastic corrections.

## 5.3.2 Inclusive meson production

At the end of Sec. 5.1.2 we have pointed out that the AGK cancellation predicts a scaling of the inclusive production cross section $\sigma_{pA \to mX}$ with the nucleon number $A$. How can such a behavior be reproduced by our semi-classical BUU transport model?

As we have discussed in the preceding chapters, the product of a high-energy hadron-hadron collision will be either a bunch of hadronic strings or diffractively excited hadrons. At not too large energies the latter is more likely since the cross section for hard scatterings is relatively small as can be seen in Fig. 2.7. In the realization of our BUU model the final state of a high-energy hadronic interaction will be determined by FRITIOF which means that the final state consists of two excited hadronic strings with a large separation in rapidity. These strings then fragment into hadrons according to the Lund model. We have already discussed production and formation times in Sec. 4.3 and found that depending on the mass of the hadrons the formation proper times in the Lund model lie in the range $\tau_f$=0.5–1.7 fm/$c$. Independently of the Lund model, one can estimate a lower boundary for the time that it takes until the reaction products have evolved to physical hadrons, i.e. until they interact with their full hadronic cross section. In the rest frame of each hadron this lower boundary is given by the time that the hadron constituents need to propagate a distance of the order of the hadronic radius, i.e. $\tau_f = 0.5$–$0.8$ fm/$c$. Due to time dilatation the formation times in the laboratory frame

$$t_f = \gamma \tau_f = \frac{E_h}{m_h} \tau_f \tag{5.34}$$

may become quite large and the corresponding formation lengths may easily exceed nuclear dimensions at high energies. In Eq. (5.34) $E_h$ and $m_h$ denote the energy and mass of the produced hadron.

**Leading hadrons**

If the reaction takes place in a nuclear environment the question arises how the strings and their color-neutral fragments interact with the surrounding nucleons during the formation time. Fig. 5.6 illustrates schematically the interaction of a high-energy proton with a nucleus. In the extreme scenario in which the reaction products do not interact at all during the formation proper time $\tau_f$ the production cross section should roughly scale with $A^{2/3}$. The reason for this is that due to its relatively small mean free path the incoming proton will mainly interact on the front side of the nucleus and produce a bunch of high-energy particles which then leave the nucleus without further interactions. This scenario, however, seems unrealistic, since it is unclear why the
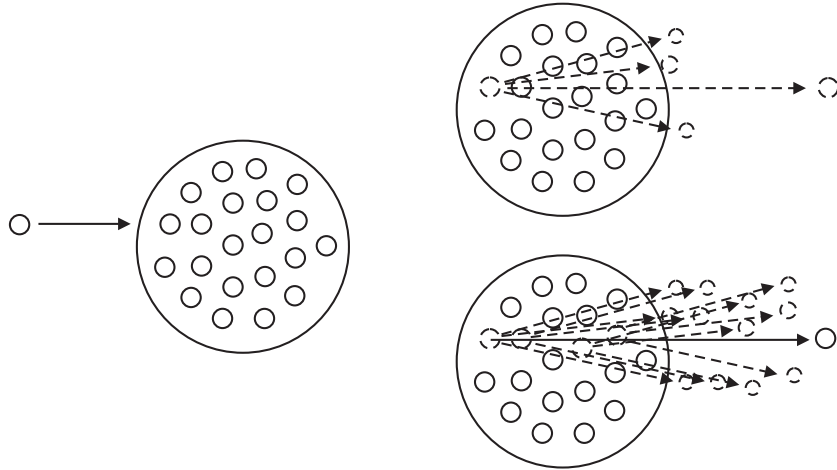
Figure 5.6: Schematic illustration of particle production in a high-energy $pA$ reaction. In the first scenario the reaction products of a collision are assumed to be non-interacting during some constant formation proper time $\tau_f$ (dashed lines). As a consequence, the incoming proton interacts on the front side of the nucleus and produces a bunch of high-energy particles which due to time dilatation escape the nucleus without further interactions. This leads to a production cross section $\sigma_{pA \to mX}$ that roughly scales with $A^{2/3}$. In the second scenario the remnant of the incoming proton interacts during the formation time (solid line) and contributes to particle production in each subsequent collision. In the latter case the production cross section $\sigma_{pA \to mX}$ scales with the number of nucleons in the nucleus.

diffractively excited nucleons should behave that much different than normal nucleons. If, however, the proton remnant could interact with the surrounding medium during the formation time the inclusive meson production cross section would approximately scale with $A$ since each subsequent scattering can contribute to meson production.

In transport models one usually assumes that each string decays instantaneously into color-neutral prehadrons which are then propagated. In the Lund model this corresponds to a vanishingly small production time of the $q\bar{q}$ vertices.

In the HSD model [Gei98a, Gei98b, Cas99] the method of *leading hadrons* is used to account for the interactions of the beam (and target) remnants during the formation time. The leading prehadrons are defined as the ones having largest and smallest longitudinal momentum in the rest frames of the two fragmenting strings that were created by FRITIOF. In most cases those prehadrons coincide with the four hadrons that emerge from the end points of the strings in the fragmentation. In the HSD model the cross sections of the four leading prehadrons are then reduced during the formation time and the cross sections of the remaining prehadrons are set to zero during $\tau_f$.

In the previous version of our BUU model [Eff99a] the leading prehadrons have been defined as the two hadrons with the largest and smallest longitudinal momentum in the center-of-mass system of the collision. Since one has now only two leading prehadrons per collision the leading prehadron cross section has to be approximately twice as large as in the HSD model to get similar results for the description of high-energy $pA$ and $AA$ reactions. Even though the two methods might produce similar results [Sor90], we
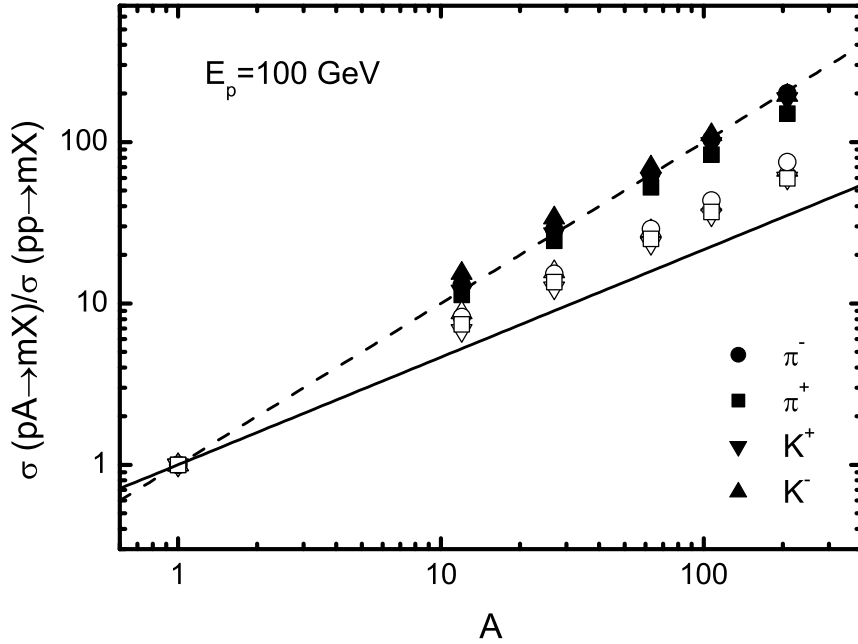
Figure 5.7: Ratio of nuclear and elementary cross section for inclusive $\pi^{\pm}$ and $K^{\pm}$ production of 100 GeV protons incident on nuclear targets. The open (solid) symbols represent the result without (with) prehadronic interactions during the formation time $\tau_f = 0.5$ fm/$c$. For comparison we also show the two lines $A$ (dashed) and $A^{2/3}$ (solid).

think that the first one is closer connected to the underlying physical process.

As we have pointed out at the end of Sec. 4.4.2 hard processes, especially the direct photon interactions simulated with PYTHIA may lead to quite complicated final states that consist of more than two strings. Hence, the recipe of identifying the fastest and slowest prehadron produced in each string decay as a beam or target remnant is not always correct. For this reason, we rather trace back the fragmentation process in JETSET and identify the prehadrons that contain constituents of the projectile or target hadron.

In our default approach we set the production times $\tau_p$ of all prehadrons to zero and rescale their cross sections during the formation time $\tau_f$ according to a simple constituent quark model:

$$
\begin{aligned}
\sigma_{\text{prebaryon}}^{\text{tot}} &= \frac{n_{\text{org}}}{3} \sigma_{\text{baryon}} \\
\sigma_{\text{premeson}}^{\text{tot}} &= \frac{n_{\text{org}}}{2} \sigma_{\text{meson}}
\end{aligned}
\tag{5.35}
$$

where $n_{\text{org}}$ denotes the number of (anti-)quarks in the prehadron stemming from the beam or target. As a consequence, the prehadrons that are no beam or target remnants, i.e. those that solely contain (anti-)quarks produced from the vacuum in the string fragmentation, do not interact during $\tau_f$. The ansatz (5.35) ensures that the summed cross section of the string fragments right after the scattering process takes on a hadronic value. This is reasonable since the excited string is a rather short color neutral object which has the transverse size of the original hadron [Cio02] and there-

fore should interact with about the same cross section. As we discuss in more detail in Sec. 6.4 the summed cross section then rises each time when a new hadron has formed. For simplicity we assume that the formation time is a constant in the rest frame of each hadron and that it does not depend on the particle species as in Ref. [Gei98b, Cas99]. In Chap. 6 we also discuss other concepts of production times, formation times and prehadronic cross sections. However, as we show in Sec. 6.4 concept (5.35) gives a good description of the available electroproduction data. This also holds for particle production in proton-nucleus and heavy-ion collisions in a wide dynamical range [Web03, Bra03].

### Integrated production cross section

In Fig. 5.7 we show our results for the normalized inclusive production cross section $\sigma_{pA \to mX}/A\sigma_{pp \to mX}$ of $\pi^{\pm}$ and $K^{\pm}$ for protons incident on nuclear targets at 100 GeV. For comparison we also show two lines which illustrate a scaling with $A$ and $A^{2/3}$ respectively.

The open symbols represent the result one gets if one assumes no interactions of any prehadrons during the formation time $\tau_f = 0.5$ fm/$c$. The production cross section $\sigma_{pA \to mX}$ then simply scales with the surface of the nucleus, i.e. with $A^{2/3}$. The reason for this is that – as already mentioned above – the incoming proton gets absorbed on the front side of the nucleus and thereby produces a bunch of particles which do not interact during the formation time. Due to time dilatation the corresponding formation lengths in the laboratory frame are larger than the nuclear dimensions and therefore the reaction products escape the nucleus without any further interaction. Hence, only the nucleons on the front side of the nucleus contribute to particle production.

The solid symbols represent the calculated cross section with our constituent quark ansatz (5.35) for the prehadronic cross sections. The beam remnants already interact during the formation time ($\tau_f = 0.5$ fm/$c$) and scatter on the surrounding target nucleons. In each scattering process, new particles are created. As a result, the production cross section $\sigma_{pA \to mX}$ is proportional to $A$ as required by AGK cancellation (5.18).

### Differential production cross section

To compare our model with experiment, we have calculated the inclusive invariant differential cross section $E d^3\sigma/d^3 p$ for $\pi^{\pm}$ and $K^{\pm}$ production of 100 GeV protons on protons and nuclei and compare our results for the ratio

$$R = \frac{E\frac{d^3\sigma}{d^3p}(pA \to mX)}{E\frac{d^3\sigma}{d^3p}(pp \to mX)} \tag{5.36}$$

with the experimental FNAL data (solid squares) of Ref. [Ba83] in Fig. 5.8. The meson momenta transverse to the direction of the incoming proton beam was required to lie in the bin 0.2 GeV$\leq p_T \leq$0.4 GeV. The data has been taken for several momentum intervals. The size of this (longitudinal) momentum binning is 10 GeV and the center values of $p$ are given in the figure. As can be seen from Fig. 5.8, the experimental data roughly scale with $A^{2/3}$.

The open squares represent the result of a BUU calculation without prehadronic interactions during the formation time $\tau_f = 0.5$ fm/$c$. The error bars on the BUU

results indicate the statistical error in our simulation. For the same reasons as for the integrated inclusive production cross section in Fig. 5.7 the ratio (5.36) scales with the surface of the nucleus, i.e. with $A^{2/3}$, in agreement with experimental data.

This, however, does not rule out the presence of prehadronic interactions since the BUU calculation with our prehadron concept (5.35) also yields an approximate scaling with $A^{2/3}$. At first sight this seems to contradict the observed scaling of the integrated production cross section but this is not the case. The reason is that the prehadronic FSI on the one hand increase the particle yield and thereby the integrated production cross section $\sigma_{pA \to mX}$. On the other hand they shift strength from high to low energies due to energy and momentum conservation in each scattering process. An interaction of a high-energy prehadron can only increase the number of mesons in a lower momentum bin. In the end one has only very few particles with very high momentum (close to $E_p = 100$ GeV) and a lot of low-energy particles which do not fall in the intermediate momentum bins shown in Fig. 5.8 but contribute to the integrated cross section. We meet this phenomenon again in Sec. 6.4 when discussing hadron attenuation in deep inelastic lepton scattering off nuclei.

Obviously, the specific data of Ref. [Ba83] that we have used to study the $A$ dependence of semi-inclusive meson production in $pA$ reactions cannot distinguish between a scenario with or without prehadronic interactions. The detailed understanding of this insensitivity in combination with an analysis of the various other $pA$ data will be a task for the future. The observed insensitivity does not imply that high-energy $pA$ collisions cannot be exploited to study the effects of formation times and prehadronic interactions. For example the authors of Ref. [Cas02] investigated antiproton production in $pA$ collisions as measured by the E910 collaboration [Chm01] at 12.3 GeV/$c$ and 17.5 GeV/$c$ and found that the antiproton rapidity distributions for heavy targets are sensitive to the $\bar{p}$ formation time. Furthermore, it was shown in Ref. [Cas04] that even at considerably higher energies, i.e. in $d + A$ reactions at RHIC ($\sqrt{s} = 200$ GeV), prehadronic interactions play an important role. Unlike in $eA$ reactions – where the hard scale is set by the virtuality $Q^2$ of the photon – one cannot trigger directly on hard reactions in $pA$ collisions by varying the momentum of the proton projectile. As discussed in Sec. 2.2 one can only increase the probability of a hard interaction by increasing the proton momentum, cf. Fig. 2.7. However, one can study the FSI of particles produced in soft and hard interactions by looking at different observables. For example, particles with a large momentum component transverse to the beam direction are predominantly produced in hard scattering events. High-energy proton-nucleus scattering therefore provides us with a supplemental tool to investigate hadron formation. A simultaneous analysis of the available $pA$ and $\gamma^* A$ data at various energies within our model may help to distinguish between different hadronization scenarios.
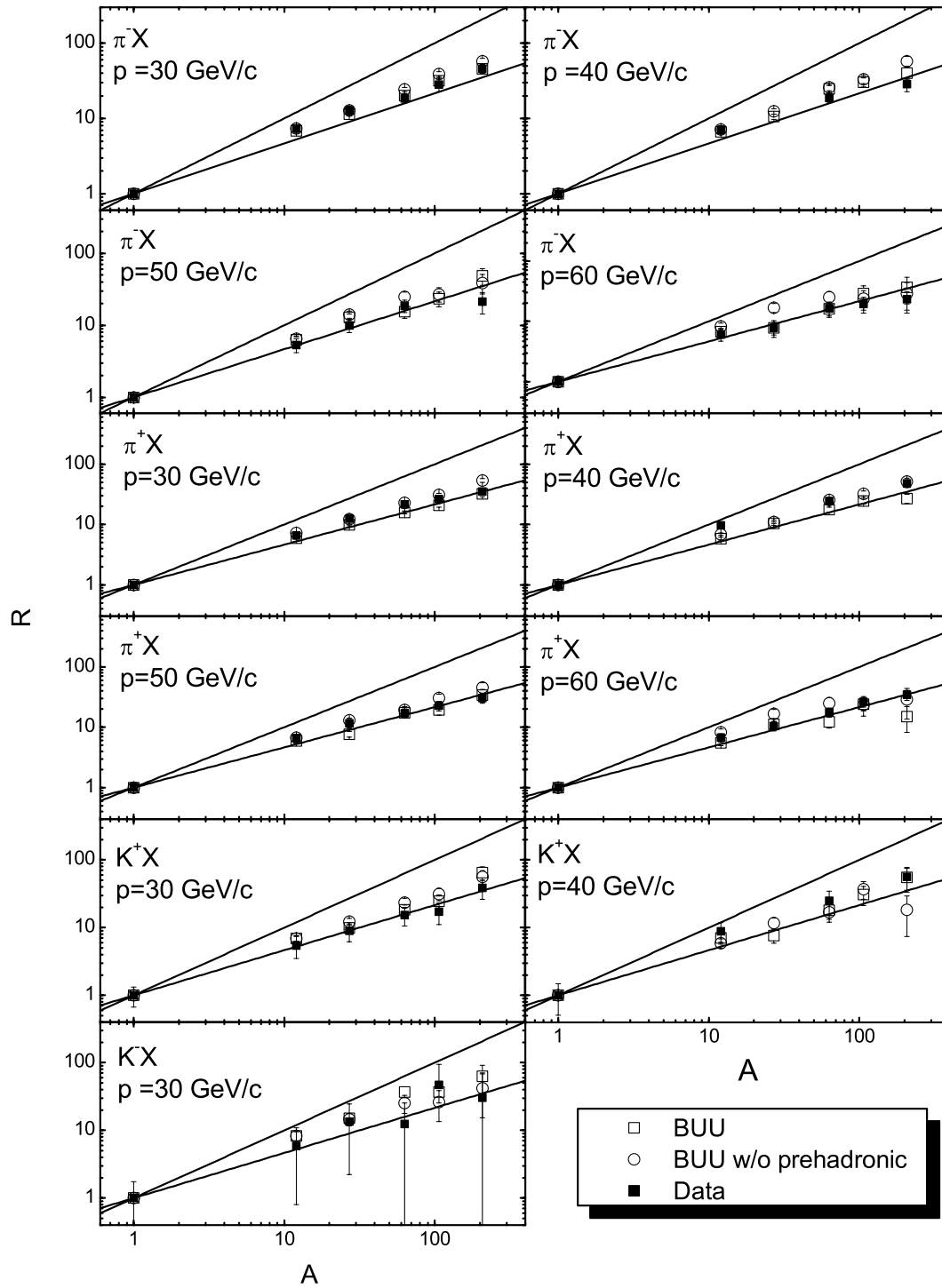
Figure 5.8: Ratio (5.36) of the inclusive invariant differential cross section for $\pi^{\pm}$ and $K^{\pm}$ production of 100 GeV protons on protons and nuclei which has been measured in Ref. [Ba83]. For all plots the transverse momentum of the observed mesons has to lie in the interval 0.2–0.4 GeV/$c$. The plots show calculations with (open squares) and without (open circles) prehadronic interactions (5.35) during the formation time $\tau_f = 0.5$ fm/$c$. The data (solid squares) are taken from Ref. [Ba83].

# Chapter 6

# Photon-nucleus and electron-nucleus interactions

In this chapter we discuss the interactions of real and virtual high-energy photons with complex nuclei. As already pointed out in Ref. [Kop96], these reactions offer a promising tool to study the physics of hadronization. Since the nucleus stays almost intact during the reaction, photon- and electron-induced reactions make it possible to study hadronization and prehadronic FSI in cold nuclear matter. The latter is essential before one tackles the problem of more complex reactions such as heavy-ion collisions where the system passes various phases of high densities and temperatures and where the collision geometry is much less under control. A further advantage of electron-induced reactions is that one can vary the energy $\nu$ and virtuality $Q^2$ of the photon independently of each other. This allows us to study the phenomenon of color transparency [Mue82, Bro82], i.e. the reduced interaction cross section of a small sized color singlet object. In the kinematic region where one is less sensitive to the resolved interactions of the virtual photon, the nuclear reactions are not contaminated by initial-state interactions which is an advantage compared to the use of hadronic projectiles. On the other hand, there is a kinematic regime where the resolved components of the photon interact coherently with many nucleons inside the nucleus and where the interactions of (virtual) photons show a striking similarity to hadron-induced reactions [Bau78, Don78].

Already in the late seventies electroproduction of hadrons from nuclei has been studied at SLAC [Osb78]. In the early nineties the European Muon Collaboration (EMC) [Ash91] and E665 [Ada94] have looked into the attenuation of fast hadrons in the scattering of high-energy muons on nuclear targets at CERN and FNAL.

In the past few years the HERMES collaboration has put a lot of effort in the study of $\pi^{\pm,0}$, $K^{\pm}$, $p$ and $\bar{p}$ production in deep inelastic scattering of a 27.6 GeV positron beam off nuclear gas targets. The HERMES experiments on nuclear targets are mainly concerned with the study of coherence-length and color-transparency effects in vector meson electroproduction [Ack99, Air03] and hadron attenuation in deep inelastic scattering off complex nuclei [Air01, Muc02, Gar02, Air03b]. Recently, Jefferson Lab has started similar experiments with a 5 GeV electron beam [Haf02, WBr02, KWa04] and there exists a proposal to repeat this investigation after the planned 12 GeV upgrade [WBr03].

This chapter is structured in the following way: In Sec. 6.1.1 we use Glauber theory to explain how the phenomenon of nuclear shadowing arises in photon- and electron-induced reactions off nuclei. In Sec. 6.1.2 we then demonstrate how one can account for such a quantum mechanical interference effect within our semi-classical BUU transport model. Coherence-length effects and color transparency in vector meson photo- and electroproduction are discussed in Sec. 6.2. Here we also compare our calculations with the HERMES results on exclusive incoherent $\rho^0$ electroproduction. In Sec. 6.3 we then demonstrate the importance of coupled-channel effects in more inclusive reactions like semi-inclusive meson photoproduction. The attenuation of pions, kaons, protons and antiprotons in deep inelastic scattering off complex nuclei is investigated in Sec. 6.4. We compare how the experimental HERMES and EMC data can distinguish between different space-time pictures of hadronization and give predictions for the kinematic region of the Jefferson Lab experiments.

# 6.1 Shadowing

In Chap. 3 we have discussed the resolved interactions of real and virtual photons. We have seen that – depending on its energy $\nu$ and virtuality $Q^2$ – the photon sometimes interacts not directly with the target nucleon but via one of its hadronic fluctuations. Depending on the time that the photon travels as such a fluctuation, one might expect similarities between photon-nucleus and hadron-nucleus interactions. In Chap. 5 we demonstrated that hadron-induced nuclear reactions are shadowed because the mean free path of the hadronic projectile is in general small compared to the size of the nucleus. As a result, the hadronic projectile primarily interacts with the nucleons on the front side of the nucleus which then shadow the downstream nucleons. If the distance $l_h$ that the photon travels as a hadronic fluctuation becomes larger than the mean free path $\lambda_h$ of the fluctuation inside the nuclear medium, one will expect shadowing also for $\gamma^* A$ reactions.

The distance that the photon travels as a hadronic fluctuation, i.e. the so-called coherence length $l_h$, can be estimated via Heisenberg's uncertainty principle. It is given by the inverse difference between the photon momentum $k$ and the momentum $k_h$ that the hadronic fluctuation would have if it was on its mass shell:

$$
\begin{aligned}
l_h &= |k - k_h|^{-1} \\
&= \left| k - \sqrt{\nu^2 - m_h^2} \right|^{-1} \\
&\approx \frac{2\nu}{Q^2 + m_h^2}
\end{aligned}
\tag{6.1}
$$

where the last expression is valid in the limit of high photon energies ($\nu^2 \gg m_h^2, Q^2$).

From Eq. (6.1) one sees that the onset energy of shadowing is determined by the lightest hadronic fluctuation, i.e. the $\rho^0$ which has the largest coherence length and a strong coupling to the photon. For a real photon with energy $\nu = 10$ GeV the coherence length of the $\rho^0$ fluctuation is 7 fm. This is not only larger than the mean free path of the $\rho^0$ in nuclear matter ($\lambda_\rho \approx 2.4$ fm) but also larger than the radii of heavy nuclei, cf. Tab. 5.1. It is therefore no surprise that at these energies the nuclear
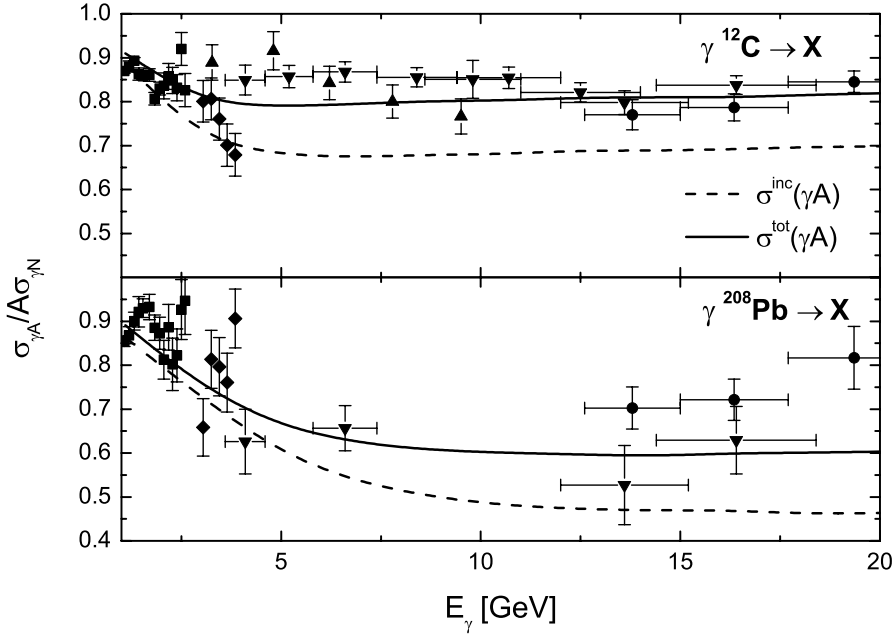
Figure 6.1: The nuclear photoabsorption cross section divided by $A\sigma_{\gamma N}$ plotted versus the photon energy $E_\gamma$. The solid line represents the result of Eq. (6.7). for the total photon nucleus cross section. The dashed line shows the contribution from incoherent reactions to $\sigma_{\gamma A}^{\text{tot}}$ and is calculated using Eq. (6.27). More than 90% of the difference between $\sigma_{\gamma A}^{\text{inc}}$ and $\sigma_{\gamma A}^{\text{tot}}$ is due to coherent $\rho^0$ photoproduction. The experimental data are taken from Refs. [Cal73, Brk73, Mic77, Ara78, Cal79].

photoabsorption cross section is smaller than $A$ times the nucleonic cross section. However, photoabsorption data [Bi96, Muc99] on C, Al, Cu, Sn and Pb display an early onset of the shadowing effect around $\nu = 1$ GeV. Substituting $m_\rho = 770$ MeV into Eq. (6.1) one finds that the $\rho^0$ coherence length of a 1 GeV photon is only 0.7 fm. This led to the interpretation [Bi99] of the low energy onset of shadowing as a signature of a decreasing $\rho^0$ mass in the nuclear medium since a decrease of the $\rho^0$ mass increases the coherence length $l_\rho$. As we have shown in Refs. [Fal00a, Fal00b, Fal01] and as we discuss at the end of Sec. 6.1.1, this interpretation is not necessarily correct.

In Sec. 6.1.1 we show how one can quantitatively understand the shadowing of high-energy photons within Glauber theory by relating the nuclear photoabsorption cross section via the optical theorem to the nuclear Compton forward-scattering amplitude. In order $\alpha_{\text{em}}$ one gets two contributions to this amplitude whose interference gives rise to nuclear shadowing.

Obviously, it is not straightforward to account for such a quantum mechanical interference effect within our semi-classical transport model. A first attempt was made in Refs. [Eff99a, Eff00]. In Sec. 6.1.2 we show how to implement the shadowing of the photon's different vector meson components in our BUU calculations.

When repeating the Glauber derivation of the total hadron-nucleus cross section (5.15) for photons, it is at first sight not clear why there should be a strong shadowing of

the total photon-nucleus cross section. Since every elastic $\gamma N$ scattering is suppressed by a factor $\alpha_{\rm em}$, the equivalent of the nuclear profile function (5.8) in order $\alpha_{\rm em}$ reads

$$\Gamma_A^{f0}(\vec{b}) = \delta_{f0} - \langle f|[1 - \sum_{i=1}^{A} \Gamma_\gamma(\vec{b} - \vec{s}_i)]|0\rangle.$$

Following the steps of Sec. 5.1.1, one can derive from this profile function the nuclear Compton forward-scattering amplitude in the independent-particle model:

$$
\begin{aligned}
F(\vec{0}) &= \frac{ik}{2\pi} \int d^2b \, \Gamma_A^{00}(\vec{b}) \\
&= \frac{ik}{2\pi} \int d^2b \, A \int dz \, \rho_1(\vec{b}, z) \frac{2\pi}{ik} f_\gamma(\vec{0}) \\
&= A f_\gamma(\vec{0})
\end{aligned}
\tag{6.2}
$$

where $f_\gamma$ denotes the Compton scattering amplitude on a nucleon. Using Eq. (6.2) in the optical theorem one gets

$$\sigma_{\gamma^*A} = A\sigma_{\gamma^*N} \tag{6.3}$$

and there seems to be no shadowing in photoabsorption up to order $\alpha_{\rm em}$. However, as can be seen from Fig. 6.1 the experimental data indicate shadowing corrections to the total $\gamma A$ cross section (6.3) as large as 20%–40%.

## 6.1.1   Shadowing in Glauber theory

The shadowing in $\gamma^*A$ reactions arises from Gribov's inelastic corrections that we already encountered as high-energy corrections to the total proton-nucleus cross section in Sec. 5.3.1. The amplitude (6.2) which leads to the unshadowed cross section corresponds to processes where the photon scatters off a single nucleon inside the nucleus (see left-hand side of Fig. 6.2). There is, however, a second amplitude in order $\alpha_{\rm em}$ which is shown on the right-hand side of Fig. 6.2. Here the photon diffractively produces a hadronic state $X$ on a nucleon at position $z_1$ which propagates through the nucleus to a nucleon at position $z_2$ and scatters into the outgoing photon.

We can derive the complete nuclear profile function for nuclear Compton scattering by following the steps that lead to Eq. (H.5) in Appx. H. Neglecting all terms that are of order $\alpha_{\rm em}^2$ or higher we obtain

$$
\Gamma^{f0}(\vec{b}) = \delta_{f0} - \langle f|\Big\{[1 - \sum_{i=1}^{A} \Gamma_\gamma(\vec{b} - \vec{s}_i)] \tag{6.4}
$$

$$
+ \sum_X \sum_{i,j}^{A} \Gamma_{\gamma X}(\vec{b} - \vec{s}_i)\Gamma_{X\gamma}(\vec{b} - \vec{s}_j)e^{iq_X(z_i - z_j)}\Theta(z_j - z_i)
$$

$$
\times \prod_{k \neq i,j}^{A} [1 - \Gamma_X(\vec{b} - \vec{s}_k)]\Theta(z_j - z_k)\Theta(z_k - z_i)\Big\}|0\rangle \tag{6.5}
$$

where the profile functions $\Gamma_\gamma$ and $\Gamma_X$ are the Fourier transforms of the elastic $\gamma N$ and $XN$ scattering amplitudes and $\Gamma_{\gamma X} = \Gamma_{X\gamma}$ denotes the Fourier transform of the
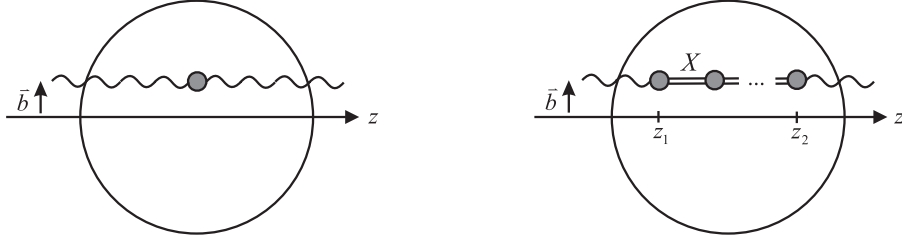
Figure 6.2: The two amplitudes of order $\alpha_{em}$ that contribute to the nuclear Compton amplitude. The left amplitude corresponds to a process where the photon scatters on a single nucleon. The right amplitude is also of order $\alpha_{em}$. Here the photon diffractively produces a hadronic state $X$ at position $z_1$ that propagates at fixed impact parameter $\vec{b}$ (eikonal approximation) through the nucleus. At position $z_2$ the hadronic state scatters back into the outgoing photon. In case of forward scattering the incoming and outgoing photon have equal energy and momentum and the nucleus is still in its ground state. The interference of the two amplitudes of order $\alpha_{em}$ gives rise to shadowing.

diffractive photoproduction amplitude $f_{\gamma X}$:

$$\Gamma_{\gamma X}(\vec{b}) = \frac{1}{2\pi i k_X} \int d^2 q_T e^{i\vec{q}_T \cdot \vec{b}} f_{\gamma X}(\vec{q}_T).$$

As explained in Appx. H, the momentum transfer

$$q_X = k - k_X \tag{6.6}$$

arises from putting the diffractive state $X$ on its mass shell and is just the inverse of the coherence length $l_X$. In $hA$ collisions the effect of the inelastic corrections is relatively small because the forward-scattering amplitude $XN \to XN$ is of the same magnitude as the scattering $NN \to NN$. Obviously, this is no longer the case for $\gamma A$ collisions since $\Gamma_\gamma$ is smaller than $\Gamma_X$ by a factor of $\alpha_{em}$.

Like in Sec. 5.1.1 we can make use of the independent-particle model and the optical theorem to calculate the photoabsorption cross section from the nuclear profile function (6.4):

$$
\begin{aligned}
\sigma_{\gamma^* A} &= A\sigma_{\gamma^* N} + \sum_X \frac{8\pi^2}{k k_X} \text{Re}\left\{ f_{\gamma X}(\vec{0}) f_{X\gamma}(\vec{0}) \int d^2 b \int_{-\infty}^{+\infty} dz_1 \int_{z_1}^{+\infty} dz_2 \, \rho(\vec{b}, z_1)\rho(\vec{b}, z_2) \right. \\
&\quad \left. \times e^{iq_X(z_1 - z_2)} \exp\left[ -\frac{1}{2}\sigma_{XN}(1 - i\alpha_X) \int_{z_1}^{z_2} dz' \, \rho(\vec{b}, z') \right] \right\}
\end{aligned} \tag{6.7}
$$

where $\alpha_X$ denotes the ratio of real and imaginary part of the $XN$ forward-scattering amplitude.

According to Eqs. (6.1) and (6.6), a small coherence length $l_X$ corresponds to a large momentum transfer $q_X$. To contribute to the forward-scattering amplitude, the nucleus has to remain in its ground state and large momentum transfers are suppressed by the elastic form factor of the nucleus. This can also be seen in Eq. (6.7) where a large value of $q_X$ leads to a rapidly oscillating factor in the integral and, hence, a vanishing

contribution to the shadowing correction. Therefore, only the intermediate states $X$ with a large coherence length contribute to shadowing. For real photons these are the low lying vector mesons $\rho^0$, $\omega$, $\phi$ and $J/\psi$. As discussed for example in Ref. [Pil00], shadowing of the $q\bar{q}$ continuum, i.e. the GVMD part of the photon, becomes important for virtual photons and gives rise to the EMC effect [EMC83, Arn94] at small Bjorken $x$.

From Eq. (6.7) we see that for very large $q_X$ the second term on the right-hand side contributes most if $z_1 \approx z_2$, that is when the first and the last nucleon in the scattering process are approximately at the same position. Replacing the product of one-particle densities by the two-particle density

$$\rho(z_1, \vec{b})\rho(z_2, \vec{b}) \rightarrow \rho_2(\vec{b}, z_1, z_2) = \rho(z_1, \vec{b})\rho(z_2, \vec{b}) + \Delta(\vec{b}, |z_1 - z_2|), \qquad (6.8)$$

as proposed in Ref. [Bof96b], avoids such unphysical contributions. Since for $z_1 \approx z_2$ the last exponential in (6.7) is approximately one, consideration of correlations between the first and the last nucleon should be sufficient. For the two-body correlation function $\Delta$ we use the same Bessel function parametrization as in Ref. [Bof96b]:

$$\Delta(\vec{b}, |z_1 - z_2|) = -j_0(q_c|z_1 - z_2|)\rho(z_1, \vec{b})\rho(z_2, \vec{b})$$

with $q_c = 780$ MeV.

For real photons and in the kinematic regime of the HERMES and Jefferson Lab experiments we can restrict the sum in (6.7) to the vector mesons $V = \rho^0, \omega, \phi, J/\psi$. The amplitudes $f_{\gamma V}$ are related to the vector meson-nucleon forward-scattering amplitudes via VMD:

$$f_{\gamma V}(\vec{0})f_{V\gamma}(\vec{0}) = \frac{e^2}{g_V^2}F_V^2(Q^2)f_V^2(\vec{0}) \qquad (6.9)$$

where we have used the VMD coupling constants from Tab. 3.1 and the form factor (4.35) for virtual photons. The $VN$ forward-scattering amplitudes can be extracted from the total $VN$ cross sections using the optical theorem

$$f_V(\vec{0}) = \frac{ik_V}{4\pi}\sigma_{VN}(1 - i\alpha_V). \qquad (6.10)$$

Except for the $J/\psi$ we use the parameterizations of Ref. [Bau78] for the calculation of the shadowing effect:

$$\sigma_{\rho^0 N} \approx \sigma_{\omega N} = 20.8 \left(1 + \frac{0.766}{\sqrt{k_{\rho,\omega}/\text{GeV}}}\right) \text{ mb} \qquad (6.11)$$
$$\sigma_\phi \approx 12 \text{ mb}$$

and

$$\alpha_{\rho^0} = \alpha_\omega = -\frac{0.766}{\sqrt{k_{\rho,\omega}/\text{GeV}} + 0.766} \qquad (6.12)$$
$$\alpha_\phi = 0.$$

At high energies these total cross sections agree within 10% with the parametrizations (3.5) and, as we have shown in Ref. [Fal00b], the use of (6.11) together with the real

part (6.12) ensures a perfect description of the shadowing effect in photoabsorption down to the onset energy of about 1 GeV. For the total $J/\psi$ cross section we use the same parametrization as in Eq. (3.5) and neglect the real part of the forward-scattering amplitude. The solid line in Fig. 6.1 shows the resulting ratio $\sigma_{\gamma A}/A\sigma_{\gamma N}$ as a function of the photon energy $E_\gamma$. As one can see, our approach yields a good description of shadowing in photoabsorption.

As we explain in Ref. [Fal00b], it is the negative real part of the production amplitude $f_{\gamma\rho}$ which leads to the early onset of the shadowing effect in nuclear photoabsorption. At high energies the scattering amplitudes are dominated by their imaginary part [WW74]. However, experiments [Alv70, Alv71, Big71] show that for energies of about 4 and 6 GeV the real part of the $\rho N$ forward-scattering amplitude is negative and already of the same order of magnitude as its imaginary part. Dispersion theoretical calculations [Ele97, Kon98] indicate that this is also the case in the onset region of shadowing. A negative real part indeed leads to a positive mass shift of the $\rho$ in medium as pointed out by Eletsky and Ioffe [Ele97]. As discussed in Ref. [Fal00b], this positive mass shift diminishes the shadowing effect. This is understandable since a larger $\rho$ mass corresponds to a smaller coherence length. The reduction arises from the $\alpha_\rho$ in the last exponential of Eq. (6.7) which accounts for mass changes of the propagating $\rho^0$ through multiple scattering in the medium. However, $\alpha_\rho$ also enters the prefactor $f_{\gamma\rho}f_{\rho\gamma}$ via (6.9) and (6.10) and thereby increases shadowing. In total, this leads to an enhancement of the shadowing effect in combination with an increased $\rho$ meson mass in nuclear medium at large momenta, which is in agreement with dispersion theoretical analyses.

Finally, we point out that some of the assumptions that are made in this simple model of shadowing, like the validity of the eikonal approximation and the neglect of the finite width of the $\rho^0$ meson become questionable at low energies. In Ref. [Fal01] we therefore used a multiple scattering approach [Gri70, Ber72, We76] that we consider as more reliable in the shadowing onset region. Within this approach we account for the vacuum self energy of the $\rho^0$ and include scattering processes in non-forward direction. We find that the latter allows for a new contribution to nuclear shadowing in photoabsorption at low energies, namely the production of $\pi^0$ as intermediate hadronic states. Since neutral pions cannot be produced in the forward direction without excitation of the nucleus they do not contribute in calculations based on the eikonal approximation.

## 6.1.2   Shadowing in BUU

From the last section it should have become clear that shadowing is a quantum mechanical interference effect which is not reproduced by our semi-classical BUU transport model. If we want to describe high-energy photo- and electroproduction we therefore have to build shadowing explicitly into our model.

In Ref. [Eff99a] shadowing was accounted for by multiplying the statistical weight $\sigma_{\gamma N}/A$ of each perturbative particle created in a $\gamma N$ interaction at position $\vec{r}$ inside the nucleus with a position- and energy-dependent shadowing factor:

$$s_{\mathrm{old}}(\vec{r}) = 1 - \frac{S_{\mathrm{old}}(\vec{r})}{\sigma_{\gamma N}}$$

where $S_{\text{old}}(\vec{r})$ was directly read off the nuclear photoabsorption cross section (6.7):

$$
\begin{aligned}
S_{\text{old}}(\vec{b}, z) = & \sum_V \frac{8\pi^2}{k k_V} \text{Re} \Bigg\{ f_{\gamma V}(\vec{0}) f_{V\gamma}(\vec{0}) \int_{-\infty}^{z} dz_1 \, \rho_2(\vec{b}, z_1, z) \\
& \times e^{iq_V(z_1 - z)} \exp\left[ -\frac{1}{2} \sigma_{VN}(1 - i\alpha_V) \int_{z_1}^{z} dz' \, \rho(\vec{b}, z') \right] \Bigg\}. \quad (6.13)
\end{aligned}
$$

This simple recipe cannot be correct for two reasons: First, it has the wrong normalization, i.e. it equates the $\gamma A$ reaction cross section in the BUU simulation with the total nuclear photoabsorption cross section (6.7). However, the total nuclear photoabsorption also includes coherent reactions[1] such as coherent vector meson production $\gamma A \rightarrow V A$. These events are missing in the BUU simulation and therefore their cross sections must be added at the end. The second phenomenon which Eq. (6.13) can obviously not account for is that different reactions are effected differently by shadowing. One expects that reactions which are mainly triggered by the $\rho^0$ component of the photon, e.g. diffractive $\rho^0$ production $\gamma N \rightarrow \rho^0 N$, are strongly reduced while direct interactions are not influenced at all by the nuclear environment. In Refs. [Fal02, Fal03b] we developed a new method which is capable to account for these effects.

We express the physical photon state $|\gamma\rangle$ in terms of the vector meson states $|V\rangle$ and a state $|\gamma_0\rangle$ which consists of the pointlike photon and the GVMD part. This makes sense if one assumes that the GVMD part does not get shadowed because of its smaller coherence length or as in our case is unimportant for kinematic reasons:

$$
|\gamma\rangle = \left( 1 - \sum_{V=\rho, \omega, \phi, J/\Psi} \frac{e^2}{2g_V^2} F_V^2 \right) |\gamma_0\rangle + \sum_{V=\rho, \omega, \phi, J/\Psi} \frac{e}{g_V} F_V |V\rangle. \quad (6.14)
$$

The formfactor is taken from Eq. (4.35) and, as discussed in Sec. 3.2, also accounts for contributions of longitudinal photons.

For a photon with momentum $k\vec{e}_z$ the wave function of the component $V$ can be written as

$$
\psi_V^{(0)}(\vec{b}, z) = \chi(\vec{b}) e^{ikz}. \quad (6.15)
$$

On the way through the nucleus the vector meson components get modified. Consider an ensemble of $A$ nucleons at positions $\{\vec{r}_i\} = \{(\vec{s}_i, z_i)\}$ which are labeled in such a way that $z_1 < z_2 < ... < z_A$. According to the Glauber model discussed in Sec. 5.1.1 the wave function $\psi_V$ behind the first nucleon looks like

$$
\begin{aligned}
\psi_V^{(1)}(\vec{b}, z) = & \ \psi_V^{(0)}(\vec{b}, z) - \Gamma_V(\vec{b} - \vec{s}_1)\psi_V^{(0)}(\vec{b}, z_1)e^{ik_V(z - z_1)} \quad (6.16) \\
= & \ \chi(\vec{b}) \left( e^{ikz} - \Gamma_V(\vec{b} - \vec{s}_1)e^{iq_V z_1} e^{ik_V z} \right)
\end{aligned}
$$

if one neglects off-diagonal scattering from one vector meson component into another (diagonal approximation). The phase factor in the second term arises from putting the vector meson component on its mass shell, i.e. $k_V = \sqrt{\nu^2 - m_V^2}$ and $q_V = k - k_V$ is the corresponding momentum transfer. According to Eq. (5.3) the profile function $\Gamma_V$

---

[1]By *coherent* we mean that the nucleus as a whole participates in the production process, i.e. it remains in its ground state and absorbs the total momentum transfer.

is related to the elastic vector meson nucleon scattering amplitude $f_V$ in the following way:

$$\Gamma_V(\vec{b}) = \frac{1}{2\pi i k_V} \int d^2 q_T e^{i\vec{q}_T \cdot \vec{b}} f_V(\vec{k}_t).$$ (6.17)

After passing the second nucleon, the wave function takes on the form

$$\psi_V^{(2)}(\vec{b}, z) = \chi(\vec{b}) \left( e^{ikz} - \Gamma_V(\vec{b} - \vec{s}_2) e^{iq_V z_2} e^{ik_V z} - \Gamma_V(\vec{b} - \vec{s}_1)[1 - \Gamma_V(\vec{b} - \vec{s}_2)] e^{iq_V z_1} e^{ik_V z} \right).$$ (6.18)

At position $z$ the whole ensemble of $A$ nucleons has led to the modification

$$
\begin{aligned}
\psi_V^{(A)}(\vec{b}, z) &= \chi(\vec{b}) \Bigg( e^{ikz} - \sum_{j=1}^{A} \Gamma_V(\vec{b} - \vec{s}_j) e^{iq_V z_j} \\
&\quad \times \prod_{k \neq j}^{A} \left[ 1 - \Gamma_V(\vec{b} - \vec{s}_k) \Theta(z_k - z_j) \right] \Theta(z - z_k) e^{ik_V z} \Bigg) \\
&= \Bigg\{ 1 - \sum_{j=1}^{A} \Gamma_V(\vec{b} - \vec{s}_j) e^{iq_V(z_j - z)} \\
&\quad \times \prod_{k \neq j}^{A} \left[ 1 - \Gamma_V(\vec{b} - \vec{s}_k) \Theta(z_k - z_j) \right] \Theta(z - z_k) \Bigg\} \psi_V^{(0)}(\vec{b}, z) \\
&= \left\{ 1 - \Gamma_V^{(A)}(\vec{b}, z; \{\vec{r}_i\}) \right\} \psi_V^{(0)}(\vec{b}, z).
\end{aligned}
$$ (6.19)

Hence, the physical photon state changes on its way through the nucleus to position $\vec{r} = (\vec{b}, z)$ according to

$$|\gamma(\vec{r})\rangle = \left( 1 - \sum_{V = \rho, \omega, \phi, J/\Psi} \frac{e^2}{2 g_V^2} F_V^2 \right) |\gamma_0\rangle + \sum_{V = \rho, \omega, \phi, J/\Psi} \frac{e}{g_V} F_V \left( 1 - \overline{\Gamma_V^{(A)}}(\vec{r}) \right) |V\rangle$$ (6.20)

where the nuclear profile function from (6.19) must be averaged over the positions of the nucleons in the nucleus

$$
\begin{aligned}
\overline{\Gamma_V^{(A)}}(\vec{b}, z) &= \langle 0 | \Gamma_V^{(A)}(\vec{b}, z; \{\vec{r}_i\}) | 0 \rangle \\
&= \int_{-\infty}^{z} dz_i \rho(\vec{b}, z_i) \frac{\sigma_{VN}}{2} (1 - i\alpha_V) e^{iq_V(z_i - z)} \\
&\quad \times \exp\left[ -\frac{1}{2} \sigma_{VN}(1 - i\alpha_V) \int_{z_i}^{z} dz_k \rho(\vec{b}, z_k) \right].
\end{aligned}
$$ (6.21)

To get to the second line of Eq. (6.21) we have followed the procedure of Sec. 5.1.1, i.e. making use of the independent-particle model and the large $A$ limit and using the optical theorem to express the elastic forward scattering amplitude in terms of the total $VN$ cross section $\sigma_V$:

$$f_V(\vec{0}) = \frac{ik_V}{4\pi} \sigma_V (1 - i\alpha_V).$$ (6.22)

As before the nucleon number density is denoted by $\rho(\vec{r})$ and normalized to $A$. If we want to account for two-body correlations (6.8) such as in photoabsorption we simply have to make the replacement

$$\rho(\vec{b}, z_i) \rightarrow \rho(\vec{b}, z_i)(1 - j_0(q_c|z_i - z|)) \tag{6.23}$$

in Eq. (6.21).

Neglecting any influence of the FSI, the reaction amplitude for the process $\gamma N \rightarrow f$ on a nucleon at position $\vec{r}$ inside a nucleus changes compared to the vacuum due to these 'initial-state interactions' of the photon:

$$\langle f|\hat{T}|\gamma\rangle \rightarrow \langle f|\hat{T}|\gamma(\vec{r})\rangle. \tag{6.24}$$

By comparing Eqs. (6.14) and (6.20), one sees that to account for shadowing in incoherent photoproduction one only has to multiply the amplitude of each vector meson states $|V\rangle$ by the corresponding factor $\left(1 - \overline{\Gamma_V^{(A)}(\vec{r})}\right)$. In the numerical realization we simply modify the corresponding VMD coupling constants in the PYTHIA generator depending on the position of the $\gamma N$ interaction inside the nucleus:

$$\frac{e^2}{g_V^2} \rightarrow \frac{e^2}{g_V^2} \left|1 - \overline{\Gamma_V^{(A)}(\vec{r})}\right|^2. \tag{6.25}$$

The cross section for the photon to react with nucleon $j$ at position $\vec{r}$ inside the nucleus can be deduced via (6.20) and (6.24) from the optical theorem:

$$\sigma_{\gamma N}(\vec{r}) = \left(1 - \sum_{V=\rho,\omega,\phi} \frac{e^2}{2g_V^2} F_V^2\right)^2 \sigma_{\gamma_0 N} + \sum_{V=\rho,\omega,\phi} \left(\frac{e}{g_V}\right)^2 F_V^2 \left|1 - \overline{\Gamma_V^{(A)}(\vec{r})}\right|^2 \sigma_{VN}. \tag{6.26}$$

Like for the photon in vacuum, each term gives the relative weight for the corresponding photon component to interact with the nucleon. When integrated over the whole nucleus one gets from Eq. (6.26) the total incoherent photonuclear cross section

$$\sigma_{\gamma A}^{\text{inc}} = \int d^3r \, \rho(\vec{r})\sigma_{\gamma N}(\vec{r}) \tag{6.27}$$

which is shown in Fig. 6.1 by the dashed line together with the total nuclear photoabsorption cross section (6.7). More than 90% of the difference between those two cross sections stems from coherent $\rho^0$ photoproduction, whose contribution has been calculated within Glauber theory in Refs. [Hüf96, Fal00a]:

$$
\begin{aligned}
\sigma_{\gamma A \rightarrow \rho^0 A} &= \sigma_{\gamma N \rightarrow \rho^0 N} \left\{ \frac{1}{4} \frac{(\sigma_{\rho^0 N})^2}{\sigma_{\rho^0 N}^{\text{el}}} \int d^2b \left| \int_{-\infty}^{+\infty} dz \, \rho(\vec{b}, z) e^{iq_V z} e^{-\frac{1}{2}\sigma_{\rho^0 N} \int_z^\infty dz' \rho(\vec{b}, z')} \right|^2 \right\} \\
&\approx \frac{1}{4} \left(\frac{e}{g_\rho}\right)^2 (\sigma_{\rho^0 N})^2 \int d^2b \left| \int_{-\infty}^{+\infty} dz \, \rho(\vec{b}, z) e^{iq_V z} e^{-\frac{1}{2}\sigma_{\rho^0 N} \int_z^\infty dz' \rho(\vec{b}, z')} \right|^2. \tag{6.28}
\end{aligned}
$$

In the second step we have used the VMD relation (3.4) between the diffractive $\rho^0$ photoproduction amplitude and the elastic $\rho^0 N$ scattering amplitude.
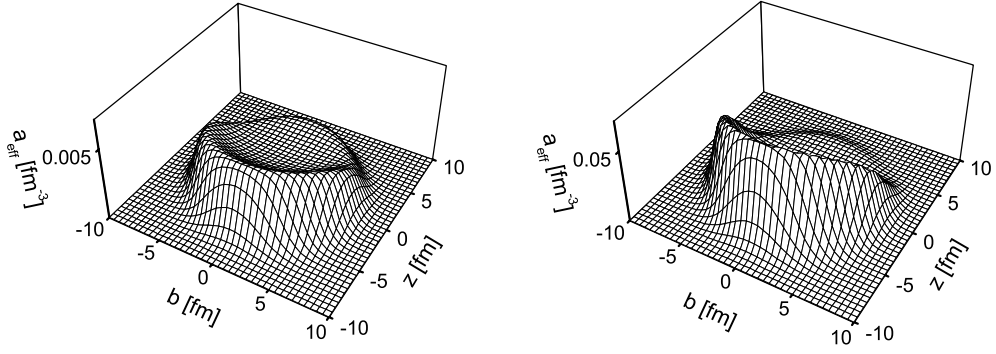
Figure 6.3: The number density of nucleons that react with the $\phi$ component (*left side*) and $\rho^0$ component (*right side*) of a real 20 GeV photon for $^{208}$Pb calculated using Eq. (6.29). In both cases the nucleons on the front side of the nucleus shadow the downstream nucleons. This effect is stronger for the $\rho^0$ component because of its larger nucleonic cross section.

Eq. (6.27) provides us with the new shadowing factor for the perturbative test particles:

$$s_{\mathrm{new}}(\vec{r}) = \frac{\sigma_{\gamma N}(\vec{r})}{\sigma_{\gamma N}}.$$

Hence, in addition to the replacement (6.25) which determines the composition of the physical photon at position $\vec{r}$ inside the nucleus each perturbative test particle now gets the statistical weight $\sigma_{\gamma N}(\vec{r})/A$.

In Fig. 6.3 we show how strongly the $\rho^0$ and the $\phi$ components of a real 20 GeV photon are separately shadowed in $^{208}$Pb. We plot the number density of the nucleons reacting with the $V$ components of the photon

$$a_{\mathrm{eff}}^V(\vec{r}) = \rho(\vec{r}) \frac{1}{\sigma_{\gamma N}} \left( \frac{e}{g_V} \right)^2 \left| 1 - \overline{\Gamma_V^{(A)}(\vec{r})} \right|^2 \sigma_{VN} \qquad (6.29)$$

as a function of $\vec{r}$. One clearly sees that due to its smaller nucleonic cross section the $\phi$ component is less shadowed than the $\rho^0$ component at the backside of the nucleus. As a consequence strangeness production (e.g. $K$ photoproduction), where the primary reaction is preferably triggered by the $\phi$ component of the photon, is less shadowed than, e.g. $\pi$ photoproduction. This dependence of the strength of shadowing on the reaction type is new compared to the treatment of shadowing in Ref. [Eff00] and can also be seen directly from the second amplitude in Fig. 6.4 because of the occurrence of the scattering process $VN \to XN$ at nucleon $j$.

Finally, we compare our method of describing shadowing of incoherent electroproduction with conventional Glauber results. We therefore calculate the incoherent vector meson electroproduction cross section off a nucleus and assume purely absorptive FSI
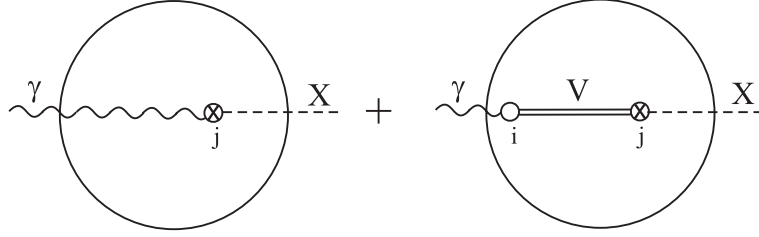
Figure 6.4: The two amplitudes of order $\alpha_{\rm em}$ that contribute to incoherent meson photoproduction in simple Glauber theory. The left amplitude alone would lead to an unshadowed cross section. Its interference with the right amplitude gives rise to shadowing.

for the moment. After averaging over all positions $\vec{r} = (\vec{b}, z)$ we get:

$$
\sigma_{\gamma A \to V A^*} = \sigma_{\gamma N \to V N} \int d^2 b \int\limits_{-\infty}^{\infty} dz\, \rho(\vec{b}, z) \Bigg| 1 - \int\limits_{-\infty}^{z} dz_i\, \rho(\vec{b}, z_i) \frac{\sigma_{VN}}{2} (1 - i\alpha_V)
$$
$$
\times e^{i q_V (z_i - z)} \exp\left[ -\frac{1}{2} \sigma_{VN}(1 - i\alpha_V) \int\limits_{z_i}^{z} dz_k\, \rho(\vec{b}, z_k) \right] \Bigg|^2
$$
$$
\times \exp\left[ -\sigma_{VN}^{\rm inel} \int\limits_{z}^{\infty} dz'\, \rho(\vec{b}, z') \right] . \tag{6.30}
$$

In (6.30) we again neglect off-diagonal scattering, i.e. $V$ production is triggered by the $V$ component of the photon only. The last factor in (6.30) includes the inelastic $VN$ cross section $\sigma_{VN}^{\rm inel}$ and accounts for the FSI.

The production process described by Eq. (6.30) is illustrated in Fig. 6.4: The incoherent vector meson production takes place on a nucleon $j$ at position $(\vec{b}, z)$. The production is triggered either directly by the photon or via an intermediate vector meson which was earlier produced on a nucleon at position $(\vec{b}, z_i)$ without excitation of the nucleus. The interactions of this vector meson on its way from $z_i$ to position $z$ are of optical potential type and leave the nucleus in its ground state. This propagation is described by the second exponential in (6.30). The interference between the direct and the indirect process leads to shadowing. The nucleus gets excited in the incoherent reaction at position $z$. The possibility that the vector meson is lost on its way from position $z$ out of the nucleus is taken care of by the last exponential.

Expression (6.30) formally differs only slightly from the approximate result for the incoherent vector meson production cross section which is given without derivation in Ref. [Yen71]. The latter can be obtained by making the following replacements in (6.30):

$$
e^{i q_V (z_i - z)} \to e^{i q_V z_i}, \qquad \sigma_{VN}^{\rm inel} \to \sigma_{VN}. \tag{6.31}
$$

The last replacement simply means that one neglects the possibility of elastic $VN$ scattering whereas the occurrence of the different phase factor is unclear. The authors of

Ref. [Hüf96] have given a seemingly different result for incoherent $V$ electroproduction:

$$
\begin{aligned}
\sigma_{\gamma A \to V A^*} &= \sigma_{\gamma N \to V N} \int d^2 b \Bigg\{ \int\limits_{-\infty}^{+\infty} dz\, \rho(\vec{b}, z) e^{-\sigma_{VN}^{\text{inel}} T_z(\vec{b})} \\
&\quad + \frac{1}{2} \frac{\sigma_{VN}}{\sigma_{VN}^{\text{el}}} (\sigma_{VN}^{\text{inel}} - \sigma_{VN}^{\text{el}}) \int\limits_{-\infty}^{+\infty} dz_1\, \rho(\vec{b}, z_1) \int\limits_{z_1}^{+\infty} dz_2\, \rho(\vec{b}, z_2) \\
&\quad \times \cos\left[q_V(z_1 - z_2)\right] e^{-\frac{1}{2}(\sigma_{VN}^{\text{inel}} - \sigma_{VN}^{\text{el}}) T_{z_2}(\vec{b}) - \frac{1}{2}\sigma_{VN} T_{z_1}(\vec{b})} \\
&\quad - \frac{1}{4} \frac{(\sigma_{VN})^2}{\sigma_{VN}^{\text{el}}} \left| \int\limits_{-\infty}^{+\infty} dz\, \rho(\vec{b}, z) e^{iq_V z} e^{-\frac{1}{2}\sigma_{VN} T_z(\vec{b})} \right|^2 \Bigg\}
\end{aligned}
\tag{6.32}
$$

with $T_z(\vec{b}) = \int_z^\infty \rho(\vec{b}, z') dz'$ and $T(\vec{b}) = T_{z=-\infty}(\vec{b})$. In Ref. [Fal00a] we present a detailed derivation of (6.32) including a finite real part of the $VN$ scattering amplitude. Expression (6.32) can be interpreted as follows: The last term represents the coherent $V$ photoproduction cross section (6.28) which is subtracted from the inclusive $V$ photoproduction cross section to yield the incoherent part. In Appx. I we show that the physically more transparent expression (6.30) is mathematically identical to (6.32).

## 6.2   Incoherent $\rho^0$ production off nuclei

Exclusive vector meson photo- and electroproduction on nuclei is an ideal tool to study effects of the coherence length, formation time and color transparency. Exclusive $\rho^0$ electroproduction on a $^{14}$N target has been investigated by the HERMES collaboration [Ack99, Air03] at photon energies between 10 GeV and 20 GeV and virtualities $Q^2 \lesssim 5$ GeV$^2$.

In this section we study exclusive incoherent $\rho^0$ photoproduction off $^{208}$Pb for real 7 GeV photons as well as $\rho^0$ electroproduction off $^{14}$N and $^{84}$Kr in the energy regime of the HERMES experiment. In this kinematic regime the coherence length of the photon's $\rho^0$ component is large and quantum mechanical interference effects play an important role. In the last section we presented a method to account for this shadowing effect within our semi-classical BUU transport model by distinguishing between the 'initial-state interactions' of the photon that give rise to shadowing and the final-state interactions (FSI) of the produced particles. The coupled-channel treatment of the FSI in the transport model allows for a broader spectrum of FSI than the generally used Glauber theory. In addition, we can account for Fermi motion and Pauli blocking during the reaction and take the finite lifetime of unstable reaction products into account.

In the case of diffractive vector meson electroproduction ($\gamma^* N \to V N$) the virtual photon initially produces a colorless $q\bar{q}$ pair whose size is expected to decrease with increasing photon virtuality $Q^2$ [Kop01]. As long as the $q\bar{q}$ pair is very small, i.e. in the early stage of its evolution into the physical vector meson, it mainly reacts via its color dipole moment. This leads to a cross section that is quadratic in the $q\bar{q}$ pair's size. At large enough energies the $q\bar{q}$ pair is frozen in this small sized configuration over a distance that, because of time dilatation, can exceed the diameter of a nucleus. This

effect is expected to lead to a large nuclear transparency for vector meson production at large photon energy $\nu$ and virtuality $Q^2$ (color transparency). For a detailed review of color transparency see e.g. [Jai96] and references therein.

It is not clear whether the energy and the virtuality of the photon in the HERMES experiment is large enough to see an onset of color transparency. As we show in Sec. 6.2.2, we do not find evidence for a finite formation time of the produced vector meson. The $^{14}$N data for the transparency ratio as function of the coherence length is compatible with the assumption that the diffractively produced $\rho^0$ starts to interact with its full hadronic cross section right after its production.

Kopeliovich et al. [Kop01] point out that this might be an accidental consequence of the specific correlation between the $Q^2$ of the photon and the coherence length of the $\rho^0$ in the HERMES data. In their work a lightcone QCD formalism was used to incorporate formation and coherence-length effects in coherent and incoherent vector meson electroproduction. The evolution of the $q\bar{q}$ pair's size – due to the transverse motion of the quarks – and the related change of the interaction cross section during the propagation through the nuclear medium was described quantum mechanically within the lightcone Green-function technique. The absorption of the $q\bar{q}$ dipole was accounted for by an imaginary part of the potential in the Schrödinger equation. Like in conventional Glauber theory, complicated coupled-channel effect had to be neglected. In addition, the effect of gluon shadowing[2] was studied, but found to be negligible in the case of incoherent $\rho^0$ production at HERMES energies.

In Ref. [Kop01] the decrease of the transparency ratio due to the finite $\rho^0$ lifetime was discussed as well. This effect is automatically included within our transport model. In Sec. 6.2.1 we show within our coupled-channel calculation that the effects of side feeding in the FSI are unimportant because of the kinematic cuts of the HERMES experiment. Therefore, Glauber theory seems to be appropriate for these reactions. However, we find that for heavy nuclei the kinematic cuts lead to an additional reduction of the transparency ratio due to elastic FSI which scatter the produced particle out of the acceptance window. For heavy nuclei one therefore has to use a larger cross section than $\sigma_{\rho N}^{\text{inel}}$ in the last exponential of Eq. (6.30) to account for the additional attenuation of $\rho^0$ mesons due to elastic scattering and in-medium decay.

## 6.2.1  Color transparency vs. coupled channels

The calculations for meson production on nuclei are in general done within Glauber theory (cf. Eq. (6.32)). As already mentioned above, the FSI in Glauber theory are usually purely absorptive. This means that for the reaction $\gamma A \to \rho^0 A^*$ the primary reaction has to be $\gamma N \to \rho^0 N$. If one treats the FSI via an absorptive optical potential one gets an exponential damping $\sim \exp[-\sigma_{\rho N}^{\text{inel}} \int_{z_j}^{\infty} dz \rho(\vec{b}, z)]$ of the nuclear production cross section similar to Eq. (6.30).

Any change in the reaction probability of a hadron $h$ during its formation time

---

[2]In Glauber theory gluon shadowing arises from off-diagonal scattering into $q\bar{q}g$ intermediate states. However, these contributions to the Glauber multiple scattering series are suppressed by a large momentum transfer, i.e. small coherence length, similar to the GVMD states. Their contribution only becomes important for very small values of Bjorken $x$.
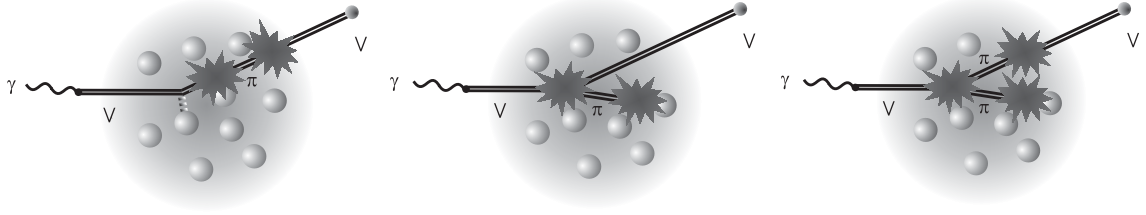
Figure 6.5: Coupled-channel effects that can mimic color transparency in $\rho^0$ photo-production by increasing the nuclear transparency ratio (6.33). *Left:* Regeneration. A primarily produced $\rho^0$ gets absorbed on a nucleon in the FSI. Thereby a pion is created which in an interaction with another nucleon produces a $\rho^0$ again. *Middle:* Inclusive $\rho^0$ production. There is a contribution to exclusive $\rho^0$ production on a nucleus from inclusive primary reactions $\gamma^* N \to \rho^0 X$ where only the $\rho^0$ escapes the nucleus. *Right:* Side feeding. A $\rho^0$ is produced in the FSI of some particle that was created in the primary $\gamma^* N$ reaction.

affects the so-called nuclear transparency

$$T_A = \frac{\sigma_{\gamma^* A \to hX}}{A \sigma_{\gamma^* N \to hX}} \tag{6.33}$$

if the formation length, i.e. the length that the hadron travels during its formation time, exceeds the average internucleon distance ($\approx 1.7$ fm) inside the nucleus.

Within Glauber theory a reduction of the $\rho N$ cross section due to color transparency leads to less attenuation in the FSI and, hence, to a larger transparency ratio (6.33). However, there exist coupled-channel effects which also enhance the nuclear transparency ratio and therefore mimic CT. They are shown in Fig. 6.5. The first effect is $\rho^0$ regeneration during the FSI. A $\rho^0$ which is absorbed in the FSI can be recreated later on in the FSI of another particle. In addition, there is the possibility of side feeding where there is no $\rho^0$ produced at all in the primary $\gamma^* N$ interaction and the $\rho^0$ emerges from the FSI of the primary reaction products. It turns out that the most important effect which influences the nuclear transparency ratio (6.33) is inclusive $\rho^0$ production in the primary $\gamma^* N$ reaction where everything except the $\rho^0$ is absorbed in the FSI.

In Fig. 6.6 we show the results of our model for the mass differential cross section of incoherent, exclusive $\rho^0$ photoproduction on $^{208}$Pb for $E_\gamma = 7$ GeV. In this case 'exclusive' means that the final state consists of a $\pi^+ \pi^-$ pair and 208 bound nucleons. The solid line represents a calculation with the primary reaction restricted to $\gamma N \to \rho^0 N$. It already includes the effects of shadowing, Fermi motion, Pauli blocking and the nucleon potential, but no FSI. The dotted line shows the effect of the FSI without a formation time of the $\rho^0$ in $\gamma N \to \rho^0 N$. The Glauber model yields quantitatively the same effect of the FSI. This means that in this case (only $\gamma N \to \rho^0 N$ as primary reaction) FSI processes like $\rho^0 N \to \pi N \to \rho^0 N$, where the primary $\rho^0$ gets absorbed first and is fed into the outgoing channel by a later FSI, are negligible.

If one assumes a formation time of $\tau_f = 0.8$ fm/$c$ for the $\rho^0$ and assumes no pre-hadronic interactions, one gets the result indicated by the dash-dotted line. Due to
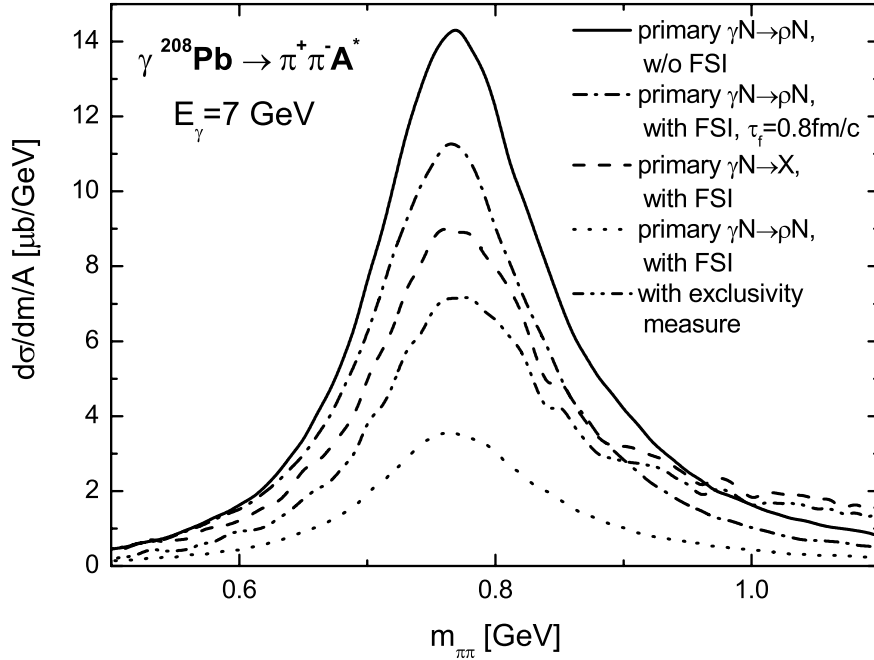
Figure 6.6: Mass differential cross section for exclusive $\rho^0$ production on $^{208}$Pb at $E_\gamma = 7$ GeV. The meaning of the different curves is explained in detail in the text. All the curves, except for the one with the explicitly given formation time $\tau_f = 0.8$ fm/$c$ have been calculated with $\tau_f = 0$. The fluctuations in the dashed and dash-dot-dotted curves are statistical only.

the finite formation time there is considerably less absorption and the nuclear production cross section increases. The neglect of the prehadronic interactions during the formation time $\tau_f$ can be interpreted as CT.

However, one will get a similar result with $\tau_f = 0$ if one allows for other primary reactions besides $\gamma N \to \rho^0 N$ and uses a coupled channel model. This can be seen by looking at the dashed line in Fig. 6.6. We find that about 60% of the additional $\rho^0$ stem from inelastic $\rho^0$ production in the primary reaction, e.g. $\gamma N \to \rho^0 \pi N$ and $\gamma N \to \rho^0 \Delta$ where the $\pi$ gets absorbed during the FSI. Since these coupled-channel effects are usually neglected in Glauber theory one would be led to the wrong conclusion that the observed spectra is again due to CT effects.

We now apply an exclusivity measure like the one used in the HERMES experiment [Ack99]

$$-2 \text{ GeV} < \Delta E = \frac{p_X^2 - m_N^2}{2m_N} < 0.6 \text{ GeV}, \qquad (6.34)$$

where $m_N$ is the nucleon mass and

$$p_X = p_N + p_\gamma - p_\rho \qquad (6.35)$$

is the four-momentum of the undetected final state (cf. Fig. 6.7). Here $p_\gamma$ and $p_\rho$ denote the four-momenta of the incoming photon and the detected $\pi^+\pi^-$ pair and $p_N$ is the four-momentum of the struck nucleon which, for the calculation of $p_X$, is assumed to
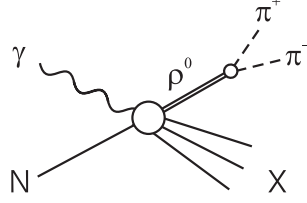
Figure 6.7: Inclusive $\rho^0$ photoproduction off a nucleon.

be at rest. Using (6.34) leads to a decrease of the cross section (dash-dot-dotted line in Fig. 6.6) because some of the inelastic primary events are excluded. If the exclusivity measure was good enough to single out only the elastic $\gamma N \to \rho^0 N$ reactions from the primary events, the dash-dot-dotted curve would coincide with the dotted line and Glauber theory would be applicable. Since this is not the case, one still extracts too large a formation time when using Glauber theory.

One therefore needs a further constraint in addition to the exclusivity measure (6.34) which becomes apparent by looking at the differential cross section $d\sigma/dt$ in Fig. 6.8; the meaning of the lines is as before. For $|t| > 0.1$ GeV$^2$, the full calculation with exclusivity measure (dash-dot-dotted line) gives the same result as the one with the primary reaction $\gamma N \to \rho^0 N$ and FSI (dotted line). In this kinematic regime Glauber theory can therefore be used. For $|t| < 0.1$ GeV$^2$, however, the exclusivity measure (6.34) cannot distinguish between elastic $\rho^0$ photoproduction ($\gamma N \to \rho^0 N$) and other primary reactions, e.g. inelastic $\rho^0$ photoproduction ($\gamma N \to \rho^0 X$, $X \neq N$). At low values of $|t|$ there exist many states $X$ with invariant masses which are not excluded by the exclusivity measure (6.34). In addition, we find that about 25% of the finally accepted $\rho^0$ in this $t$ region are not produced in the primary reaction but stem from side feeding in the FSI. In the HERMES experiment one makes a lower $|t|$ cut to get rid of the coherent $\rho^0$ photoproduction contribution. The Glauber expression for the differential coherent $\rho^0$ photoproduction cross section is [Yen71]

$$\frac{d\sigma_{\gamma A \to \rho^0 A}^{\text{coh}}}{dt} = \left. \frac{d\sigma_{\gamma N \to \rho^0 N}}{dt} \right|_{t=0}$$
$$\times \left| \int d^2 b \, dz \, \rho(\vec{b}, z) e^{i(\vec{q}_T \cdot \vec{b} + q_V z)} \exp\left[ -\frac{1}{2}\sigma_{\rho^0 N}(1 - i\alpha_\rho) T_z(\vec{b}) \right] \right|^2$$

where the four momentum squared is given by $t = -(\vec{q}_T^2 + q_V^2)$. For large enough values of $t$ the strongly oscillating exponential under the integral leads to a vanishing of the coherent photoproduction cross section. Note that this just reflects the suppression of large momentum transfers by the elastic formfactor of the nucleus because the nucleus has to remain in its ground state. In the case of lead and $E_\gamma = 7$ GeV the coherent part turns out to be negligible for $|t| \gtrsim 0.05$ GeV$^2$. However, to get rid of the coupled-channel effects one has to increase this threshold to approximately $|t| = 0.1$ GeV$^2$. Glauber theory can thus be trusted only under certain kinematic constraints.

In this section we have shown that it is necessary to have a reliable model of the FSI to extract the formation time from the production cross sections of high-energy photo- and electroproduction off nuclei. Whereas Glauber models allow for a straightforward
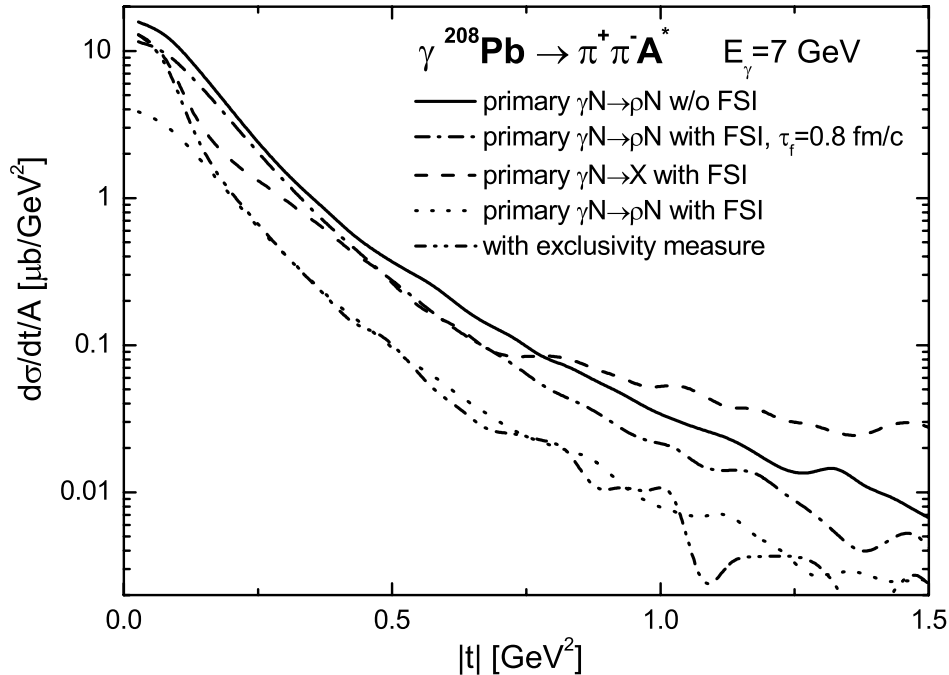
Figure 6.8: Calculated $\frac{d\sigma}{dt}$ for exclusive $\rho^0$ production on $^{208}$Pb at $E_\gamma = 7$ GeV. The meaning of the different curves is the same as in Fig. 6.6. The structures in the curves at large $|t|$ are statistical only.

implementation of the nuclear shadowing effect they usually have the disadvantage of a purely absorptive treatment of the FSI. In Sec. 6.3 we show that in particular the production of mesons with long mean free path will be affected by the coupled-channel effects in the FSI.

## 6.2.2   Color transparency vs. coherence-length effects

In this section we want to compare the results of our model with recent $\rho^0$ electroproduction data of the HERMES collaboration. Before we turn to nuclear targets we first verify that the input of our model is reasonable and look at exclusive $\rho^0$ production off hydrogen. We use the same kinematic cuts as in the HERMES experiment [Air00], i.e. the final state has to consist of two oppositely charged pions[3] with invariant mass between 0.6 GeV and 1 GeV. The four-momentum transfer $|t - t_{\max}|$ between the virtual photon and the $\pi^+\pi^-$ pair has to be smaller than 0.4 GeV$^2$ and we apply the exclusivity measure

$$\Delta E = \frac{p_X^2 - m_N^2}{2m_N} < 0.4 \text{ GeV}.$$

In Fig. 6.9 we compare our calculation of the exclusive $\rho^0$ production cross section off hydrogen with experimental data [Air00, Ada95, Cle69]. In the whole $Q^2$ region covered by the HERMES experiment we find very good agreement for a broad range of

---

[3]Nucleons with momenta below 1 GeV have been neglected.
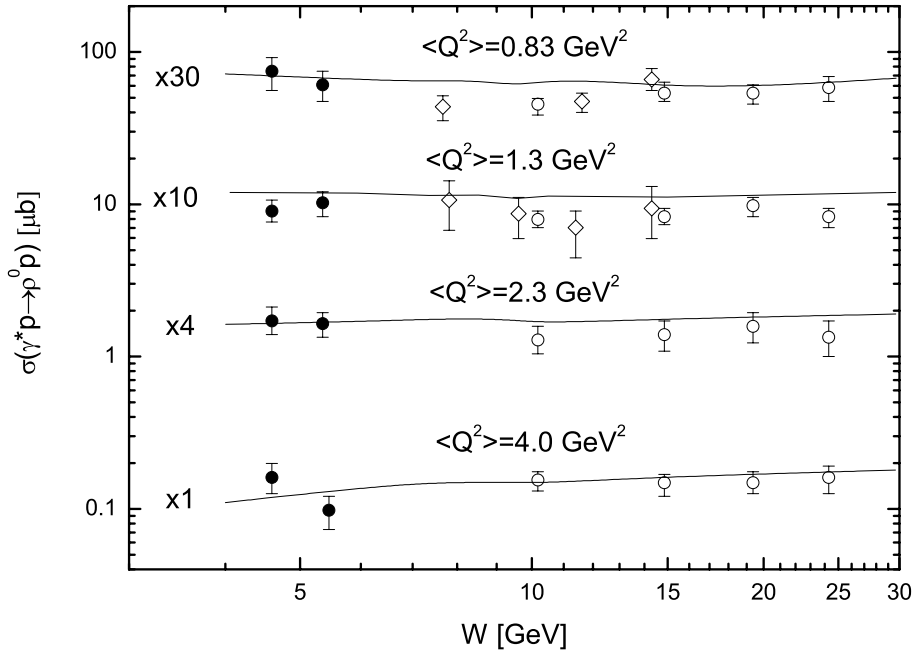
Figure 6.9: Calculated virtual photoproduction cross section for $\rho^0$ production versus invariant mass $W$ at average $Q^2$ values of 0.83, 1.3, 2.3 and 4.0 GeV$^2$. The data have been taken from the HERMES collaboration (filled circles) and E665 (open circles).

the invariant mass $W$ of the photon-nucleon system. Also the slope of the differential production cross section is reproduced very well by the PYTHIA model as can be seen from the solid line in Fig. 6.10 where we show our calculation of $d\sigma/dt(\gamma^*p \rightarrow \rho^0 p)$ together with the HERMES data.

For our calculations on exclusive $\rho^0$ electroproduction off nuclei we again use the kinematic cuts of the HERMES collaboration [Ack99]. This means that we restrict our exclusivity measure to the region

$$-2 \text{ GeV} < \Delta E < 0.6 \text{ GeV},$$

and introduce a lower boundary for the four-momentum transfer $|t - t_{\max}| > 0.09$ GeV$^2$ as imposed by the HERMES collaboration to get rid of coherently produced $\rho^0$. From the dashed line in Fig. 6.10 one sees that the differential $\rho^0$ electroproduction cross section off $^{14}$N is again in excellent agreement with the HERMES data. Throughout our calculations the effect of the nucleon potential turns out to be negligible. This is reasonable since the involved energies are much larger than the typical binding energies which are in the order of a few MeV. A combined effect of Fermi motion and Pauli blocking on the incoherent differential production cross section is visible at $|t - t_{\max}| < 0.1$ GeV$^2$. At $|t - t_{\max}| \approx 0.05$ GeV$^2$ the differential cross section is about 25% smaller than the calculation without Fermi motion and Pauli blocking (dotted curve). The reason for this reduction is that in the case that the bound nucleon moves towards the incoming photon, the outgoing nucleon might be Pauli blocked for
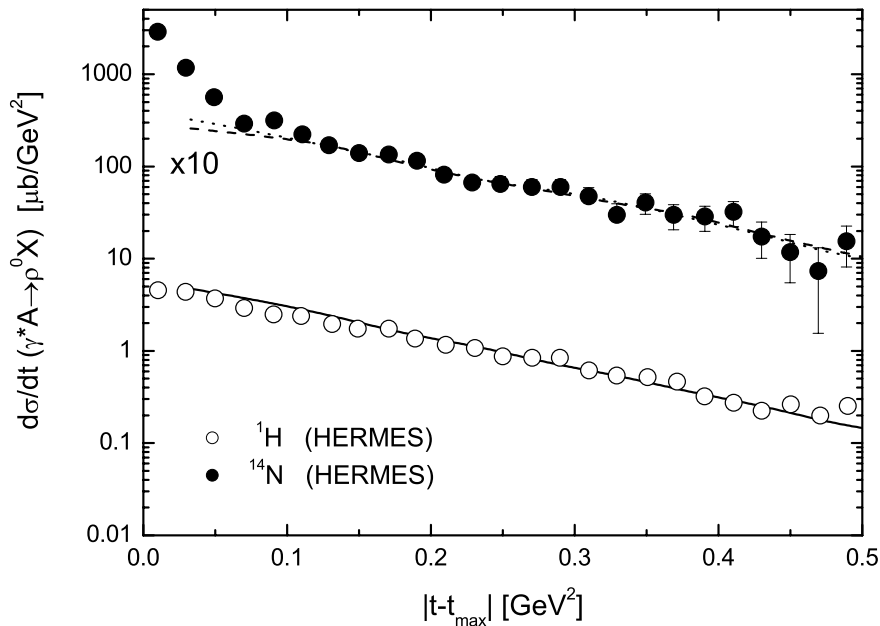
Figure 6.10: The exclusive incoherent differential $\rho^0$ production cross section for $^1$H (solid line) and $^{14}$N (dashed line) in comparison with experimental data from the HERMES collaboration [Ack99]. The calculation has been performed for $\nu = 13$ GeV and $Q^2 = 1.7$ GeV$^2$. The dotted curve represents a calculation for $^{14}$N without Pauli blocking and Fermi motion. For details on the exclusivity measure see text.

small momentum transfers. Note that this Pauli blocking just means that the whole nucleus absorbs the transferred momentum, i.e. this event contributes to the coherent production cross section which we do not consider here.

In Fig. 6.11 we show the transparency ratio $T_A$ for exclusive $\rho^0$ production as a function of the coherence length $l_\rho = q_\rho^{-1}$. The solid line is the result that one gets if one uses Eq. (6.30) and accounts for two-body correlations by making the substitution (6.23) to avoid unphysical contributions from processes where $z_i \approx z$ which would contribute for small values of the coherence length $l_\rho$. In Ref. [Fal00a, Fal00b] we showed that this replacement yields a good description of shadowing in photoabsorption. In Eq. (6.30) we use for the total $\rho^0 N$ cross section $\sigma_{\rho^0 N} = 25$ mb and for the elastic part $\sigma^{\text{el}}_{\rho^0 N} = 3$ mb. These two values correspond to the $\rho N$ cross sections used within the transport model for the involved $\rho^0$ momenta.

The result of the transport model using our prehadron concept (5.35) together with $\tau_f = 0.5$ fm/$c$ is represented by the open squares. For each data point we have made a separate calculation with the corresponding $\nu$ and $Q^2$. In the case of $^{14}$N the Glauber and the transport calculation are in perfect agreement with each other and the experimental data. This demonstrates that, as we have discussed in the preceding section, Glauber theory can be used for the FSI if the right kinematic constraints are applied. For comparison we also show the result of Hüfner et al. [Hüf96] (dashed curve) as well as the result that one gets when using the approximate expression by Yennie [Yen71], i.e. the replacements (6.31) including two-body correlations (dotted
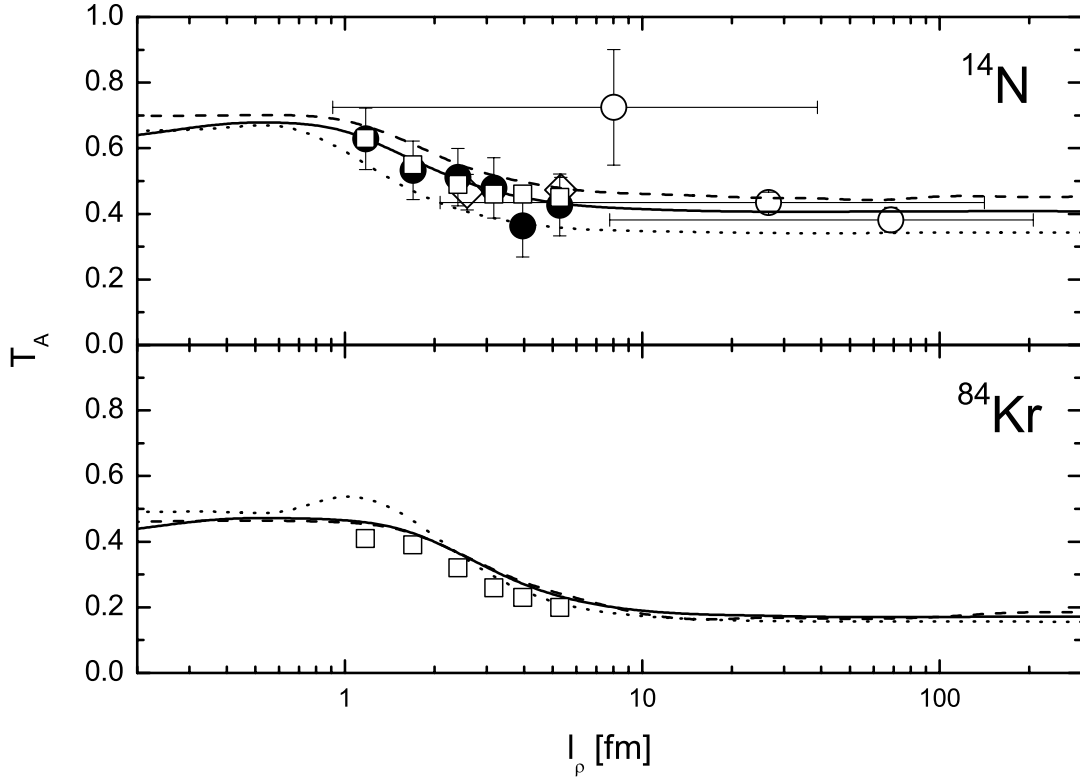
Figure 6.11: Nuclear transparency ratio $T_A$ for $\rho^0$ electroproduction plotted versus the coherence length of the $\rho^0$ component of the photon. The data is taken from [Air03] (filled circles), [Ada95] (open circles) and [Cle69] (open diamonds). The solid line represents the Glauber result when using (6.30) including nucleon-nucleon correlations. The dashed curve represents the Glauber result using (6.32) with the density distribution of Ref. [Hüf96]. For each transparency ratio calculated within our transport model (open squares), we use the average value of $Q^2$ and $\nu$ of the corresponding data point.

curve). The somewhat larger transparency ratio of Hüfner et al. is caused by the density distribution that the authors of Ref. [Hüf96] use and that differs from our parametrization (5.25). The difference of the Yennie result (dotted curve) and our calculation arises mainly from the different cross section in the FSI (second replacement in (6.31)). The different phase factor leads to the change in the transparency ratio at small coherence lengths, since $q_V = l_V^{-1}$.

After applying all of the above cuts, nearly all of the detected $\rho^0$ stem from diffractive $\rho^0$ production. The diffractively produced vector meson contains both the quark and the antiquark from the resolved photon and according to our concept (5.35) interacts with its full cross section during the formation time $\tau_f$. The $^{14}$N data therefore seem to support the assumption that the time needed to put the preformed $\rho^0$ fluctuation on its mass shell and let the wave function evolve to that of a physical $\rho^0$ is small for the considered values of $Q^2$. Furthermore, the photon energy is too low to yield a large enough $\gamma$ factor to make the formation length exceed the internucleon distance and make color transparency visible. This conclusion is at variance with that reached in Ref. [Kop01].
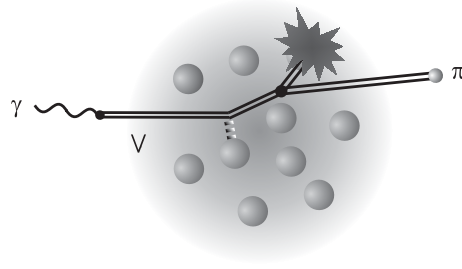
Figure 6.12: The decay of the $\rho^0$ inside the nucleus reduces the transparency ratio (6.33) because the probability that at least one of the pions interacts on its way out of the nucleus is about twice as large as that of the $\rho^0$. The probability for an in-medium decay is higher for large nuclei and low energies where the decay is less time dilated.

We now turn to $^{84}$Kr where we expect a stronger effect of the FSI. Unfortunately, there are yet no data available to compare with. As can be seen from Fig. 6.11, the transport calculation for $^{84}$Kr gives a slightly smaller transparency ratio than the Glauber calculation, especially at low values of the coherence length, i.e. small momenta of the produced $\rho^0$. There are two reasons for this: About 10% of the difference arises from the fact that within the transport model the $\rho^0$ is allowed to decay into two pions (cf. Fig. 6.12). The probability that at least one of the pions interacts on its way out of the nucleus is about twice as large as that of the $\rho^0$. The other reason is that in the Glauber calculation (6.30) only the inelastic part of the $\rho^0 N$ cross section enters whereas the transport calculation contains the elastic part as well. Thus all elastic scattering events out of the experimentally imposed $t$ window are neglected in the Glauber description. It is because of this $t$ window that also elastic $\rho^0 N$ scattering reduces the transport transparency ratio shown in Fig. 6.11. Both effects are more pronounced at lower energies and become negligible for the much smaller $^{14}$N nucleus.

We have shown that our method to account for coherence-length effects within the BUU model gives a perfect description of the measured transparency ratio for exclusive incoherent $\rho^0$ photoproduction off $^{14}$N. Furthermore it allows us to distinguish between the initial-state interactions of the photon (shadowing) and the FSI of the reaction products. As we have shown in Sec. 6.1.2, our result is equivalent to the exact result of Glauber theory if one treats the FSI as purely absorptive. In the case of $^{14}$N Glauber theory is applicable after the kinematic cuts of the HERMES experiment are applied. The deviations from the simple Glauber model caused by the finite life time of the $\rho^0$ and elastic scattering out of the kinematically allowed $|t|$ region should be taken into account when evaluating the $^{84}$Kr data in search of color transparency.

In our calculations the diffractively produced vector meson interacts with its full cross section during the formation time. We therefore conclude that there is no sign for color transparency in the presented HERMES data. As discussed by Kopeliovich et al. [Kop01], one might see an onset of color transparency when investigating the transparency ratio as a function of $Q^2$ for fixed coherence length. In fact our calculated multiplicity ratio does not show any $Q^2$ dependence if we keep the coherence length fixed. An increase of the measured transparency ratio with $Q^2$ for fixed coherence
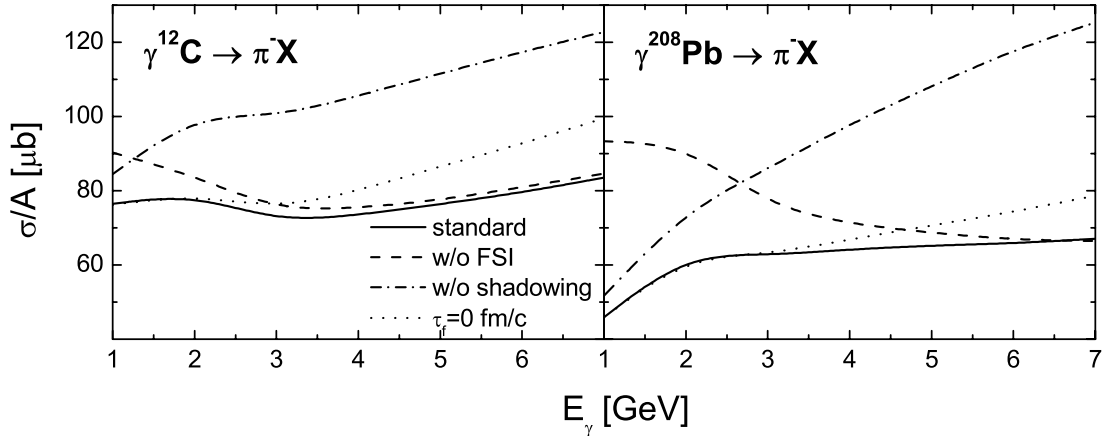
Figure 6.13: Photoproduction cross section for $\pi^- X$ on $^{12}$C and $^{208}$Pb plotted as a function of the photon energy in the energy range 1–7 GeV. The solid line represents the full calculation with no prehadronic interactions during $\tau_f = 0.8$ fm/$c$. The dash-dotted line shows the result without shadowing of the incoming photon, the dashed line the result without FSI and the dotted line the calculation with formation time $\tau_f = 0$.

length would therefore require a $VN$ cross section that decreases with $Q^2$. The present data situation [Air03] on this subject is not very conclusive. We expect a cleaner signal from the current Jefferson Lab experiment on $\rho^0$ electroproduction off nuclei [Haf02].

We finally point out that the inclusion of a CT effect during the formation time for exclusive $V$ production is not straightforward within our model since a change of the $VN$ cross section during the vector meson formation will influence both the initial- as well as the final-state interactions. This is planned for future work, when hopefully also the HERMES data for $^{84}$Kr has become available.

## 6.3 Photoproduction of mesons at high energies

In the previous section we have discussed how one can reduce the coupled-channel effects to a minimum by applying the appropriate kinematic cuts on the experimental data. In the end, one could describe these very exclusive photoproduction cross sections by a purely absorptive Glauber treatment of the FSI, since any interaction simply removes the event form the experimental acceptance window. This changes if one describes less exclusive reactions such as semi-inclusive photoproduction $\gamma A \to mX$.

Semi-inclusive meson production at GeV energies has already been investigated in Refs. [Eff99a, Eff00] for photon energies $E_\gamma =$1–7 GeV. Besides our new, improved treatment of shadowing the main difference to the old calculations is the more realistic modeling of photon-nucleon interactions above the resonance region. In the old approach of Refs. [Eff99a, Eff00] the photon was always passed as a massless $\rho^0$ to the event generator FRITIOF in contrast to our new method that we have outlined in Sec. 4.4.2. Furthermore, our new calculations provide a more sophisticated treatment
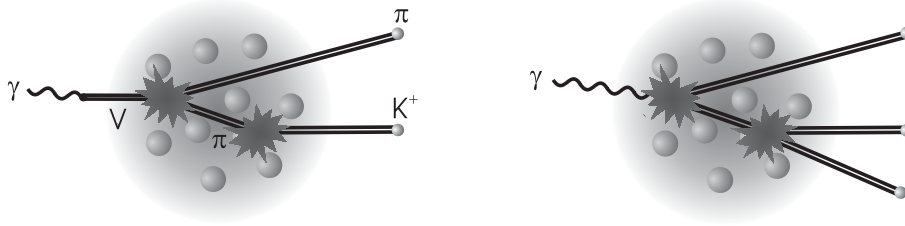
Figure 6.14: *Left:* Side feeding that leads to an enhancement of $K^+$ photoproduction on nuclei via the reaction $\pi N \to K^+ Y$ in the FSI. *Right:* At high energies the FSI enhance the multiplicities of all particle species in photoproduction on nuclei.

of high-energy FSI, e.g. the elastic channel is treated independently of FRITIOF and we use more realistic parameterizations of the various hadronic cross sections.

In this section we present our new results for semi-inclusive $\pi^-$ and $K^{\pm}$ photoproduction on $^{12}$C and $^{208}$Pb targets in the energy region 1–7 GeV as well as semi-inclusive photoproduction of $\pi^{\pm}$, $K^{\pm}$ and $D^{\pm}$ in the energy region 10–30 GeV.

Fig. 6.13 shows the result for the semi-inclusive photoproduction cross section of negatively charged pions off $^{12}$C and $^{208}$Pb nuclei as a function of the photon energy $E_\gamma$. The solid curve shows the result of a full BUU calculation that includes shadowing, FSI and a hadron-formation time $\tau_f = 0.8$ fm/$c$. To compare with the old results of Ref. [Eff99a] we assumed no prehadronic FSI during the formation time. The production cross section per nucleon is smaller for the heavier lead target for the following reasons.

The dashed-dotted line represents a calculation without shadowing. The shadowing effect seen in $\pi^-$ production is stronger for the $^{208}$Pb target than for the lighter $^{12}$C nucleus. This is also the case for the (incoherent) nuclear photoabsorption cross section shown in Fig. 6.1. In addition, one sees that shadowing is more important at high photon energies due to the increase of the coherence lengths. Since both the strength of the shadowing effect and the subsequent FSI depend on the position of the primary production process, it is obvious why the effect of shadowing is different in size for photoproduction and photoabsorption. Because of the wrong normalization of the former shadowing factor (6.13) the shadowing effect at 7 GeV is now about 10% stronger than in the old results of Ref. [Eff99a].

As can be seen from comparison with a calculation without FSI (dashed line), the pion attenuation caused by the shadowing effect and the absorption of pions in the FSI via the combined process $\pi NN \to \Delta N \to NN$ is (partly) compensated at high energies by the production of secondary pions in FSI of the kind $\pi N \to \pi\pi N$ (cf. right-hand side of Fig. 6.14). The dotted curve in Fig. 6.13 shows that this effect is even more pronounced for a vanishing formation time since the latter increases the number of FSI and therefore the integrated multiplicity.

So far we have only discussed the production of strongly interacting particles such as the $\rho^0$ or $\pi^-$. In the following we discuss the special effects that appear in a coupled-channel treatment of the FSI when a weakly interacting particle, such as the kaon, is considered. In Fig. 6.15 we show the cross section for the reaction $\gamma A \to K^{\pm} X$ in the photon energy range 1-7 GeV for $^{12}$C and $^{208}$Pb. This reaction had also been
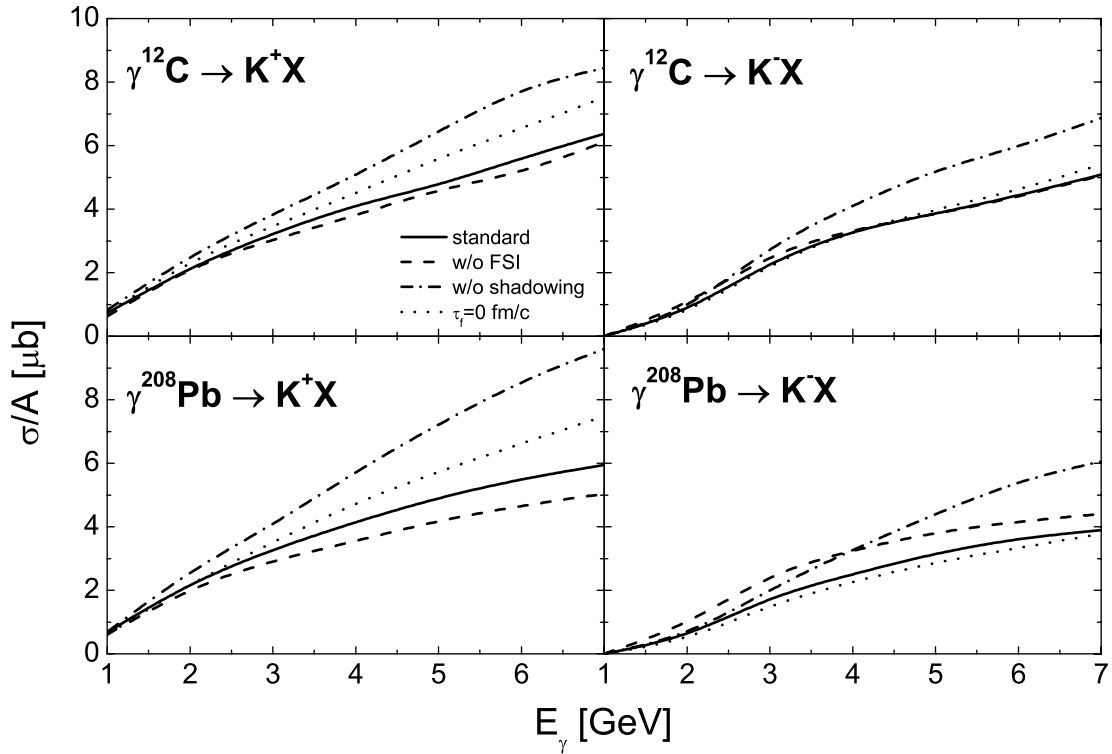
Figure 6.15: Photoproduction cross section for $K^{\pm}X$ on $^{12}$C and $^{208}$Pb plotted as a function of the photon energy in the energy range 1–7 GeV. The solid line represents the full calculation with no prehadronic interactions during $\tau_f = 0.8$ fm/$c$. The dash-dotted line shows the result without shadowing of the incoming photon, the dashed line the result without FSI and the dotted line the calculation with formation time $\tau_f = 0$.

investigated in Ref. [Eff00], however, our explicit consideration of the $\phi$ component increases the elementary production of $K^+$ by about 25% and that of $K^-$ by more than 50% at 7 GeV. Furthermore, by comparing to a calculation without shadowing (dash-dotted line) one finds that the shadowing in $K^{\pm}$ production is about 10% smaller than the shadowing in pion production observed in Fig. 6.13. This was not the case in the old results of Ref. [Eff99a]. The reason for this is the different coherence length and the different attenuation of the photon's $\phi$ and $\rho^0$ components shown in Fig. 6.3 which has not been accounted for in Ref. [Eff99a].

The importance of a coupled-channel treatment of the FSI becomes clear when comparing the full calculation with the one without FSI (dashed line). Since the $\bar{s}$ quark cannot be absorbed in the nuclear medium, the FSI can just increase the $K^+$ yield via processes like the one shown on the left-hand side of Fig. 6.14, $\pi N \rightarrow K^+ Y$ ($Y = \Sigma, \Lambda$). With decreasing formation time the primarily produced pions have a greater chance to produce $K^+$ in the FSI. As a consequence of this, a shorter formation time leads to an increase of the nuclear $K^+$ photoproduction cross section, as can be seen from the dotted line. The effect is more enhanced for the heavier lead target. An enhancement of the $K^+$ production cross section due to FSI cannot be explained
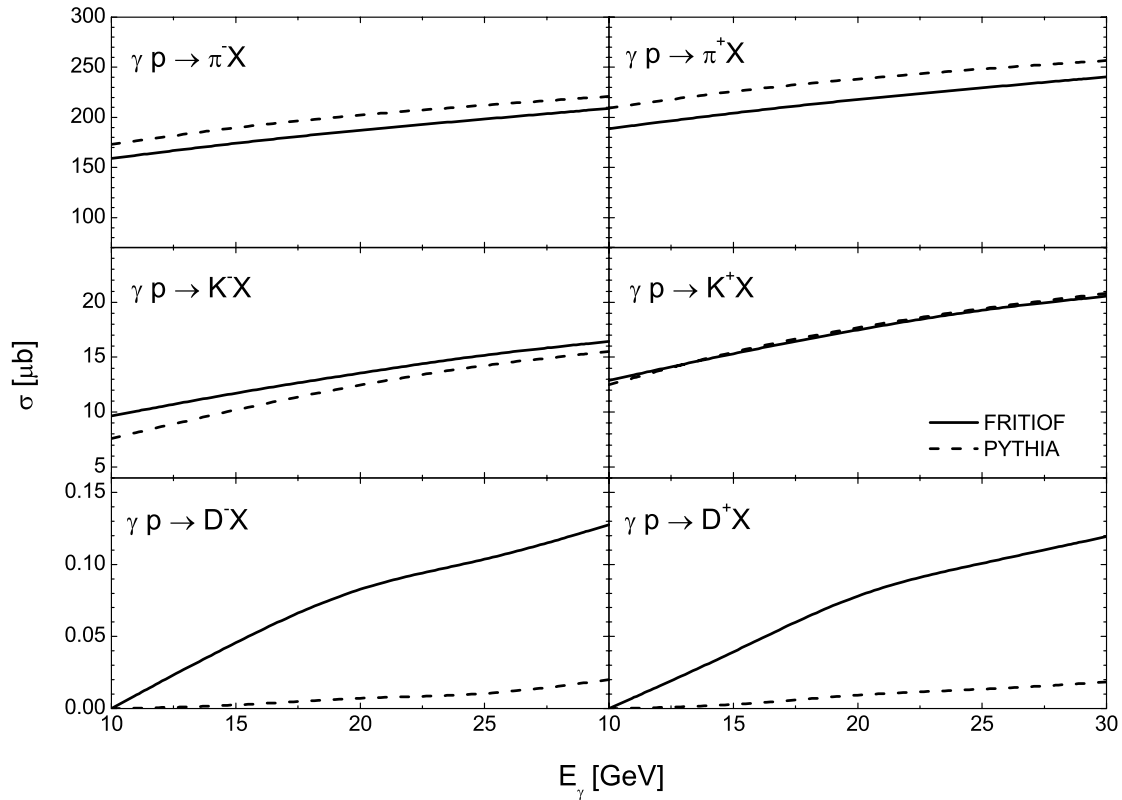
Figure 6.16: Comparison of the FRITIOF and PYTHIA results for the elementary photoproduction cross section of $\pi^{\pm}X$, $K^{\pm}X$ and $D^{\pm}X$ in the photon energy range 10–30 GeV. The solid line represents the FRITIOF+VMD result using the method described in Sec. 4.4.2 and the dashed line shows the cross sections of the PYTHIA model.

by purely absorptive FSI as in simple Glauber theory where it would necessarily be interpreted as being due to a longer formation time of the $K^+$.

In contrast to the $K^+$, the $K^-$ may also get absorbed in the nuclear medium via reactions like $K^- N \to \pi Y$. For the light $^{12}$C nucleus the $K^-$ absorption is compensated by $K^-$ production in the pionic FSI. In the case of $^{208}$Pb, absorption exceeds and the FSI reduce the $K^-$ yield. Setting the formation time to zero (dotted line) leads to less changes than in $K^+$ photoproduction since now both the absorption of $K^-$ and the production through pions in the FSI is increased.

Finally, we take a look at photoproduction of $\pi^{\pm}$, $K^{\pm}$ and $D^{\pm}$ on $^{208}$Pb for photon energies $E_\gamma = 10$–30 GeV. Like in the transition energy region discussed in Sec. 4.4.2, we use the FRITIOF model together with VMD to describe the $\gamma N$ reactions above the resonance region.

In Fig. 6.16 we compare our FRITIOF+VMD recipe with the elementary production cross sections of the PYTHIA model. Since the hadronic interaction of real photons is dominated by VMD, we do not see much difference between the two approaches except for the charmed mesons. By comparing to experimental SLAC data on open charm
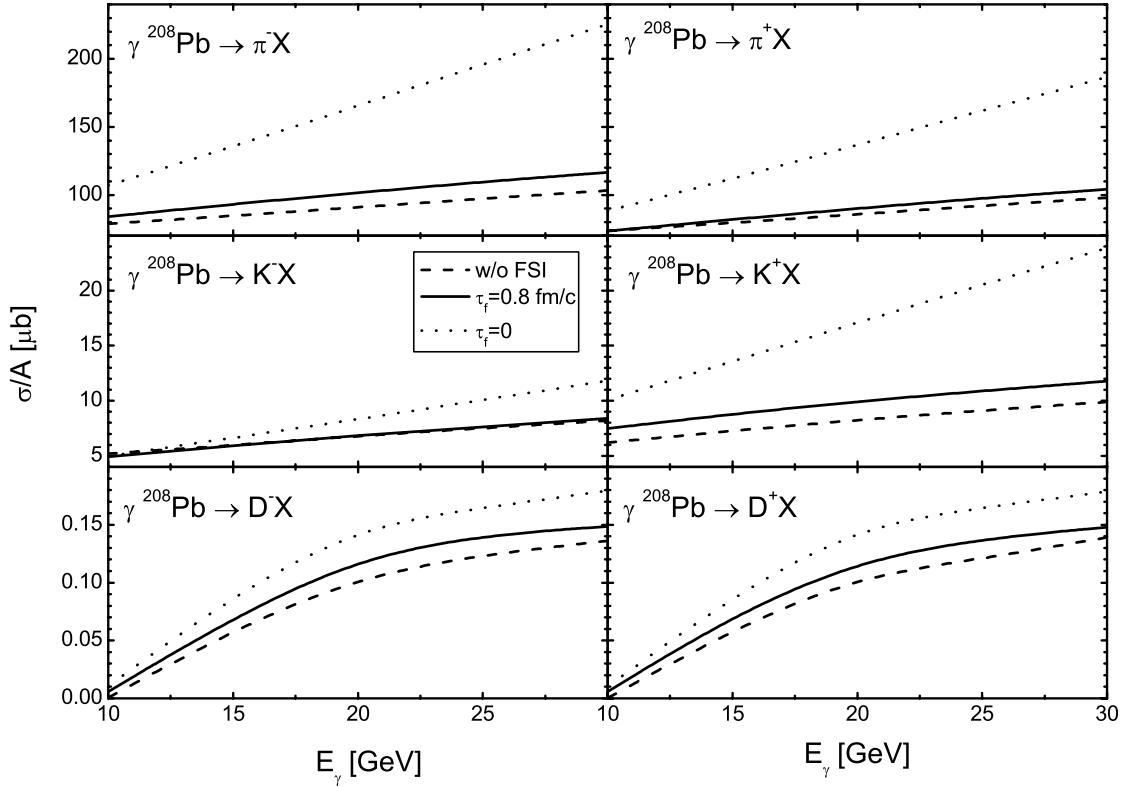
Figure 6.17: Photoproduction cross section for $\pi^{\pm}X$, $K^{\pm}X$ and $D^{\pm}X$ on $^{208}$Pb plotted as a function of the photon energy in the energy range 10–30 GeV. The solid line represents the full calculation with no prehadronic interactions during $\tau_f = 0.8$ fm/$c$. The dashed line shows the result without FSI and the dotted line a calculation with zero formation time.

photoproduction at $E_\gamma = 20$ GeV [Abe86]:

$$
\begin{aligned}
\sigma(\gamma p \to D\bar{D}X)_{\mathrm{exp}} &= 17 \pm 8\,\mathrm{nb} \\
\sigma(\gamma p \to D\bar{D}X)_{\mathrm{FRITIOF}} &= 145\,\mathrm{nb} \\
\sigma(\gamma p \to D\bar{D}X)_{\mathrm{PYTHIA}} &= 38\,\mathrm{nb}
\end{aligned}
$$

and data from FNAL [Bin82] on inclusive $J/\psi$ production at $E_\gamma = 67.5$ GeV:

$$
\begin{aligned}
\sigma(\gamma p \to J/\psi X)_{\mathrm{exp}} &= 26 \pm 3\,\mathrm{nb} \\
\sigma(\gamma p \to J/\psi X)_{\mathrm{FRITIOF}} &= 393\,\mathrm{nb} \\
\sigma(\gamma p \to J/\psi X)_{\mathrm{PYTHIA}} &= 33\,\mathrm{nb}
\end{aligned}
$$

we see that our FRITIOF+VMD recipe overestimates the cross sections for charm production by one order of magnitude. Since the massive charmed quarks are not produced in the string fragmentation due to their large suppression factor (4.19), we conclude that Eqs. (3.5) and (4.32) yield too large a $J/\psi$ ($c\bar{c}$) contribution to the hadronic interactions of the photon.

Fig. 6.17 shows the results for semi-inclusive meson photoproduction on a $^{208}$Pb nucleus using the FRITIOF+VMD recipe. Since we overestimate the elementary charm photoproduction cross section on a nucleon by one order of magnitude we expect that also the production cross sections for open charm on a nucleus is one order of magnitude too large. The solid line in Fig. 6.17 shows the result of our BUU model assuming a formation time $\tau_f = 0.8$ fm/$c$ for all hadrons. As can be seen from the simulation without FSI (dashed line) the particle multiplicities and, hence, the inclusive photoproduction cross section are enhanced by FSI of the kind as shown in Fig. 6.14. As discussed above, this effect is less pronounced for the $K^-$ whose production probability is small because of their quark content $u\bar{s}$. Since we assume no prehadronic interactions during the formation time, a reduction of $\tau_f$ (dotted line) enhances the particle production in the FSI especially at high energies where time dilatation gives rise to long formation lengths. Since $c\bar{c}$ pairs are only produced in hard interactions and not in the string fragmentation, the enhancement of the $D^+$ and $D^-$ yield is mainly due to open charm production in the FSI of $\eta_c$ and $J/\psi$ mesons that have been produced in the primary $\gamma N$ interaction.

## 6.4   Hadron formation and attenuation in DIS

Hadron production in deep inelastic lepton-nucleus scattering offers a promising tool to study the physics of hadronization [Kop96]. The reaction of the exchanged virtual photon with a bound nucleon leads to the production of several hadrons. While the primary production is determined by the fragmentation function – in medium possibly different from that in vacuo – the number of ultimately observed hadrons and their energy distribution depends also on their rescattering in the surrounding nuclear medium. Consequently, the particle spectrum of a lepton-nucleus interaction will differ from that of a reaction on a free nucleon. In order to explore such attenuation effects the HERMES collaboration [Air01, Muc02, Gar02, Air03b] has investigated the multiplicity ratio

$$R_M^h(z_h, \nu, p_T, Q^2) = \left(\frac{N_h(z_h, \nu, p_T, Q^2)}{N_e(\nu, Q^2)}\right)_A \bigg/ \left(\frac{N_h(z_h, \nu, p_T, Q^2)}{N_e(\nu, Q^2)}\right)_D \tag{6.36}$$

of pions, charged kaons, protons and antiprotons in deep inelastic positron scattering at 27.6 GeV off $^2$D, $^{14}$N, $^{20}$Ne and $^{84}$Kr targets. Here $z_h = E_h/\nu$ is the fractional energy of the detected hadron and $p_T$ its momentum transverse to the direction of the virtual photon. $N_h(z_h, \nu, p_T, Q^2)$ denotes the number of semi-inclusive hadrons in a given $(z_h, \nu, p_T, Q^2)$-bin and $N_e(\nu, Q^2)$ the number of deep inelastically scattered leptons in the same $(\nu, Q^2)$-bin. For the deuterium target, i.e. the nominator of Eq. (6.36), we simply use the isospin averaged results of a proton and a neutron target. Like the other theoretical approaches discussed in Sec. 6.4.1, we thus neglect the FSI of the produced hadrons, shadowing and Fermi motion in case of deuterium.

To illustrate the situation shortly after the photon nucleon reaction, Fig. 6.18 shows the excitation and fragmentation of a hadronic string in a deep inelastic scattering process. For simplicity we do not show any gluon bremsstrahlung of the struck quark in this figure. Note, however, that the possibility of such final state gluon radiation plus subsequent $q\bar{q}$ splitting is included in the PYTHIA part of our model and leads to
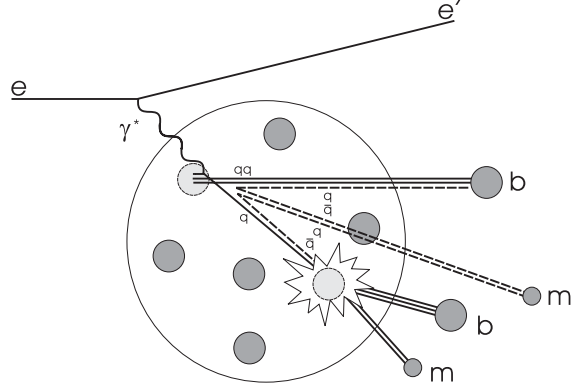
Figure 6.18: Illustration of an electron nucleus interaction: The virtual photon $\gamma^*$ excites a hadronic string by hitting a quark $q$ inside a bound nucleon. In our example the string between the struck quark $q$ and diquark $qq$ fragments due to the creation of two quark-antiquark pairs. One of the antiquarks combines with the struck quark to form a premeson $m$, one of the created quarks combines with the diquark to form a prebaryon $b$. Both the premeson $m$ and the prebaryon $b$ are target remnants. The remaining partons combine to a premeson $m'$ that, depending on the mass of the meson, might leave the nucleus before it hadronizes (see Eq. (5.34)). Note that in our default approach the actual production time $t_p$ of the prehadrons that solely contain (anti-)quarks created from the vacuum in the string fragmentation has no effect on our results since we neglect any interaction until $t_f$. See text for details.

the creation of additional strings as pointed out in Sec. 4.4.2. It has been emphasized in Ref. [Cio02] that the string propagating through the nucleus is a rather short (white) object of length $\approx 1$ fm since the slow end of the string is accelerated very fast. When the primary string fragments – due to the creation of $q\bar{q}$ pairs from the vacuum – new colorless prehadrons are produced, which we propagate in space-time.

As discussed in Sec. 4.3 the production time $t_p$ of these prehadrons has to be distinguished from the total formation time $t_f$ of the final hadrons. Furthermore, the 'production time' for the first constituent of the beam and target remnants is always zero. As explained in Sec. 5.3.2 we approximate this behavior by setting the production time $t_p$ to zero for *all* prehadrons in the default numerical realization of our model. In this section we also discuss the effect of a finite production time.

Right after the photon-nucleon interaction the primary string should interact with a hadronic cross section because its transverse size is essentially that of the original nucleon (cf. Eq. (6.37)). Motivated by the constituent-quark model we assume that this hadronic cross section is shared by the quark/diquark at the string ends and after the fragmentation by the so called target remnants that contain this quark or diquark. Our PYTHIA simulations in Fig. 4.29 show that in most cases the prehadrons with $z_h \approx 1$ are such beam or target remnants that either contain constituents (valence or sea quarks) from the target nucleon or the hadronic component of the photon. They can therefore interact directly after the photon-nucleon interaction with a constant effective cross section that is determined by the constituent-quark ansatz (5.35). The cross sections of the other prehadrons, that solely contain quarks and antiquarks cre-

ated from the vacuum, emerge at intermediate $z_h$. According to Eq. (5.35) they are non-interacting until $t_f$. After the hadron-formation time $t_f$ by definition all hadrons interact with their full hadronic cross section $\sigma_h$. This assures that the summed cross section of the complete final state right after the photon-nucleon interaction is approximately that of the original nucleon and that each time when a new hadron has formed, the summed cross section rises like in the approach of Ref. [Cio02].

In Ref. [Cio02] another type of semi-inclusive process, denoted $A(e, e'(A-1))X$, has been investigated in which the deep inelastically scattered lepton $e'$ is detected in coincidence with a heavy nuclear fragment, namely a nucleus $A-1$ in a low energy and momentum state. Without the presence of FSI, the momentum distribution of the nucleus $A-1$ is directly related to the momentum distribution of the struck nucleon before the $\gamma^* N$ interaction. Any rescattering of the struck nucleon debris with the medium after the $\gamma^* N$ interaction affects the momentum distribution of $A-1$ in a way which is very sensitive to the details of the effective cross section. The effective cross section of the partonic nucleon debris rises as function of time $t$ due to the subsequent creation of hadrons in the fragmentation of the color string as well as the production of hadrons originating from gluon radiation:

$$\sigma_{\text{eff}}(t) = \sigma_{NN} + \sigma_{mN} \left( n_m(t) + n_g(t) \right). \tag{6.37}$$

In Eq. (6.37) it is assumed that, before the first breaking, the string interacts with the nuclear medium with the nucleonic cross section $\sigma_{NN}$. With increasing time $n_m(t) + n_g(t)$ mesons are produced in the subsequent fragmentation of the string and from $q\bar{q}$ splitting of the radiated bremsstrahlung gluons, respectively. In Ref. [Cio02] the time dependence of $n_m(t)$ was estimated via the decay width of heavy resonances, while the number $n_g(t)$ of bremsstrahlung gluons radiated by the struck quark was calculated within pQCD.

In Fig. 6.19 we compare Eq. (6.37) with the increase of the summed cross section in our constituent-quark concept for two values of the formation times $\tau_f = 0.5$ fm/$c$ (solid line) and $\tau_f = 0.8$ fm/$c$ (dashed line). One sees that the two approaches yield compatible results.

Since the lighter (intermediate $z_h$) hadrons – due to time dilatation – have large formation times in the target frame (see Eq. (5.34)) they may escape the nucleus without being attenuated if they are no beam or target remnants. However, many ($\approx 2/3$) of the observed hadrons with intermediate $z_h$ are not directly produced in the string fragmentation but stem from decays of the much heavier vector mesons with correspondingly shorter formation times (cf. Fig. 4.29). These vector mesons may therefore form inside the nuclear volume and thus be subjected to FSI. The effect of the FSI, finally, will depend dominantly on the nuclear geometry, i.e. the size of the target nucleus.

We already pointed out in the introduction that the formation time also plays an important role in studies of ultra-relativistic heavy-ion reactions. For example, the observed quenching of high transverse momentum hadrons in $Au+Au$ reactions relative to $p+p$ collisions is often thought to be due to jet quenching in a quark gluon plasma. However, the attenuation of high $p_T$ hadrons might at least partly be due to hadronic rescattering processes [Gal03, Cas04].

Unfortunately, the average hadron-formation time is not well known and the number of $\tau_f \approx 1$ fm/$c$ as used commonly in the Bjorken estimate for the energy density [Bjo83]
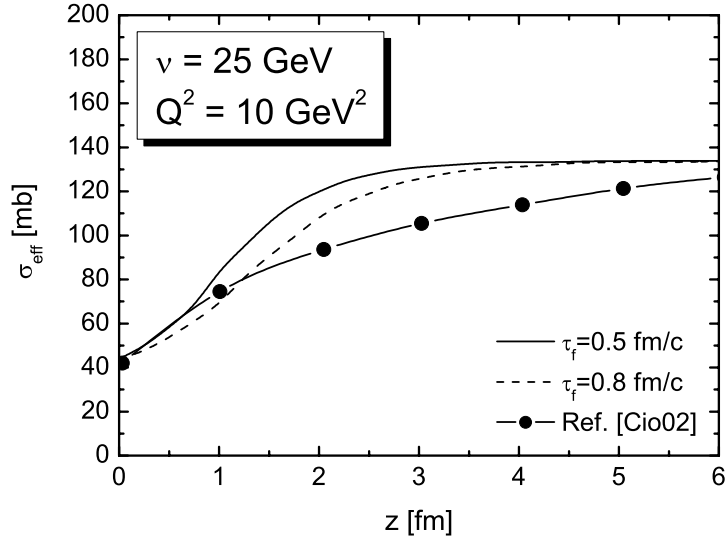
Figure 6.19: Summed cross section of the reaction products of a virtual $\gamma^* N$ interaction as a function of the propagation length $z$ at photon energy $\nu = 25$ GeV and virtuality $Q^2 = 10$ GeV$^2$. The solid line represents the result of the prehadron concept (5.35) using a formation proper time $\tau_f = 0.5$ fm/$c$ for all hadrons. For the dashed line we use $\tau_f = 0.8$ fm/$c$. The solid circles represent the result of Ref. [Cio02] which also accounts for gluon-bremsstrahlung.

is nothing but an educated guess. The nonperturbative nature of this number – due to time scales of $\sim 1$ fm/$c$ and hadronic size scales of 0.5–1 fm – excludes perturbative evaluation schemes; it is hard to calculate $\tau_f$ from first principles and formation times cannot be addressed in present lattice QCD simulations. As pointed out in Sec. 4.3 the rather successful Lund string model shed some light on this number, since the intrinsic time scale $\tau_V$ for the $q\bar{q}$-production vertex can be related to the fragmentation function and string tension, respectively. However, the actual parameters employed in current transport codes are not unique, with hadron-formation times ranging from 0.3–2 fm/$c$ [Cas99], depending on the flavor, momentum and energy of the created hadrons. In fact, the rapidity and transverse mass spectra from relativistic nucleus-nucleus collisions are not very sensitive to the formation time $\tau_f$ [Cas04]. It is therefore essential to check whether these times are compatible with constraints extracted from reactions, where the collision geometry is much better under control.

To this aim the attenuation of antiprotons produced in $pA$ reactions at the AGS energies of 12.3 GeV and 17.5 GeV has been investigated on various nuclear targets in Ref. [Cas02] and a range of values for $\tau_f = 0.4 - 0.8$ fm/$c$ has been extracted in comparison to the data from the E910 Collaboration [Chm01].

We begin this section with a brief discussion of the various models on hadron attenuation in Sec. 6.4.1.

We then investigate different concepts of hadron production and formation in the framework of our probabilistic coupled-channel transport model which allows for a realistic treatment of the FSI. We demonstrate that the coupled-channel effects in the

FSI lead to deviations from the results of simple absorption models since particles produced in the FSI affect the low energy part of the hadron spectra and thereby all energy-integrated observables. A strong effect of the coupled channels becomes also visible in the attenuation of kaons. As discussed in the Sec. 6.3 kaon absorption is partially compensated by kaon recreation in the FSI via secondary channels like $\pi N \to KYX$. Furthermore, our event-by-event simulation allows us to investigate how the observed attenuation ratios depend on the kinematic cuts and the detector acceptance. We show that there is a sizable effect of the detector acceptance on the multiplicity ratios, which does not drop out by taking the multiplicity ratio and, therefore, has to be considered explicitly when addressing any robust interpretation of the data.

Being able to compare with almost every observable that is experimentally accessible we can test the limits of a purely hadronic model and figure out at what point an extension becomes necessary. For this reason we also include the EMC data [Ash91] on hadron attenuation at 100 and 200 GeV muon energy in our analysis where the hard scale – set by the photon virtuality $Q^2$ – is closer to that of the high $p_T$ events at RHIC [PH03, PH04, ST03, ST03b]. Finally, we make predictions for hadron attenuation at current and future Jefferson Lab energies in Sec. 6.4.4.

## 6.4.1   Existing models

### (Pre-)hadronic absorption models

It was suggested in Ref. [Air01] that a phenomenological description of the $\nu$ and $z_h$ dependence of the $R^h_M$ data for charged hadrons can be achieved if the production time, i.e. the time that elapses from the moment when the photon strikes the nucleon until the reaction products start to interact, is assumed to be proportional to $(1-z_h)\nu$ in the target rest frame. This $(1-z_h)\nu$ dependence of the production time $t_f$ is compatible with the gluon-bremsstrahlung model of Kopeliovich et al. [Kop96, Kop03]. In the investigations of Ref. [Air01] any interaction of the reaction products with the remaining nucleus before the production time has been neglected. After the formation time the hadrons could get absorbed according to their full hadronic cross section.

In Ref. [Kop03] it is suggested that the main source of nuclear suppression arises from the attenuation of colorless prehadrons in the medium. After a valence quark of the nucleon is struck by the virtual photon it starts to radiate gluons which leads to a energy loss that is linear in time. This energy loss is also present in vacuum and is equivalent to the string model expression (4.5). In the large $N_c$ limit each radiated gluon is equivalent to a $q\bar{q}$ pair, and the gluon bremsstrahlung can be seen as a production of a system of color dipoles. The leading hadron, i.e. the most energetic one, then originates from the struck quark and the antiquark from the last radiated gluon. Because of energy conservation the gluon radiation has to stop very early if the struck quark forms a leading hadron with $z_h \to 1$ and the production time vanishes proportionally to $1 - z_h$. Note that, like in the Lund model, the production time of the colorless prehadron has to be distinguished from the formation time, i.e. the time needed to form the hadronic wave function. Due to time dilatation the latter is proportional to $z_h$.

In Ref. [Kop03] the production time of the leading prehadron was calculated within pQCD and its propagation through the nuclear medium was described using the light-

cone Green-function technique that has already been applied for the description of vector meson electroproduction off nuclei in Ref. [Kop01], cf. Sec. 6.2. All other pre-hadrons that emerge from the initial gluon radiation have been neglected. The average production time for the leading prehadron at $z_h \approx 0.9$ is more than ten times smaller than the prehadron-production time $t_{p2}$ that we extract from JETSET, cf. dotted line in Fig. 6.20. In fact, the magnitude of the average leading prehadron-production time in Ref. [Kop03] is rather compatible with the size of the JETSET time $t_{p1}$ (dashed-dot-dotted line in Fig. 6.20) or the average starting time of the prehadronic interactions in our constituent-quark concept (solid squares in Fig. 6.20).

Since the gluon-bremsstrahlung model of Ref. [Kop03] only accounts for the atten-uation of the leading prehadrons, it is useless for small values of $z_h$. For this reason, the authors could only compare with experimental data in the region $z_h > 0.5$. In this regime they achieve a good agreement with the experimental HERMES data for the charged hadron multiplicity ratio as function of $z_h$. Because of their restriction to leading hadrons the authors of Ref. [Kop03] could only integrate the multiplicity spectra down to $z_h = 0.5$ for the calculation of the $\nu$ dependence of $R_M^h$, whereas exper-imentally it is determined from all hadrons with $z_h > 0.2$. From Fig. 4.29 one sees that most hadrons have smaller $z_h$ and therefore dominate the behavior of the integrated $\nu$ spectrum. Nevertheless, the authors get a satisfying description of the observed $\nu$ dependence of the charged hadron multiplicity ratio. In Sec. 6.4.2 we show that the basic features of the $\nu$ dependence of $R_M^h$ are caused by the special geometry of the HERMES detector, which is not accounted for in Ref. [Kop03]. In view of these facts, it seems as if the correct description of $R_M^h(\nu)$ in Ref. [Kop03] is purely accidental.

Besides absorption of the prehadron in the nuclear medium, the effect of induced gluon radiation has been calculated in Ref. [Kop03]. As pointed out by the authors, multiple interactions of the quark during the time interval between the $\gamma^* N$ interac-tion and the production or the colorless prehadron cannot stop or absorb the quark. Nevertheless, the additional soft kicks gained by the quark force it to radiate more bremsstrahlung gluons. The inclusion of this induced energy loss improves the agree-ment with HERMES data but merely gives rise to about 15–20% of the total observed attenuation. However, it is the main source for the observed rise of $R_M^h$ at transverse hadron momenta $p_T > 1$ GeV/$c$, cf. Fig. 6.24. Since the production time in the gluon-bremsstrahlung model becomes smaller with increasing $z_h$, the rise of the multiplicity ratio at large $p_T$ should be dominated by low $z_h$ hadrons. However, like for the $\nu$ dependence of $R_M^h$, the authors had to neglect all hadrons with $z_h < 0.5$.

The approach of Ref. [Kop03] also predicts a dependence of the multiplicity ratio on the virtuality $Q^2$ of the photon. In the gluon-bremsstrahlung model the increase of $Q^2$ leads to two competing effects: The prehadron-production time decreases because of rising vacuum energy loss, and the interaction cross section of the prehadron decreases because the initial size of the prehadron shrinks at larger $Q^2$ (color transparency). In total one obtains a weak increase of $R_M^h$ with rising $Q^2$ that is in accordance with the experimental HERMES data [HERM].

Finally, the authors of Ref. [Kop03] predict a weaker absorption of $K^+$ mesons compared to pions. The intuitive explanation is that the projection to a wave function with a larger mean radius emphasizes larger $q\bar{q}$ separations in the prehadron, leading to stronger absorption. Since the pion has a larger radius than the kaon, the former

is expected to be attenuated stronger in the nuclear medium. The calculated $K^+$ attenuation as a function of $z_h$ is again in satisfying agreement with experimental data for $z_h > 0.5$. However, the description of the $\nu$ dependence is only very poor, i.e. it deviates by up to a factor of two from the experimental data. The latter may again be due to the neglect of kaons with $0.2 < z_h < 0.5$. Since antikaons and antiprotons do not contain valence quarks common to the target nucleon, while proton production may be contaminated with the target nucleons, no calculations for $K^-$, $\bar{p}$ and $p$ could be done in Ref. [Kop03].

In Ref. [Acc03] Accardi et al. explain the attenuation of hadrons at HERMES and EMC energies as a combined effect of a rescaling of the quark fragmentation function in the nuclear medium and (pre-)hadronic absorption in the FSI. The fragmentation function $D_q^h(z)$ describes the probability that a quark of flavor $q$ hadronizes into a definite hadron $h$ with energy fraction

$$z = E_h/E_q. \tag{6.38}$$

Consequently, the semi-inclusive leptoproduction cross section in the quark model is given as

$$\frac{1}{\sigma^{\text{tot}}} \frac{d\sigma}{dz}(eN \to hX) = \frac{\sum_q e_q^2 f_q(x, Q^2) D_q^h(z)}{\sum_q e_q^2 f_q(x, Q^2)}, \tag{6.39}$$

where $e_q$ denotes the charge of the quark flavor $q$ and $f_q$ is the quark distribution function as measured in inclusive DIS, cf. Eq. (3.22). Both the quark distribution function and the fragmentation function depend on the virtuality $Q^2$ of the DIS process, cf. Fig. 2.12. The authors of Ref. [Acc03] assume that partial deconfinement of color modifies the gluon radiation in the nuclear medium and thus a rescaling of the distribution function $f_q$ and fragmentation function $D_q$ becomes necessary. This rescaling alone is already strong enough to explain the observed attenuation on $^{63}$Cu in the EMC experiment without any further attenuation due to (pre-)hadronic FSI. We point out that the partial deconfinement also affects the string tension $\kappa$ in the nuclear medium. According to Ref. [Acc03] the string tension in a $^{14}$N and $^{131}$Xe nucleus is reduced by a factor of 0.87 and 0.80, respectively.

The authors of Ref. [Acc03] extract the production times of the hadron constituents from the Lund model using the simplified fragmentation function (4.21) which neither depends on the hadron mass nor does it lead to a symmetric string fragmentation. Similar to the derivations of Eqs. (4.22) and (4.23) the finite mass of the string is neglected and the production times are calculated by averaging over infinitely many ranks. According to our findings in Sec. 4.3, we therefore do expect deviations from the real production and formation times in the Lund model.

In Fig. 6.20 we show the formation and production times of Ref. [Acc03] in the kinematic regime of the HERMES experiment. For comparison we also show the starting times of the (pre-)hadronic interactions within our constituent-quark concept, i.e. Eq. (5.35) and $\tau_f = 0.5$ fm/$c$. In addition we included the times $t_{p1}$, $t_{p2}$ and $t_f$ that we have extracted from JETSET and averaged over all hadron species. The authors define the *smaller* production time $t_{p1}$ as the starting time of the prehadronic interactions, whereas the Lund model intuitively suggests $t_{p2}$ as the time when the colorless prehadron is formed. Because of this different definition the prehadrons in Ref. [Acc03] (solid line) are produced much earlier than in JETSET (dotted line). Except for the
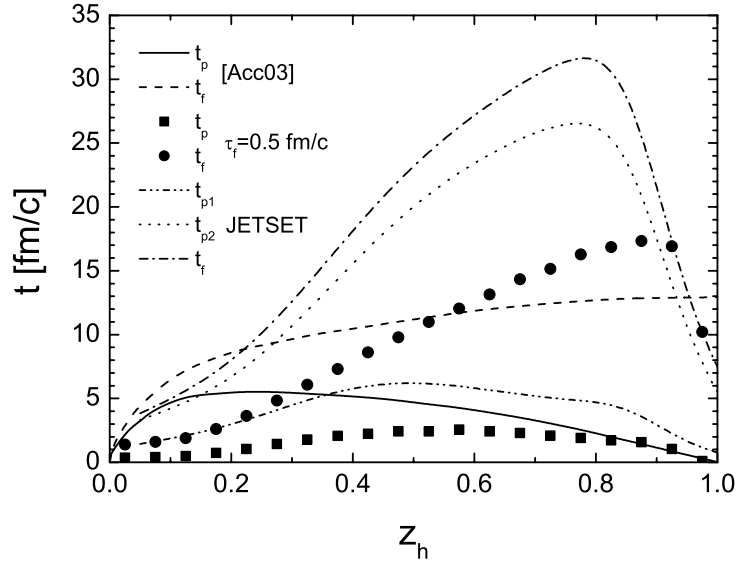
Figure 6.20: Average (pre-)hadron production and formation times at HERMES energies. We compare the results of Ref. [Acc03] with our constituent-quark concept (5.35) using a formation proper time $\tau_f = 0.5$ fm/$c$ and the times extracted from JETSET.

region $z_h > 0.8$, the production time of Ref. [Acc03] (solid line) is always larger than the starting time of the prehadronic interactions in our constituent-quark model (solid squares).

The (pre-)hadronic interactions are described in Ref. [Acc03] by a probabilistic absorption model where the prehadronic cross section is either set to the full or to half of the hadronic value. In the calculation of pion and kaon attenuation the isospin averaged hadron-nucleon cross sections are used. For the calculation of charged hadron attenuation an average cross section is computed as a weighted sum of individual cross section of pions, kaons, protons and antiprotons. Obviously, this recipe allows only for a very crude estimate of hadron attenuation even if there were no coupled-channel effects in the FSI.

The authors find that reducing the prehadronic cross section to half the hadronic value yields a too weak charged hadron attenuation at HERMES energies. Despite the large prehadron-production times, the FSI increase the hadron attenuation at EMC energies which was already described by the rescaling of the fragmentation function alone. While the absolute strength of the charged hadron attenuation is in satisfying agreement with both the HERMES and EMC data the shapes are not.

The calculated attenuation of charged pions and $K^+$ mesons agrees with experimental data, however, the model underestimates the attenuation of $K^-$ mesons. The authors point out that the discrepancy between the theoretical $K^-$ attenuation and data may point to a different formation mechanism for the negative kaons, as they do not contain any nucleon valence quarks. This may imply a shorter formation time for the $K^-$ than for the $K^+$. However, as can be seen from our findings shown in Fig. 4.16, this is not the case in the Lund model: While the production time $t_{p2}$ and formation time $t_f$ are approximately equal for $K^+$ and $K^-$, the production time $t_{p1}$ is in average

shorter for the $K^+$ than for the $K^-$. This is reasonable since the $K^+$ meson can contain a $u$ quark from the nucleon and therefore may have $t_{p1} = 0$.

## Partonic models

Besides the prehadronic absorption models discussed above there are alternative explanations for the observed hadron attenuation in DIS off complex nuclei at HERMES and EMC.

In Refs. [Guo00, Wan01, Wan02, Wan03] Wang et al. have assumed that there are no prehadronic interactions at all before the actual formation time $t_f$, and that the struck quark propagates a large distance before the hadron is finally formed outside the nucleus. In fact, the formation time $t_f$ of fast pions is much larger than the nuclear radius as we have shown in Fig. 4.16. However, one has to keep in mind that many of the pions – that are finally detected in the HERMES experiment – stem from the decay of vector mesons that are created in the primary $\gamma^* N$ interaction, cf. Fig. 4.29. Due to their larger mass these vector mesons may already form inside the nucleus and be subject to *hadronic* FSI. In Sec. 6.4.2 we show how these hadronic FSI affect the multiplicity ratio in the HERMES experiment. For large enough formation times the effect of hadronic FSI is indeed small at HERMES energies and certainly negligible at EMC energies because of the larger time dilatation effects.

As discussed above, the struck quark is subject to multiple scattering in the nucleus which induces gluon bremsstrahlung before the hadronization. The induced gluon radiation may have a coherent character like in the Landau-Pomeranchuk-Migdal (LPM) effect of QED. This coherence, in combination with the non-Abelian nature of QCD, leads to an energy loss of the quark that is quadratic in the propagation length through the nuclear medium. If the ad hoc assumption that the quark traverses the whole nucleus before hadronization is right, the energy loss would cause a change of the fragmentation function that is quadratic in the nuclear size, i.e. $A^{2/3}$. Wang et al. have claimed that this scaling is verified by the HERMES data on charged hadron production on $^{14}$N and $^{84}$Kr. However, depending on the values of $\nu$ an $z_h$ the measured multiplicity ratios of charged hadrons on $^{14}$N and $^{84}$Kr scale with an exponent 0.6–1, as can be seen from Fig. 6.23. Nevertheless, Wang et. al achieve an excellent description of $R_M^h(\nu)$ and $R_M^h(z_h)$ of charged hadrons on $^{14}$N and $^{84}$Kr.

In the approach of Ref. [Arl03] the struck quark is assumed to reduce its energy from $E = \nu$ to $E = \nu - \epsilon$ due to medium-induced gluon radiation prior to hadronization. This quark energy shift than leads to a rescaling of the energy fraction (6.38)

$$z \rightarrow z^* = \frac{z}{1 - \epsilon/\nu} \qquad (6.40)$$

which enters the fragmentation function (6.39). The radiated gluon spectrum has been computed perturbatively in Refs. [Bai97, Bai98] and depends on the length of matter covered by the struck quark and the medium gluon density which is poorly known. Besides the extreme scenario discussed above, where hadronization always occurs outside the nucleus, the author of Ref. [Arl03] also investigates the effect of the prehadron-production time $t_p$ from Eq. (4.22). In the latter case any (pre-)hadronic interactions *after* $t_p$ have been neglected. In fact, this is just the opposite approach as in Ref. [Acc03] where all interactions *before* $t_p$ are neglected.

The medium-modified fragmentation functions of Ref. [Arl03] yield an excellent description of the $\nu$ and $z_h$ dependence of $R_M^h$ for charged hadrons at EMC energies. In this kinematic regime the neglect of (pre-)hadronic FSI after $t_p$ is not very dramatic because the production length is in general large compared to the nuclear radius because of time dilatation. However, because of the $z_h$ dependence of $t_p$, which is illustrated by the dashed line in Fig. 4.12, the results of Ref. [Arl03] become doubtful when $z_h \to 0$ or $z_h \to 1$.

The author of Ref. [Arl03] has also calculated the multiplicity ratios for positively and negatively charged hadrons $h^\pm$ as well as $\pi^\pm$ and $K^\pm$ by using the corresponding vacuum fragmentation functions (6.39) as input. Except for $z_h \to 1$ the results for the attenuation of positively and negatively charged hadrons are in satisfying agreement with the $^{14}$N and $^{84}$Kr data from the HERMES experiment. However, the attenuation of $\pi^\pm$ is not well described neither for the $^{14}$N target nor for the $^{84}$Kr or $^{20}$Ne nuclei. The calculated attenuation of $K^+$ is compatible with the $^{84}$Kr data while it fails to describe the $^{20}$Ne data. Furthermore, the attenuation of $K^-$ mesons is not much stronger than that of $K^+$ in contradiction with experiment. In fact, it seems as if the approach of Ref. [Arl03] is far away from a complete description of the various HERMES data.

### Common deficiencies of the existing models

In all of the above models the contribution of the resolved photon component to the $\gamma^* N$ interaction is neglected and it is assumed that DIS can be treated as electron-quark scattering with energy transfer $\nu$ to the knocked out valence quark. However, this assumption is questionable because the lower $x$-cut in the HERMES experiment is not larger than 0.02. As indicated by Fig. 4.29, one therefore has strong contributions from the quark sea and resolved photon interactions. The peak in the $\rho^0$ and $\phi$ spectra at $z_h \approx 1$ – due to diffractively produced vector mesons that contain the two quarks from the resolved photon – underlines the importance of resolved events, especially at large $z_h$. Furthermore, the significance of sea quarks is stressed by the fact that many antikaons contain quarks from the proton or from the resolved photon. The neglect of resolved $\gamma^* N$ interactions also implies the omission of shadowing effects. However, due to the normalization of $N_h$ to the number of DIS leptons $N_e$, shadowing yields only a few percent correction to the multiplicity ratio (6.36).

Furthermore, the (pre-)hadronic FSI have been treated purely adsorptively, i.e. the production of hadrons with $z_h' < z_h$, in a collision of a (pre-)hadron that carries momentum fraction $z_h$ with a nucleon inside the nucleus, has been neglected. As we show in the following sections, these coupled-channel effects turn out to be very important, especially for the production of weakly interacting particles like kaons.

Finally, none of the above models accounts rigorously for the kinematics of the electron-nucleon interaction but instead calculate observables at average values of the photon energy $\nu$ and virtuality $Q^2$. This may indeed be a problem. For example an average value of $\langle \nu \rangle = 14$ GeV in a certain $z_h$ bin of the HERMES experiment does not mean that there are no photons with energy $\nu = 7$ GeV. The corresponding Lorentz $\gamma$'s are different by a factor of two, which has a strong effect on time dilatation. Also the detector geometry has not been accounted for in the various approaches. As we show in Sec. 6.4.2, the naive expectation that all detector effects cancel when taking the ratio is not true except for the large $z_h$-part of the hadron spectra.
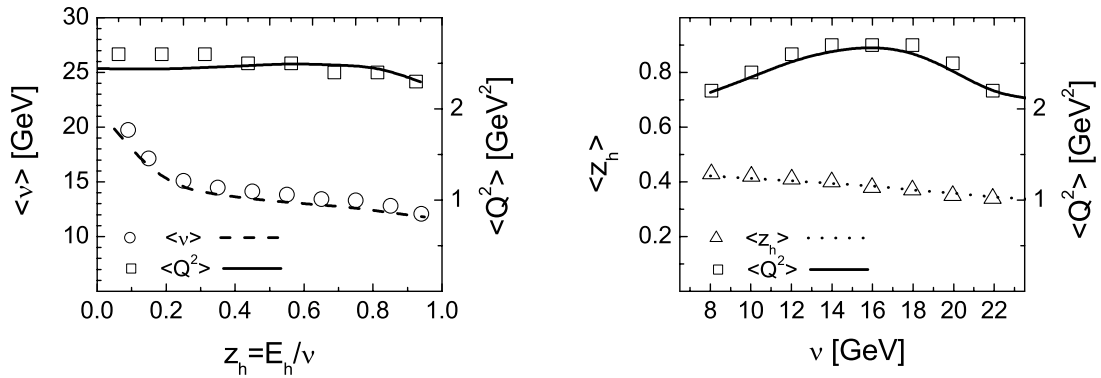
Figure 6.21: Model predictions for the average values of the kinematic variables in charged hadron production off $^{84}$Kr in comparison with the experimental numbers at HERMES [Muc]. For the calculation we use the formation time $\tau_f = 0.5$ fm/$c$ and the constituent-quark concept (5.35) for the prehadronic cross sections. *Left:* $\langle \nu \rangle$ and $\langle Q^2 \rangle$ as a function of $z_h$ compared to the experimental values for a $^{84}$Kr target (open symbols). *Right:* Same for $\langle z_h \rangle$ and $\langle Q^2 \rangle$ as a function of $\nu$.

## 6.4.2   Hadron attenuation at HERMES energies

We start with an investigation of charged hadron attenuation in semi-inclusive DIS of 27.6 GeV positrons off nitrogen and krypton. We apply the same kinematic cuts as in experiment [Air03b]: $Q^2 > 1$ GeV$^2$, $W > 2$ GeV, $\nu > 7$ GeV, $y < 0.85$, $x > 0.02$ and $E_h > 1.4$ GeV as well as the cut $z_h > 0.2$ for the $\nu$ and $p_T$ spectra. Furthermore, we account for the angular acceptance of the HERMES detector, i.e. $\pm 170$ mrad horizontally and $\pm (40 - 140)$ mrad vertically, for both the scattered positrons and the produced hadrons. The left panel in Fig. 6.21 shows the average values of the photon energy $\nu$ and the virtuality $Q^2$ as a function of the energy fraction $z_h$ of the charged hadrons produced on a $^{84}$Kr target; the right panel shows the average values of $z_h$ and $Q^2$ as a function of $\nu$. In the simulation we use the prehadron concept (5.35) and a formation time $\tau_f = 0.5$ fm/$c$. Obviously, our simulation is in perfect agreement with the experimental values for the average kinematic variables (open symbols). The increase of $\langle \nu \rangle$ at small values of $z_h$ is due to the energy cut $E_h > 1.4$ GeV and the finite angular acceptance of the HERMES detector. Both require that a hadron with low energy fraction $z_h$ is produced by a high energy photon in order to be detected.

**No prehadronic interactions**

Before discussing the effect of prehadronic interactions we show the modifications of the multiplicity ratio due to the conventional hadronic FSI after the formation time $\tau_f$ and explore the sensitivity of the results on $\tau_f$. We, therefore, neglect any interactions during $\tau_f$ and for simplicity assume that $\tau_f$ is a constant in the rest frame of each hadron independent of the particle species. Due to time dilatation the formation time $t_f$ in the laboratory frame is then proportional to the particle's energy

$$t_f = \gamma \cdot \tau_f = \frac{z_h \nu}{m_h} \cdot \tau_f. \tag{6.41}$$
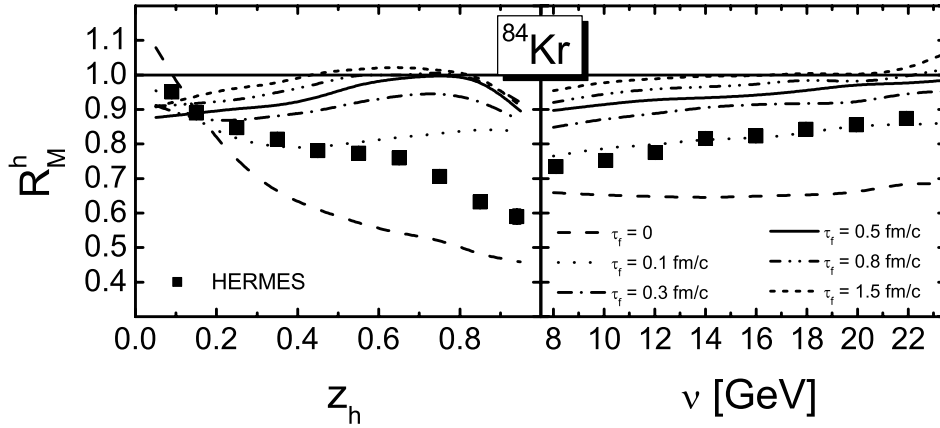
Figure 6.22: Calculated multiplicity ratio of charged hadrons for the $^{84}$Kr target (at HERMES) assuming no prehadronic interactions during the formation time $\tau_f = 0$–1.5 fm/$c$. The data are taken from Ref. [Air03b].

Fig. 6.22 shows the result for the $^{84}$Kr target using formation times in the range $\tau_f = 0$–1.5 fm/$c$. For $\tau_f=0$ (dashed line) we get a much too strong attenuation both in the $z_h$ and $\nu$ spectrum. In this case all reaction products start to interact immediately after the $\gamma^* N$ interaction and there is no effect of time dilatation ($t_f = \tau_f = 0$). As a consequence this limit leads to an almost flat $\nu$ dependence of $R_M^h$. We note that without the cut on the hadron energy $E_h$ and without the limitation by the HERMES detector acceptance one would find a strong increase of the hadron multiplicity at low $z_h$ due to particle creation in the FSI (cf. Fig. 6.25). However, after applying all cuts one is left with a 10% effect only, as can be seen from the $z_h$ spectrum in Fig. 6.22.

A slight increase of the formation time $\tau_f$ from zero to 0.1 fm/$c$ (dotted line) already leads to a dramatic change in $R_M^h$. By using this unphysically small formation time one obtains a good description of the $\nu$ dependence, but fails to reproduce the high energy part of the spectrum in $z_h$. The reason is that many of the high-energy particles, which are directly created in the primary $\gamma^* N$ interaction, now escape the nucleus due to time dilatation. Especially the formation times $t_f$ of the light pions start to exceed the dimension of the $^{84}$Kr nucleus for energies larger than $E_\pi \approx 13$ GeV. One also sees that the multiplicity ratio at low $z_h$ drops below one because both the absolute number of FSI and the energy available for particle production in the FSI is reduced. The latter decreases the probability that the secondaries end up in the HERMES detector and survive the experimental cut $E_h > 1.4$ GeV.

At larger values of $\tau_f$ one still has some attenuation due to the FSI of more massive hadrons. As seen in Fig. 4.29 a large fraction of the finally detected pions stem from the decay of neutral (and charged) $\rho$ mesons created in the string fragmentation. Due to their relatively large mass the latter have a smaller formation time in the lab frame and are subject to hadronic FSI, especially if they carry only a small fraction $z_h$ of the photon energy. For example, the formation length of a $\rho$ meson produced by a 7 GeV photon is always smaller than about $\gamma \cdot \tau_f \cdot c \approx 9 \cdot \tau_f \cdot c$. For $\tau_f = 1.5$ fm/$c$ (short dashed line) only the formation lengths of the massive vector mesons and nucleons with
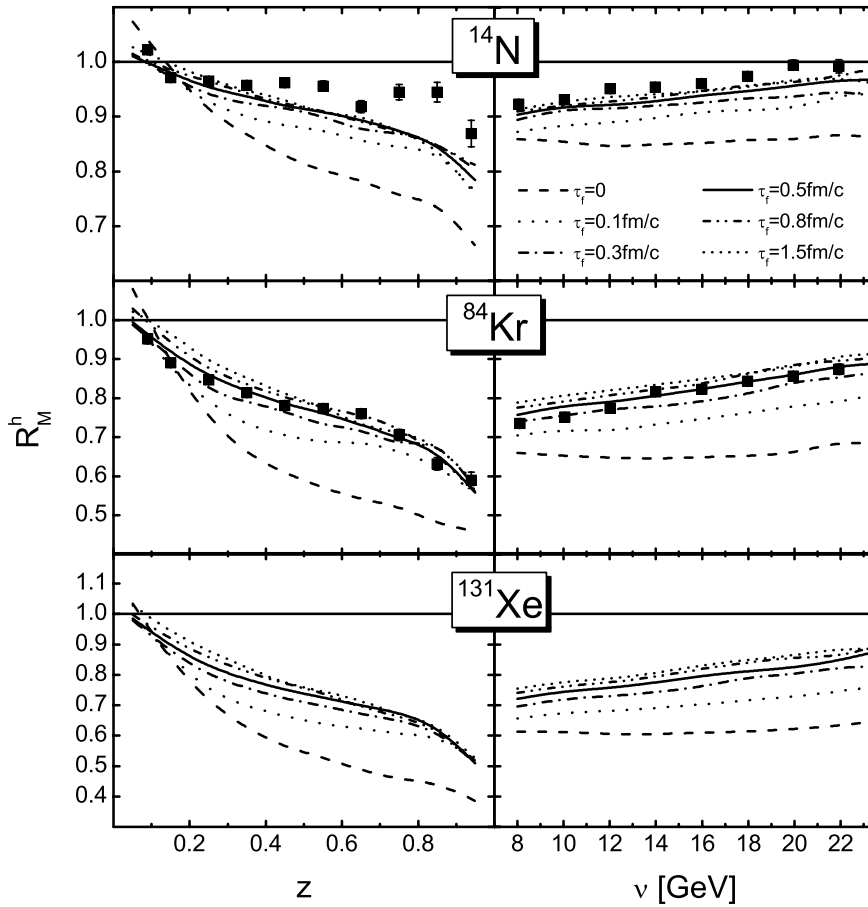
Figure 6.23: Calculated multiplicity ratio of charged hadrons for $^{14}$N, $^{84}$Kr and $^{131}$Xe nuclei (at HERMES) using the constituent-quark model (5.35) for the prehadronic cross section and different values of the formation time $\tau_f = 0$–1.5 fm/$c$. The data are taken from Ref. [Air03b].

$z_h \lesssim 0.6$–0.7 are short enough to give rise to attenuation. The small deviation from unity of $R_M^h$ at $z_h \approx 1$ is due to the Fermi motion of the bound nucleons that affects the maximum energy available for hadron production in the initial $\gamma^* N$ interaction.

**Constituent quark model**

From Fig. 6.22 one extracts that for reasonable formation times $\tau_f \gtrsim 0.5$ fm/$c$ the prehadronic interactions have to set in quite early after the $\gamma^* N$ interaction, especially for the hadrons at large $z_h$. We now set the production time of *all* prehadrons to zero and rescale the prehadronic cross sections according to the constituent-quark concept (5.35).

Fig. 6.23 shows the results of our simulation for $^{14}$N, $^{84}$Kr and $^{131}$Xe using formation times $\tau_f = 0$–1.5 fm/$c$. The dashed lines ($\tau_f = 0$) coincide with the ones in Fig. 6.22 since they only involve hadronic FSI. By comparing the $\nu$ spectra of Figs. 6.23 and 6.22 for finite formation times one observes that $R_M^h(\nu)$ is reduced by the prehadronic

FSI, which also improve the agreement of $R_M^h(z_h)$ with the experimental $^{84}$Kr data at large $z_h$. However, the attenuation of the $z_h$ spectra is too strong for the $^{14}$N target which might already indicate a deficiency of our simple prehadron concept. The experimental $^{84}$Kr data favor formation times $\tau_f \gtrsim 0.3$ fm/$c$ with only little sensitivity for larger values because of the finite size of the $^{84}$Kr nucleus. These times are in line with our simple estimate via the hadronic radius and with the values $\tau_f = 0.4$–$0.8$ fm/$c$ [Cas02] extracted from antiproton attenuation in $pA$ reactions at AGS energies of 12.3 GeV and 17.5 GeV on various nuclear targets [Chm01]. A cleaner discrimination between $\tau_f = 0.3$ fm/$c$ and larger formation times will be possible in an experimental investigation at Jefferson Lab [WBr02, KWa04, WBr03, Arr03] with heavier targets and lower photon energies.

In the pQCD parton model of Ref. [Guo00, Wan01, Wan02, Wan03] the multiple parton scattering leads to a modification of the fragmentation function and predicts a hadron attenuation $\sim A^{2/3}$. In our approach, however, the fragmentation is assumed to be decided on time scales of the nucleon dimension itself such that only the 'free' fragmentation function enters. All attenuation effects then are attributed to FSI of the leading and secondary (pre-)hadrons. In order to distinguish experimentally between the different concepts, it is thus important to get the scaling with target mass $A$. To this aim Fig. 6.23 also shows predictions for a $^{131}$Xe target. In accordance with the authors of Ref. [Acc03] we predict only a small change in the multiplicity spectra compared to the $^{84}$Kr target. From the charged hadron attenuation $(1 - R_M^h)$ for $^{14}$N, $^{84}$Kr and $^{131}$Xe we extract a scaling exponent 0.33–0.39 at $z_h = 0.95$. If the attenuation was simply proportional to the distance that the particles propagate through the medium, one would expect a scaling exponent $\alpha = 1/3$. The deviation from this naive expectation is caused by the finite formation time and the nonuniform density distribution in nuclei. At lower values of $z_h$ or in the integrated $\nu$ spectra the scaling behavior is hidden by the coupled-channel effects.

In Fig. 6.24 we show the transverse momentum dependence of the multiplicity ratio (6.36), where the transverse component $p_T$ of the hadron is defined with respect to the momentum direction of the virtual photon. In the simulation we use the constituent-quark concept (5.35) for the prehadronic cross sections and the formation time $\tau_f = 0.5$ fm/$c$. We expect that the $p_T$ distribution of the observed hadrons is broadened for complex nuclei compared to deuterium due to multiple scattering of the (pre-)hadrons. Up to $p_T^2 \approx 1$ GeV$^2$ the $p_T^2$ dependence of the multiplicity ratio is well reproduced for both the nitrogen and the krypton target. However, the data of Ref. [Air03b] show a strong increase of $R_M^h$ for $p_T^2 \gtrsim 1$ GeV$^2$, which is not reproduced by our (pre-)hadronic FSI even if one assumes that all elastic scattering events are isotropic in the center-of-mass system (dashed line). This can be considered a signal for a partonic origin of the enhancement of high-$p_T$ hadrons in $eA$ collisions either via a change of the parton distributions inside the nuclear medium and/or the Cronin effect [Cro75, Kop02, Acc04].

The Cronin effect was first observed in 1975 [Cro75] via an enhancement of high-$p_T$ hadrons in $pA$ collisions and has become especially important recently in connection with data from high-$p_T$ hadron production in heavy ion collisions [PH03, PH04, ST03, ST03b]. Similar to $pA$ collisions [Kop01], a high-energy parton produced in a direct $\gamma^* N$ interaction may be subject to soft coherent and incoherent multiple rescatterings in
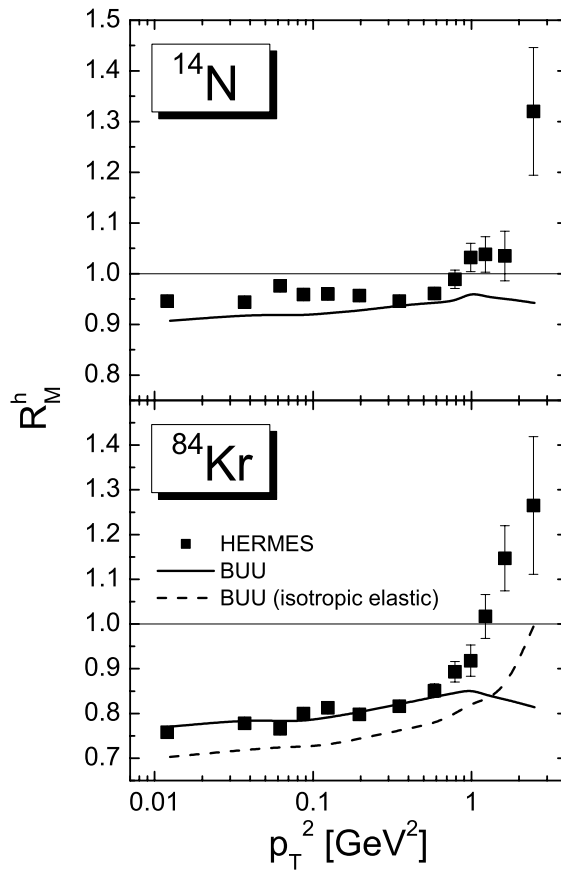
Figure 6.24: The multiplicity ratio of charged hadrons for $^{14}$N and $^{84}$Kr (at HERMES) as a function of the transverse momentum squared $p_T^2$. In the simulation we use the constituent-quark concept (5.35) for the prehadronic cross sections and a formation time $\tau_f = 0.5$ fm/$c$. In the simulation indicated by the dashed line we additionally assume that all elastic scatterings are isotropic in their center-of-mass frame. The data are taken from Ref. [Air03b].

the nuclear medium which are accompanied by gluon radiation. While the incoherent rescatterings can be interpreted intuitively as a random walk in transverse momentum space [Joh01], the coherent gluon radiation from different nucleons is subject to LPM-interference effects. The authors of Ref. [Kop03] have calculated the transverse momentum broadening that is caused by the multiple scattering of the struck parton before the prehadron-production time. Their calculation reproduces the strong increase of $R_M^h(p_T)$ for $p_T > 1$ GeV/$c$ and thus supports the interpretation in terms of a Cronin effect.

In our simulation we do not find any dependence of the charged hadron multiplicity ratio (6.36) on the photon virtuality $Q^2$. This is no surprise since in the ratio $R_M^h$ the $Q^2$ dependence of the primary electroproduction cross section cancels out and our prehadronic cross sections (5.35) do not depend on the virtuality of the photon. Therefore, an experimentally observed enhancement of $R_M^h$ with $Q^2$ could be interpreted as a signature for color transparency [Jai96, Kop01]. We show in Sec. 6.4.3 that indeed the
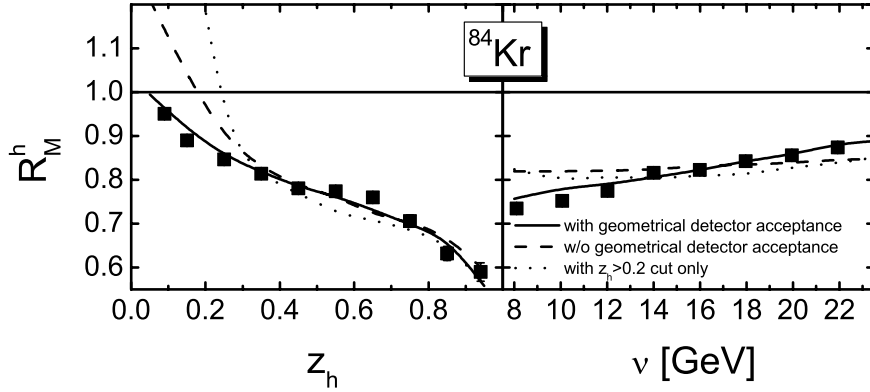
Figure 6.25: Influence of the HERMES detector geometry on the observed multiplicity ratios for a $^{84}$Kr target. In the simulation we use the constituent-quark concept (5.35) for the prehadronic cross sections and a formation time $\tau_f = 0.5$ fm/$c$. The solid line represents the result of our simulation when accounting for the geometrical acceptance of the HERMES detector. In the simulation indicated by the dashed line no acceptance cuts have been employed. The dotted line represents the result of a simulation where in addition to the detector acceptance the $E_h > 1.4$ GeV cut has been neglected. The data are taken from Ref. [Air03b].

simple constituent-quark ansatz for the prehadronic cross sections (5.35) overestimates the attenuation in the kinematic regime of the EMC experiment, i.e. at larger values of $\nu$ and $Q^2$.

**Acceptance cuts**

We now discuss how the geometrical acceptance of the HERMES detector and the kinematic cuts affect the multiplicity ratio (6.36). In Fig. 6.25 we compare the results of our simulation using the constituent-quark concept (5.35) and a formation time $\tau_f = 0.5$ fm/$c$ for the HERMES acceptance (solid line) in comparison to a $4\pi$-detector (dashed line). In both calculations we still account for all kinematic cuts in the HERMES experiment. As can be seen from the $z_h$ spectrum, a detector with full angular coverage (dashed line) will detect many more of the low-energy particles – produced in the FSI – which simply do not end up in the HERMES detector. As a result, the $\nu$ spectrum for a $4\pi$-detector is almost flat since an increase of the formation time with $\nu$ due to time dilatation not only reduces the attenuation but also the particle production in the FSI. According to our simulations the slope in the $\nu$ spectrum experimentally observed at HERMES partly arises because at lower photon energies particle production in the FSI is less forward peaked and, therefore, less particles are seen by the HERMES detector. Note that this problem is usually neglected in other approaches [Guo00, Wan01, Wan02, Wan03, Arl03, Acc03, Kop03] that intend to describe the observed multiplicity ratios. The dotted line in Fig. 6.25 shows the result of a simulation where in addition to the geometrical acceptance the $E_h > 1.4$ GeV cut has been neglected. As can be seen from the low $z_h$ part of the multiplicity ratio, one now detects even more of the low-$z_h$
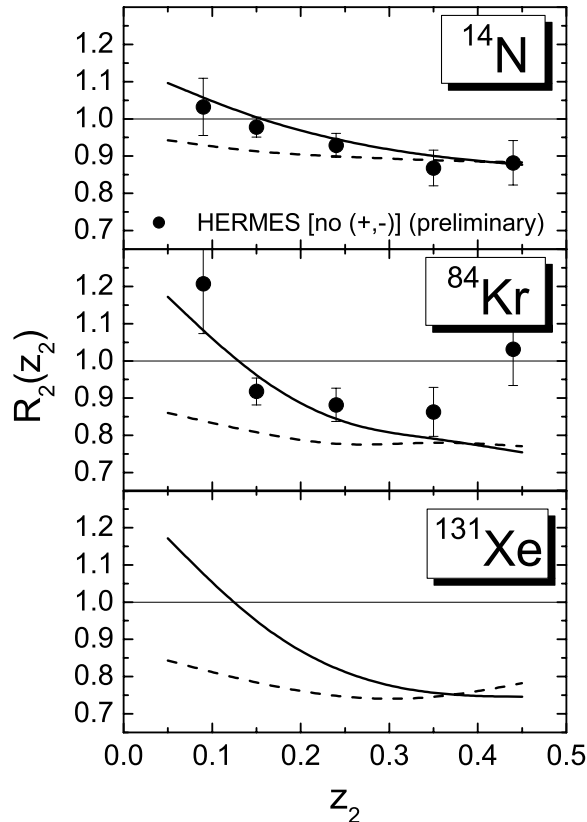
Figure 6.26: Double-hadron attenuation ratio $R_2$ for a $^{14}$N, $^{84}$Kr and $^{131}$Xe target as a function of the energy fraction $z_2$ of the subleading hadron. In the simulation we use the constituent-quark concept (5.35) for the prehadronic cross sections and a formation time $\tau_f = 0.5$ fm/$c$. To exclude contributions from $\rho^0$ decay into $\pi^+\pi^-$ the charge combinations '$+-$' and '$-+$' have been excluded both in experiment and in the simulation. The dashed line shows a calculation with a purely absorptive treatment of the FSI. The preliminary HERMES data are taken from Ref. [Nez04].

hadrons. Without the cut $z_h > 0.2$ the multiplicity ratio as a function of the photon energy rises to $R_M^h(\nu) \approx 1.5$.

Summarizing this paragraph we stress that one has to take the geometrical acceptance of the HERMES detector into account if one wants to draw conclusions from a comparison of experimental with theoretical results for the low-$z_h$ part and the $\nu$ dependence of the multiplicity ratio.

**Double hadron attenuation**

Before we turn to the individual attenuation of the various identified hadrons we compare our simulation with the recently measured double-hadron attenuation at HERMES [Nez04]. In each event only the two (charged *or* neutral) hadrons with the highest energies are considered. In the following we denote the hadron with the highest $z_h$ as the leading hadron and the other one as the subleading hadron. The experimental

observable is the double-hadron attenuation ratio

$$R_2(z_2) = \frac{\left.\frac{N_2(z_2)}{N_1}\right|_A}{\left.\frac{N_2(z_2)}{N_1}\right|_D}.$$

(6.42)

Here $N_2(z_2)$ denotes the number of events where the leading and subleading hadron carry the energy fraction $z_1 > 0.5$ and $z_2 < z_1$, respectively, and $N_1$ is the number of events where at least one of them has $z_h > 0.5$. The kinematic cuts are the same as for charged hadrons except for the Bjorken variable $x$, which now has the new boundary $x > 0.01$.

Fig. 6.26 shows the double-hadron multiplicity ratio (6.42) for $^{14}$N, $^{84}$Kr and $^{131}$Xe. To exclude contributions from $\rho^0$ decay into $\pi^+\pi^-$ the charge combinations '$+-$' and '$-+$' have been excluded both in experiment and in the simulation. The solid line shows the result of a full coupled-channel calculation using the constituent-quark concept (5.35) and the formation time $\tau_f = 0.5$ fm/$c$.

The shape of the spectrum is similar to that of $R_M^h(z_h)$ of the charged hadron multiplicity ratio shown in Fig. 6.23. The reason is quite simple: For the interpretation we discard for a moment the constant factors $N_1$ in Eq. (6.42) and the factors $N_e$ in Eq. (6.36) which have no influence on the shape of the $z_h$ dependence. The only difference between $N_h(z_h)|_A/N_h(z_h)|_D$ and $N_2(z_2)|_A/N_2(z_2)|_D$ then is that one restricts the detected hadron to the subleading particle in the latter case. If the subleading particle (with energy fraction $z_2$) of the initial $\gamma^*N$ reaction interacts with the nuclear environment, it will produce a bunch of low-energy particles. The *new* subleading hadron in the event then has a energy fraction $z_2' < z_2$. As for the usual charged hadron multiplicity spectrum the coupled-channel FSI shuffle strength from the high $z_h$ part to the low $z_h$ part of the spectrum. This is not the case for purely absorptive FSI (dashed line in Fig. 6.26).

As one can see, our coupled-channel calculations (solid line) – using the constituent-quark concept (5.35) and the formation time $\tau_f = 0.5$ fm/$c$ – are again in quantitative agreement with the experimental data apart from the last data point in the $^{84}$Kr data, which indicates a multiplicity ratio $R_2(z_2 = 0.5) \approx 1$. This behavior cannot be explained within our model.

As can be seen from Fig. 6.26, our calculations predict about the same double-hadron attenuation ratio for $^{131}$Xe and $^{84}$Kr. The reason is that the attenuation of leading and subleading hadrons increases in the same way when going from the krypton to the xenon target. Hence, the double-hadron attenuation ratio (6.42) stays roughly the same. Note, that this does not necessarily imply the same hadron attenuation for $^{84}$Kr and $^{131}$Xe. As we have pointed out in the discussion of Fig. 6.23, and as one can also see by comparing the multiplicity ratios for the two targets in Figs. 6.27 and 6.29, the hadron attenuation in the $^{131}$Xe nucleus is on average 5% larger than for $^{84}$Kr.

### Attenuation of identified hadrons

We finally consider the attenuation of $\pi^\pm$, $\pi^0$, $K^\pm$, $p$ and $\bar{p}$ in DIS of 27.6 GeV positrons off $^{20}$Ne, $^{84}$Kr and $^{131}$Xe nuclei. For the krypton and xenon target the cuts are the same as for charged hadrons plus the momentum cuts necessary for particle identification at HERMES [Air03b], i.e. 2.5 GeV/$c$ < $p_{\pi,K}$ < 15 GeV/$c$ and 4 GeV/$c$ < $p_{p,\bar{p}}$ < 15

GeV/$c$. The following cuts are different for the neon target [Elb03]: 2 GeV$< \nu <$ 24 GeV, 0.6 GeV/$c < p_\pi <$ 15 GeV/$c$ and 2 GeV/$c < p_K <$ 15 GeV/$c$.

For the moment we stick again to the prehadron concept (5.35) and the formation time $\tau_f = 0.5$ fm/$c$ in our simulation. Figs. 6.27 and 6.28 show the multiplicity ratios on $^{84}$Kr and $^{20}$Ne, respectively. The attenuation of pions is well described for the $^{84}$Kr nucleus while it is slightly too strong for the light $^{20}$Ne target. This is no surprise since for $^{84}$Kr our model already reproduced the multiplicity ratio of charged hadrons – dominated by pions – while the attenuation was too strong in the case of the lighter $^{14}$N nucleus.

The attenuation of $K^+$ mesons is well described for the heavier krypton target while it is in poor agreement with the $^{20}$Ne data. In the latter case the calculated multiplicity ratio is larger than 1 at small $z_h$ in contradiction to the experimental data. For both nuclei our simulation yields approximately the same attenuation for $K^-$ and $K^+$ mesons at large $z_h$. The reason for this is directly related to the $K^+$ and $K^-$ spectra in Fig. 4.29, which show that due to the quark content ($\bar{u}s$) the $K^-$ contain less quarks from the beam or target than the $K^+$. The few $K^-$ that are not solely made of quarks and antiquarks created from the vacuum in the string fragmentation carry (anti-)quarks from the resolved photon component or the nucleon sea. According to the constituent-quark concept (5.35) one has thus less prehadronic interactions of $K^-$. This is compensated by the larger $K^-$-nucleon cross section. In total this leads to a similar attenuation of $K^+$ and $K^-$. From Fig. 4.29 it can also be seen that a large part of the kaons at high $z_h$ stem from $\phi$ decay into $K^+K^-$. The attenuation of $K^\pm$ at high $z_h$, therefore, strongly depends on the FSI of the $\phi$ meson; this is in analogy to the attenuation of charged hadrons (pions) which are strongly affected by the FSI of the $\rho$ meson.

There is a further complication connected with the multiplicity ratio of kaons, which is neglected in a purely absorptive treatment of the FSI. The initial $\gamma^*N$ interaction produces many more pions and $\rho$ mesons than strange particles (cf. Fig. 4.29). These high-energy particles can produce secondary $K^+$ and $K^-$ in the nuclear FSI and thereby enhance the multiplicity ratio for $K^\pm$ at low $z_h$. This is illustrated by the dotted lines in Fig. 6.28 which shows the result of a purely absorptive treatment of the FSI, in which every particle that undergoes FSI is simply removed from the simulation. One clearly sees that kaon absorption in the FSI is compensated to a large extent by the production of kaons in the nuclear FSI of pions and $\rho$ mesons. For $z_h \lesssim 0.35$ the $K^+$ production exceeds the absorption in the light $^{20}$Ne and leads to a multiplicity ratio larger than 1. This is not the case for the $^{84}$Kr nucleus which is large enough to also absorb some of the secondary kaons. Of course this effect strongly depends on the strangeness production cross section used in the FSI. Unless one does not have all these coupled-channels under control it is, therefore, hard to draw any conclusion from the kaon attenuation in DIS off nuclei.

From Fig. 4.29 one also sees that there are only very few protons that contain no quarks from the beam or target because diquark-antidiquark creation is strongly suppressed in the string fragmentation due to the relatively large diquark masses. The latter also explains why most protons contain two of the original quarks, i.e. the diquark from the target nucleon. These remnants have a very large prehadronic cross section according to the constituent-quark concept (5.35). As a result, the proton multiplicity
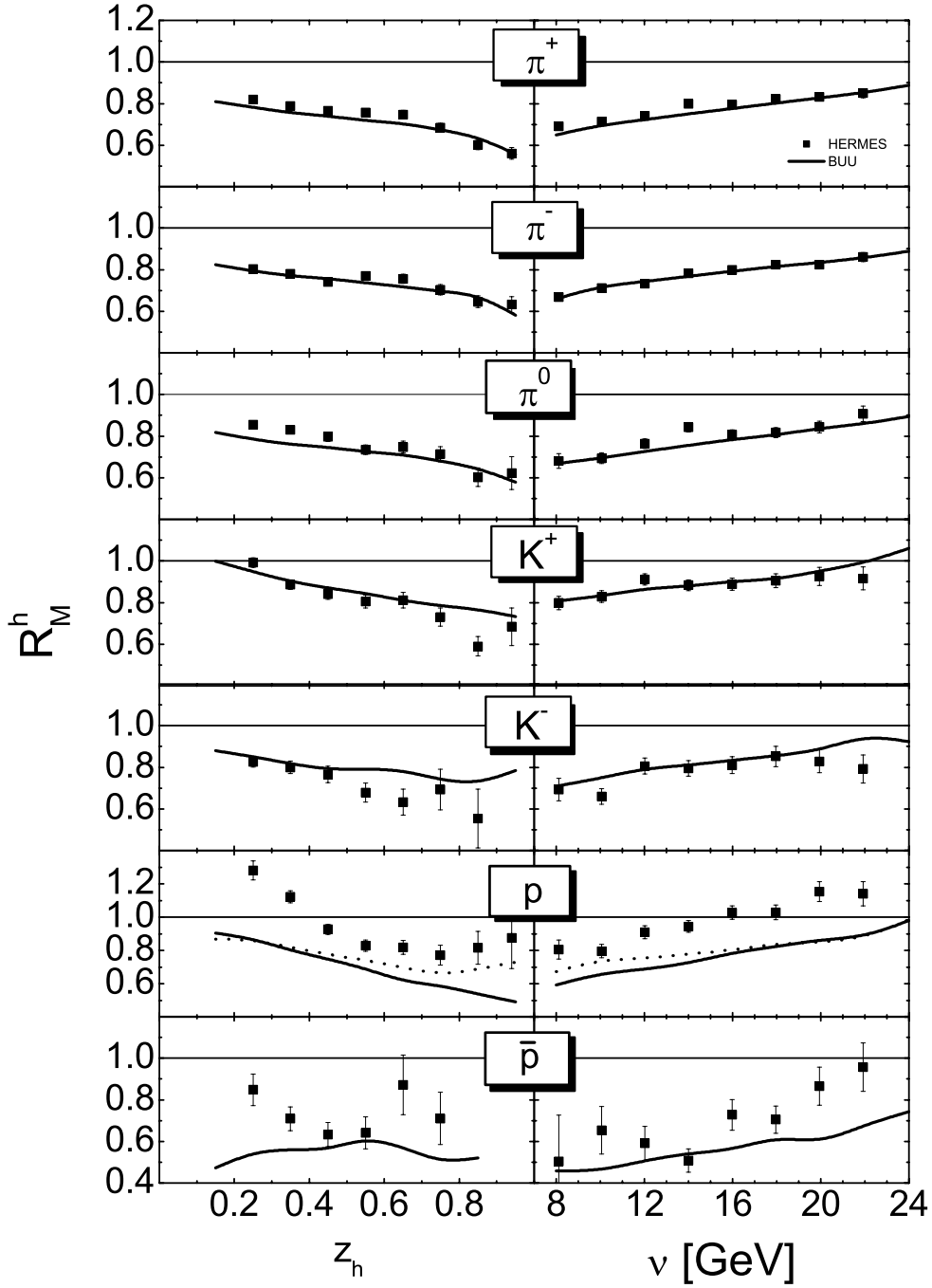
Figure 6.27: Multiplicity ratios of $\pi^{\pm,0}$, $K^{\pm}$, $p$ and $\bar{p}$ for a $^{84}$Kr nucleus (at HERMES) as a function of the hadron energy fraction $z_h = E_h/\nu$ and the photon energy $\nu$. The solid line represents the result of a simulation, where we use the constituent-quark concept (5.35) for the prehadronic cross sections and a formation time $\tau_f = 0.5$ fm/$c$. The dotted line in the proton spectrum indicates the result of a simulation where all $\gamma^* N$ events are created by PYTHIA. The data are taken from Ref. [Air03b].
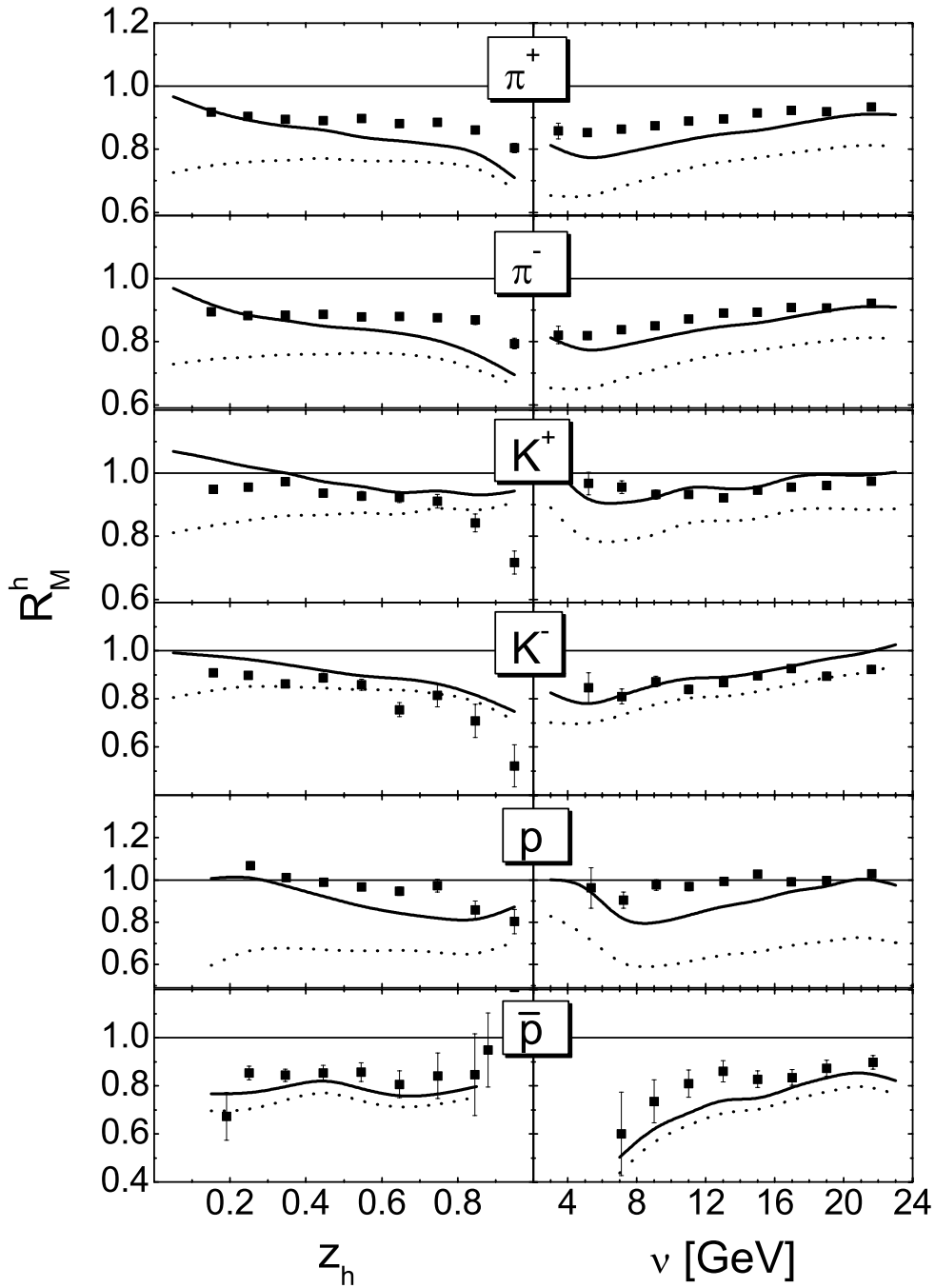
Figure 6.28: Multiplicity ratios of $\pi^{\pm}$, $K^{\pm}$, $p$ and $\bar{p}$ for a $^{20}$Ne nucleus (at HERMES) as a function of the hadron energy fraction $z_h$ and the photon energy $\nu$. The solid line represents the result of a simulation where we use the constituent-quark concept (5.35) for the prehadronic cross sections and a formation time $\tau_f = 0.5$ fm/$c$. The dotted line represent the result of a simulation with a purely absorptive treatment of the FSI. The data are taken from Ref. [Elb03].
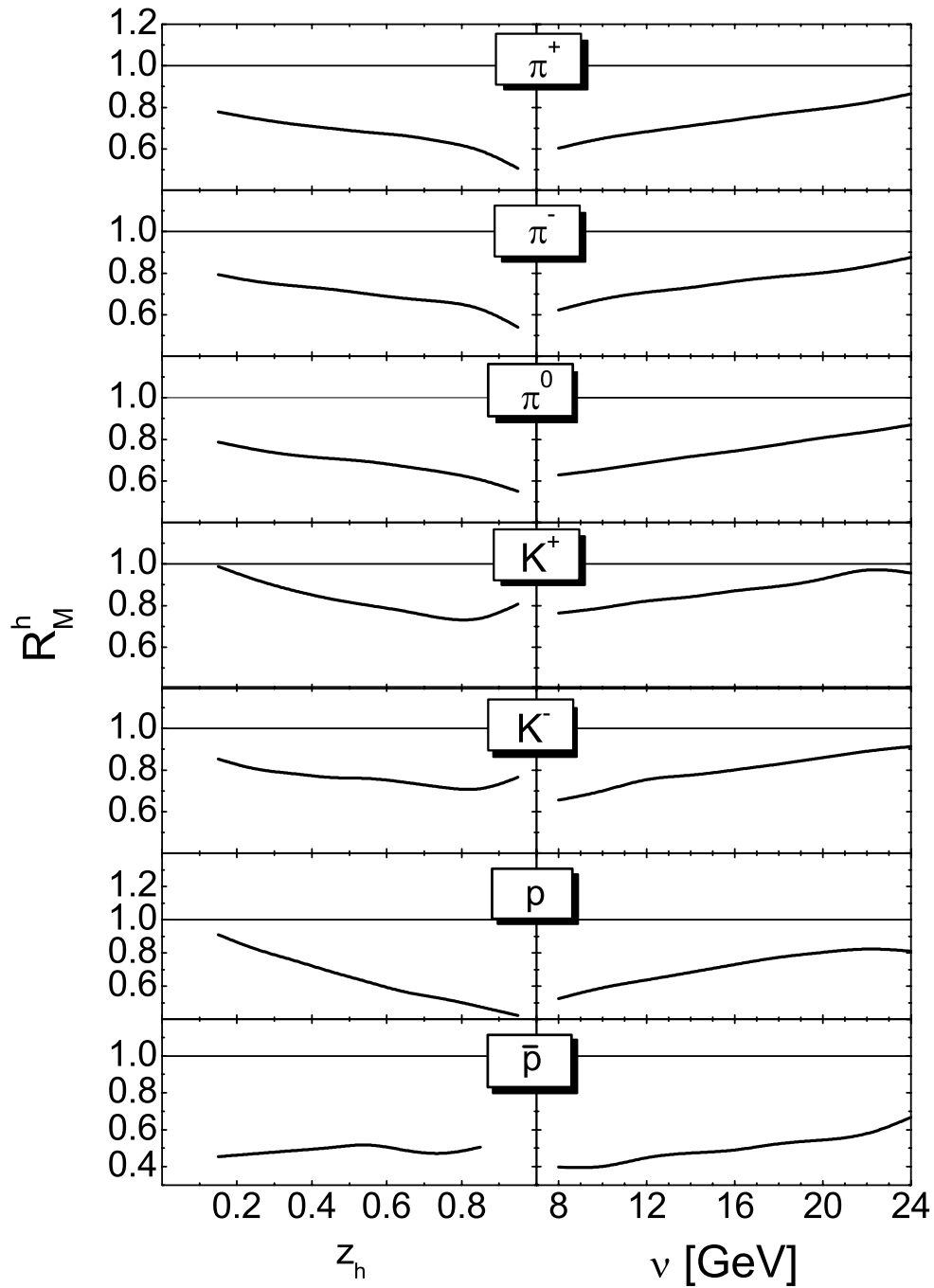
Figure 6.29: Predictions for the multiplicity ratios of $\pi^{\pm}$, $\pi^0$, $K^{\pm}$, $p$ and $\bar{p}$ for a $^{131}$Xe nucleus (at HERMES) as a function of the hadron energy fraction $z_h$ and the photon energy $\nu$. In the simulation we use the constituent-quark concept (5.35) for the prehadronic cross sections and a formation time $\tau_f = 0.5$ fm/$c$.

ratio comes out too small for both the $^{84}$Kr and the $^{20}$Ne nucleus. As discussed in Sec. 4.3, the Lund model points to a larger formation time for protons than for the lighter pions, $\rho$ mesons and kaons. However, as we have shown in Fig. 6.23, a further increase of the formation time to $\tau > 0.5$ fm$/c$ does not change our result at large $z_h$ as long as the production time is zero. Since proton attenuation at large $z_h$ is solely due to prehadronic interactions this either points towards a smaller prebaryonic cross section or a finite production time.

A further problem connected with the proton spectra is the strong increase of the multiplicity ratio for $z_h < 0.4$ which is seen in the experimental $^{84}$Kr data. At small proton energies $R_M^p$ becomes larger than 1 which might be understood in our model by a slowing down of high-energy protons in the FSI. Alternatively, protons might be knocked out of the nucleus in the FSI of a high-energy meson produced in the primary $\gamma^* N$ interaction. We do indeed see these effects in our simulation, however, in both cases the experimental momentum cut $p_p > 4$ GeV$/c$ removes most of these protons from the acceptance. Thus, the protons in our transport simulation loose too much energy per collision in the (pre-)hadronic FSI scenario.

As we have pointed out in the discussion of Fig. 6.9 the use of FRITIOF in the simulation of $\gamma^* N$ events has a small effect on the proton spectra. In Fig. 6.27 we, therefore, also show the proton attenuation in a simulation where *all* $\gamma^* N$ interactions above $W_{\rm PY} = 3$ GeV are simulated by PYTHIA. One observes that besides a slight improvement at large $z_h$ and low photon energies $\nu$ this has no effect on our result.

Within our simulation the attenuation of antiprotons also comes out slightly too large in the (pre-)hadronic FSI scenario. We find that the antiprotons with $z_h \gtrsim 0.5$ are mainly beam or target remnants that contain an antiquark from the resolved photon or the nucleon sea, whereas most of the antiprotons with $z_h \lesssim 0.5$ are solely made of antiquarks that are produced in the fragmentation of the string excited in the $\gamma^* N$ interaction. According to the constituent-quark concept (5.35) the attenuation of antiprotons with $z_h < 0.5$ is, therefore, only caused by hadronic FSI after $\tau_f$.

In Fig. 6.29 we also show predictions for the attenuation of identified hadrons on a $^{131}$Xe target. In the simulation we have used the constituent-quark concept (5.35) and a formation time $\tau_f = 0.5$ fm$/c$. By comparing the multiplicity ratios $R_M^h$ of negatively and positively charged pions for $^{20}$Ne, $^{84}$Kr, and $^{131}$Xe nuclei, we find that the attenuation $(1 - R_M^h)$ scales like $A^\alpha$ with an exponent $\alpha = 0.22$ and 0.29 at $z_h = 0.95$, respectively. This scaling exponent is slightly smaller than the one that we have extracted before from the attenuation of charged hadrons in $^{14}$N, $^{84}$Kr, $^{131}$Xe nuclei. This is no contradiction since, as pointed out before, the scaling behavior is strongly influenced by numerous effects like the nonuniform density distributions in nuclei, isospin asymmetries in nuclei, formation lengths of particles, etc. Consequently, the scaling exponent is in general not unique for the various particle species as we have just seen for $\pi^+$ and $\pi^-$. We note that a scaling of the attenuation with the target mass $\sim A^{2/3}$, as predicted by Refs. [Guo00, Wan01, Wan02, Wan03], would imply an increase of about 34% when using $^{131}$Xe instead of $^{84}$Kr.

### Lund production and formation times

Before we consider the prehadron-production times extracted from the fragmentation routines implemented in JETSET we discuss the effect of the $z_h$ dependent production
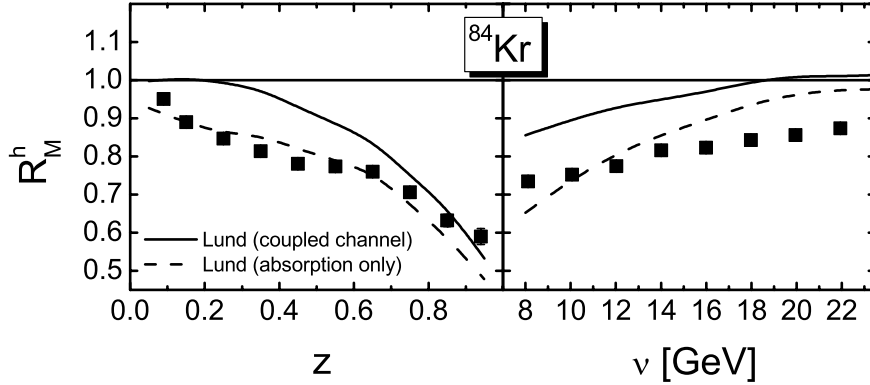
Figure 6.30: Calculated multiplicity ratios of charged hadrons for a $^{84}$Kr target assuming the finite production time $t_p$ given by Eq. (4.22). For $t \geq t_p$ the prehadrons interact with their full hadronic cross section. The dashed line shows the result of a simulation with a purely absorptive treatment of the FSI. The solid line represents the coupled-channel result.

time $t_p$ (in the lab frame) of Ref. [Bia87], i.e. Eq. (4.22). We point out that in our calculation – due to technical reasons – all particles that emerge from the primary $\gamma^* N$ interaction start to propagate from the interaction vertex, while the production time $t_p$ only affects the beginning of their interactions with the nuclear medium. One may therefore expect slight deviations from the real reaction geometry, where the excited string propagates over a small distance prior to fragmentation. In the following we assume no interaction before $t_p$ and the full hadronic cross section for prehadrons for $t \geq t_p$, i.e. there is no dependence on the formation time $t_f$ anymore. The dashed line in Fig. 6.30 represents the result of a Glauber-like treatment of the FSI where every time a prehadron interacts with another particle it is removed from the outgoing channel. As the authors of Ref. [Acc03] we get a good description of the $z_h$ dependence of the multiplicity ratio. However, the $\nu$ spectrum is not attenuated strongly enough at higher values of $\nu$ (r.h.s. of Fig. 6.30). The solid curves show the effect of the coupled channels, i.e., a particle is not only absorbed in a collision but produces a bunch of low energy particles, thereby shifting strength to the low $z_h$ part of the spectrum and thereby underestimating the attenuation at low $z$. Similarly, the attenuation is also too weak in the $\nu$-spectrum. Since an additional formation time with reduced cross sections would further enhance these discrepancies, we conclude that the data cannot be described with the production time (4.22).

We now test the result of a simulation where both the production times of the prehadrons and the formation time $\tau_f$ of each individual particle are explicitly extracted from the corresponding string fragmentation in JETSET (cf. Fig. 4.16). As described in Sec. 4.3 there are in principle three time scales involved in the Lund fragmentation process: i) The production proper time $\tau_{p1}$ of the hadron's first constituent, which is obviously zero if the hadron contains a constituent from a string end, ii) the production proper time $\tau_{p2}$ when the second constituent is produced and a color neutral object is formed, and iii) the formation proper time $\tau_f$ when the two world lines of the
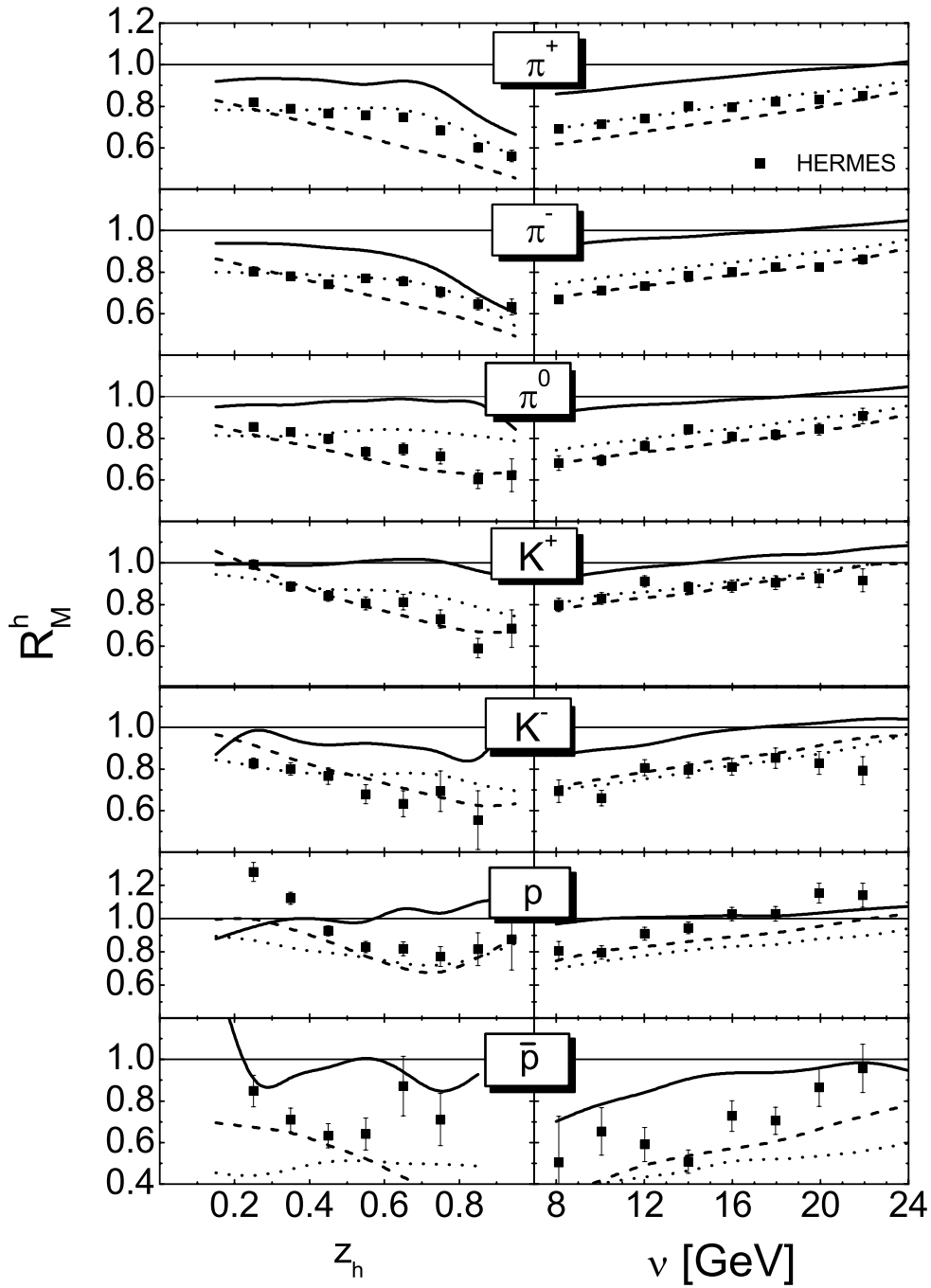
Figure 6.31: Multiplicity ratios of $\pi^{\pm}$, $\pi^0$, $K^{\pm}$, $p$ and $\bar{p}$ for a $^{84}$Kr nucleus (at HERMES) as a function of the hadron energy fraction $z_h$ and the photon energy $\nu$. In the simulation we use the proper times $\tau_{p_2}$ (solid line), $0.2\tau_{p_2}$ (dotted line) and $\tau_{p_1}$ (dashed line) from the JETSET routines as the prehadron-production time. The prehadronic cross section is set to the full hadronic cross section and interactions before the production time are neglected.

constituents cross for the first time.

One could now proceed and introduce two effective cross sections: $\sigma_1$ which accounts for the 'partonic' interaction between $\tau_{p1}$ and $\tau_{p2}$, and $\sigma_2$ which accounts for the 'prehadronic' interactions of the color neutral object between $\tau_{p2}$ and $\tau_f$. We first neglect the 'partonic' interactions ($\sigma_1 = 0$) and set the 'prehadronic' cross section $\sigma_2$ equal to the full hadronic cross section $\sigma_h$. In such a scenario we are no longer sensitive to the formation time $\tau_f$ but only on $\tau_{p2}$. The solid lines in Fig. 6.31 show the result of such a simulation for a $^{84}$Kr target. Since the resulting attenuation is much too weak we conclude that the strong FSI have to start earlier. Note that a reduction of $\sigma_2$ will further enhance the discrepancy with experimental data. To achieve reasonable results for the multiplicity ratio one has to rescale $\tau_{p2}$ by about a factor of 0.2 (dotted line), which is quite dramatic. According to the Lund model (cf. Eq. (4.28)) this has to be interpreted as an *increase* of the string tension $\kappa$ by an unreasonably large factor of about *five* in the nuclear medium. Note that, in a partial deconfinement of color in the nuclear medium would lead to a decrease of the string tension as pointed out in Sec. 6.4.1. Setting $\sigma_1$ to zero means implies to neglect any interaction of the nucleon debris with the nuclear medium between the moment of the $\gamma^* N$ interaction and $\tau_{p2}$. This might be a problem, since the hadronic string that is produced in the DIS may interact with a hadronic cross section right from the beginning [Cio02].

The average size of the prehadron-production times of the gluon-bremsstrahlung model [Kop03] is about a factor of ten smaller than the times $t_{p2}$ extracted from JETSET. In fact, their average size is rather compatible with $t_{p1}$. If one assumes that strong FSI already set in right after $\tau_{p1}$ and sets $\sigma_1 = \sigma_2 = \sigma_h$ one gets the result indicated by the dashed curves in Fig. 6.31, which are in satisfactory agreement with the experimental data. However, such a large interaction cross section $\sigma_1$ is definitely not of perturbative nature. Furthermore, this recipe again implies that all beam and target remnants can interact right after the photon-nucleon interaction since the production time $\tau_{p1}$ of their first constituent is zero. In fact, this scenario is not much different from our constituent-quark ansatz discussed before. The solid symbols in Fig. 6.20 indicate the average starting times of the prehadronic and hadronic interactions according to the constituent-quark model (5.35) with $\tau_f = 0.5$. The $z_h$ dependence of these two times has to be compared with $t_{p1}$ (dash-dot-dotted line) and $t_f$ (dash-dotted line), respectively. In both cases the shape looks quite similar while the average times of our constituent-quark concept are somewhat smaller. The latter is partly compensated by the reduced prehadronic cross section, cf. Eq. (5.35). Due to time dilatation the production times $t_{p1}$ are in general already of the order of the nuclear radius. This explains why the beam and target remnants – for which $t_{p1} = 0$ – dominate the shape of the spectra.

## 6.4.3 Hadron attenuation at EMC energies

In this section we test different space-time pictures of hadronization in comparison to the EMC data with 100 and 200 GeV muon beams [Ash91]. In the previous section we have seen that almost all of the HERMES data can be described with the simple prehadron concept of Sec. 5.3.2, i.e. setting the production time $\tau_p$ to zero for all hadrons and using the constituent-quark concept (5.35) for the prehadronic cross
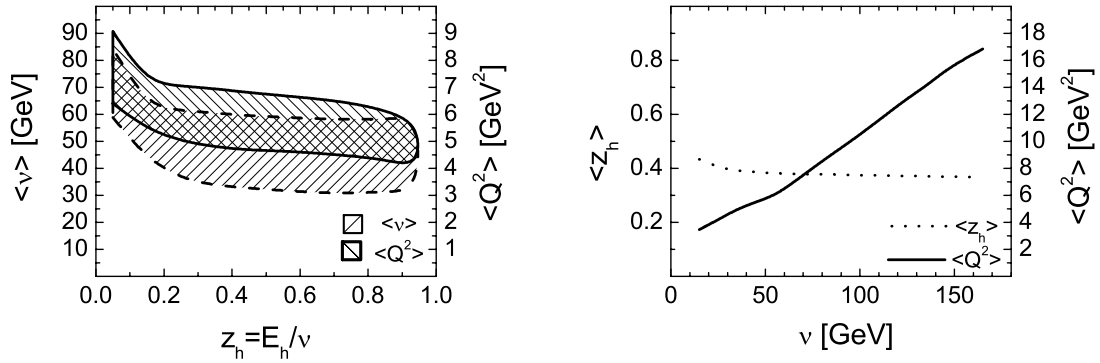
Figure 6.32: Model predictions for the average values of the kinematic variables in charged hadron production off deuterium at EMC energies. The shaded areas are bounded by simulations using a 100 GeV (lower boundary) and 200 GeV (upper boundary) muon beam. *Left:* $\langle\nu\rangle$ and $\langle Q^2\rangle$ as a function of $z_h$ compared to the experimental values for a $^{84}$Kr target. *Right:* Same for $\langle z_h\rangle$ and $\langle Q^2\rangle$ as a function of $\nu$.

sections during the formation time $\tau_f$. Obviously, this picture can only represent a rough approximation to the real hadronization process. Neither is it very likely that the string fragments convert *instantaneously* into color neutral prehadrons nor do the cross sections *instantaneously* jump from the rescaled values (5.35) to the full hadronic size.

The kinematic regime of the EMC experiment, which uses a 100 GeV (200 GeV) muon beam, is different from that of the HERMES experiment. Here, the kinematic cuts are $Q^2 > 2\,\text{GeV}^2$, $W > 4\,\text{GeV}$, $x > 0.02$, $10\,\text{GeV}< \nu < 85\,\text{GeV}$ ($30\,\text{GeV}< \nu < 170$ GeV) and $E_h > 3\,\text{GeV}$. In addition we again account for the angular acceptance of detector, i.e. $\pm 5°$ horizontally and $\pm 8°$ vertically [Alk81]. In Fig. 6.32 we show the resulting values for the average kinematic variables $\langle\nu\rangle$, $\langle Q^2\rangle$ and $\langle z_h\rangle$ as function of $z_h$ and $\nu$ respectively. The average photon energy is about five times larger than in the HERMES experiment. Also the average values of $Q^2$ in the various $z_h$ bins are twice as large as at HERMES energies. At large photon energies $\langle Q^2\rangle$ increases to 17 GeV$^2$.

In the upper panel of Fig. 6.33 we show the EMC result for the multiplicity ratio of charged hadrons on a $^{63}$Cu target as a function of the hadron energy fraction $z_h$. The solid line shows the result for the simple prehadron concept (5.35) with the constant formation time $\tau_f$. The shaded area indicates the region between the results of calculations using 100 GeV and 200 GeV muon beam energy. Obviously, we get a much too strong attenuation for $z_h > 0.3$. This either implies that the prehadronic interactions set in too early or that the cross sections (5.35) are too large.

The dashed line shows the result for a simulation when assuming that during $\tau_f$ the prehadron cross section increases quadratically in proper time $\tau$ from zero to the asymptotic value $\sigma_h$. Such an ansatz can be motivated by color transparency, which states that the cross sections of the color neutral prehadron scales with its diameter squared. While giving the right attenuation for EMC energies, such an ansatz fails to explain the HERMES data as long as the initial cross section is exactly zero (see lower panel of Fig. 6.33). For the calculation indicated by the dash-dotted line in the lower panel of Fig. 6.33 we assumed an initial prehadronic cross section $0.3\sigma_h$
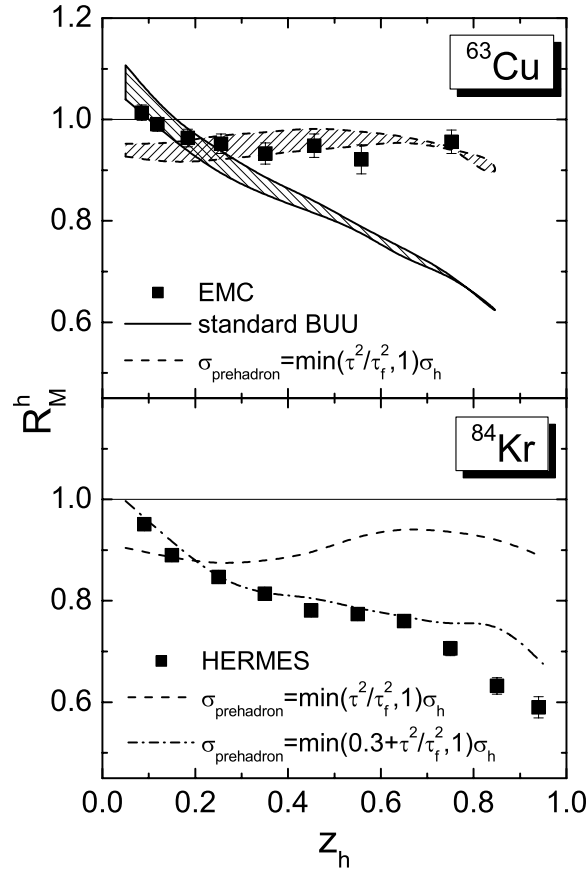
Figure 6.33: *Upper panel:* Multiplicity ratio of charged hadrons for a $^{63}$Cu target as a function of the fractional energy $z_h$ in the kinematic regime of the EMC experiment. The shaded areas are bounded by simulations using a 100 GeV (lower boundary) and 200 GeV (upper boundary) muon beam. The data are taken from Ref. [Ash91]. *Lower panel:* Multiplicity ratio of charged hadrons for a $^{84}$Kr target as a function of the fractional energy $z_h$ in the kinematic regime of the HERMES experiment. The data are taken from Ref. [Air03b]. The solid line shows the result of our simulation using the constituent quark concept (5.35) for the prehadronic cross sections and a formation time $\tau_f = 0.5$ fm/$c$. In the simulation represented by the dashed line we assumed a prehadronic cross section increasing quadratically in proper time during $\tau_f = 0.5$ fm/$c$ from zero up to the full hadronic size. The dash-dotted line represents a simulation where the prehadronic cross section increases quadratically in proper time from $0.3\sigma_h$ to the full hadronic cross section.

followed by a quadratic increase in proper time up to the full hadronic value $\sigma_h$. The difference between the initial prehadronic cross sections at HERMES and EMC might be explained if one assumes that the cross section right after the $\gamma^* N$ interaction is set by the resolution of the virtual photon, i.e. $Q^2$. Indeed, the average values of $Q^2$ in the EMC experiment are more than twice as large as at HERMES energies. However, the HERMES data [HERM] do not indicate a strong enough $Q^2$ dependence of the multiplicity ratio to explain such a dramatic difference between the two 'initial' values for the prehadron cross section.
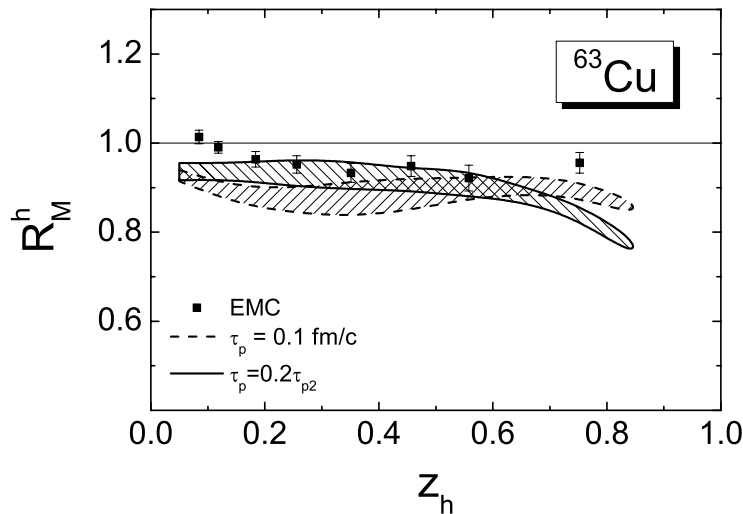
Figure 6.34: Multiplicity ratio of charged hadrons for a $^{63}$Cu target as a function of the fractional energy $z_h$ in the kinematic regime of the EMC experiment. The shaded areas are bounded by simulations using a 100 GeV (lower boundary) and 200 GeV (upper boundary) muon beam. The data are taken from Ref. [Ash91]. The dashed line shows the result of our simulation using a constant prehadron production time $\tau_p = 0.1$ fm/$c$. In the calculation indicated by the solid line we used the Lund production time $\tau_p = 0.2\tau_{p2}$, where $\tau_{p2}$ has been directly extracted from JETSET. In both calculation we set the prehadronic cross section equal to the full hadronic cross section and neglect interactions before the production time.

In Sec. 6.4.2 we have shown that, as long as one neglects a strong partonic energy loss [Guo00, Wan01, Wan02, Wan03, Arl03] right after the $\gamma^* N$ interaction, the (pre) hadronic interactions have to set in very early (cf. Fig. 6.22) to explain the various HERMES data. Since the Lorentz $\gamma$ factors involved in the EMC experiment are about five times larger than at HERMES energies, a finite (but small) production time will have a larger impact on the calculated multiplicity ratios. In Fig. 6.34 we, therefore, also show the results of a calculation with a constant production time $\tau_p = 0.1$ fm/$c$ as well as the production time $\tau_p = 0.2\tau_{p2}$ with $\tau_{p2}$ extracted directly from JETSET. For simplicity we neglect all (partonic) interactions before the production time of the prehadrons and set the prehadronic cross to the full hadronic cross section $\sigma_h$.

The result for $\tau_p = 0.1$ fm/$c$ in the kinematic region of the HERMES experiment is shown in Fig. 6.22 and yields a too weak attenuation at large $z_h$. An additional formation time with reduced cross sections would further enhance this discrepancy. On the other hand, the production time $\tau_p = 0.1$ fm/$c$ is still too small to give the right attenuation at EMC energies as can be seen from the dashed line in Fig. 6.34.

In Sec. 6.4.2 we have found that using $\tau_{p1}$ as the prehadron production time yields a satisfactory description of the HERMES data. However, using $\tau_{p1}$ as the prehadron production time leads to the same problem observed for our constituent quark concept in Fig. 6.33, i.e. a too strong attenuation of the high-$z_h$ hadrons. The reason is again the strong prehadronic interactions of the beam and target remnants right after the
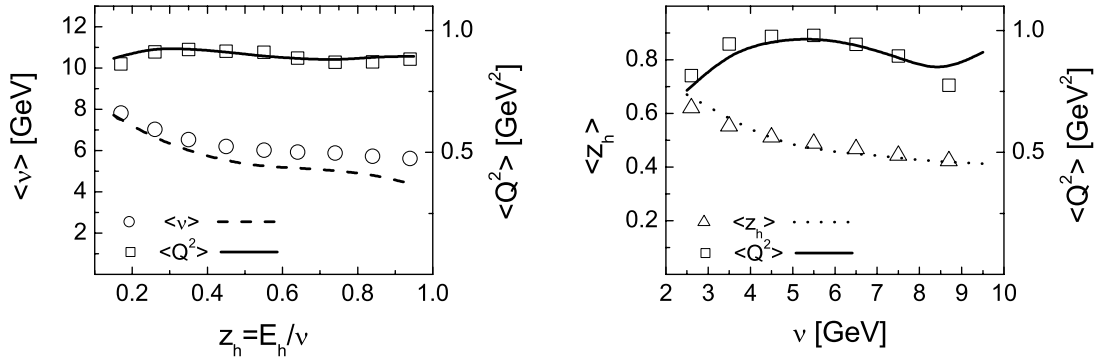
Figure 6.35: Model predictions for the average values of the kinematic variables in charged hadron production off $^{84}$Kr in comparison with the experimental numbers at HERMES [Nez04] using the 12 GeV positron beam. For the calculation we use the formation time $\tau_f = 0.5$ fm/$c$ and the constituent-quark concept (5.35) for the prehadronic cross sections. *Left:* $\langle \nu \rangle$ and $\langle Q^2 \rangle$ as a function of $z_h$ compared to the experimental values for a $^{84}$Kr target. *Right:* Same for $\langle z_h \rangle$ and $\langle Q^2 \rangle$ as a function of $\nu$.

$\gamma^* N$ interaction.

When setting the prehadron production time to $0.2\tau_{p2}$ (solid line in Fig. 6.34), we observe again a slightly too strong attenuation. However, this concept is in better agreement with the experimental data at EMC energies than our previous approaches.

In summary, it does not seem to be possible to simultaneously describe both the HERMES and the EMC data with (pre-)hadronic FSI only, as long as one does not account for additional effects like color transparency.

## 6.4.4   Hadron attenuation at Jefferson Lab energies

In the previous sections we have shown that most features of the HERMES data arise because of (pre-)hadronic FSI while the EMC experiment points to new phenomenons at *higher* energies. To confirm that our excellent description of the HERMES observables was not just a lucky coincidence it would be nice if we could also test our model at *lower* energies.

### HERMES at 12 GeV

The CLAS collaboration at Jefferson Lab is currently investigating the attenuation of hadrons in DIS of a 5 GeV electron beam incident on various nuclear targets [WBr02, KWa04] but there is no data available yet. However, the HERMES collaboration has also looked into DIS off $^{14}$N and $^{84}$Kr at about half of the maximum positron-beam energy, i.e. 12 GeV [Nez04]. This coincides with the electron beam energy that will be reached at Jefferson Lab after the upgrade of the electron accelerator [Arr03, WBr03].

In the HERMES experiment at $E_{\text{beam}} = 12$ GeV basically the same cuts as for the 27.6 GeV beam on $^{20}$Ne have been applied: $W > 2$ GeV, $\nu > 2$ GeV, $y < 0.85$ as well as $z_h > 0.2$ except for the $z_h$ spectra. However, some of the experimental cuts
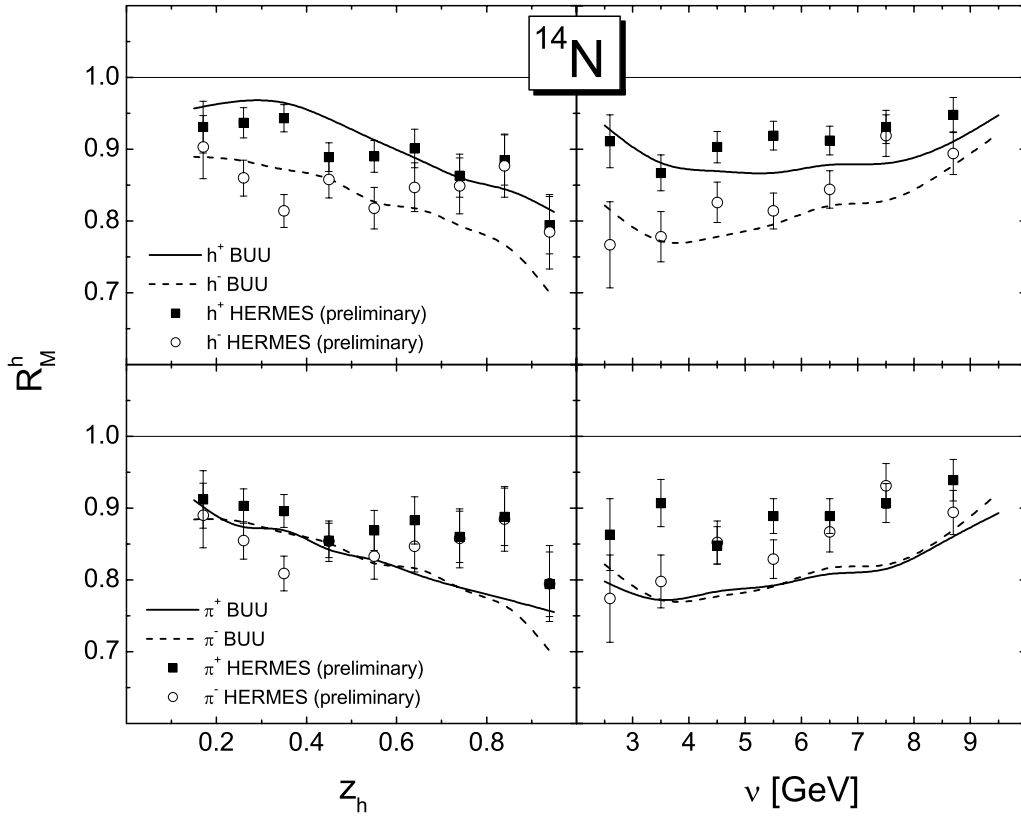
Figure 6.36: Calculated multiplicity ratio of positively and negatively charged hadrons (*upper panel*) and positive and negative pions (*lower panel*) for a $^{14}$N target when using a 12 GeV electron beam at HERMES. For the calculation we use the formation time $\tau_f = 0.5$ fm/$c$ and the constituent-quark concept (5.35) for the prehadronic cross sections. The data are taken from Ref. [Nez04].

had to be released because of the lower statistics. The lower limit of $Q^2$ was shifted from 1 GeV$^2$ to 0.5 GeV$^2$ and the lower cut on Bjorken $x$ was removed completely. In addition the lower limit of the hadron momenta was required to be 1 GeV/$c$ for all hadron species.

We have used these cuts in a simulation at 12 GeV positron-beam energy and again accounted for the geometrical acceptance of the HERMES detector. In our calculation we use the prehadron concept (5.35) and a formation time $\tau_f = 0.5$ fm/$c$ which yields an excellent description of most features of the HERMES data at higher beam energy. In Fig. 6.35 we show the average kinematic variables $\langle Q^2 \rangle$, $\langle \nu \rangle$ and $\langle z_h \rangle$ for a krypton target as a function of $z_h$ and $\nu$ respectively. It turns out that, also in the lower kinematic regime, our model perfectly reproduces the kinematics. For the $^{14}$N target we find a similar good agreement.

The calculated $z_h$ and $\nu$ dependence of the multiplicity ratios $R_M^h$ are shown in Figs. 6.36 and 6.37 for a $^{14}$N and a $^{84}$Kr target, respectively. We compare both with the data on positively (solid lines) and negatively (dashed lines) charged hadrons and pions. Considering, the fact that we did not change any aspect of our model we get an astonishingly good description of all of the experimental data in this very different
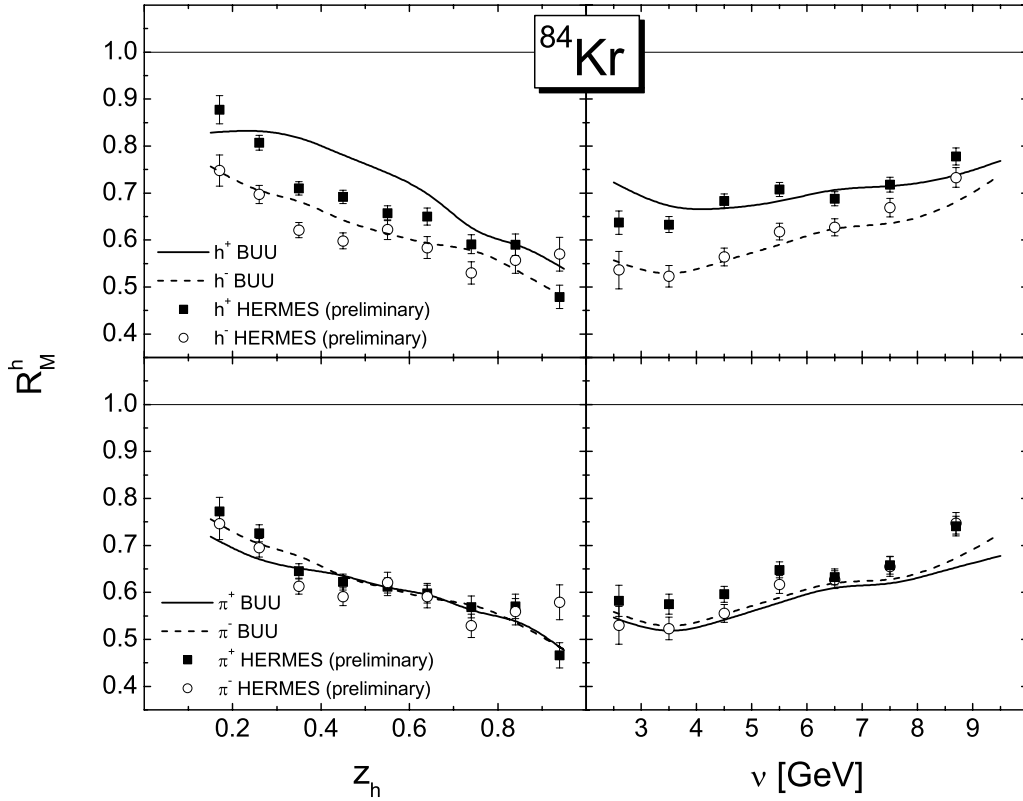
Figure 6.37: Calculated multiplicity ratio of positively and negatively charged hadrons (*upper panel*) and positive and negative pions (*lower panel*) for a $^{84}$Kr target when using a 12 GeV electron beam at HERMES. For the calculation we use the formation time $\tau_f = 0.5$ fm/$c$ and the constituent-quark concept (5.35) for the prehadronic cross sections. The data are taken from Ref. [Nez04].

kinematic regime. Note that both the average photon energy $\langle \nu \rangle$ and the average virtuality $\langle Q^2 \rangle$ are reduced by a factor of two compared to our previous calculations, cf. Fig. 6.21.

The attenuation for both nuclei is in average about 10–15 % larger than for $E_{\text{beam}} = 27.6$ GeV mainly because of two reasons: First of all, time dilatation is less pronounced at smaller energies and therefore more hadrons form inside the nucleus. Since the hadronic cross section is in general larger than the prehadronic one, the hadrons are subject to stronger FSI. The second reason for the stronger attenuation, especially at small $z_h$, is the experimental $p_h$ cut which removes a large fraction of the secondary particles from the acceptance. From Fig. 6.35 on sees that the average photon energy is only about 6 GeV. Even if a primarily produced hadron carries a large fraction of the photon energy, it is very unlikely that the secondaries of a FSI fly into the detector and, in addition, have momenta larger than 1 GeV. As a result, the characteristic strong increase of the multiplicity ratio at small $z_h$ is less pronounced as for the 27.6 GeV positron beam.

Like before the attenuation of pions and charged hadrons is stronger for the heavier krypton nucleus because of its larger radius. While the attenuation is the same for
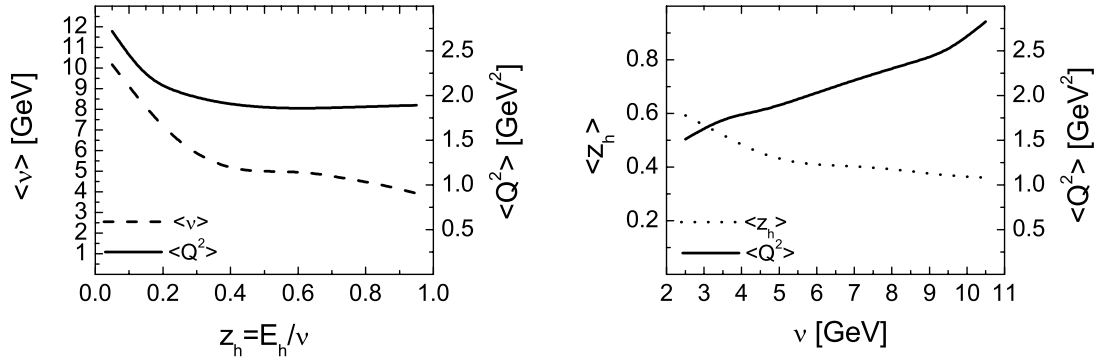
Figure 6.38: Model predictions for the average values of the kinematic variables in charged hadron production off deuterium using a 12 GeV electron beam and the CLAS detector. This kinematic regime corresponds to the one that will be available at Jefferson Lab after its upgrade. *Left:* $\langle \nu \rangle$ and $\langle Q^2 \rangle$ as a function of $z_h$. *Right:* Same for $\langle z_h \rangle$ and $\langle Q^2 \rangle$ as a function of $\nu$. Note that as usual the cut $z_h > 0.2$ is applied for the $\nu$ dependence.

positive and negative pions we see a difference between the positively and negatively charged hadrons. This is solely due to the different attenuation of protons – that contribute to the positive hadrons spectrum – and the contamination by protons that are knocked out of the nucleus in the FSI.

## Jefferson Lab at 12 GeV

Based on our successful description of the 12 GeV HERMES data, we now go ahead and make predictions for the observed particle spectra at Jefferson Lab after the 12 GeV upgrade. We use the same experimental cuts as before except for the photon virtuality which will be restricted to $Q^2 > 1$ GeV$^2$ [WBr]. In addition we account for the larger geometrical acceptance of the CLAS detector which covers angles from 6° to 147°. We therefore expect to see many more of the low-$z_h$ particles that are produced in the FSI and simply miss the detector in the HERMES experiment, cf. Fig. 6.25.

   Before we turn to the multiplicity ratio we again discuss the average kinematic variables $\langle Q^2 \rangle$, $\langle \nu \rangle$ and $\langle z_h \rangle$ as a function of $z_h$ and $\nu$ respectively. Fig. 6.38 shows that the average value of $Q^2$ is considerably larger than in the HERMES experiment at 12 GeV. The reason is not only the different lower $Q^2$ cut but also the extension of the detector acceptance to very large angles. In the HERMES experiment the scattering angle $\theta$ of the electron was limited to the very forward direction which strongly affected the maximum value of $Q^2$, cf. Eq. (D.2). The larger geometrical coverage also decreases the average value of $z_h$ because more of the low-energy particles reach the detector. Note that as usual the cut $z_h > 0.2$ is applied for the $\nu$ dependence. Otherwise we would end up with even a larger difference between the HERMES and the Jefferson Lab result on $\langle z_h \rangle$. The different angular acceptance also gives a natural explanation for the larger average photon energy at HERMES since the probability for a hadron to fly into the HERMES forward detector increases with photon energy.

   In Fig. 6.39 we show the calculated multiplicity ratio $R_M^h$ for $\pi^\pm$, $\pi^0$, $K^\pm$, $K^0$
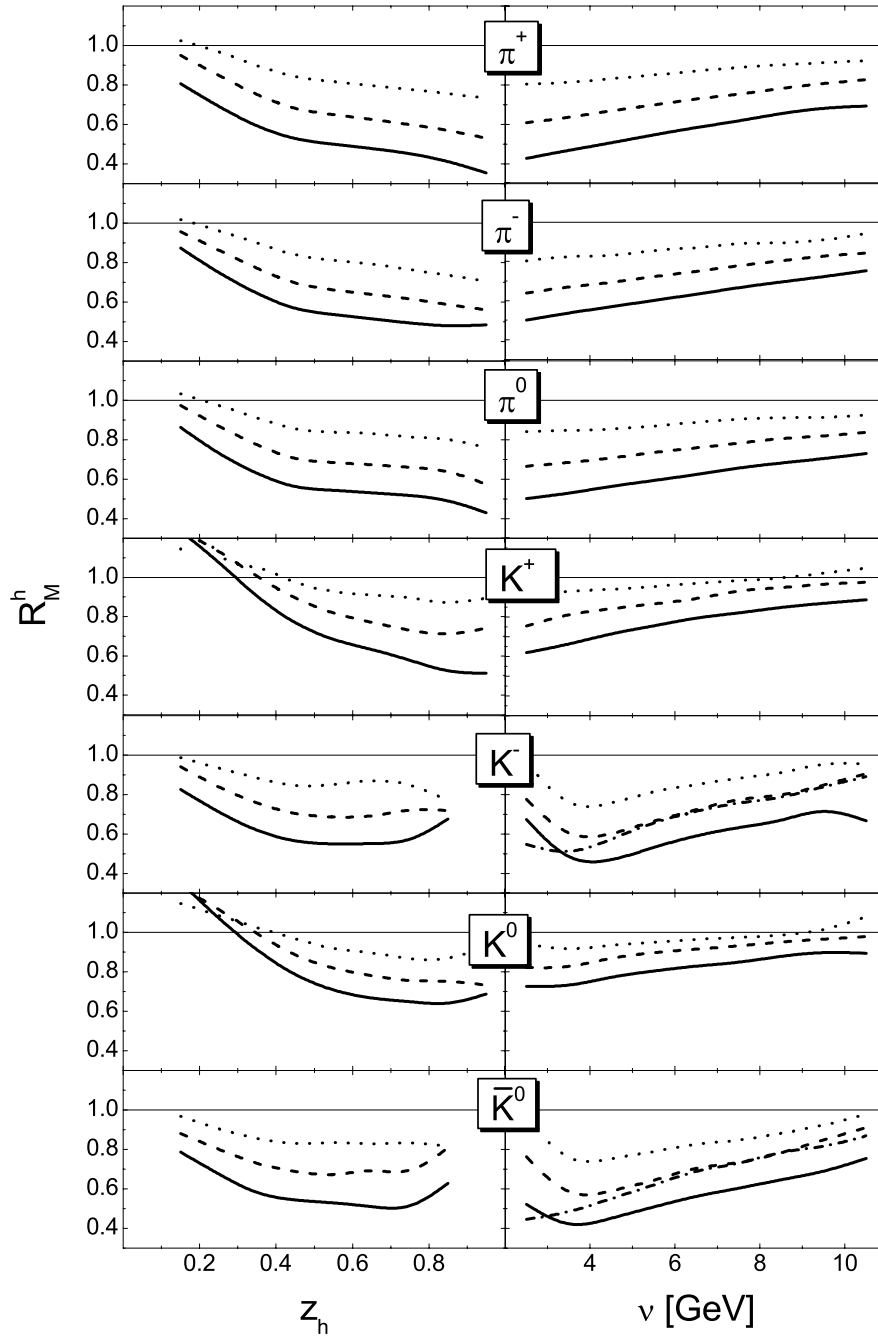
Figure 6.39: Calculated multiplicity ratio of identified $\pi^{\pm}$, $\pi^0$, $K^{\pm}$, $K^0$ and $\bar{K}^0$ for $^{12}$C (dotted lines), $^{56}$Fe (dashed lines) and $^{208}$Pb nuclei (solid lines). The simulation has been done for a 12 GeV electron beam and the CLAS detector. The dash-dotted line represents a calculation for $^{56}$Fe without Fermi motion. In all calculations we use the formation time $\tau_f = 0.5$ fm/$c$ and the constituent-quark concept (5.35) for the prehadronic cross sections.
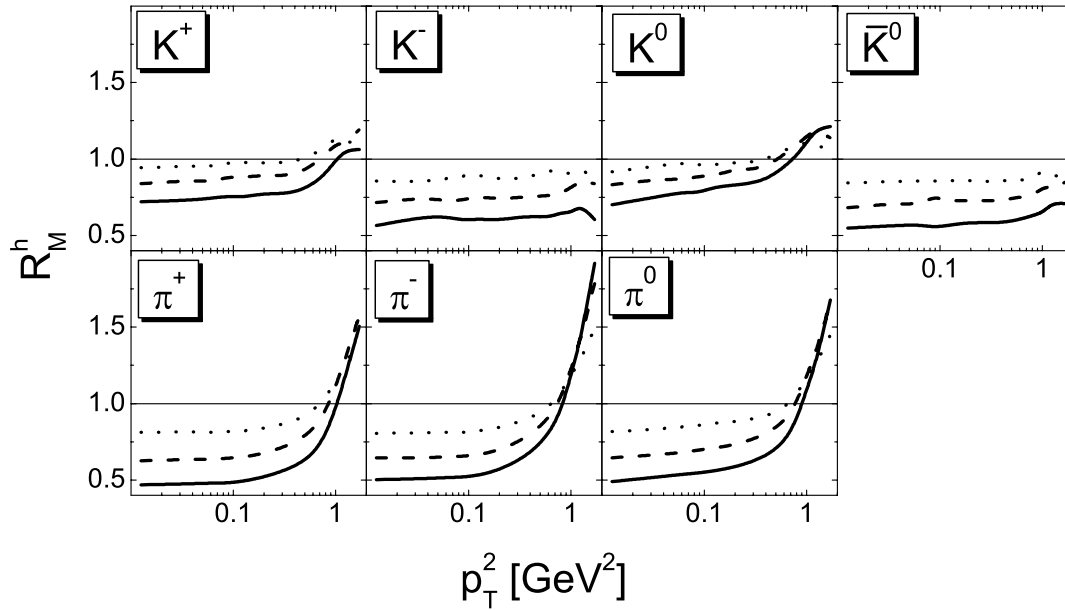
Figure 6.40: Calculated multiplicity ratio of identified $\pi^\pm$, $\pi^0$, $K^\pm$, $K^0$ and $\bar{K}^0$ for $^{12}$C (dotted lines), $^{56}$Fe (dashed lines) and $^{208}$Pb nuclei (solid lines) as a function of the transverse momentum $p_T$. The simulation was done for a 12 GeV electron beam and the CLAS detector. In all calculations we use the formation time $\tau_f = 0.5$ fm/$c$ and the constituent-quark concept (5.35) for the prehadronic cross sections.

and $\bar{K}^0$ production on $^{12}$C (dotted lines), $^{56}$Fe (dashed lines) and $^{208}$Pb nuclei (solid lines). The dependence of the hadron attenuation at large $z_h$ on the nucleon number $A$ is not much different from the one in the HERMES experiment shown in Fig. 6.23. The attenuation roughly increases like $A^\alpha$ with a scaling exponent $\alpha$ in the range 0.2–0.4. A scaling with $A^{1/3}$ would have been expected from the fact that the interaction probability for a produced hadron on its way out of the nucleus is proportional to the distance that it passes through nuclear matter. However, if the hadron is still inside the nucleus after its formation time, the interaction probability is instantaneously increased in our approach. This and other effects like a nonuniform density distribution lead to a deviation from the naively expected scaling behavior.

Like our previous HERMES results the multiplicity ratio $R_M^h$ increases as a function of $\nu$ because of time dilatation effects and decreases with $z_h$ due to a redistribution of spectral strength to lower energies in the FSI. Because of the lower photon energies a part of the (anti-)kaons can form inside the nucleus and undergo hadronic FSI. The larger interaction cross section of the $K^-$ and the $\bar{K}^0$ then leads to a considerably stronger attenuation than for the $K^+$ and the $K^0$.

The $K^-$ and $\bar{K}^0$ spectrum exhibit an increase of $R_M^h$ at low photon energies which is absent for pions and kaons. Because of strangeness conservation the primary $\gamma^* N$ reaction can only produce an antikaon together with a kaon which means that there are at least three particles in the final state. For kaons the reaction $\gamma N \to KY$ is always possible and, hence, the average momentum of kaons is larger than that of antikaons. At the lower end of the photon-energy spectrum only very few antikaons survive the
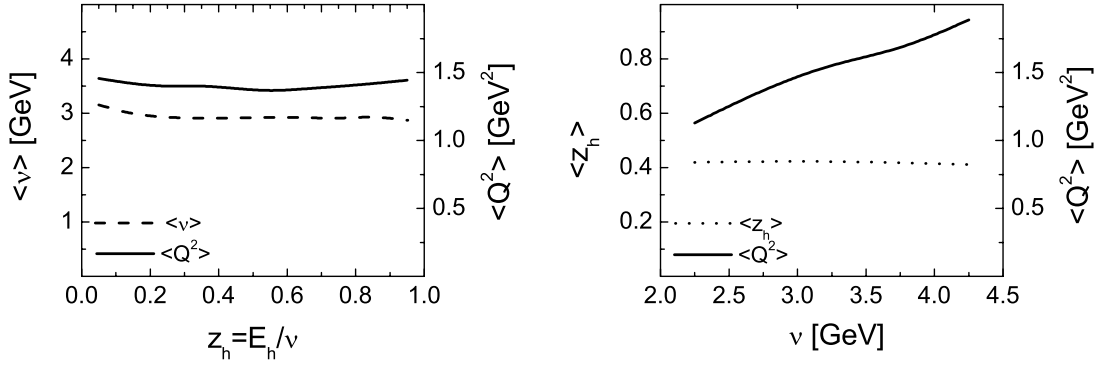
Figure 6.41: Model predictions for the average values of the kinematic variables in charged hadron production off deuterium using a 5 GeV electron beam and the CLAS detector. This kinematic regime corresponds to the one that is currently available at Jefferson Lab. *Left:* $\langle\nu\rangle$ and $\langle Q^2\rangle$ as a function of $z_h$. *Right:* Same for $\langle z_h\rangle$ and $\langle Q^2\rangle$ as a function of $\nu$.

lower momentum cuts. The Fermi motion in the nuclear target increases this yield and leads to a larger multiplicity ratio at small photon energies. For comparison, the dash-dotted line in Fig. 6.39 shows a calculation for a $^{56}$Fe nucleus without Fermi motion. Without Fermi motion the strong rise of the antikaon multiplicity ratio at small photon energies is gone. As we show in the next section, a further decrease of the photon energy further enhances the effect of Fermi motion.

In Fig. 6.40 we give a prediction for the $p_T$ dependence of the multiplicity ratio for $\pi^\pm$, $\pi^0$, $K^\pm$, $K^0$ and $\bar{K}^0$ on carbon, iron and lead nuclei. The multiplicity ratio for pions is now larger than 1 for $p_T > 1$ GeV/$c$. This means that the attenuation of high-$p_T$ pions is overbalanced by their increase due to elastic and inelastic (pre-)hadronic FSI of low-$p_T$ hadrons. This was not the case at HERMES energies, as can be seen from Fig. 6.24. One reason may be the fact that the initial $p_T$ distribution of pions directly after the $\gamma^* N$ reaction is not as broad as in the HERMES experiment. However, also the average $p_T$ that the hadrons gain in the FSI may be different for the two energy regimes.

The attenuation for the $K^-$ and $\bar{K}^0$ is again much stronger than for the $K^+$ and the $K^0$ and, in contrast to the kaons, the $K^-$ and $\bar{K}^0$ do not show an increase of the multiplicity ratio for high $p_T$. The reason is again the quark content of the kaons ($\bar{u}s$ and $\bar{d}s$) which leads to a larger absorption cross section and reduces the probability of side feeding by fast pions in the FSI.

**Jefferson Lab at 5 GeV**

In the following we discuss hadron attenuation in the kinematic regime that is currently accessible at Jefferson Lab using a 5 GeV electron beam. As before, we use the constituent-quark model (5.35) for the prehadronic interactions and the formation time $\tau_f = 0.5$ fm/$c$. The cuts in our simulation have been adjusted to the ones that will most likely be used in the data analysis [WBr]: 2 GeV$< W < 3.2$ GeV, $\nu > 2$ GeV, $y < 0.85$, $Q^2 > 1$ GeV$^2$. Like before, we account for the geometrical acceptance of the

CLAS detector and use the cut $z_h > 0.2$ for all spectra except the $z_h$ dependence. We use no cut on the final hadron momenta.

Fig. 6.41 shows the model predictions for the average kinematic variables at Jefferson Lab using the cuts that have been stated above. The average value of $Q^2$ is about 1.5 GeV$^2$ which is quite large considering the small average photon energy $\langle \nu \rangle \approx 3$ GeV. In contrast to the results of our previous simulations shown in Fig. 6.38 neither $\langle \nu \rangle$ nor $\langle Q^2 \rangle$ increase at low $z_h$. The reason is the missing lower cut on the final hadron momentum which required large photon energies for the low-$z_h$ hadrons. The increase of $\langle Q^2 \rangle$ was just a consequence of the increasing value for $\langle \nu \rangle$ since higher photon energies allow for higher $Q^2$. The latter also manifests itself in the increase of $\langle Q^2 \rangle$ with photon energy $\nu$ seen in Figs. 6.38 and 6.41. Because of the constraint on $Q^2$ which is set by the geometry of the HERMES detector, this increase is not seen in Fig. 6.35.

The predictions for the multiplicity ratios at current Jefferson Lab energies are shown in Fig. 6.42. Again we calculate $R_M^h$ as a function of $z_h$ and $\nu$ for $^{12}$C (dotted line), $^{56}$Fe (dashed line) and $^{208}$Pb (solid line).

There is not much new about the pion spectra. As before we observe an increase of $R_M^h$ with decreasing $z_h$ which is caused by the redistribution of energy in the (pre-) hadronic FSI. In the narrow $\nu$ window that we are considering in Fig. 6.42 the multiplicity ratio stays almost constant. The explanation is the same as for the vanishing $\nu$ dependence in Fig. 6.25 when we discussed a detector with complete angular coverage. The CLAS detector comes very close to such a hermetic detector. Any interaction of a pion in the FSI will produce new particles which contribute to the integrated $\nu$ spectra if their fractional energy $z_h$ is larger than 0.2. An increase of $R_M^h$ at larger $\nu$ due to time dilatation is compensated by less particle production in the FSI. The constance of $R_M^h(\nu)$ is lost if one applies an additional lower momentum cut of the order of the photon energy as can be seen in Fig. 6.39.

Note that the average photon energy is much smaller than in our previous simulations and that the maximum photon energy is only 4.25 GeV. Since the virtual photon cannot produce antikaons without an additional strange meson, e.g. $\gamma^* N \rightarrow K \bar{K} N$ ($m_K$=0.496 GeV), the maximum fractional energy $z_h$ is limited to 0.9 for antikaons. Because of the energy distribution in the three body final state and the finite virtuality of the photon ($Q^2 > 1$ GeV$^2$) the maximum fractional energy of antikaons is further reduced. As a result, the $z_h$ spectra for $K^-$ and $\bar{K}^0$ in Fig. 6.42 do not exceed $z_h \approx 0.8$. For the same reason the production of antikaons with $z_h > 0.2$ is reduced at the lower end of the photon spectrum. The Fermi motion in the nucleus enhances the yield of antikaons in these two extreme kinematic regions as can be seen by comparison with the dash-dotted line in Fig. 6.42 which represents the result of a calculation for $^{54}$Fe where Fermi motion has been neglected. Certainly, the kaons can be produced in a two body final state (e.g. $\gamma^* N \rightarrow K \Lambda$), however, the accompanying hyperon has a relatively large mass. Therefore, similar, although less pronounced, effects show also up for the kaons. Beside the effects of Fermi motion the multiplicity ratios of kaons and antikaons show the same features as for higher energies.

In Fig. 6.43 we present our model results for the dependence of $R_M^h$ on the transverse momentum $p_T$ of identified hadrons which will also be a subject of investigation at Jefferson Lab [KWa04]. Compared to the results of Fig. 6.40 for a 12 GeV electron beam, the enhancement of high-$p_T$ hadrons is even more pronounced. The reason
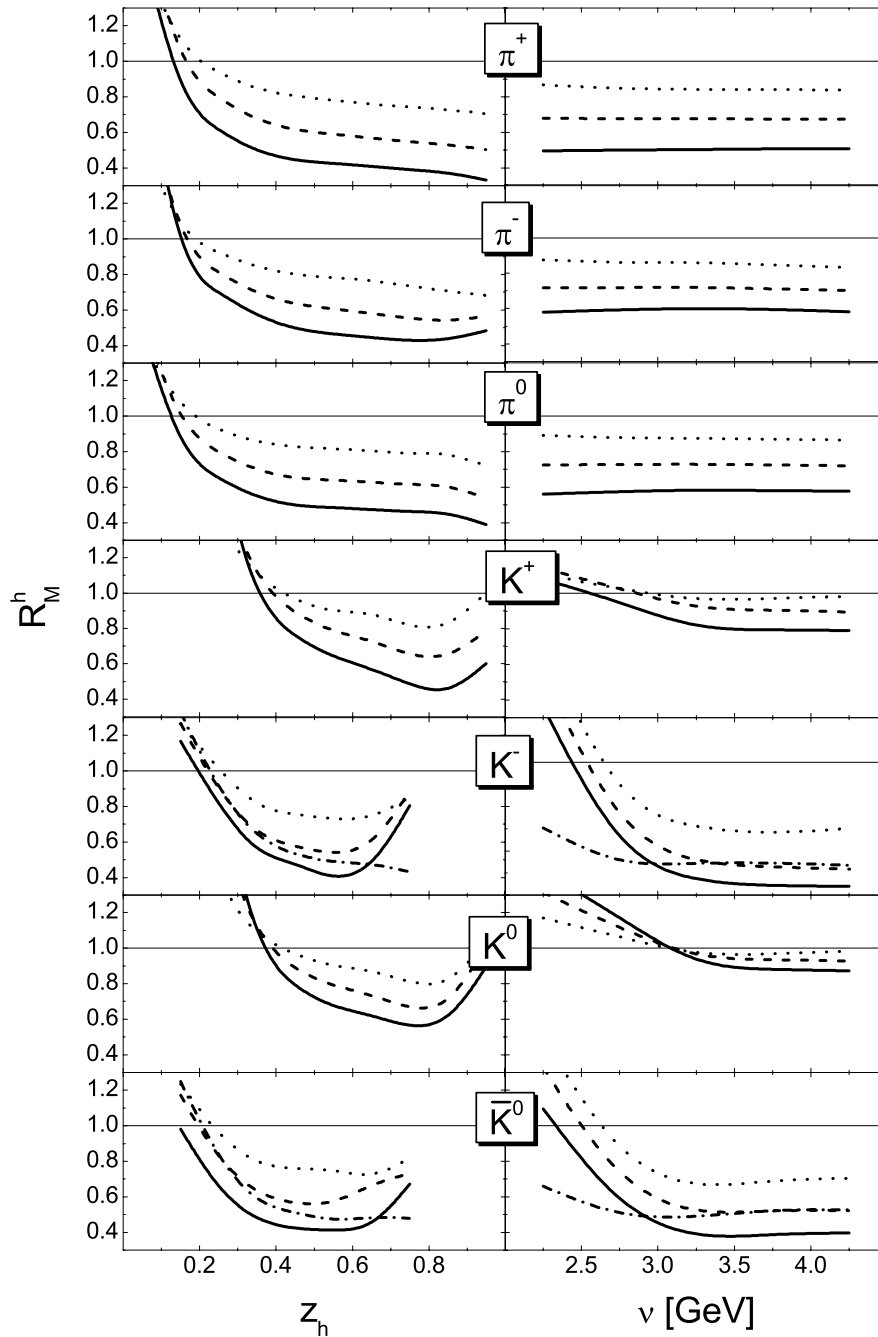
Figure 6.42: Calculated multiplicity ratio of identified $\pi^{\pm}$, $\pi^0$, $K^{\pm}$, $K^0$ and $\bar{K}^0$ for $^{12}$C (dotted lines), $^{56}$Fe (dashed lines) and $^{208}$Pb nuclei (solid lines). The simulation has been done for a 5 GeV electron beam and the CLAS detector. The dash-dotted line represents a calculation for $^{56}$Fe without Fermi motion. In all calculations we use the formation time $\tau_f = 0.5$ fm/$c$ and the constituent-quark concept (5.35) for the prehadronic cross sections.
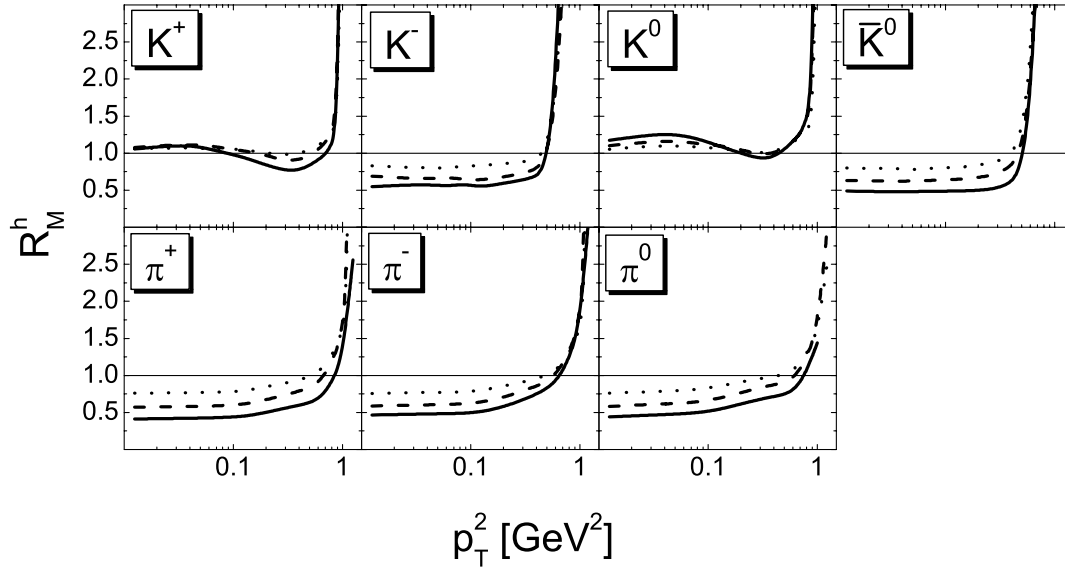
Figure 6.43: Calculated multiplicity ratio of identified $\pi^\pm$, $\pi^0$, $K^\pm$, $K^0$ and $\bar{K}^0$ for $^{12}$C (dotted lines), $^{56}$Fe (dashed lines) and $^{208}$Pb nuclei (solid lines) as a function of the transverse momentum $p_T$. The simulation was done for a 5 GeV electron beam and the CLAS detector. In all calculations we use the formation time $\tau_f = 0.5$ fm/$c$ and the constituent-quark concept (5.35) for the prehadronic cross sections.

is that we have further reduced the average photon energy and thereby the relative number of high $p_T$ hadrons that emerge from the primary $\gamma^* N$ interaction. Most hadrons with $p_T > 1$ GeV are produced in the FSI. The most dramatic effect is again seen for the kaons whose attenuation is compensated by kaon production in the FSI for a large region of $p_T$. The fact that the strong increase of the multiplicity ratio starts again slightly below $p_T = 1$ GeV/$c$ may be related to the average value of $p_T$ that the hadrons gain in the FSI.

# Chapter 7

# Summary and Outlook

In the present work we have studied the hadronic interactions of high-energy protons, photons and leptons.

Below invariant energies of about 2 GeV, hadronic interactions can be described by the excitation and decay of resonances. At higher energies the resonant structure of the cross section vanishes and hadronic interactions are dominated by single gluon, Pomeron and Reggeon exchange. As we have discussed in Chap. 2, the latter two can be interpreted as the exchange of multiple soft gluons and (anti-)quarks. At even higher energies hard interactions between the constituents of the hadrons become important.

In Chap. 3 we have pointed out that photon and electron-induced reactions show some striking similarities to hadron-hadron interactions because of the hadronic fluctuations of the photon. Depending on the energy and virtuality of the photon, the same event classes as in high-energy hadron-hadron interactions may occur. These events include elastic and diffractive scattering as well as hard scatterings between the constituents of the hadronic fluctuation and the target. In addition the (virtual) photon can couple directly to a quark inside the target. The latter dominates the cross section in deep inelastic lepton scattering at sufficiently large Bjorken $x \gtrsim 0.2$.

The various high-energy interactions lead to the excitation of hadronic strings which decay into hadrons due to the creation of quark-antiquark pairs from the vacuum. In Chap. 4 we have described the fragmentation of these strings within the Lund model which is also the basic ingredient of the Monte Carlo generators FRITIOF and PYTHIA that are employed in our transport simulation. The advantage of the Lund model is its capability to determine the complete final state of a fragmenting string, including the particle species and their four-momenta.

The Lund model involves three time scales for the production of a hadron in the fragmentation of a string. The first two are the production times of the hadron's first and second constituent, the third time is the formation time of the hadron, i.e. the time when the hadronic wave function has build up. Since the production of the second hadron constituent already leads to the creation of a colorless system, the corresponding production time is usually called the production time of a (color neutral) prehadron.

In Sec. 4.3 we have used the Lund model to calculate the production times of the quark-antiquark vertices in the string fragmentation as well as the formation times of the hadrons. We thereby accounted for the finite mass of the decaying string which limits the number of decay products to about 3–5 at the energies considered throughout

this work. In contrast to previous investigations [Bia87], where a simplistic fragmentation function was used, we have found a non-trivial mass dependence of the production and formation times. The tendency thereby is that the production and formation times increase with hadron mass.

At the end of Sec. 4.3 we have directly extracted the production and formation times of hadrons in deep inelastic positron-nucleon scattering at HERMES energies from PYTHIA. Depending on the energy and mass of the produced hadron, the average production proper time for the first constituent lies in the range 0–0.8 fm/$c$ while the production proper time of the second constituent and the formation proper time of the hadrons can become as large as 1.5–1.7 fm/$c$. Due to time dilatation the production and formation lengths in the lab frame can exceed nuclear dimensions. By using nuclear targets one can therefore learn something about the space-time picture of hadronization.

In Chap. 5 we have given an introduction to Glauber theory and the BUU transport model. Both models can be used for the description of high-energy nuclear reactions with each having its pros and cons. While the Glauber model allows for a full quantum mechanic treatment of the scattering process, its application is limited to very few experimental observables. As we show in Chaps. 5 and 6, the main reason is the neglect of complicated coupled channel effects that may strongly influence the outcome of a nuclear reaction. The latter can be accounted for in our probabilistic coupled-channel transport model. However, it is not clear how to incorporate quantum mechanic interference effects that show up in high energy nuclear reactions, such as the AGK cancellation or coherence length effects in photon- and electron-induced reactions.

In Sec. 5.3 we compare the results of the Glauber and the BUU model for proton-nucleus collisions at 100 GeV incident proton energy. While the mass dependence $A^{0.68}$ of the total proton-nucleus cross section in the BUU model is in perfect agreement with experimental data, the simple Glauber model yields a too large scaling exponent. The latter may be due to the neglect of Gribov's inelastic corrections, cf. Appx. H. Because of the AGK cancellation the inclusive meson production cross section in the Glauber model is proportional to the mass number $A$ of the nucleus. This scaling behavior is reproduced by the probabilistic coupled channel model, if one accounts for the interactions of the beam and target remnants during the formation time. In our default approach we therefore set the production times of all prehadrons to zero and rescale their cross sections during the formation time $\tau_f$ according to a simple constituent-quark model which determines the prehadronic cross section from the number of (anti-)quarks in the prehadron stemming from the beam or target. However, the experimental $pA$ data on pion and kaon production that we have used to study the $A$ dependence of the semi-inclusive production cross section cannot distinguish between a scenario with and without prehadronic interactions.

A more promising tool to study the space-time picture of hadronization is provided by photon and electron-induced reactions which have been discussed in Chap. 6. However, complications arise if a hadronic fluctuation of the photon persists over a distance that exceeds its mean free path in the nuclear medium. In that case coherent multiple scattering on several nucleons induces interference effects. While these coherence length effects arise naturally within Glauber theory, it is not straight forward to account for them in our probabilistic coupled channel model. In Sec. 6.1 we have discussed the phe-

nomenon of nuclear shadowing in high-energy photon- and electron-induced reactions and presented a possible implementation into our transport model.

In Sec. 6.2 we have investigated exclusive $\rho^0$ photo- and electroproduction off nuclei and demonstrated that our transport model indeed reproduces the coherence length effects that have been observed by the HERMES collaboration. Furthermore, we demonstrated how the coupled-channel FSI mimic the effect of color transparency and discussed the experimental cuts that are necessary to make calculations based on Glauber theory work. In our analysis of the experimental HERMES data we find no sign for color transparency, i.e. an increase of the nuclear transparency during the formation time of the $\rho^0$. In fact, our results indicate that, in the kinematic regime of the HERMES experiment, the $\rho^0$ starts to interact with its full hadronic cross section right after its production.

In Sec. 6.3 we have investigated semi-inclusive photoproduction of charged pions, kaons and $D$ mesons for photon energies in the range 1–30 GeV. In these less exclusive reactions we find a strong enhancement of the particle multiplicities due to the FSI which cannot be explained within the Glauber model. Especially the production of $K^+$ mesons – that cannot be absorbed in the nuclear medium – is strongly increased by side feeding in the FSI.

A detailed investigation of hadron attenuation in deep-inelastic lepton scattering at HERMES, EMC and Jefferson Lab energies has been presented in Sec. 6.4. For the space-time picture of the hadronization process we have basically considered two different scenarios. In the first scenario we use the constituent-quark concept that we have already employed for proton-nucleus interactions. In the second approach we use the production and formation times that we have extracted from the Lund model. Due to our transport description, we explicitly account for particle creation in the interactions of the primary reaction products emerging from the initial $\gamma^* N$ interaction. These secondary particles are found to strongly influence the low-energy part of the experimentally observed multiplicity ratios.

Furthermore, we have studied how the kinematic cuts and the finite detector acceptance influence the experimental observables. We find strong effects that have to be taken into account in any robust interpretation of the data.

We have investigated the attenuation of charged and neutral pions, kaons, protons and anti-protons as a function of the fractional energy $z_h$, the photon energy $\nu$ and the transverse momentum $p_T$ as well as the double-hadron attenuation. While in the kinematic region of the HERMES experiment most phenomena can be attributed to (pre-)hadronic FSI, we find limitations of our model for EMC energies and for large $p_T$. The latter supports a partonic origin for the Cronin effect in electron-nucleus interactions.

Motivated by our successful description of the experimental HERMES data we have also made predictions for the present and future Jefferson Lab experiments in Sec. 6.4.4. Because of the considerably smaller photon energy, we find a strong influence of Fermi motion on the multiplicity ratios. Furthermore, the hadronic FSI yield a strong enough $p_T$ broadening to produce a multiplicity ratio larger than one at $p_T > 1$ GeV/$c$.

In the following we like to draw attention to possible improvements of our model as well as potential future physics applications:

- **Event generation**

Up to now we use the event generator PYTHIA 6.2 only for the generation of the primary $\gamma^* N$ interaction and model the hadronic FSI with FRITIOF. As we have pointed out in Chap. 4, it is in principle possible to reduce the kinematic limit for $\gamma^* N$ event simulation with PYTHIA to 3 GeV by a suitable change of the parameter set. This may also work for hadronic interactions and has to be tested against experimental data. The event generator FRITIOF could then be completely removed from our transport model, and photon and hadron-induced reactions at high energies could both be described by the same Monte Carlo generator.

- **String propagation**
  We have seen in Sec. 6.4 that a scenario in which any interactions before the production of the color neutral prehadrons at proper time $\tau_{p2}$ are neglected does not yield enough hadron attenuation. Instead, we had to assume strong interactions right after the production times $\tau_{p1}$ of the hadron's first constituent. However, this does not necessarily imply that there is a freely interacting quark that sees strong FSI. As pointed out in Sec. 6.4 the longitudinal dimension of the string and its (color neutral) fragments is not expected to be larger than 1 fm [Cio02]. Therefore, one has in principle to deal with the propagation of color neutral strings that subsequently fragment into prehadrons and color neutral remainder strings. A collision of a (remainder) string – before its fragmentation – will most likely lead to a different final state than an undisturbed decay.

- **pQCD effects**
  In a direct photon-nucleon interaction at very high $Q^2$ and energy $\nu$ the photon is expected to knock out a highly virtual point-like quark that immediately may radiate gluons. The gluons then can split into quark-antiquark pairs and finally the various colored quarks and gluons combine to form the hadronic strings. While these processes are in principle taken into account in our present simulations via PYTHIA, we have completely neglected their space-time evolution so far and assumed that they take place instantaneously at the interaction point. This simplification may have considerable consequences at EMC energies and possibly explain our difficulties in describing the data. Depending on the spatial extension of this process and the density of the surrounding medium the quark may be subject to multiple scattering before the strings are formed. We can calculate the connected energy loss within pQCD and account for it by reducing the invariant mass of the strings.

- **Color transparency at Jefferson Lab**
  We plan to extend our previous investigation of incoherent vector meson production off complex nuclei from HERMES energies to the current [WBr03] and future [KWa04] Jefferson Lab energies. Our simulations will be useful to extract a clear signal for color transparency from the measured nuclear transparency ratios since they will allow us to separate the coherence length and coupled channel effects. On the other hand we can implement different models of color transparency in our transport description and see what signals survive after the FSI and what experimental cuts can improve the signal. In an analogous way we can address

the search for color transparency and nuclear filtering in pion photoproduction off nuclei which is another anticipated experiment after the upgrade [KWa04].

Our model for high-energy photonuclear reactions will therefore provide a strong support for the ongoing and future experiments at Jefferson Lab. In principle, one might even think of a possible implementation of our Monte Carlo simulation into the detector simulation at CLAS.

- **Shadowing of the photon's GVMD component**
  One of our next steps will be a more thorough consideration of the GVMD part of the virtual photon [Pil00]. So far we have only accounted for the shadowing of the photon's vector meson fluctuations in our model and neglected the contribution to nuclear shadowing that arises from coherent multiple scattering of its perturbative quark-antiquark component. This is possible as long as we restrict our investigations to the kinematic regime of the Jefferson Lab and the HERMES experiments. Considering possible future applications of our model at EIC energies, however, it is important to also take the modification of the GVMD part of the photon into account. In close analogy to our treatment of the VMD component, we can also calculate the modifications of the GVMD part within Glauber theory. The complication will be that the coherence length of each quark-antiquark fluctuation depends on its intrinsic transverse momentum so that each of the infinitely many quark-antiquark configurations will be modified differently in the nuclear medium.

- **EMC effect**
  After the incorporation of shadowing for the photons's GVMD component, our model accounts for Fermi motion, nuclear binding as well as shadowing down to very small values of the Bjorken scaling variable. Therefore, it contains all ingredients that are necessary to study the EMC effect, i.e. the difference between the nuclear and the nucleonic structure functions as measured in deep inelastic lepton scattering at moderate Bjorken $x$. By comparing to inclusive DIS data we can determine to what extent the parton distributions of the bound nucleons are really modified in the nuclear medium. These modified parton distributions can then be used in our model as an input for the calculations of more exclusive reactions like hadron production.

- **Photo- and electroproduction of charm**
  We have seen in Sec. 6.3 that by simply using VMD and Eq. (3.5) we overestimate the charm content in the photon. Furthermore, it is questionable whether we correctly describe the side feeding of charm in the FSI. After an improvement of both deficiencies it will be interesting to look for subthreshold electroproduction of charm at upgraded Jefferson Lab energies.

- **EIC**
  After the improvements discussed above, our model may also be used for calculations at energies of the Electron-Ion Collider (EIC) [Des02] which will collide polarized electron and (un)polarized (nuclear) nucleon beams over a wide energy range and with a higher luminosity ($L = 10^{33} \text{cm}^2\text{s}^{-1}$) than any existing collider.

The center-of-mass energy per nucleon lies in the range from 15 GeV to 100 GeV which corresponds to a 2.1 TeV electron beam in a fixed target configuration. Since the accessible values of $x$ are limited by the available collision center-of-mass energy, the EIC will enable precision DIS measurements on nucleon and nuclear targets in a completely new territory: $10^{-4} < x < 1$ and $1 < Q^2 < 10000$ GeV$^2$. Due to its collider geometry and dedicated hermetic detectors it will be able to reconstruct the complete final state and to study the hadronization process in the complete kinematic range.

- **$pA$ and $\pi A$ reactions** Besides photon- and electron-induced reactions also semi-inclusive particle production in high-energy $pA$ and $\pi A$ collisions can be studied in our model. Although the primary interaction of the hadronic projectile will in general take place on the front side of the nucleus, the string and its fragments will interact with the nuclear medium on their way through the target prior to hadronization. A simultaneous understanding of the experimental data obtained with electromagnetic and hadronic probes will help to distinguish between different hadronization scenarios.

- **Jet quenching at RHIC**
  Momentarily, we are at a stage where the ongoing DIS experiments at DESY and Jefferson Lab are about to reveal some details about the space-time picture of hadronization in cold nuclear matter. Meanwhile, RHIC explores the transition from confined to deconfined matter, i.e. the quark-gluon plasma (QGP) in ultra-relativistic heavy-ion collisions. As pointed out in the introduction, the detailed understanding of hadron attenuation in cold nuclear matter can provide us with essential input for the interpretation of jet quenching as a signature for the QGP. Hence, one important task is to learn to what extent the attenuation of hadrons in cold and hot nuclear matter are related.

  Our BUU transport simulation can serve as a starting point for a unified description of electron-nucleus and heavy-ion reactions from Jefferson Lab to RHIC energies.

# Appendix A

# Optical Theorem

In this chapter we derive the optical theorem from the unitarity postulate of Sec. 2.1.3:

$$\mathcal{S}^\dagger \mathcal{S} = \mathbb{1}. \tag{A.1}$$

Using Eq. (2.1) one can express the scattering matrix $\mathcal{S}$ in (A.1) in terms of the $T$ matrix:

$$\mathbb{1} + iT - iT^\dagger + T^\dagger T = \mathbb{1}$$
$$\Leftrightarrow \quad i(T^\dagger - T) = T^\dagger T. \tag{A.2}$$

We now look at the matrix element of (A.2) for the process $ab \rightarrow cd$ and insert the unit operator in form of a complete set of states $\{\vec{p}_f\}$ on the right-hand side:

$$\langle \vec{p}_c, \vec{p}_d | i(T^\dagger - T) | \vec{p}_a, \vec{p}_b \rangle = \sum_n \left( \prod_{f=1}^{n} \int \frac{d^3 p_f}{(2\pi)^3 2E_f} \right) \langle \vec{p}_c, \vec{p}_d | T^\dagger | \{\vec{p}_f\} \rangle \langle \{\vec{p}_f\} | T | \vec{p}_a, \vec{p}_b \rangle. \tag{A.3}$$

Eq. (A.3) can be rewritten in terms of the invariant amplitude $\mathcal{M}$ defined by (2.2):

$$(2\pi)^4 \delta^{(4)}(p_a + p_b - (p_c + p_d)) \, i(\mathcal{M}^*(p_c, p_d \rightarrow p_a, p_b) - \mathcal{M}(p_a, p_b \rightarrow p_c, p_d)) =$$

$$\sum_n \left( \prod_{f=1}^{n} \int \frac{d^3 p_f}{(2\pi)^3 2E_f} \right) \mathcal{M}^*(p_c, p_d \rightarrow \{p_f\}) \mathcal{M}(p_a, p_b \rightarrow \{p_f\})$$

$$\times (2\pi)^8 \delta^{(4)}(p_a + p_b - \sum_{f=1}^{n} p_f) \delta^{(4)}(p_c + p_d - \sum_{f=1}^{n} p_f). \tag{A.4}$$

Using the identity

$$\delta^{(4)}(p_a + p_b - \sum_{f=1}^{n} p_f) \delta^{(4)}(p_c + p_d - \sum_{f=1}^{n} p_f) = \delta^{(4)}(p_a + p_b - \sum_{f=1}^{n} p_f) \delta^{(4)}(p_a + p_b - (p_c + p_d))$$

one gets from Eq. (A.4) the following expression for the forward-scattering amplitude $(p_c = p_a, \, p_d = p_b)$:

$$2\mathrm{Im}\mathcal{M}(p_a, p_b \rightarrow p_a, p_b) = \sum_n \left( \prod_{f=1}^{n} \int \frac{d^3 p_f}{(2\pi)^3 2E_f} \right) |\mathcal{M}(p_a, p_b \rightarrow \{p_f\})|^2$$

$$\times (2\pi)^4 \delta^{(4)}(p_a + p_b - \sum_{f=1}^{n} p_f).$$

$$\sigma_{\text{tot}} = \frac{1}{2s} \sum_X \left| \begin{matrix} a \\ b \end{matrix} \bigcirc\!\!\equiv X \right|^2 = \frac{1}{2s} \sum_X \begin{matrix} a & & a \\ & \bigcirc\!\!\equiv\!\!\bigcirc & \\ b & X & b \end{matrix} = \frac{1}{s} \text{Im} \begin{matrix} a & & a \\ & \bigcirc & \\ b & & b \end{matrix}$$

Figure A.1: Pictorial representation of the optical theorem. First the definition of the total cross section and then the completeness and in the unitarity relation have been used.

The cross section is related to the invariant amplitude $\mathcal{M}$ in the following way [Pes95]:

$$d\sigma = \frac{1}{2E_a 2E_b |v_a - v_b|} \left( \prod_{f=1}^{n} \frac{d^3 p_f}{(2\pi)^3 2E_f} \right) |\mathcal{M}(p_a, p_b \to \{p_f\})|^2 (2\pi)^4 \delta^{(4)} \left( p_a + p_b - \sum_{f=1}^{n} p_f \right).$$

By expressing the flux factor either in the center-of-mass frame

$$2E_a 2E_b |v_a - v_b| = 4p_{\text{cm}}\sqrt{s}$$

or in the laboratory frame where particle $b$ is at rest and $p_{\text{lab}} = p_a$

$$2E_a 2E_b |v_a - v_b| = 4p_{\text{lab}} m_b$$

one ends up with the optical theorem (2.4) for the invariant amplitude $\mathcal{M}$:

$$\begin{aligned} \text{Im}\mathcal{M}(p_a, p_b \to p_a, p_b) &= 2p_{\text{cm}}\sqrt{s}\,\sigma^{\text{tot}}(a + b \to X) \\ &= 2p_{\text{lab}} m_b\,\sigma^{\text{tot}}(a + b \to X). \end{aligned}$$

In Fig. A.1 we summarize the derivation of the optical theorem diagrammatically.

In this work we often deal with the classical scattering amplitude $f$ whose absolute value squared gives the differential cross section for elastic scattering in the laboratory frame where particle $b$ is at rest:

$$\left( \frac{d\sigma^{\text{el}}}{d\Omega} \right)_{\text{lab}} = |f(p_{\text{lab}}, \theta_{\text{lab}})|^2.$$

Here $\theta_{lab}$ denotes the scattering angle of particle $a$ in the laboratory frame. For this amplitude the optical theorem takes on the form:

$$\sigma^{\text{tot}} = \frac{4\pi}{p_{\text{lab}}} \text{Im} f(p_{\text{lab}}, \theta_{\text{lab}} = 0). \tag{A.5}$$

For the sake of completeness we also state the optical theorem for the amplitude $f_{\text{cm}} = \mathcal{M}/(8\pi E_{\text{cm}})$ which is related to the elastic scattering cross section in the center-of-mass frame

$$\left( \frac{d\sigma^{\text{el}}}{d\Omega} \right)_{\text{cm}} = |f_{\text{cm}}(p_{\text{cm}}, \theta_{\text{cm}})|^2.$$

It is formally identical to Eq. (A.5):

$$\sigma^{\text{tot}} = \frac{4\pi}{p_{\text{cm}}} \text{Im} f_{\text{cm}}(p_{\text{cm}}, \theta_{\text{cm}} = 0).$$

# Appendix B

# Regge amplitude

In this chapter we sketch the derivation of the Regge amplitude (2.11) which is valid in the Regge limit $s \gg t$. A detailed introduction to Regge theory can be found in the work of Collins [Col77] and references therein. We start with the partial-wave expansion of the scattering amplitude for the $t$-channel process $a\bar{c} \to \bar{b}d$:

$$\mathcal{M}_{a\bar{c} \to \bar{b}d}(s,t) = \sum_{l=0}^{\infty} (2l+1) a_l(s) P_l(\cos \theta_{\mathrm{cm}}). \tag{B.1}$$

At large energies the scattering angle $\theta_{\mathrm{cm}}$ in the center-of-mass frame can be expressed in terms of $s$ and $t$:

$$\cos \theta_{\mathrm{cm}} \approx 1 + \frac{2t}{s}.$$

In Eq. (B.1) $a_l$ denotes the amplitude of the partial wave with angular momentum $l$. Using the crossing symmetry relation (2.6), i.e. interchanging $s$ and $t$ in Eq. (B.1), one obtains the following expansion of the $s$-channel amplitude in terms of Legendre polynomials

$$\mathcal{M}_{ab \to cd}(s,t) = \sum_{l=0}^{\infty} (2l+1) a_l(t) P_l(1 + 2s/t). \tag{B.2}$$

For simplicity, we denote the $s$-channel amplitude by $\mathcal{M}$ in the following. After analytical continuation into the complex $l$ plane one can make use of the residue theorem [Br95] and rewrite the series (B.2) in terms of a contour integral (Sommerfeld-Watson transformation)

$$\mathcal{M}(s,t) = \frac{1}{2i} \oint_C dl\,(2l+1) \frac{a_l(t)}{\sin(\pi l)} P_l(1 + 2s/t). \tag{B.3}$$

The contour $C$ is depicted in Fig. B.1. It encloses all poles on the positive real axis which arise because of the $\sin(\pi l)$ in the denominator:

$$\sin(\pi l) \xrightarrow{l \to n} (-1)^n (l-n)\pi \quad , \qquad n \in \mathbb{Z}.$$

We now deform the contour $C$ into $C' = C_1' \cup C_2'$ as shown in Fig. B.1. $C_1'$ runs parallel to the imaginary $l$ axis at $\mathrm{Re}\,l = -1/2$ and the contour is closed via $C_2'$ at infinity. All poles that $a_l(t)$ may have in the right complex plane have to be encircled.
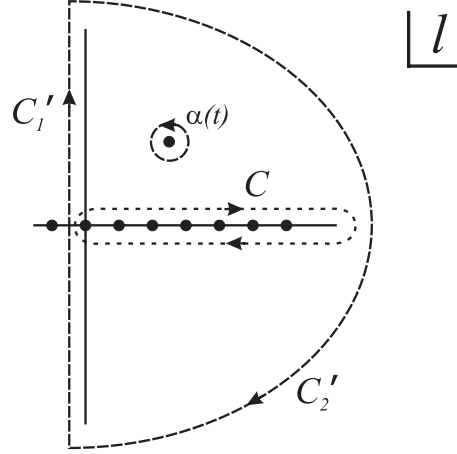
Figure B.1: Contour $C$ of the integral in Eq. (B.3). When deforming $C$ (dotted line) to $C' = C_1' \cup C_2'$ (dashed line), one has to encircle all poles that $a_l(t)$ may have at $l = \alpha(t)$ and pick up $2\pi i$ times the residue.

Before we discuss the contributions of the poles to the integral (B.3) we check whether $a_l(t)$ vanishes for $|l| \to \infty$. Consider the partial-wave expansion (B.2). Using the orthogonality of the Legendre polynomials [Br95], one gets for the partial-wave amplitude

$$a_l(t) = \frac{1}{2} \int_{-1}^{+1} dz \mathcal{M}(s(z), t) P_l(z)$$

where we have made the substitution

$$z = 1 + 2s/t.$$

We now express the invariant amplitude $\mathcal{M}$ via the dispersion relation (2.9) assuming for simplicity that no subtraction is needed and obtain:

$$a_l(t) = \frac{1}{2} \int_{-1}^{+1} dz P_l(z) \frac{1}{\pi} \left( \int_{z^+}^{\infty} dz' \frac{\mathrm{Im}\mathcal{M}(z', t)}{z' - z} + \int_{-\infty}^{z^-} dz' \frac{\mathrm{Im}\mathcal{M}(z', t)}{z' - z} \right)$$

with $z^{\pm} = 1 + 2s_{\mathrm{th}}^{\pm}/t$. By introducing the Legendre functions of the 2$^{\text{nd}}$ kind [Col77]

$$Q_l(z) = \frac{1}{2} \int_{-1}^{+1} dz' \frac{P_l(z')}{z - z'}$$

with the property

$$Q_l(-z) = (-1)^{l+1} Q_l(z)$$

one ends up with the so-called Froissart-Gribov projection of the partial-wave amplitude

$$
\begin{aligned}
a_l(t) &= \frac{1}{\pi} \left( \int_{z^+}^{\infty} dz' Q_l(z') \mathrm{Im}\mathcal{M}(z', t) + \int_{-\infty}^{z^-} dz' Q_l(z') \mathrm{Im}\mathcal{M}(z', t) \right) \\
&= \frac{1}{\pi} \left( \int_{z^+}^{\infty} dz' Q_l(z') \mathrm{Im}\mathcal{M}(z', t) - (-1)^l \int_{-z^-}^{+\infty} dz' Q_l(z') \mathrm{Im}\mathcal{M}(-z', t) \right) \quad \text{(B.4)}
\end{aligned}
$$

In the last step we have rewritten the second integral in such a way that the argument of the Legendre functions $Q_l$ is always positive. The asymptotic behavior of the $Q_l$ [Col77]:

$$Q_l(z) \xrightarrow{|l| \to \infty} l^{-\frac{1}{2}} e^{-(l+\frac{1}{2}) \ln(z+\sqrt{z^2-1})} \tag{B.5}$$

then would ensure the vanishing of the partial-wave amplitude along the contour $C_2'$ if there was not the factor $(-1)^l$ in front of the second integral which diverges for $l \to i\infty$. We can avoid this problem by introducing two different types of partial waves

$$a_l^{(\eta=\pm)}(t) = \frac{1}{\pi} \left( \int_{z^+}^{\infty} dz' Q_l(z') \text{Im} \mathcal{M}(z',t) - \eta \int_{-z^-}^{+\infty} dz' Q_l(z') \text{Im} \mathcal{M}(-z',t) \right)$$

which are the analytic continuations of the even and odd partial-wave amplitudes:

$$
\begin{aligned}
a_l(t) &= a_l^{(+)}(t) \quad, \quad l = 0, 2, 4, \ldots \\
a_l(t) &= a_l^{(-)}(t) \quad, \quad l = 1, 3, 5, \ldots
\end{aligned}
$$

and which both vanish on the contour $C_2'$. From those one can construct amplitudes of definite signature $\eta$ via the Sommerfeld-Watson transformation (B.3):

$$
\begin{aligned}
\mathcal{M}^{(\eta)}(z,t) &= \frac{1}{2i} \oint_{C'} dl \, (2l+1) \frac{a_l^{(\eta)}(t)}{\sin(\pi l)} P_l(z) \\
&= \frac{1}{2i} \int_{-\frac{1}{2}-i\infty}^{-\frac{1}{2}+i\infty} dl \, (2l+1) \frac{a_l^{(\eta)}(t)}{\sin(\pi l)} P_l(z) \\
&\quad + \frac{2\pi i}{2i} \sum_{n_\eta} (2\alpha_{n_\eta}(t)+1) \frac{\beta_{n_\eta}(t)}{\sin(\pi \alpha_{n_\eta}(t))} P_{\alpha_{n_\eta}(t)}(z)
\end{aligned} \tag{B.6}
$$

where we have assumed isolated simple poles at positions $l = \alpha_{n_\eta}(t)$:

$$a_l^{(\eta)}(t) \xrightarrow{l \to \alpha_{n_\eta}(t)} \frac{\beta_{n_\eta}(t)}{l - \alpha_{n_\eta}(t)}.$$

There is no contribution from the semi-circle $C_2'$ because of the well-defined behavior of the $a_l^{(\eta)}(t)$ (see Eq. (B.5)) and the asymptotic form of the factor [Col77]

$$\left| \frac{P_l(z)}{\sin(\pi l)} \right| < l^{-\frac{1}{2}} f(z) \qquad \text{for } |l| \to \infty.$$

We are interested in the Regge region $s \gg t$ where the Legendre polynomials take on the form [Col77]

$$P_l(z) \xrightarrow{z \to \infty} \pi^{-\frac{1}{2}} \frac{\Gamma(l+\frac{1}{2})}{\Gamma(l+1)} (2z)^l \quad, \qquad \text{Re } l \geq -\frac{1}{2} \tag{B.7}$$

and the contribution from the first integral to the amplitude $\mathcal{M}^{(\eta)}$ in Eq. (B.6) behaves like $s^{-1/2}$. Considering only the contribution from the leading Regge pole, i.e. the one with the largest real part of $\alpha_{n_\eta}(t) = \alpha(t)$ we end up with

$$\mathcal{M}^{(\eta)}(z,t) = \pi(2\alpha(t)+1) \frac{\beta(t)}{\sin(\pi \alpha(t))} P_{\alpha(t)}(z).$$

The physical amplitude $\mathcal{M}$ can be obtained by adding the even ($\eta = +$) and odd ($\eta = -$) signature amplitudes in a way that ensures the right symmetry properties of $\mathcal{M}$ under the exchange of the Mandelstam variables $s$ and $u$ [Col77]:

$$\mathcal{M}(s,t) = \frac{1}{2}\left[\mathcal{M}^{(+)}(z,t) + \mathcal{M}^{(+)}(-z,t) + \mathcal{M}^{(-)}(z,t) - \mathcal{M}^{(-)}(-z,t)\right].$$

Therefore, we have

$$\mathcal{M}(s,t) = \pi(2\alpha(t)+1)\frac{\beta(t)}{\sin(\pi\alpha(t))}\frac{1}{2}\left[P_{\alpha(t)}(z) + \eta P_{\alpha(t)}(-z)\right]$$

where $\eta$ denotes the signature of the leading Regge pole. Using the equality [Col77]

$$P_l(-z) = e^{-i\pi l}P_l(z) - \frac{2}{\pi}\sin(\pi l)Q_l(z)$$

and neglecting the term proportional to $Q_{\alpha(t)}(z)$ which vanishes in the large $s$ limit because of [Col77]

$$Q_l(z) \xrightarrow{z\to\infty} \pi^{\frac{1}{2}}\frac{\Gamma(l+1)}{\Gamma(l+\frac{3}{2})}(2z)^{-l-1},$$

we end up with the Regge amplitude:

$$\begin{aligned}
\mathcal{M}(s,t) &= \pi(2\alpha(t)+1)\frac{\beta(t)}{\sin(\pi\alpha(t))}\frac{(1+\eta e^{-i\pi\alpha(t)})}{2}P_{\alpha(t)}(z) \\
&= -\pi^{\frac{1}{2}}(2\alpha(t)+1)\frac{\beta(t)}{\sin(\pi\alpha(t))}\frac{(1+\eta e^{-i\pi\alpha(t)})}{2}\frac{\Gamma(\alpha(t)+\frac{1}{2})}{\Gamma(\alpha(t)+1)}(2z)^{\alpha(t)}. \quad \text{(B.8)}
\end{aligned}$$

In the last step we have used the asymptotic form of the Legendre polynomials (B.7) for $\operatorname{Re}\alpha(t) > -1/2$.

Depending on the signature of the leading Regge pole, the amplitude (B.8) peaks at even or odd positive integer values of $\operatorname{Re}\alpha(t)$ due to the $\sin(\pi\alpha(t))$ in the denominator. Since $\alpha(t)$ is a pole of the partial-wave amplitude $\mathcal{M}_l^{(\eta)}(t)$, this situation corresponds to the $t$-channel exchange of a resonance particle with integer spin $l = \operatorname{Re}\alpha(t)$ and mass $m = \sqrt{t}$.

In rewriting and combining some of the terms in (B.8) one can cast the Regge amplitude into the commonly used form (2.11):

$$\mathcal{M}_{ab\to cd}(s,t) = \frac{\gamma_{ac}(t)\gamma_{bd}(t)}{\Gamma(\alpha(t))}\frac{(\eta + e^{-i\pi\alpha(t)})}{\sin(\pi\alpha(t))}\left(\frac{s}{s_0}\right)^{\alpha(t)}$$

where a factor of $\Gamma(\alpha(t))$ has explicitly been extracted in defining the couplings $\gamma$ to show the vanishing of the 'nonsense poles' at negative integer values of spin $\alpha(t) = -1, -2, \ldots$. The couplings $\gamma_{ac}$ and $\gamma_{bd}$ are real functions of $t$ and the scale factor $s_0$ is the hadronic mass scale $s_0 \approx 1$ GeV$^2$. We discuss the structure of the factorized Regge amplitude in Sec. 2.1.

# Appendix C

# Kinematics in hard parton-parton scattering

Consider two incoming hadrons in their center-of-momentum frame. In the following we will neglect all masses. Then each hadron has energy $E_{\text{beam}}$ and the total center-of-mass energy squared is $s = 4E_{\text{beam}}^2$. The two partons that enter the hard scattering carry momentum fractions $x_1$ and $x_2$ respectively, i.e. they have four-momenta

$$
\begin{aligned}
p_1 &= E_{\text{beam}}(x_1, 0, 0, x_1) \\
p_2 &= E_{\text{beam}}(x_2, 0, 0, -x_2),
\end{aligned}
$$

where we have again neglected the masses of the partons as well as any possible transverse momentum component. The invariant energy squared of the two incident partons is

$$
\begin{aligned}
\hat{s} &= (p_1 + p_2)^2 = 2p_1 p_2 \\
&= 4x_1 x_2 E_{\text{beam}}^2 = x_1 x_2 s.
\end{aligned} \tag{C.1}
$$

For the scattering into two outgoing (massless) partons 3 and 4 the other two Mandelstam variables are given as

$$
\begin{aligned}
\hat{t} &= (p_1 - p_3)^2 = (p_2 - p_4)^2 = -\frac{\hat{s}}{2}(1 - \cos\hat{\theta}) \\
\hat{u} &= (p_1 - p_4)^2 = (p_2 - p_3)^2 = -\frac{\hat{s}}{2}(1 + \cos\hat{\theta})
\end{aligned}
$$

where $\hat{\theta}$ is the polar angle of parton 3 in the center-of-mass frame of the hard scattering (see Fig. C.1). As usual, $\hat{u}$ is not an independent variable since

$$
\hat{s} + \hat{t} + \hat{u} = 0
$$

as it must be for massless partons because of Eq. (2.3).

The transverse momentum transfer $p_T$ of the hard scattering is given according to Fig. C.1 as

$$
p_T = \hat{E} \sin\hat{\theta}
$$
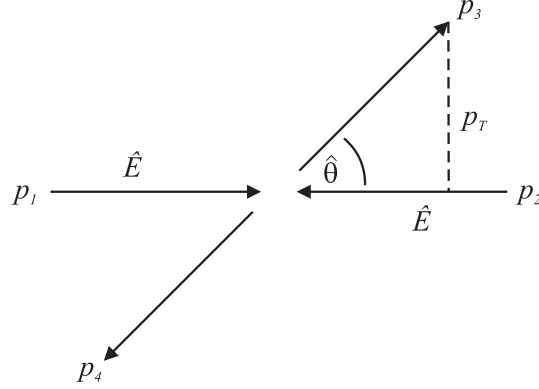
Figure C.1: Scattering kinematics for the process $p_1 p_2 \rightarrow p_3 p_4$.

where $\hat{E} = \sqrt{\hat{s}}/2$ denotes the energy of a parton in the center-of-mass frame of the hard scattering. Hence, one has for the transverse momentum transfer squared

$$p_T^2 = \frac{\hat{s}}{4} \sin^2 \hat{\theta} = \frac{\hat{t}\,\hat{u}}{\hat{s}} \tag{C.2}$$

which enters the delta function in Eq. (2.23). Since $\hat{s}$ cannot be larger than the total center-of-mass energy of the two colliding hadrons squared (cf. Eq. (C.1)) one can determine the upper limit of the integral (2.24) directly from Eq. (C.2).

# Appendix D

# High-energy electron-nucleon scattering

In this chapter we derive the high-energy form of the Lorentz-invariant electron-nucleon scattering cross section (3.15). Let us first define some Lorentz-invariant quantities which characterize the scattering process of Fig. 3.6:

$$\nu = \frac{p\,q}{m_N}, \qquad x = \frac{Q^2}{2p\,q}, \qquad y = \frac{p\,q}{p\,k}. \tag{D.1}$$

In the rest frame of the nucleon we have

$$p = (m_N, \vec{0}), \qquad k_0 = E, \qquad q_0 = (E - E')$$

and the variables (D.1) take on the form of Sec. 3.2.1

$$\nu = E - E', \qquad x = \frac{Q^2}{2m_N\nu}, \qquad y = \frac{E - E'}{E}.$$

The interpretation of $x$ as the momentum fraction carried by the struck quark implies that $0 \leq x \leq 1$. This is indeed the case as can easily be shown: The invariant mass of the final hadronic state $X$ must be at least that of the nucleon which is supposed to be the lightest baryon:

$$W^2 = (p + q)^2 = m_N^2 + 2p\,q - Q^2 \geq m_N^2$$
$$\Rightarrow \quad 2p\,q = W^2 - m_N^2 + Q^2 \geq Q^2$$
$$\Rightarrow \quad x = \frac{Q^2}{2p\,q} \leq 1.$$

On the other hand, $Q^2 \geq 0$ as was shown in (3.10) and, hence,

$$2p\,q \geq Q^2 \geq 0$$
$$\Rightarrow \quad x = \frac{Q^2}{2p\,q} \geq 0.$$

Also the dimensionless variable $y$, which in the rest frame of the nucleon can be interpreted as the fraction of the electron energy $E$ carried away by the photon, has to lie

in the region $0 \le y \le 1$:

$$p\,q \ge 0$$
$$\Rightarrow \quad \nu = E - E' = \frac{p\,q}{m_N} \ge 0$$
$$\Rightarrow \quad 0 \le y = \frac{E - E'}{E} \le 1$$

since both energies $E$ and $E'$ are positive.

We now express the polarization parameter $\epsilon$ in terms of the invariant quantities (D.1). In the rest frame of the nucleon one can write for the virtuality

$$Q^2 = 2EE'(1 - \cos\theta) = 2E^2(1 - y)(1 - \cos\theta) \tag{D.2}$$

and hence

$$\tan^2\frac{\theta}{2} = \frac{1 - \cos\theta}{1 + \cos\theta} = \frac{Q^2}{4E^2(1 - y) - Q^2}.$$

Inserting this into Eq. (3.13) one obtains

$$\begin{aligned}
\epsilon &= \left[1 + 2\left(1 + \frac{y^2 E^2}{Q^2}\right)\frac{Q^2}{4E^2(1 - y) - Q^2}\right]^{-1} \\
&= \frac{1 - y - \frac{Q^2}{4E^2}}{1 - y + y^2/2 + \frac{Q^2}{4E^2}}.
\end{aligned}$$

If the electron energy is much larger than the nucleon mass $m_N$ one gets:

$$\frac{Q^2}{4E^2} = \frac{2m_N x\,y}{4E} < \frac{m_N}{2E} \to 0 \tag{D.3}$$

and the polarization parameter simplifies to expression (3.16):

$$\epsilon \approx \frac{1 - y}{1 - y + y^2/2}. \tag{D.4}$$

Making the variable transformation $(E', \cos\theta) \to (y, Q^2)$ one gets

$$dy\,dQ^2 = 2E'\,dE'\,d\cos\theta$$

and

$$\begin{aligned}
\frac{d^2\sigma}{dy\,dQ^2} &= \frac{\pi}{E'}\frac{d^2\sigma}{dE'\,d\Omega} \\
&= \frac{\pi}{E'}\Gamma(\sigma_T^{\gamma^* N} + \epsilon\sigma_L^{\gamma^* N}). \tag{D.5}
\end{aligned}$$

One may express the equivalent photon energy (3.14) as

$$K = \frac{Q^2}{2m_N x}(1 - x).$$

Using the approximation for the polarization parameter (D.4) one writes

$$\frac{1}{1-\epsilon} \approx \frac{1+(1-y)^2}{y^2}.$$

Inserting both into the definition of the photon flux (3.12) we end up with

$$\begin{aligned}
\frac{\pi}{E'}\Gamma &\approx \frac{\alpha_{\text{em}}}{2\pi}\frac{(1-x)}{2m_N E x}\left(\frac{1+(1-y)^2}{y^2}\right) \\
&= \frac{\alpha_{\text{em}}}{2\pi}\frac{(1-x)}{Q^2}\left(\frac{1+(1-y)^2}{y}\right)
\end{aligned} \qquad (\text{D.6})$$

which together with Eq. (D.5) gives the high-energy expression for the invariant cross section (3.15).

# Appendix E

# Lund fragmentation function

In this chapter we derive the Lund fragmentation function $f(z)$ that determines the breakup distribution via Eq. (4.12). We thereby assume that the invariant mass $W = p_0^+ p_0^-$ of the fragmenting string is large so that many yoyo hadrons are produced. Consider now a hadron that is formed in the middle of the string by a quark of vertex $A$ and an antiquark created at vertex $B$, cf. Fig. E.1. This process can be interpreted as a result of taking many steps along the positive lightcone to reach vertex $A$ and then taking a further step to reach vertex $B$. The positive lightcone momentum remaining before hadron $m$ is produced is then given by $W_A^+ = \kappa x_A^+$. The probability of arriving at vertex $A$ can be written as

$$H'(A)dx_A^+ dx_A^- = H(\Gamma_A)d\Gamma_A dy_A \,,$$

where the last equality follows from the variable transformation

$$
\begin{aligned}
\Gamma_A &= \kappa^2 x_A^+ x_A^- \\
y_A &= \frac{1}{2}\ln\left(\frac{x_A^+}{x_A^-}\right).
\end{aligned}
$$

Since the distribution function $H$ should be Lorentz invariant it can only depend on $\Gamma_A$ which is the only Lorentz invariant available. From Fig. E.1 it can be seen that $\Gamma_A$ is proportional to the area of the rectangle below vertex $A$. It is directly related to the proper time of vertex $A$:

$$\Gamma_A = \kappa^2 x_A^+ x_A^- = \kappa^2(t_A^2 - x_A^2). \tag{E.1}$$

Having arrived at vertex $A$, it takes a further step to vertex $B$ to produce the hadron with mass $m$. The probability therefore is given by

$$f(z^+)dz^+,$$

i.e. the probability of taking a fraction $z^+$ of the remaining positive lightcone momentum $W_A^+$. The joint probability of stepping along the positive lightcone to vertex $A$ and then taking a final step to vertex $B$ producing hadron $m$ can therefore be written as the product

$$H(\Gamma_A)d\Gamma_A dy_A f(z^+)dz^+.$$
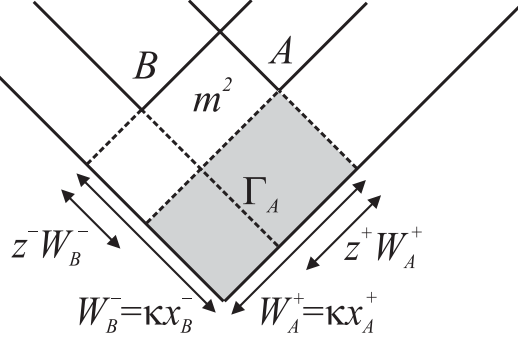
Figure E.1: Production of a hadron with mass $m$ between two adjacent vertices $A$ and $B$.

On the other hand, one could equally well have stepped along the negative lightcone to reach vertex $B$ and then take a final step to vertex $A$. The Lund model postulates that these two probabilities should be the same, i.e.

$$H(\Gamma_A)d\Gamma_A dy_A f(z^+)dz^+ = H(\Gamma_B)d\Gamma_B dy_B f(z^-)dz^-. \tag{E.2}$$

From Fig. E.1 one obtains the following relations:

$$\begin{aligned} \Gamma_A &= W_A^+(1-z^-)W_B^- \\ \Gamma_B &= (1-z^+)W_A^+W_B^- \\ m^2 &= (z^+W_A^+)(z^-W_B^-). \end{aligned}$$

After taking the two quantities $dy_{A,B}$ to be equal, one is therefore left with two independent variables which we choose to be $z^\pm$:

$$\Gamma_A = \frac{m^2(1-z^-)}{z^+z^-} \tag{E.3}$$

$$\Gamma_B = \frac{m^2(1-z^+)}{z^+z^-} \tag{E.4}$$

$$\Rightarrow z^-\frac{d\Gamma_A}{dz^-} = z^+\frac{d\Gamma_B}{dz^+}$$

and which can be inserted into Eq. (E.2) to get the condition

$$H(\Gamma_A(z^+,z^-))z^+f(z^+) = H(\Gamma_B(z^+,z^-))z^-f(z^-). \tag{E.5}$$

Taking the logarithm of (E.5) and defining

$$\begin{aligned} h(\Gamma) &= \ln(H(\Gamma)) \tag{E.6} \\ g(z) &= \ln(zf(z)), \tag{E.7} \end{aligned}$$

one obtains the expression

$$h(\Gamma_A) + g(z^+) = h(\Gamma_B) + g(z^-) \tag{E.8}$$

which we differentiate with respect to $z^+$ and $z^-$ to get rid of the $g$ dependence:

$$\frac{\partial^2 h(\Gamma_A)}{\partial z^- \partial z^+} = h''(\Gamma_A)\left(\frac{m^2}{z^+ z^{-2}}\right)\left(\frac{m^2(1-z^-)}{z^- z^{+2}}\right) + h'(\Gamma_A)\left(\frac{m^2}{z^{-2} z^{+2}}\right)$$

$$\frac{\partial^2 h(\Gamma_B)}{\partial z^- \partial z^+} = h''(\Gamma_B)\left(\frac{m^2(1-z^+)}{z^+ z^{-2}}\right)\left(\frac{m^2}{z^{+2} z^-}\right) + h'(\Gamma_B)\left(\frac{m^2}{z^{-2} z^{+2}}\right)$$

$$\frac{\partial^2 g(z^+)}{\partial z^- \partial z^+} = \frac{\partial^2 g(z^-)}{\partial z^- \partial z^+} = 0.$$

Using Eqs. (E.3) and (E.4), this leads to the following differential equation for $h$:

$$h'(\Gamma_A) + \Gamma_A h''(\Gamma_A) = h'(\Gamma_B) + \Gamma_B h''(\Gamma_B) \tag{E.9}$$

which can easily be solved. Since the left-hand side of (E.9) only depends on $\Gamma_A$ and the right-hand side only on the independent variable $\Gamma_B$, the whole expression has to be constant and can be integrated:

$$-b = h'(\Gamma) + \Gamma h''(\Gamma) = \frac{d}{d\Gamma}(\Gamma h'(\Gamma))$$

$$\Rightarrow h(\Gamma) = -b\Gamma + a\ln\Gamma + \ln C \tag{E.10}$$

$$\Rightarrow H(\Gamma) = C\Gamma^a \exp(-b\Gamma), \tag{E.11}$$

where in the last step (E.6) has been used. Here $a$, $b$ and $C$ are constants with $b$ being equal for all vertices, $a$ possibly depending on the flavor of the quark pair created at the vertex with proper time $\Gamma$ and $C$ playing the role of a normalization constant. Because of relation (E.1), Eq. (E.11) gives us the distribution of proper times of vertices in a string fragmentation at very large invariant mass $W = p_0^+ p_0^-$.

To obtain the remaining distribution function $g(z)$ we insert (E.10) into Eq. (E.8):

$$-b\Gamma_A + a_A \ln \Gamma_A + \ln C_A + g_{AB}(z^+) = -b\Gamma_B + a_B \ln \Gamma_B + \ln C_B + g_{BA}(z^-),$$

use Eqs. (E.3) and (E.4) to express $\Gamma_{A,B}$ in terms of $z^\pm$ and $m$ and separate variables:

$$b\frac{m^2}{z^+} + a_A \ln\left(\frac{m^2}{z^+}\right) - a_B \ln\left(\frac{1-z^+}{z^+}\right) + \ln C_A + g_{AB}(z^+)$$

$$= b\frac{m^2}{z^-} + a_B \ln\left(\frac{m^2}{z^-}\right) - a_A \ln\left(\frac{1-z^-}{z^-}\right) + \ln C_B + g_{BA}(z^-) = \ln N_C.$$

Since the left-hand side of this equation now depends only on $z^+$ and the other side only on $z^-$ they must both be equal to the same constant, i.e. $\ln N_C$. Solving for $g_{AB}$, we get

$$g_{AB}(z) = \ln\left[\frac{N_C}{C_A m^{2a_A}} z^{a_A}\left(\frac{1-z}{z}\right)^{a_B}\exp\left(-b\frac{m^2}{z}\right)\right] \tag{E.12}$$

and using the definition (E.7) we finally end up with the general form of the fragmentation function

$$f_{AB}(z) = N_{AB}\frac{z^{a_A}}{z}\left(\frac{1-z}{z}\right)^{a_B}\exp\left(-b\frac{m^2}{z}\right)$$

where the normalization constants $N_{AB}$ and $N_{BA}$ are related according to Eq. (E.12) as

$$N_{AB} = \frac{N_C}{C_A m^{2a_A}}, \quad N_{BA} = \frac{N_C}{C_B m^{2a_B}}.$$ (E.13)

Phenomenologically, it has up to now not been necessary to assign different values $a_{A,B}$ to adjacent vertices. If there is only a single value of the $a$ parameter, the general form (E.13) simplifies to Eq. (4.17) of Sec. 4.2:

$$f(z) = N \frac{(1-z)^a}{z} \exp(-b\frac{m^2}{z}).$$

# Appendix F

# Determination of $\tau_V$ and $\tau_O$ from the decay kinematics of a Lund string

Consider the decay of a string in its rest frame into $n$ hadrons with four-momenta $\{p_i\}$. The invariant mass $W$ of the original string is given as

$$W^2 = \left(\sum_{i=1}^{n} p_i\right)^2 = p_0^+ p_0^- \, ,$$

where $p_0^\pm$ denote the initial lightcone momenta of the end points of the string. If one neglects the masses of the endpoints one gets $p_0^+ = p_0^- = W$. Let us label the hadrons according to their rank. In case that the rank is not known one can try to number the hadrons with decreasing $\zeta_i = p_i^+/p_0^+$ where $p_i^+ = E_i + p_{zi}$. Because of Eq. (4.24) this should in most cases be equivalent to the ordering in rank. With the help of Eq. (4.24) one can subsequently derive the $\{z_i\}$:

$$z_i = \frac{\zeta_i}{\prod_{j=1}^{i-1}(1 - z_j)}.$$

Knowing the set of $\{z_i\}$ allows for the reconstruction of the vertices $\{(x_i^+, x_i^-\}$ using the method described in Sec. 4.2. Note that in the on-shell step (4.13) one now has to use the transverse mass squared $m_{Ti}^2 = m_i^2 + p_{Ti}^2$ of the hadrons. The proper times of the vertices and yoyo meeting points are then given by Eqs. (4.26) and (4.27). In our actual model calculations we directly extract the proper times $\tau_V$ and $\tau_O$ from the Lund fragmentation routines in JETSET.

# Appendix G

# Glauber theory and AGK cancellation

We now demonstrate how the AGK cancellation (5.18) arises within Glauber theory. For a detailed investigation of the connection between Glauber theory, unitarity and the AGK cancellation we refer the reader to Ref. [Ber77].

Let us first consider the summed elastic cross section for $hA$ scattering where the nucleus can be in any final state $|f\rangle$ including the ground state:

$$\sigma_{hA}^{\mathrm{el}} = \sum_f \int d\Omega_h |F^{0\to f}(\vec{q}_T)|^2 \tag{G.1}$$

with the Glauber amplitude given by Eq. (5.8):

$$
\begin{aligned}
F^{0\to f} &= \frac{ik}{2\pi} \int d^2 b \, e^{i\vec{q}_T \cdot \vec{b}} \Gamma^{f0}(\vec{b}) \\
&= \frac{ik}{2\pi} \int d^2 b \, e^{i\vec{q}_T \cdot \vec{b}} \left\{ \delta_{0f} - \langle f| \prod_{i=1}^{A} [1 - \Gamma(\vec{b} - \vec{s}_i)]|0\rangle \right\}.
\end{aligned}
$$

Insertion in Eq. (G.1) gives

$$
\begin{aligned}
\sigma_{hA}^{\mathrm{el}} &= \sum_f \int \frac{d^2 q_T}{k^2} \frac{k^2}{4\pi^2} \int d^2 b \int d^2 b' e^{i\vec{q}_T(\vec{b}-\vec{b}')} \\
&\quad \times \left( \delta_{0f} - \langle 0| \prod_{j=1}^{A} [1 - \Gamma^*(\vec{b}' - \vec{s}_j)]|f\rangle \right) \left( \delta_{f0} - \langle f| \prod_{i=1}^{A} [1 - \Gamma(\vec{b} - \vec{s}_i)]|0\rangle \right) \\
&= \int d^2 b \left\{ 1 + \langle 0| \prod_{i=1}^{A} |1 - \Gamma(\vec{b} - \vec{s}_i)|^2|0\rangle - 2\mathrm{Re}\langle 0| \prod_{i=1}^{A} [1 - \Gamma(\vec{b} - \vec{s}_i)]|0\rangle \right\} \tag{G.2}
\end{aligned}
$$

where we have used closure ($\sum |f\rangle\langle f| = \mathbb{1}$) in the second step.

In Analogy to Eq. (5.6) the total hadron-nucleus cross section is given by the nuclear profile function (5.8) with $f = 0$ as

$$\sigma_{hA}^{\mathrm{tot}} = 2 \int d^2 b \left\{ 1 - \mathrm{Re}\langle 0| \prod_{i=1}^{A} [1 - \Gamma(\vec{b} - \vec{s}_i)]|0\rangle \right\}. \tag{G.3}$$

The total inelastic cross section is given by the difference

$$
\begin{aligned}
\sigma_{hA}^{\text{inel}} &= \sigma_{hA}^{\text{tot}} - \sigma_{hA}^{\text{el}} \\
&= \int d^2b \left\{ 1 - \langle 0| \prod_{i=1}^{A} |1 - \Gamma(\vec{b} - \vec{s}_i)|^2 |0\rangle \right\} \\
&= \int d^2b \left\{ 1 - \left[ \int d^2s \int dz |1 - \Gamma(\vec{b} - \vec{s})|^2 \rho_1(\vec{s}, z) \right]^A \right\} \\
&= \int d^2b \left\{ 1 - \left[ 1 - \sigma_{hN}^{\text{inel}} \tilde{T}(\vec{b}) \right]^A \right\}
\end{aligned}
\tag{G.4}
$$

where we have used the independent-particle model of Sec. 5.1.1 and defined the normalized nuclear thickness function

$$
\tilde{T}(\vec{b}) = \int dz \rho_1(\vec{b}, z).
$$

In the last step of (G.4) we have used

$$
\int d^2s \int dz |1 - \Gamma(\vec{b} - \vec{s})|^2 \rho_1(\vec{s}, z)
$$

$$
= 1 - \tilde{T}(\vec{b}) \int d^2s \left(2\text{Re}\Gamma(\vec{s}) - |\Gamma(\vec{s})|^2\right)
$$

and the expression of the inelastic $hN$ cross section (5.7) in terms of the profile function $\Gamma$.

Let us now expand the total inelastic cross section (G.4)

$$
\sigma_{hA}^{\text{inel}} = \sum_{n=1}^{A} \sigma_n
\tag{G.5}
$$

with

$$
\sigma_n = \binom{A}{n} \int d^2b \left( \sigma_{hN}^{\text{inel}} \tilde{T}(\vec{b}) \right)^n \left( 1 - \sigma_{hN}^{\text{inel}} \tilde{T}(\vec{b}) \right)^{A-n}.
\tag{G.6}
$$

Obviously, $\sigma_n$ corresponds to the cross section of a process where $n$ nucleons have undertaken production of particle $m$ while the remaining $(A - n)$ nucleons have only provided inelastic absorption. Eq. (G.5) holds because

$$
\sigma_0 = \int d^2b \left[ 1 - \sigma_{hN}^{\text{inel}} \tilde{T}(\vec{b}) \right]^A
$$

and

$$
\sum_{n=0}^{A} \sigma_n = \int d^2b \left[ \sigma_{hN}^{\text{inel}} \tilde{T}(\vec{b}) + \left( 1 - \sigma_{hN}^{\text{inel}} \tilde{T}(\vec{b}) \right) \right]^A = \int d^2b.
$$

The inclusive production cross section for particle $m$ (including its multiplicity) can directly be expressed in terms of $\sigma_n$:

$$
\begin{aligned}
\sigma(hA \to mX) &= \sum_{n=1}^{A} n\sigma_n \\
&= A\sigma_{hN}^{\text{inel}}.
\end{aligned}
$$

which just represents the result of the AGK cancellation. The last equality can be profen by induction. Let us define

$$a = \sigma_{hN}^{\text{inel}} \tilde{T}(\vec{b})$$

Since $\tilde{T}$ is normalized to one, we are left to show that

$$\sum_{n=1}^{A} n \binom{A}{n} a^n (1-a)^{A-n} = Aa. \tag{G.7}$$

Eq. (G.7) is obviously fulfilled for $A = 1$ and because of

$$\sum_{n=1}^{A+1} n \binom{A+1}{n} a^n (1-a)^{A+1-n}$$

$$= a \sum_{n=1}^{A+1} \frac{(A+1)!}{(A-(n-1))!(n-1)!} a^{n-1} (1-a)^{A-(n-1)}$$

$$= (A+1)a \sum_{n=0}^{A} \frac{A!}{(A-n)!n!} a^n (1-a)^{A-n}$$

$$= (A+1)a(a+1-a)^A$$

$$= (A+1)a$$

it is also true for $A + 1$.

# Appendix H

# Inelastic corrections to $\sigma_{hA}$

Let us consider the scattering of a hadron $h$ with energy $E_h$ and momentum $k_h = \sqrt{E_h^2 - m_h^2}$ on an ensemble of $A$ nucleons. In contrast to the derivation of the nuclear profile function (5.8), we now include the possibility of diffractive excitation $hN \to XN$. The incoming hadron is again described by a plane wave

$$\psi_h^{(0)}(\vec{r}) = e^{ik_h z}.$$

As before, the hadron wave directly behind the first nucleon can be written as:

$$
\begin{aligned}
\psi_h^{(1)}(\vec{r}) &= [1 - \Gamma_h(\vec{b} - \vec{s}_1)]\psi_h^{(0)}(z_1)e^{ik_h(z-z_1)} \\
&= [1 - \Gamma_h(\vec{b} - \vec{s}_1)]e^{ik_h z}.
\end{aligned}
$$

The diffractively produced state $X$ is concentrated in the shadow region behind the target and is described by the wave

$$\psi_X^{(1)}(\vec{r}) = -\Gamma_{hX}(\vec{b} - \vec{s}_1))\psi_h^{(0)}(z_1)e^{ik_X(z-z_1)} \tag{H.1}$$

where $k_X = \sqrt{E_h^2 - m_X^2}$ denotes the momentum of the diffractive state $X$ and the new profile function $\Gamma_{hX}$ is related to the diffractive production amplitude $f_{hX}$ similar to (5.3)

$$\Gamma_{hX}(\vec{b}) = \frac{1}{2\pi i k_X} \int d^2 q_T e^{i\vec{q}_T \cdot \vec{b}} f_{hX}(\vec{q}_T).$$

Introducing the momentum difference

$$q_X = k_h - k_X,$$

one can rewrite Eq. (H.1) as

$$\psi_X^{(1)}(\vec{r}) = -\Gamma_{hX}(\vec{b} - \vec{s}_1)e^{iq_X z_1}e^{ik_X z}. \tag{H.2}$$

Behind the second nucleon the two wave functions look like

$$
\begin{aligned}
\psi_h^{(2)}(\vec{r}) &= \big\{[1 - \Gamma_h(\vec{b} - \vec{s}_1)][1 - \Gamma_h(\vec{b} - \vec{s}_2)] \\
&\quad + \Gamma_{hX}(\vec{b} - \vec{s}_1)\Gamma_{Xh}(\vec{b} - \vec{s}_2)e^{iq_X(z_1-z_2)}\big\}e^{ik_h z} \tag{H.3} \\
\psi_X^{(2)}(\vec{r}) &= \big\{ -[1 - \Gamma_h(\vec{b} - \vec{s}_1)]\Gamma_{hX}(\vec{b} - \vec{s}_2))e^{iq_X z_2} \\
&\quad - \Gamma_{hX}(\vec{b} - \vec{s}_1)[1 - \Gamma_X(\vec{b} - \vec{s}_2)]e^{iq_X z_1}\big\}e^{ik_X z}. \tag{H.4}
\end{aligned}
$$

From Eqs. (H.3) and (H.4) one sees that already with only one intermediate state $X$ the possibility of subsequent transitions $hN \to XN \to hN \to \ldots$ make things very complicated. By allowing for only two non-diagonal transitions $hN \to XN$ and $XN \to hN$ one can write down the nuclear profile function for (quasi-)elastic $hA$ scattering:

$$
\begin{aligned}
\Gamma^{f0}(\vec{b}) &= \delta_{f0} - \sum_X \langle f| \{ \prod_{i=1}^{A}[1 - \Gamma_h(\vec{b} - \vec{s}_i)] \\
&\quad + \sum_{i,j}^{A} \Gamma_{hX}(\vec{b} - \vec{s}_i)\Gamma_{Xh}(\vec{b} - \vec{s}_j)e^{iq_X(z_i - z_j)}\Theta(z_j - z_i) \\
&\quad \times \prod_{k \neq i,j}^{A}[1 - \Gamma_X(\vec{b} - \vec{s}_k)]\Theta(z_k - z_i)\Theta(z_j - z_k) \\
&\quad \times \prod_{l \neq i,j}^{A}[1 - \Gamma_h(\vec{b} - \vec{s}_l)]\Theta(z_i - z_l)\Theta(z_l - z_j) \} |0\rangle.
\end{aligned}
\tag{H.5}
$$

The inverse of $q_X$ is the so-called coherence length $l_X \approx 2E_h/(m_X^2 - m_h^2)$ which plays an important role in the discussion of high-energy $\gamma^* A$ reactions in Sec. 6.1.1.

Similarly, the nuclear profile function for diffractive production of particle $X$ neglecting multiple off-diagonal transitions is given as

$$
\begin{aligned}
\Gamma^{f0}_{f \to X}(\vec{b}) &= -\langle f| \{ \sum_{i=1}^{A} \Gamma_{hX}(\vec{b} - \vec{s}_i)e^{iq_X z_i} \\
&\quad \times \prod_{k \neq i}^{A}[1 - \Gamma_h(\vec{b} - \vec{s}_k)]\Theta(z_i - z_k) \prod_{l \neq i}^{A}[1 - \Gamma_X(\vec{b} - \vec{s}_l)]\Theta(z_l - z_i) \} |0\rangle.
\end{aligned}
$$

# Appendix I

# Incoherent $V$ photoproduction off nuclei

In the following we show the equality of Eqs. (6.30) and (6.32). Since the real part of the $VN$ scattering amplitude was neglected in the derivation of (6.32) we also set $\alpha_V = 0$ in Eq. (6.30) and end up with:

$$
\begin{aligned}
\sigma_{\gamma A \to V A^*} =\ & \sigma_{\gamma N \to VN} \int d^2 b \int_{-\infty}^{\infty} dz\, \rho(\vec{b}, z) e^{-\sigma_{VN}^{\mathrm{inel}} \int_z^{\infty} dz'\, \rho(\vec{b}, z')} \\
& \times \left| 1 - \int_{-\infty}^{z} dz_i\, \rho(\vec{b}, z_i) \frac{\sigma_{VN}}{2} e^{iq_V(z_i - z)} \exp\left[ -\frac{1}{2}\sigma_{VN} \int_{z_i}^{z} dz_k\, \rho(\vec{b}, z_k) \right] \right|^2 \\
=\ & \sigma_{\gamma N \to VN} \int d^2 b \int_{-\infty}^{\infty} dz\, \rho(\vec{b}, z) e^{-\sigma_{VN}^{\mathrm{inel}} \int_z^{\infty} dz'\, \rho(\vec{b}, z')} \\
& \times \left\{ 1 - \sigma_{VN} \int_{-\infty}^{z} dz_i\, \rho(\vec{b}, z_i) \cos\left[ q_V(z_i - z) \right] \exp\left[ -\frac{1}{2}\sigma_{VN} \int_{z_i}^{z} dz_k\, \rho(\vec{b}, z_k) \right] \right. \\
& \left. + \frac{\sigma_{VN}^2}{4} \left| \int_{-\infty}^{z} dz_i\, \rho(\vec{b}, z_i) e^{iq_V z_i} \exp\left[ -\frac{1}{2}\sigma_{VN} \int_{z_i}^{z} dz_k\, \rho(\vec{b}, z_k) \right] \right|^2 \right\} \\
=\ & \sigma_{\gamma N \to VN} \int d^2 b \left\{ \int_{-\infty}^{\infty} dz\, \rho(\vec{b}, z) e^{-\sigma_{VN}^{\mathrm{inel}} T_z(\vec{b})} \right. \\
& - \sigma_{VN} \int_{-\infty}^{\infty} dz_1\, \rho(\vec{b}, z_1) \int_{z_1}^{\infty} dz_2\, \rho(\vec{b}, z_2) \cos\left[ q_V(z_1 - z_2) \right] \\
& \left. \times \exp\left[ -\sigma_{VN}^{\mathrm{inel}} \int_{z_2}^{\infty} dz'\, \rho(\vec{b}, z') - \frac{1}{2}\sigma_{VN} \int_{z_1}^{z_2} dz'\, \rho(\vec{b}, z') \right] \right.
\end{aligned}
$$

$$+ \frac{\sigma_{VN}^2}{4} \int\limits_{-\infty}^{\infty} dz\, \rho(\vec{b}, z)$$

$$\times \left| \int\limits_{-\infty}^{z} dz_i\, \rho(\vec{b}, z_i) e^{iq_V z_i} \exp\left[ -\frac{1}{2}\sigma_{VN} \int\limits_{z_i}^{z} dz'\, \rho(\vec{b}, z') - \frac{1}{2}\sigma_{VN}^{\text{inel}} \int\limits_{z}^{\infty} dz'\, \rho(\vec{b}, z') \right] \right|^2 \Bigg\}. \tag{I.1}$$

In the second step we have renamed the integration variables and rewritten the integration limits. The first term of (I.1) already equals the first term of Eq. (6.32). The exponent in the second term of (I.1) yields

$$-\sigma_{VN}^{\text{inel}} T_{z_2}(\vec{b}) - \frac{1}{2}\sigma_{VN}\left( T_{z_1}(\vec{b}) - T_{z_2}(\vec{b}) \right) = -\frac{1}{2}\left( \sigma_{VN}^{\text{inel}} - \sigma_{VN}^{\text{el}} \right) T_{z_2}(\vec{b}) - \frac{1}{2}\sigma_{VN} T_{z_1}(\vec{b}) \tag{I.2}$$

and the exponent of the third term in (I.1) is

$$-\frac{1}{2}\sigma_{VN}\left( T_{z_i}(\vec{b}) - T_z(\vec{b}) \right) - \frac{1}{2}\sigma_{VN}^{\text{inel}} T_z(\vec{b}) = -\frac{1}{2}\sigma_{VN} T_{z_i}(\vec{b}) + \frac{1}{2}\sigma_{VN}^{\text{el}} T_z(\vec{b}). \tag{I.3}$$

We now further manipulate the last term of (I.1):

$$\frac{\sigma_{VN}^2}{4} \int\limits_{-\infty}^{\infty} dz\, \rho(\vec{b}, z) e^{\sigma_{VN}^{\text{el}} T_z(\vec{b})} \left| \int\limits_{-\infty}^{z} dz_i\, \rho(\vec{b}, z_i) e^{iq_V z_i} e^{-\frac{1}{2}\sigma_{VN} T_{z_i}(\vec{b})} \right|^2$$

$$= \frac{\sigma_{VN}^2}{4} \int\limits_{-\infty}^{\infty} dz \int\limits_{-\infty}^{z} dz_1 \int\limits_{-\infty}^{z} dz_2\, \rho(\vec{b}, z)\, \rho(\vec{b}, z_1)\, \rho(\vec{b}, z_2) e^{\sigma_{VN}^{\text{el}} T_z(\vec{b})} \cos\left[ q_V(z_1 - z_2) \right]$$

$$\times e^{-\frac{1}{2}\sigma_{VN}(T_{z_1}(\vec{b}) + T_{z_2}(\vec{b}))}. \tag{I.4}$$

Rewriting the integral in the following form

$$\int\limits_{-\infty}^{\infty} dz \int\limits_{-\infty}^{z} dz_1 \int\limits_{-\infty}^{z} dz_2 = \int\limits_{-\infty}^{\infty} dz_2 \int\limits_{-\infty}^{z_2} dz_1 \int\limits_{z_2}^{\infty} dz + \int\limits_{-\infty}^{\infty} dz_1 \int\limits_{-\infty}^{z_1} dz_2 \int\limits_{z_1}^{\infty} dz$$

and using the symmetry of the integrand with respect to the variables $z_1$ and $z_2$ we can rewrite (I.4) as

$$\frac{\sigma_{VN}^2}{2} \int\limits_{-\infty}^{\infty} dz_2\, \rho(\vec{b}, z_2) \int\limits_{-\infty}^{z_2} dz_1\, \rho(\vec{b}, z_1) \cos\left[ q_V(z_1 - z_2) \right]$$

$$\times e^{-\frac{1}{2}\sigma_{VN}(T_{z_1}(\vec{b}) + T_{z_2}(\vec{b}))} \int\limits_{z_2}^{\infty} dz\, \rho(\vec{b}, z) e^{\sigma_{VN}^{\text{el}} T_z(\vec{b})}$$

$$= -\frac{1}{2}\frac{\sigma_{VN}^2}{\sigma_{VN}^{\text{el}}} \int\limits_{-\infty}^{\infty} dz_2\, \rho(\vec{b}, z_1) \int\limits_{-\infty}^{z_2} dz_1\, \rho(\vec{b}, z_2) \cos\left[ q_V(z_1 - z_2) \right]$$

$$\times e^{-\frac{1}{2}\sigma_{VN}(T_{z_1}(\vec{b}) + T_{z_2}(\vec{b}))} \left( 1 - e^{\sigma_{VN}^{\text{el}} T_{z_2}} \right)$$

$$
= -\frac{1}{2}\frac{\sigma_{VN}^2}{\sigma_{VN}^{\mathrm{el}}} \int\limits_{-\infty}^{\infty} dz_1\, \rho(\vec{b}, z_1) \int\limits_{z_1}^{\infty} dz_2\, \rho(\vec{b}, z_2) \cos\left[q_V(z_1 - z_2)\right] e^{-\frac{1}{2}\sigma_{VN}(T_{z_1}(\vec{b}) + T_{z_2}(\vec{b}))}
$$

$$
+ \frac{1}{2}\frac{\sigma_{VN}^2}{\sigma_{VN}^{\mathrm{el}}} \int\limits_{-\infty}^{\infty} dz_1\, \rho(\vec{b}, z_1) \int\limits_{z_1}^{\infty} dz_2\, \rho(\vec{b}, z_2) \cos\left[q_V(z_1 - z_2)\right]
$$

$$
\times\, e^{-\frac{1}{2}(\sigma_{VN}^{\mathrm{inel}} - \sigma_{VN}^{\mathrm{el}})T_{z_2}(\vec{b}) - \frac{1}{2}\sigma_{VN}T_{z_1}(\vec{b})}. \tag{I.5}
$$

In the first step we have performed the integral over $z$. In the last step we have again rewritten the integral over $z_1$ and $z_2$ to be able to combine the second term of (I.5) with the second term of (I.1) to get the second term in (6.32). Now we only have to show the equality of the last term in (6.32) and the first one in (I.5). Therefore, we rewrite

$$
-\frac{1}{4}\quad \frac{\sigma_{VN}^2}{\sigma_{VN}^{\mathrm{el}}} \left| \int\limits_{-\infty}^{\infty} dz\, \rho(\vec{b}, z) e^{iq_V z} e^{-\frac{1}{2}\sigma_{VN}T_z(\vec{b})} \right|^2
$$

$$
= -\frac{1}{4}\frac{\sigma_{VN}^2}{\sigma_{VN}^{\mathrm{el}}} \int\limits_{-\infty}^{\infty} dz_1 \int\limits_{-\infty}^{\infty} dz_2\, \rho(\vec{b}, z_1)\, \rho(\vec{b}, z_2) \cos\left[q_V(z_1 - z_2)\right] e^{-\frac{1}{2}\sigma_{VN}(T_{z_1}(\vec{b}) + T_{z_2}(\vec{b}))}
$$

and reformulate the integral as

$$
\int\limits_{-\infty}^{\infty} dz_1 \int\limits_{-\infty}^{\infty} dz_2 \;=\; \int\limits_{-\infty}^{\infty} dz_1 \int\limits_{z_1}^{\infty} dz_2 + \int\limits_{-\infty}^{\infty} dz_2 \int\limits_{z_2}^{\infty} dz_1
$$

$$
=\; 2\int\limits_{-\infty}^{\infty} dz_1 \int\limits_{z_1}^{\infty} dz_2
$$

where the second equality again follows from the symmetry of the integrand with respect to the exchange of $z_1$ and $z_2$. The two expressions (6.30) and (6.32) are therefore equivalent.

# Bibliography

[Aba94]    S. Abatzis *et al.*,
           *Observation of a narrow scalar meson at 1450-MeV in the reaction pp →*
           *$p_f(\pi^+\pi^-\pi^+\pi^-)p_s$ at 450-GeV/c using the CERN Omega Spectrometer*,
           Phys. Lett. B **324**, 509 (1994).

[Abe86]    K. Abe *et al.*,
           *Lifetimes, cross sections, and production mechanisms of charmed particles*
           *produced by 20-GeV photons*,
           Phys. Rev. D **33**, 1 (1986).

[Acc03]    A. Accardi, V. Muccifora, and H.-J. Pirner,
           *Hadron production in deep inelastic lepton-nucleus scattering*,
           Nucl. Phys. A **720**, 131 (2003).

[Acc04]    A. Accardi and M. Gyulassy,
           *Cronin effect vs. geometrical shadowing in $d + Au$ collisions at RHIC*,
           Phys. Lett. B **586**, 244 (2003).

[Ack98]    K. Ackerstaff *et al.* [HERMES collaboration],
           *HERMES spectrometer*,
           Nucl. Instrum. Meth. A **417**, 230 (1998).

[Bin82]    M. Binkley *et al.*,
           *J/ψ photoproduction from 60 to 300 GeV/c*,
           Phys. Rev. Lett. **48**, 73 (1982).

[Ack99]    K. Ackerstaff *et al.* [HERMES collaboration],
           *Observation of a coherence length effect in exclusive $\rho^0$ electroproduction*,
           Phys. Rev. Lett. **82**, 3025 (1999).

[Ack00]    K. Ackerstaff *et al.* [HERMES collaboration],
           *Nuclear effects on $R = \sigma_L/\sigma_T$ in deep inelastic scattering*,
           Phys. Lett. B **475**, 386 (2000).

[Ada94]    M. R. Adams *et al.* [E665],
           *Scaled energy (z) distributions of charged hadrons observed in deep-inelastic*
           *muon scattering at 490 GeV from xenon and deuterium targets*,
           Phys. Rev. D **50**, 1836 (1994).

[Ada95]   M. R. Adams *et al.*,
          *Measurement of nuclear transparencies from exclusive $\rho^0$ meson production in muon-nucleus scattering at 470 GeV,*
          Phys. Rev. Lett. **74**, 1525 (1995).

[Adl97]   C. Adloff *et al.* [H1 collaboration],
          *Determination of the longitudinal proton structure function $F_L(x, Q^2)$ at low x,*
          Phys. Lett. B **393**, 452 (1997).

[AGK74]   V. A. Abramovsky, V. N. Gribov, and O. V. Kancheli,
          *Character of inclusive spectra and fluctuations produced in inelastic processes by multipomeron exchange,*
          Sov. J. Nucl. Phys. **18**, 308 (1974).

[Air00]   A. Airapetian *et al.* [HERMES Collaboration],
          *Exclusive leptoproduction of $\rho^0$ mesons from hydrogen at intermediate virtual photon energies,*
          Eur. Phys. J. C **17**, 389 (2000).

[Air01]   A. Airapetian *et al.* [HERMES Collaboration],
          *Hadron formation in deep-inelastic positron scattering in a nuclear environment,*
          Eur. Phys. J. C **20**, 479 (2001).

[Air03]   A. Airapetian *et al.* [HERMES Collaboration],
          *The $Q^2$-dependence of nuclear transparency for exclusive $\rho^0$ production,*
          Phys. Rev. Lett. **90**, 052501 (2003).

[Air03b]  A. Airapetian *et al.* [HERMES Collaboration],
          *Quark fragmentation to $\pi^\pm$, $\pi^0$, $K^\pm$, p and anti-p in the nuclear environment,*
          Phys. Lett. B **557**, 37 (2003).

[Alk81]   J. J. Aubert *et al.* [EMC],
          *A large magnetic spectrometer system for high-energy muon physics,*
          Nucl. Inst. Meth. **179**, 445 (1981).

[Alv70]   H. Alvensleben *et al.*,
          *Determination of the photoproduction phase of $\rho^0$ mesons,*
          Phys. Rev. Lett. **25**, 1377 (1970).

[Alv71]   H. Alvensleben *et al.*,
          *Determination of the photoproduction phase of $\phi$ mesons,*
          Phys. Rev. Lett. **27**, 444 (1971).

[Alv73]   H. Alvensleben *et al.*,
          *Experimental verification of the Kramers-Kronig relation at high energies,*
          Phys. Rev. Lett. **30**, 328 (1973).

[And83]  B. Andersson, G. Gustafson, G. Ingelman, and T. Sjöstrand,
         *Parton fragmentation and string dynamics*,
         Phys. Rep. **97**, 31 (1983).

[And87]  B. Andersson, G. Gustafson, and B. Nilsson-Almqvist,
         *A model for low-$p_T$ hadronic reactions with generalizations to hadron-nucleus and nucleus-nucleus collisions*,
         Nucl. Phys. B **281**, 289 (1987).

[And93]  B. Andersson, G. Gustafson, and Hong Pi,
         *The FRITIOF model for high energy hadronic collisions*,
         Z. Phys. C **57**, 485 (1993).

[And98]  B. Andersson,
         *The Lund Model*,
         Cambridge University Press (1998).

[Ara78]  E. A. Arakelyan *et al.*,
         *Measurement of total hadronic photoproduction cross sections on the nuclei C, Cu and Pb for energies $E_\gamma = (12 - 30)$ GeV*,
         Phys. Lett. B **79**, 143 (1978).

[Arl03]  F. Arleo,
         *Quenching of hadron spectra in DIS on nuclear targets*,
         Eur. Phys. J. C **30**, 213 (2003).

[Arn94]  M. Arneodo,
         *Nuclear effects in structure functions*,
         Phys. Rep. **240**, 301 (1994).

[Arr03]  J. Arrington *et al.*,
         *Pre-Conceptual Design Report (pCDR) for the Science and Experimental Equipment for the 12 GeV Upgrade of CEBAF*,
         available electronically from *http://www.jlab.org* (2003).

[Ash91]  J. Ashman *et al.* [EMC],
         *Comparison of forward hadrons produced in muon interactions on nuclear targets and deuterium*,
         Z. Phys. C **52**, 1 (1991).

[Ba83]   D. S. Barton *et al.*,
         *Experimental study of the A dependence of inclusive hadron fragmentation*,
         Phys. Rev. D **27**, 2580 (1983).

[Bai97]  R. Baier, Yu. L. Dokshitzer, A. H. Mueller, S. Peigné, and D. Schiff,
         *Radiative energy loss of high energy quarks and gluons in a finite-volume quark-gluon plasma*,
         Nucl. Phys. B **483**, 291 (1997).

[Bai98]    R. Baier, Yu. L. Dokshitzer, A. H. Mueller, and D. Schiff,
           *Medium-induced radiative energy loss: Equivalence between the BDMPS and
           Zakharov formalisms*,
           Nucl. Phys. B **531**, 403 (1998).

[Bai00]    R. Baier *et al.*,
           *Energy loss in perturbative QCD*,
           Ann. Rev. Nucl. Part. Sci. **50**, 37 (2000).

[Bal88]    A. Baldini, V. Flaminio, W. G. Moorhead, and D. R. O. Morrison,
           *Total cross sections for reactions of high energy particles*,
           Landolt-Börnstein, New Series vol. 12, Springer, Berlin (1988).

[Bar84]    D. P. Barber *et al.*,
           *A study of the reactions $\gamma p \to \omega p$ and $\gamma p \to \omega \Delta^+$*,
           Z. Phys. C **26**, 343 (1984).

[Bas98]    S. A. Bass *et al.*,
           *Microscopic models for ultrarelativistic heavy ion collisions*,
           Prog. Part. Nucl. Phys. **41**, 225 (1998).

[Bau78]    T. H. Bauer, F. Pipkin, R. Spital, and D. R. Yennie,
           *The hadronic properties of the photon in high-energy interactions*,
           Rev. Mod. Phys. **50**, 261 (1978).

[Beh78]    H. J. Behrend *et al.*,
           *Elastic and inelastic $\phi$-photoproduction*,
           Nucl. Phys. B **144**, 22 (1978).

[Ben89]    A.C. Benvenuti *et al.* [BCDMS collaboration],
           *A high statistics measurement of the proton structure function $F_2(x, Q^2)$ and
           R from deep inelastic muon scattering at high $Q^2$*,
           Phys. Lett. B **223**, 485 (1989).

[Ber72]    L. Bertocchi,
           *Graphs and Glauber*,
           Nuovo Cimento A **11**, 45 (1972).

[Ber77]    L. Bertocchi and D. Treleani,
           *Glauber theory, unitarity and the AGK cancellation*,
           J. Phys. G **2**, 147 (1977).

[Bi96]     N. Bianchi *et al.*,
           *Total hadronic photoabsorption cross section on nuclei in the nucleon reso-
           nance region*,
           Phys. Rev. C **54**, 1688 (1996).

[Bi99]     N. Bianchi, E. De Sanctis, M. Mirazita, and V. Muccifora,
           *Shadowing in nuclear photoabsorption above the resonance region*,
           Phys. Rev. C **60**, 064617 (1999).

[Bia87]   A. Bialas and M. Gyulassy,
          *Lund model and an outside-inside aspect of the inside-outside cascade,*
          Nucl. Phys. B **291**, 793 (1987).

[Big71]   P. J. Biggs *et al.,*
          *Determination of the real part of the $\rho$-nucleon forward scattering amplitude
          and the relative $\rho - \omega$ production phase,*
          Phys. Rev. Lett. **27**, 1157 (1971).

[Bjo83]   J. D. Bjorken,
          *Highly relativistic nucleus-nucleus collisions: The central rapidity region,*
          Phys. Rev. D **27**, 140 (1983).

[Bof96a]  S. Boffi, C. Giusti, F. D. Pacati, and N. Radici,
          *Electromagnetic response of atomic nuclei,*
          Clarendon Press, Oxford (1996).

[Bof96b]  S. Boffi, Ye. Golubeva, L. A. Kondratyuk, and M. I. Krivoruchenko,
          *Generalized photonuclear sum rule, resonance broadening and shadowing
          effects,*
          Nucl. Phys. A **606**, 421 (1996).

[Br95]    I. N. Bronstein, K. A. Semendjajew, G. Musiol, and H. Mühlig,
          *Taschenbuch der Mathematik,*
          $2^{nd}$ edition, Verlag Harri Deutsch (1995).

[Bra98]   E. L. Bratkovskaya, W. Cassing, R. Rapp, and J. Wambach,
          *Dilepton production and $m_T$ scaling at BEVELAC/SIS energies,*
          Nucl. Phys. A **634**, 168 (1998).

[Bra03]   E. L. Bratkovskaya, W. Cassing, and H. Stöcker,
          *Open charm and charmonium production at RHIC,*
          Phys. Rev. C **67**, 054905 (2003).

[Brk73]   G. R. Brookes *et al.,*
          *Total hadronic photoabsorption cross section of nuclei for photons in the
          GeV energy range,*
          Phys. Rev. D **8**, 2826 (1973).

[Bro82]   S. J. Brodsky,
          *Testing quantum chromodynamics,*
          in *Proceedings of the 13th International Symposium of Multiparticle Dynamics,* edited by W. Kittel, W. Metzger, and A. Stergiou,
          World Scientific, Singapore (1982).

[Bro00]   S. J. Brodsky, E. Chudakov, P. Hoyer, and J. M. Laget,
          *Photoproduction of charm near threshold,*
          Phys. Lett. B **498**, 23 (2001).

[Brt84] G. F. Bertsch, H. Kruse, and S. Das Gupta,
*Boltzmann equation for heavy-ion collisions*,
Phys. Rev. C **29**, 673 (1984).

[Byk73] E. Byckling and K. Kajantie,
*Particle kinematics*,
John Wiley and Sons, London (1973).

[Cal73] D. O. Caldwell, V. B. Elings, W. P. Hesse, R. J. Morrison, and F. V. Murphy,
*Total hadronic photoabsorption cross sections on hydrogen and complex nuclei from 4 to 18 GeV*,
Phys. Rev. D **7**, 1362 (1973).

[Cal79] D. O. Caldwell *et al.*,
*Measurement of shadowing in photon-nucleus total cross sections from 20 to 185 GeV*,
Phys. Rev. Lett. **42**, 553 (1979).

[Cap99] A. Capella, A. Kaidalov, and J. Tran Thanh Van,
*Gribov theory of nuclear interactions and particle densities at future heavy-ion colliders*,
Acta Phys. Hung. New Ser. Heavy Ion Phys. **9**, 169 (1999).

[Car79] A. S. Carroll *et al.*,
*Absorption cross-sections of $\pi^{\pm}$, $K^{\pm}$, p and anti-p on nuclei between 60 GeV/c and 280 GeV/c*,
Phys. Lett. B **80**, 319 (1979).

[Cas99] W. Cassing and E. L. Bratkovskaya,
*Hadronic and electromagnetic probes of hot and dense nuclear matter*,
Phys. Rep. **308**, 65 (1999).

[Cas02] W. Cassing, E. L. Bratkovskaya, O. Hansen,
*Probing hadronic formation times with antiprotons in $p + A$ reactions at AGS energies*,
Nucl. Phys. A **707**, 224 (2002).

[Cas04] W. Cassing, K. Gallmeister, and C. Greiner,
*Suppression of high transverse momentum hadrons at RHIC by prehadronic final state interactions*,
Nucl. Phys. A **735**, 277 (2004).

[Che61] G. F. P. Chew and S. C. Frautschi,
*Principle of equivalence for all strongly interacting particles within the S matrix framework*,
Phys. Rev. Lett. **7**, 394 (1961).

[Che62]   G. F. P. Chew and S. C. Frautschi,
          *Regge trajectories and the principle of maximum strength for strong inter-actions*,
          Phys. Rev. Lett. **8**, 41 (1962).

[Chm01]   I. Chemakin *et al.*,
          *Antiproton production in $p + A$ collisions at 12.3 and 17.5 GeV/c*,
          Phys. Rev. C **64**, 064908 (2001).

[Cio02]   C. Ciofi degli Atti and B. Z. Kopeliovich,
          *Final state interaction in semi-inclusive DIS off nuclei*,
          Eur. Phys. J. A **17**, 133 (2003).

[Cle69]   G. N. McClellan *et al.*,
          *Incoherent photoproduction of $\rho^0$ mesons from complex nuclei and comparison with vector-dominance predictions*,
          Phys. Rev. Lett. **23**, 554 (1969).

[Col77]   P. D. B. Collins,
          *An introduction to Regge theory and high energy physics*,
          Cambridge University Press (1977).

[Col84]   P. D. B. Collins and A. D. Martin,
          *Hadron interactions*,
          Adam Hilger Ltd, Bristol (1984).

[Cro75]   J. W. Cronin *et al.*,
          *Production of hadrons at large transverse momentum at 200, 300, and 400 GeV*,
          Phys. Rev. D **11** 3105 (1975).

[Des02]   A. Deshpande *et al.*,
          *The Electron-Ion Collider: A high luminosity probe of the partonic substructure of nucleons and nuclei*,
          available electronically from *http://www.doe.gov/bridge* (2002).

[Dam70]   M. Damashek and F. J. Gilman,
          *Forward Compton scattering*,
          Phys. Rev. D **1**, 1319 (1970).

[Don78]   A. Donnachie and G. Shaw,
          *Generalized vector dominance*,
          in *Electromagnetic interactions of hadrons: Volume 2*, p. 169, edited by
          A. Donnachie and G. Shaw,
          Plenum, New York (1978).

[Don92]   A. Donnachie and P. V. Landshoff,
          *Total cross-sections*,
          Phys. Lett. B **296**, 227 (1992).

[Don00]   A. Donnachie and P. V. Landshoff,
          *Exclusive vector production: Confirmation of Regge theory*,
          Phys. Lett. B **478**, 146 (2000).

[Dur88]   L. Durand and H. Pi,
          *High-energy nucleon-nucleus scattering and cosmic-ray cross sections*,
          Phys. Rev. D **38**, 78 (1988).

[Ede00]   P. Edén,
          *On energy conservation in Lund string fragmentation*,
          JHEP **05**, 029 (2000).

[Eff96]   M. Effenberger,
          *Gammaabsorption an Kernen*,
          Diploma thesis, University of Giessen (1996).

[Eff99a]  M. Effenberger,
          *Eigenschaften von Hadronen in Kernmaterie in einem vereinheitlichten Transportmodell*,
          PhD thesis, University of Giessen (1999).

[Eff99b]  M. Effenberger, E. L. Bratkovskaya, W. Cassing, and U. Mosel,
          *$e^+e^-$ pairs from $\pi^- A$ reactions: Comment*,
          Phys. Rev. C **60**, 27601 (1999).

[Eff99c]  M. Effenberger, E. L. Bratkovskaya, and U. Mosel,
          *$e^+e^-$ pair production from $\gamma A$ reactions*,
          Phys. Rev. C **60**, 44614 (1999).

[Eff00]   M. Effenberger and U. Mosel,
          *Photoproduction of mesons in nuclei at GeV energies*,
          Phys. Rev. C **62**, 014605 (2000).

[Elb03]   G. Elbakyan [HERMES collaboration],
          *Nuclear attenuation in Semi-Inclusive Electroproduction of Hadrons at HERMES*,
          in *Proceedings of DIS 2003*, St. Petersburg, 2003, edited by V. T. Kim and L. N. Lipatov, p. 597.

[Ele97]   V. L. Eletsky and B. L. Ioffe,
          *Meson masses in nuclear matter*,
          Phys. Rev. Lett. **78**, 1010 (1997).

[EMC83]   J. J. Aubert *et al.* [EMC],
          *The ratio of the nucleon structure functions $F_2^N$ for iron and deuterium*,
          Phys. Lett. B **123**, 275 (1983).

[Eri88]   T. Ericson and W. Weise,
          *Pions and nuclei*,
          Clarendon Press, Oxford (1988).

[Fal00a]   T. Falter,
           *Der Abschattungseffekt im nuklearen Photoabsorptionsquerschnitt,*
           Diploma thesis, University of Giessen (2000).

[Fal00b]   T. Falter, S. Leupold, and U. Mosel,
           *Low energy onset of nuclear shadowing in photoabsorption,*
           Phys. Rev. C **62**, 031602 (2000).

[Fal01]    T. Falter, S. Leupold, and U. Mosel,
           *Nuclear shadowing at low photon energies,*
           Phys. Rev. C **64**, 024608 (2001).

[Fal02]    T. Falter and U. Mosel,
           *Hadron formation in high-energy photonuclear reactions,*
           Phys. Rev. C **66**, 024608 (2002).

[Fal03a]   T. Falter, J. Lehr, U. Mosel, P. Mühlich, and M. Post,
           *In-medium properties of hadrons: Observables,*
           Proceedings of the International School on Nuclear Physics: $25^{th}$ Course:
           Heavy Ion Reactions from Nuclear to Quark Matter, Erice, Italy, 16-24
           Sep. 2003, nucl-th/0312093 (2003).

[Fal03b]   T. Falter, K. Gallmeister, and U. Mosel,
           *Incoherent $\rho^0$ electroproduction off nuclei,*
           Phys. Rev. C **67**, 054606 (2003).

[Fal04]    T. Falter, W. Cassing, K. Gallmeister, and U. Mosel,
           *Hadron formation and attenuation in deep inelastic lepton scattering off
           nuclei,*
           Phys. Lett. B **594**, 61 (2004).

[Fal04b]   T. Falter, W. Cassing, K. Gallmeister, and U. Mosel,
           *Hadron attenuation in deep inelastic lepton-nucleus scattering,*
           nucl-th/0406023.

[Fol63]    L. F. Foldy and R. F. Peierls,
           *Isotopic spin of exchanged systems,*
           Phys. Rev. **130**, 1585 (1963).

[For97]    J. R. Forshaw and D. A. Ross,
           *Quantum chromodynamics and the Pomeron,*
           Cambridge University Press (1997).

[Fr00a]    C. Friberg and T. Sjöstrand,
           *Jet production by virtual photons,*
           Eur.Phys. J. C **13**, 151 (2000).

[Fr00b]    C. Friberg and T. Sjöstrand,
           *Effects of longitudinal photons,*
           Phys. Lett. B **492**, 123 (2000).

[Fr00c]  C. Friberg and T. Sjöstrand,
*Total cross sections and event properties from real to virtual photons*,
JHEP **0009**, 010 (2000).

[Fri77a]  R. Friedberg and T. D. Lee,
*Fermion field nontopological solitons. 1*,
Phys. Rev. D **15**, 1694 (1977).

[Fri77b]  R. Friedberg and T. D. Lee,
*Fermion field nontopological solitons. 2. Models for hadrons*,
Phys. Rev. D **16**, 1096 (1977).

[Frö03]  F. Frömel, S. Leupold, and U. Mosel,
*Spectral function of quarks in quark matter*,
Phys. Rev. C **67**, 015206 (2003).

[Frö]  F. Frömel,
private communication.

[Ga90]  C. Gale, G. M. Welke, M. Prakash, S. J. Lee, and S. Das Gupta,
*Transverse momenta, nuclear equation of state, and momentum-dependent interactions in heavy-ion collisions*,
Phys. Rev. C **41**, 1545 (1990).

[Gal03]  K. Gallmeister, C. Greiner, and Z. Xu,
*Quenching of high p(T) hadron spectra by hadronic interactions in heavy ion collisions at RHIC*,
Phys. Rev. C **67**, 044905 (2003).

[Gar02]  E. Garutti [HERMES Collaboration],
*Hadron formation in nuclei in DIS*,
Act. Phys. Pol. B **33**, 3013 (2002).

[Gei98a]  J. Geiss,
*Produktion von Strangeness und Charmonium in Kern-Kern-Kollisionen*,
PhD thesis, University of Giessen (1998).

[Gei98b]  J. Geiss, W. Cassing, and C. Greiner,
*Strangeness production in the HSD approach from SIS to SPS energies*,
Nucl. Phys. A **644**, 107 (1998).

[Gel61]  M. Gell-Mann and F. Zachariasen,
*Form factors and vector mesons*,
Phys. Rev. **124**, 953 (1961).

[Gel64]  M. Gell-Mann,
*A schematic model of baryons and mesons*,
Phys. Lett. **8**, 214 (1964).

[Gla59]   R. J. Glauber,
*High energy collision theory*,
in *Lectures in Theoretical Physics*, Vol. I, p. 315, edited by W. E. Brittin
and L. G. Dunham,
Wiley Interscience, New York (1959).

[Gla70]   R. J. Glauber,
*Theory of high energy hadron-nucleus collisions*,
in *High Energy Physics and Nuclear Structure*, p. 207, edited by S. Devons,
Plenum, New York (1970).

[Gle83]   N. K. Glendenning and T. Matsui,
*Creation of $q\bar{q}$ pairs in a chromoelectric flux tube*,
Phys. Rev. D **28**, 2890 (1983).

[Glü92]   M. Glück, F. Reya, and A. Vogt,
*Pionic parton distributions*,
Z. Phys. C **53**, 651 (1992).

[Gou83]   K. Goulianos,
*Diffractive interactions of hadrons at high energies*,
Phys. Rep. **101**, 170 (1983).

[Gre73]   H. Grenz and W. Schmidt,
*On a proportionality of hadronic and electromagnetic amplitudes*,
Nucl. Phys. B **59**, 629 (1973).

[Gri69]   V. N. Gribov,
*Glauber corrections and the interaction between high energy hadrons and
nuclei*,
Sov. Phys. JETP **29** 483 (1969).

[Gri70]   V. N. Gribov,
*Interactions of gamma quanta and electrons with nuclei at high energies*,
Sov. Phys. JETP **30**, 709 (1970).

[Guo00]   X. Guo and X. N. Wang,
*Multiple scattering, parton energy loss, and modified fragmentation func-
tions in deeply inelastic eA scattering*,
Phys. Rev. Lett. **85**, 3591 (2000).

[Gyu03]   M. Gyulassy, I. Vitev, X. N. Wang, and B. Zhang,
*Jet Quenching and radiative energy loss in dense nuclear matter*,
in *Review for: Quark Gluon Plasma 3*, edited by R. C. Hwa and X.-N. Wang,
World Scientific, Singapore, 2003, nucl-th/0302077 (2003).

[Haf02]   K. Hafidi, M. Holtrop, and B. Mustapha,
*$Q^2$ dependence of nuclear transparency for incoherent $\rho^0$ electroproduction*,
Jefferson Lab proposal E-02-110 (2002).

[Hal84]    F. Halzen and A. D. Martin,
*Quarks and Leptons,*
John Wiley and Sons, New York (1984).

[Han63]    L. N. Hand,
*Experimental investigation of pion electroproduction,*
Phys. Rev. **129**, 1834 (1963).

[HERM]    HERMES data available from:
*http://www-hermes.desy.de/notes/pub/trans-public-
subject.html#HADRONATTENUATION.*

[Hil03]    A. Hillenbrand,
*Tuning of the Lund model for fragmentation functions and purities,*
in *Proceedings of DIS 2003*, St. Petersburg, 2003, edited by V. T. Kim and
L. N. Lipatov, DESY-HERMES-03-26.

[Hom99]    A. Hombach, W. Cassing, S. Teis, and U. Mosel,
*Analysis of flow effects in relativistic heavy-ion collisions within the CBUU
approach,*
Eur. Phys. J. A **5**, 157 (1999).

[Hüf96]    J. Hüfner, B. Z. Kopeliovich, and J. Nemchik,
*Glauber multiple scattering theory for the photoproduction of vector mesons
off nuclei and the role of the coherence length,*
Phys. Lett. B **383**, 362 (1996).

[Jai96]    P. Jain, B. Pire, and J. P. Ralston,
*Quantum color transparency and nuclear filtering,*
Phys. Rep. **271**, 67 (1996).

[Joh01]    M. B. Johnson, B. Z. Kopeliovich, and A. V. Tarasov,
*Broadening of transverse momentum of partons propagating through a
medium,*
Phys. Rev. C **63**, 035203 (2001).

[Kod84]    T. Kodama *et al.*,
*Causality and relativistic effects in intranuclear cascade calculations,*
Phys. Rev. C **29**, 2146 (1984).

[Kon98]    L. A. Kondratyuk, A. Sibirtsev, W. Cassing, Y. S. Golubeva, and M. Effen-
berger,
*Rho meson properties at finite nuclear density,*
Phys. Rev. C **58**, 1078 (1998).

[Kop96]    B. Z. Kopeliovich, J. Nemchik, and E. Predazzi,
*Hadronization in nuclear environment,*
in Proceedings of the workshop on Future Physics at HERA (DESY,
1995/96), vol 2, p. 1038, edited by G. Ingelman, A. De Roeck, and R. Klan-
ner, nucl-th/9607036 (1996).

[Kop01] B. Z. Kopeliovich, J. Nemchik, A. Schaefer, and A. V. Tarasov,
*Color transparency versus quantum coherence in electroproduction of vector mesons off nuclei*,
Phys. Rev. C **65**, 035201 (2001).

[Kop02] B. Z. Kopeliovich, J. Nemchik, A. Schäfer, and A. V. Tarasov,
*Cronin effect in hadron production off nuclei*,
Phys. Rev. Lett. **88**, 232303 (2002).

[Kop03] B. Z. Kopeliovich, J. Nemchik, E. Predazzi, and A. Hayashigaki,
*Nuclear hadronization: within or without?*,
Talk given at the 4th International Conference on Perspectives in Hadronic Physics, Trieste, Italy, May 12–16, 2003, hep-ph/0311220 (2003).

[KWa04] K. Wang, J. P. Chen, and B. Norum,
*Hadronization in nuclei by deep inelastic electron scattering*,
Jefferson Lab proposal PR 04-002 (2004).

[Leh99] J. Lehr,
*Elektroproduktion von Mesonen an Kernen*,
Diploma thesis, University of Giessen (1999).

[Leh00] J. Lehr, M. Effenberger, and U. Mosel,
*Electron and photon induced reactions on nuclei in the nucleon resonance region*,
Nucl. Phys. A **671**, 503 (2000).

[Leh03] J. Lehr,
*In-Medium-Eigenschaften von Nukleonen und Nukleonresonanzen in einem semiklassischen Transportmodell*,
PhD thesis, University of Giessen (2003).

[Leh] J. Lehr,
private communication.

[Lön92] L. Lönnblad,
*ARIADNE-4*,
preprint, DESY 92-046 (1992).

[Man92] D. M. Manley and E. M. Saleski,
*Multichannel parameterization of $\pi N$ scattering amplitudes*,
Phys. Rev. D **45**, 4002 (1992).

[Mar] G. Martens,
private communication.

[Mar04] G. Martens,
PhD thesis, University of Giessen, in preparation.

[Mic77]     S. Michalowsky, D. Andrews, J. Eickmeyer, T. Gentile, N. Mistry, R. Talman, and K. Ueno,
*Experimental study of nuclear shadowing in photoproduction,*
Phys. Rev. Lett. **39**, 737 (1977).

[Mis73]     C. W. Misner, K. S. Thorne, and J. A. Wheeler,
*Gravitation,*
W. H. Freeman and Company (1973).

[Mos98]     U. Mosel,
*Field, Symmetries and Quarks,*
Springer, Berlin (1998).

[Muc99]     V. Muccifora *et al.,*
*Photoabsorption on nuclei in the energy range 0.5-2.6 GeV,*
Phys. Rev. C **60**, 064616 (1999).

[Muc02]     V. Muccifora [HERMES Collaboration],
*Hadron formation in DIS from nuclear target and nuclear transparency,*
Nucl. Phys. A **711**, 254 (2002).

[Muc]     V. Muccifora,
private communication.

[Mue70]     A. H. Mueller,
*O(2,1) analysis of single particle spectra at high energy,*
Phys. Rev. D **2**, 2963 (1970).

[Mue82]     A. H. Mueller,
*Topics in high-energy perturbative QCD including interactions with nuclear matter,*
in *Proceedings of the 17th Recontre de Moriond, Moriond, 1982,* edited by J. Tran Tanh Van,
Editions Frontieres, Gif-sur-Yvette Cedex, France (1982).

[Müh03]     P. Mühlich, T. Falter, C. Greiner, J. Lehr, M. Post, and U. Mosel,
*Photoproduction of $\phi$ mesons from nuclei,*
Phys. Rev. C **67**, 024605 (2003).

[Müh04]     P. Mühlich, T. Falter, and U. Mosel,
*Inclusive $\omega$ photoproduction off nuclei,*
nucl-th/0310067 (2003).

[Mut87]     T. Muta,
*Foundations of quantum chromodynamics: An introduction to perturbative methods in gauge theories,*
World Scientific (1987).

[Nak03]     T. Nakano *et al.,*
*Evidence of a narrow $S = +1$ baryon resonance in photoproduction from*

*the neutron*,
Phys. Rev. Lett. **91**, 012002 (2003).

[Nez04]    P. Di Nezza [HERMES Collaboration],
*Hadron suppression in DIS at HERMES* in *Proceedings of Quark Matter 2004*, Oakland, January 11–17, to be published in J. Phys. G.

[Osb78]    L. S. Osborne *et al.*,
*Electroproduction of hadrons from nuclei*,
Phys. Rev. Lett. **40**, 1624 (1978).

[Owe78]    G. F. Owens, F. Reya, and M. Glück,
*Detailed quantum chromodynamic predictions for high $p_T$ processes*,
Phys. Rev. D **18**, 1501 (1978).

[PDG94]    L. Montanet *et al.* [Particle Data Group],
*Review of particle properties*,
Phys. Rev. D **50**, 1173 (1994).

[PDG98]    C. Caso *et al.* [Particle Data Group],
*Review of particle physics*,
Eur. Phys. J. C **3**, 1 (1998).

[PDG02]    K. Hagiwara *et al.* [Particle Data Group],
*Review of particle physics*,
Phys. Rev. D **66**, 010001 (2002).

[Pen02a]   G. Penner and U. Mosel,
*Vector meson production and nucleon resonance analysis in a coupled channel approach for energies $m_N < \sqrt{s} < 2$ GeV. I: Pion induced results and hadronic parameters*,
Phys. Rev. C **66**, 055211 (2002).

[Pen02b]   G. Penner and U. Mosel,
*Vector meson production and nucleon resonance analysis in a coupled channel approach for energies $m_N < \sqrt{s} < 2$ GeV. II: Photon induced results*,
Phys. Rev. C **66**, 055212 (2002).

[Per87]    D. H. Perkins,
*Introduction to high energy physics*,
Addison-Wesley Publishing Company (1987).

[Pes95]    M. E. Peskin and D. V. Schroeder,
*An introduction to quantum field theory*,
Addison-Wesley Publishing Company (1995).

[PH03]     S. S. Adler *et al.* [PHENIX Collaboration],
*Absence of suppression in particle production at large transverse momentum in $s(NN)^{1/2} = 200$ GeV $d + Au$ collisions*,
Phys. Rev. Lett. **91**, 072303 (2003).

[PH04]      S. S. Adler *et al.* [PHENIX Collaboration],
*High $p_T$ charged hadron suppression in $Au + Au$ collisions at $S(NN)^{1/2} = 200\ GeV$,*
Phys. Rev. C **69**, 034910 (2004).

[Pi92]       Hong Pi,
*An event generator for interactions between hadrons and nuclei – FRITIOF version 7,*
Comput. Phys. Commun. **71**, 173 (1992).

[Pil95]      G. Piller, W. Ratzka, and W. Weise,
*Phenomenology of nuclear shadowing in deep inelastic scattering,*
Z. Phys. A **352**, 427 (1995).

[Pil00]      G. Piller and W. Weise,
*Nuclear deep-inelastic lepton scattering and coherence phenomena,*
Phys. Rep. **330**, 1 (2000).

[Plo93]     H. Plothow-Besch,
*PDFLIB: A library of all available parton density functions of the nucleon, the pion and the photon and the corresponding $\alpha_S$ calculations,*
Computer Physics Commun. **75**, 396 (1993).

[Plo95]     H. Plothow-Besch,
*The parton distribution function library,*
Int. J. Mod. Phys. A **10**, 2901 (1995).

[Pov97]    B. Povh, K. Rith, C. Scholz, and F. Zetsche,
*Teilchen und Kerne,*
Springer, Berlin (1997).

[Reg59]    T. Regge,
*Introduction to complex orbital momenta,*
Nuovo Cimento **14**, 951 (1959).

[Reg60]    T. Regge,
*Bound states, shadow states and Mandelstam representation,*
Nuovo Cimento **18**, 947 (1960).

[Sak60]    J. J. Sakurai,
*Theory of strong interactions,*
Ann. Phys. (USA) **11**, 1 (1960).

[Sak69]    J. J. Sakurai,
*Vector meson dominance and high-energy electron proton scattering,*
Phys. Rev. Lett. **22**, 981 (1969).

[Sak94]    J. J. Sakurai,
*Modern quantum mechanics,*
Addison-Wesley Publishing Company (1994).

[Sch93a]  G. A. Schuler and T. Sjöstrand,
*The hadronic properties of the photon in γp interactions*,
Phys. Lett. B **300**, 169 (1993).

[Sch93b]  G. A. Schuler and T. Sjöstrand,
*Towards a complete description of high energy photoproduction*,
Nucl. Phys. B **407**, 539 (1993).

[Sch94]  G. A. Schuler and T. Sjöstrand,
*Hadronic diffractive cross sections and the rise of the total cross section*,
Phys. Rev. D **49**, 2257 (1994).

[Sch95]  G. A. Schuler and T. Sjöstrand,
*Low and high mass components of the photon distribution functions*,
Z. Phys. C **68**, 607 (1995).

[Sch96]  G. A. Schuler and T. Sjöstrand,
*Parton distributions of the virtual photon*,
Phys. Lett. B **376**, 193 (1996).

[Sjö01a]  T. Sjöstrand *et al.*,
*High-energy-physics event generation with PYTHIA 6.1*,
Comput. Phys. Commun. **135**, 238 (2001).

[Sjö01b]  T. Sjöstrand, L. Lonnblad, and S. Mrenna,
*PYTHIA 6.2 Physics and manual*,
hep-ph/0108264 (2001).

[Sjö04]  T. Sjöstrand,
*A manual to the Lund Monte Carlo for jet fragmentation and $e^+e^-$ physics: JETSET version 7.3*,
available upon request to the author.

[ST03]  J. Adams *et al.* [STAR Collaboration],
*Evidence from $d + Au$ measurements for final-state suppression of high-$p_T$ hadrons in $Au + Au$ collisions at RHIC* ,
Phys. Rev. Lett. **91**, 072304 (2003).

[ST03b]  J. Adams *et al.* [STAR Collaboration],
*Transverse-momentum and collision-energy dependence of high-$p_T$ hadron suppression in $Au + Au$ collisions at ultrarelativistic energies*,
Phys. Rev. Lett. **91**, 172302 (2003).

[Sor90]  H. Sorge *et al.*,
*String dynamics in hadronic matter*,
Z. Phys. C **47**, 629 (1990).

[Tei96]  S. Teis,
*Transporttheoretische Beschreibung von relativistischen Schwerionenkollisionen bei SIS-Energien*,
PhD thesis, University of Giessen (1996).

[Tei97] S. Teis, W. Cassing, M. Effenberger, A. Hombach, U. Mosel, and G. Wolf,
*Pion production in heavy-ion collisions at SIS energies*,
Z. Phys. A **356**, 421 (1997).

[Tra99] C. T. Traxler, U. Mosel, and T. S. Biro,
*Hadronization of a quark-gluon plasma in the chromodielectric model*,
Phys. Rev. C **59**, 1620 (1999).

[Wag04] M. Wagner,
*Kaon and pion production at CBM energies*,
Diploma thesis, University of Giessen (2004).

[Wan92] X. N. Wang and M. Gyulassy,
*Gluon shadowing and jet quenching in $A + A$ collisions at $s^{1/2} = 200$ GeV*,
Phys. Rev. Lett. **68**, 1480 (1992).

[Wan98] X. N. Wang,
*Effects of jet quenching on high $p_T$ hadron spectra in high-energy nuclear collisions*,
Phys. Rev. C **58**, 2321 (1998).

[Wan01] X. N. Wang and X. Guo,
*Multiple parton scattering in nuclei: parton energy loss*,
Nucl. Phys. A **696**, 788 (2001).

[Wan02] E. Wang and X. N. Wang,
*Jet tomography of hot and cold nuclear matter*,
Phys. Rev. Lett. **89**, 162301 (2002).

[Wan03] X. N. Wang,
*Probe initial parton density and formation time via jet quenching*,
Nucl. Phys. A **715**, 775 (2003).

[WBr] W. Brooks,
private communication.

[WBr02] W. Brooks *et al.*,
*Quark propagation through cold QCD matter*,
Jefferson Lab proposal E-02-104 (2002).

[WBr03] W. Brooks,
*Space-time properties of hadronization from nuclear deep inelastic scattering*,
in *Proceedings of the 2nd Conference on Nuclear and Particle Physics with CEBAF at Jlab (NAPP 2003)*, Dubrovnik, Croatia, 2003, nucl-ex/0310032 (2003).

[We76] J. H. Weis,
*Regge theory and high energy hadron-nucleus scattering*,
Acta. Phys. Pol. B **7**, 851 (1976).

[Web03]  H. Weber, E. L. Bratkovskaya, W. Cassing, and H. Stöcker,
*Hadronic observables from SIS to SPS energies: Anything strange with strangeness?*,
Phys. Rev. C **67**, 014904 (2003).

[Wei99]  T. Weidmann, E. L. Bratkovskaya, W. Cassing, and U. Mosel,
$e^+e^-$ *pairs from $\pi^- A$ reactions*,
Phys. Rev. C **59**, 919 (1999).

[Wel88]  G. M. Welke, M. Prakash, T. T. S. Kuo, and S. Das Gupta,
*Azimuthal distributions in heavy ion collisions and the nuclear equation of state*,
Phys. Rev. C **38**, 2101 (1988).

[WW74]  W. Weise,
*Hadronic aspects of photon-nucleus interaction*,
Phys. Rep. **13**, 53 (1974).

[Yen71]  D. R. Yennie,
*Interactions of high-energy photons with nuclei as a test of vector meson dominance*,
in *Hadronic Interactions of Electrons and Photons*, p. 321, edited by J. Cumings and H. Osborn,
Academic, New York/London (1971).

# Deutsche Zusammenfassung

Der Urknall-Theorie zufolge begann das Universum in einem Zustand unendlich hoher Dichte und Temperatur, gefolgt von einer schnellen Ausdehnung und Abkühlung [Mis73]. Circa $10^{-30}$ Sekunden nach seinem Anfang entstanden Quarks, Leptonen und Eichbosonen. Nur wenige Mikrosekunden später verbanden sich die Quarks zu Nukleonen, ein Prozeß, der als *Hadronisierung* bezeichnet wird. Die sichtbare Materie im uns heute bekannten Universum besteht fast vollständig aus Nukleonen (=Protonen, Neutronen) und Elektronen.

Neben den Nukleonen wurden in den vergangenen 60 Jahren noch Hunderte weitere instabile Bindungszustände von Quarks (und Antiquarks) in Experimenten mit Teilchenbeschleunigern und kosmischer Strahlung entdeckt. Diese stark wechselwirkenden Teilchen werden Hadronen genannt und können in zwei Quark-Kombinationen eingeteilt werden [Gel64]: *Baryonen* (aus drei Quarks bestehende Fermionen $qqq$) und *Mesonen* (aus Quark und Antiquark bestehende Bosonen $q\bar{q}$). Da die Quarks selbst Fermionen sind, verbietet die Fermi-Statistik die Existenz eines aus drei Quarks bestehenden, gebundenen Spin-3/2-Zustands. Ein solcher Zustand wurde jedoch 1951 durch Fermi und Mitarbeiter entdeckt: Das $\Delta^{++}$ besteht aus drei $u$-Quarks mit parallel ausgerichteten Spins. Diese Beobachtung erforderte die Einführung der *Farbe* als weitere Quantenzahl für Quarks. Man nimmt an, daß Quarks in drei Farbzuständen (rot, grün und blau) vorkommen[1] und daß alle freien Teilchen farbneutral sein müssen. Letzteres wird von der experimentellen Beobachtung gestützt, daß keine Hadronen verschiedener Farbe existieren. Die Existenz von exakt drei Farbzuständen wird durch Experimente zur Elektron-Positron-Paarvernichtung in Hadronen sowie dem Zwei-Photonen-Zerfall des neutralen Pions bestätigt [Per87].

Die Forderung, daß alle freien Teilchen farbneutral sein müssen, erklärt auch, warum man keine freien Quarks sondern nur Farb-Singulett-Kombinationen beobachtet[2]. Dieses Phänomen wird als *Confinement* bezeichnet und impliziert, daß die potentielle Energie zweier farbiger Objekte mit zunehmendem Relativabstand stark anwächst. Die Feldkonfiguration, die dem linear anwachsenden Potential entspricht, hat eine zylindrische Form und ist zwischen den Farbladungen konzentriert. Sie wird daher oft auch als *String* bezeichnet. Durch eine Ausdehnung des Strings um 1–2 fm erhöht sich die Feldenergie soweit, daß Quark-Antiquark-Paare aus dem Vakuum erzeugt werden. Diese verbinden sich dann mit den beiden farbigen Teilchen an den String-Enden und bilden farbneutrale Hadronen.

Die Quarkstruktur der Hadronen legt es nahe, die starke Wechselwirkung auf Farb-

---

[1]Die Antiquarks tragen Antifarbe.

[2]Vor kurzem fand sich ein experimenteller Hinweis auf die Existenz eines farbneutralen Pentaquark-Zustands [Nak03].

wechselwirkungen zwischen den Quarks zurückzuführen. Die zugrundeliegende Theorie ist die Quantenchromodynamik (QCD). Im Gegensatz zur Quantenelektrodynamik (QED) ist die QCD eine *nicht-Abelsche* Eichfeldtheorie. Daraus folgt, daß die Eichbosonen (Gluonen), welche die Farbwechselwirkung vermitteln, selbst Farbe tragen und untereinander wechselwirken können. Dies führt zu einer Anti-Abschirmung von Farbladungen, was zwei bemerkenswerte Konsequenzen in sich birgt. Für kleine Abstände bzw. große Impulsüberträge wird die Kopplung klein, und die Quarks im Inneren der Hadronen verhalten sich im wesentlichen wie freie, nicht wechselwirkende Teilchen (asymptotische Freiheit). In diesem kinematischen Bereich sind daher störungstheoretische Techniken zur Berechnung der Quark-Gluon-Wechselwirkung anwendbar. Andererseits entspricht die Anti-Abschirmung in der QCD einem farbdielektrischen Medium mit verschwindend kleiner Dielektrizitätskontante $\epsilon \ll 1$. In einem solchen Medium hätte eine isolierte Farbladung eine extrem hohe Energie, was das beobachtete Confinement begründet.

Da die Kopplung in der QCD mit abnehmendem Impulsübertrag anwächst, können störungstheoretische Methoden nicht zur Beschreibung der Niederenergie-QCD herangezogen werden. Daher steht bis heute ein vollständiger Beweis dafür, daß die QCD tatsächlich Confinement bedingt, aus. Aus dem gleichen Grund können die Eigenschaften von Hadronen, wie beispielsweise Massen und Anregungspektren, nicht im Rahmen der Störungstheorie berechnet werden. Hierzu ist man auf die numerische Lösung einer diskretisierten Version der QCD auf einem Raum-Zeit-Gitter angewiesen. Diese Rechnungen sind jedoch mit einem erheblichen Rechenaufwand sowie vielen konzeptionellen Problemen verbunden, so daß man von einer vollständigen Beschreibung der Hadronenspektren und hadronischen Wechselwirkungen noch weit entfernt ist.

Eine der großartigsten Leistungen der Hochenergiephysik der letzten 30 Jahre ist die quantitative Bestätigung der QCD in sehr harten Kollisionen. Aufgrund der asymptotischen Freiheit verhalten sich die Konstituenten der Hadronen in solchen Kollisionen wie freie Teilchen. Wie schon erwähnt, verschwindet diese Eigenschaft bei kleinen Impulsüberträgen, und die Quarks und Gluonen werden durch die starke Wechselwirkung in Hadronen gebunden. Dieser Phasenübergang von Quark- und Gluon-Freiheitsgraden zu wechselwirkenden Hadronen – wie er im Universum kurz nach dem Urknall stattfand – ist ein zentrales Forschungsthema der modernen Hadronenphysik. Zur Zeit werden Experimente mit ultrarelativistischen Schwerionenkollisionen am SPS und RHIC durchgeführt, um die Dynamik und relevanten Skalen dieses Phasenübergangs zu verstehen. Die Komplexität von Schwerionenkollisionen, die verschiedene Dichte- und Temperaturphasen durchlaufen, erschwert es jedoch, Rückschlüsse auf den genauen raumzeitlichen Ablauf des Hadronisierungsprozesses ziehen zu können.

In den frühen 70er Jahren wurde die Quarkstruktur des Nukleons in tiefinelastischer Elektron-Proton-Streuung am SLAC nachgewiesen. In der tiefinelastischen Streuung emittiert das Elektron ein virtuelles Photon mit hoher Energie und Impuls, welches von einem Quark im Proton absorbiert wird. Dabei kann man den vom Quark getragene Impulsbruchteil des Protons aus dem übertragenen Viererimpuls berechnen. Durch Variation von Energie und Impuls des virtuellen Photons können daher die Quarkverteilungen im Nukleon bestimmt werden. Seit dieser Pionierarbeit hat man viel über die Quark- und Gluon-Struktur hadronischer Materie aus tiefinelastischen Streuexperimenten am CERN, DESY, FNAL und SLAC gelernt.

Durch die tiefinelastische Streuung an Atomkernen ist die Modifikation von Quark- und Gluonverteilungen in Kernmaterie zugänglich. Allerdings hat die Verwendung von Atomkernen noch einen weiteren Vorteil. Wenn sich das vom Photon getroffene Quark vom restlichen System entfernt, vergeht eine gewisse Zeit bis die Reaktionsprodukte hadronisieren. Aufgrund von Zeitdilatationseffekten liegen die entsprechenden Formationslängen in der Größenordnung der Kernradien. Die Reaktionsprodukte in Lepton-Kern-Reaktionen können daher während der Formationszeit mit der umgebenden Kernmaterie wechselwirken. Der Atomkern dient dabei als Mikro-Labor, das uns mittels des Kerndurchmessers eine intrinsische (variable) Zeitskala liefert. Dies kann man ausnutzen, um Informationen über die eigentliche Hadronisierungszeit zu erhalten. Die Verwendung verschiedener Atomkerne und die Variation der Photonkinematik ermöglichen es daher, die Propagation des Quarks und die Regeneration seines Farbfeldes zu studieren.

Erste Experimente zur hochenergetischen Elektroproduktion von Hadronen wurden in den späten 70er Jahren am SLAC durchgeführt [Osb78]. Anfang der 90er Jahre untersuchte die European Muon Collaboration (EMC) [Ash91] am CERN und das E665 Experiment [Ada94] am FNAL die Unterdrückung schneller Hadronen in der Streuung hochenergetischer Myonen an Atomkernen. Vor kurzem hat die HERMES-Kollaboration am DESY eine detaillierte experimentelle Untersuchung der Hadronproduktion in der tiefinelastischen Streuung von 27.7 GeV Positronen an Kernen durchgeführt [Air01, Air03b]. Ein ähnliches Experiment mit einem 6-GeV-Elektronenstrahl läuft zur Zeit am Jefferson Lab [WBr02, KWa04]; ein weiteres ist nach dem Upgrade auf 12 GeV Strahlenergie geplant [Arr03, WBr03]. Außerdem ist die Untersuchung der Hadronisierung in Nukleonen und Kernen ein Teil des Forschungsprogramms am geplanten Electron-Ion-Collider (EIC) [Des02], in welchem 5–10-GeV-Elektronen/Positronen mit 100-$A$GeV-Ionenstrahlen kollidieren.

Eng verbunden mit der Produktion von Hadronen in tiefinelastischer Streuung ist das Phänomen der Farbtransparenz [Mue82, Bro82]. In der tiefinelatischen Streuung überträgt das virtuelle Photon seine gesamte Energie und Impuls auf ein einzelnes Quark im Nukleon und das Nukleon wird zerstört. Das Photon kann jedoch auch vor der eigentlichen Wechselwirkung in ein virtuelles Quark-Antiquark-Paar fluktuieren, welches anschließend am Nukleon streut. Dieser Streuprozeß muß nicht notwendigerweise hart sein. Ein bekanntes Beispiel ist die diffraktive Vektormesonproduktion, in der eine hadronische Fluktuation des Photons durch einen kleinen Impulsaustausch mit dem Nukleon auf seine Massenschale gesetzt wird und das Nukleon intakt bleibt. Es ist zu erwarten, daß die geometrische Ausdehnung des ursprünglichen Quark-Antiquark-Paares mit steigender Photonvirtualität $Q^2$ abnimmt. Daher befindet sich das farbneutrale Quark-Antiquark-Paar für große $Q^2$ anfänglich in einer räumlich kleinen Konfiguration und wechselwirkt vorwiegend über sein Farb-Dipolmoment. Der resultierende Wirkungsquerschnitt ist proportional zum Quadrat des Paardurchmessers. Aufgrund von Zeitdilatationseffekten kann das hochenergetische Quark-Antiquark-Paar in dieser kleinen Konfiguration eine große Distanz zurücklegen. Liegt diese in der Größenordnung des Atomkerns, führt dies zu einer gesteigerten Durchlässigkeit in Kernmaterie und damit zu einem erhöhten nuklearen Vektormeson-Produktionsquerschnitt.

Die exklusive Elektroproduktion von $\rho^0$-Mesonen an Stickstoff wurde kürzlich von der HERMES-Kollaboration gemessen [Ack99, Air03]; ein ähnliches Experiment wird

derzeit am Jefferson Lab durchgeführt [Haf02]. Die kohärente Mehrfachstreuung der Vektormesonkomponente des Photons im Kern erschwert die Extraktion eines deutlichen Signals für Farbtransparenz aus diesen Experimenten. Die Wechselwirkungen des Photons im Eingangskanal der Reaktion führen zum nuklearen Abschattungseffekt, d.h. einer Reduzierung des Produktionsquerschnitts. Dieser Effekt wird auch im nuklearen Photoabsorptionsquerschnitt beobachtet [Bau78] und ist die Ursache des EMC-Effekts [EMC83, Arn94] bei kleinen Werten der Bjorken-Skalenvariable $x$.

Im kinematischen Bereich der EMC-, HERMES- und Jefferson Lab-Experimente ist eine klare Trennung zwischen den direkten Photon-Quark-Wechselwirkungen und denen, die durch die hadronischen Fluktuationen des Photons vermittelt werden, nicht möglich. Es muß daher beiden Aspekten der Wechselwirkung hochenergetischer Photonen Rechnung getragen werden, wenn man aus diesen Experimenten etwas über das Raum-Zeit-Verhalten des Hadronisierungsvorgangs lernen möchte.

Der raumzeitliche Ablauf des Hadronisierungsprozesses stellt allein schon eine faszinierende Fragestellung dar. Außerdem vermag er auch Aufschluß über aktuelle Beobachtungen in Schwerionenkollisionen am RHIC [PH03, PH04, ST03, ST03b] zu geben. Es ist unklar, in welchem Ausmaß die hier beobachtete Unterdrückung hadronischer Jets durch hadronische [Gal03, Kop03, Cas04] oder partonische [Wan92, Wan98, Bai00, Gyu03] Endzustandswechselwirkungen verursacht wird. Üblicherweise führt man die Unterdrückung hochenergetischer Jets in $Au + Au$-Reaktionen relativ zu $p + p$-Kollisionen auf eine Wechselwirkung der hochenergetischen Teilchen im Quark-Gluon-Plasma zurück. Hiermit wird ein Zustand bezeichnet, bei dem nicht länger Hadronen sondern freie Quarks und Gluonen die relevanten Freiheitsgrade darstellen. Die beobachtete Verminderung kann jedoch auch teilweise von hadronischen Endzustandswechselwirkungen verursacht werden.

Elektron-Kern-Reaktionen haben den Vorteil, daß der Atomkern während der Reaktion mehr oder weniger im Grundzustand bleibt. Im Gegensatz zu Kern-Kern-Kollisionen, in denen sich der produzierte 'Feuerball' schnell ausdehnt, finden Lepton-Kern-Reaktionen in einer wohldefinierten geometrischen Umgebung statt, die sich experimentell gut kontrollieren läßt.

Einen üblichen theoretischen Zugang zu hochenergetischen Kernreaktionen stellt die Glauber-Theorie [Gla59, Gla70] dar, welche die Kernreaktion auf elementare Wechselwirkungen mit individuellen Nukleonen reduziert. Sie ermöglicht eine quantenmechanische Beschreibung des Streuvorgangs durch eine kohärente Summation der Mehrfachstreuamplituden. Eine komplette quantenmechanische Beschreibung ist allerdings nur unter vielen Näherungen möglich. Daher vernachlässigt man in der Regel alle Gekoppelten-Kanal-Effekte in der Rechnung und beschränkt sich auf eine rein absorptive Beschreibung der Endzustandswechelwirkungen der Reaktionsprodukte.

Die gekoppelten Kanäle in den Endzustandswechselwirkungen können in einem semiklassischen Transportmodells berücksichtigt werden. In den letzten 20 Jahren wurden auf der Boltzmann-Uehling-Uhlenbeck-(BUU)-Gleichung basierende Transportmodelle [Brt84] erfolgreich zur Beschreibung der Teilchenproduktion in Schwerionenkollisionen eingesetzt. Ein Nachteil dieser Modelle ist die große Anzahl freier Parameter. Es ist daher notwendig, die Resultate des Modells mit möglichst vielen experimentellen Observablen zu vergleichen und dabei den gleichen Satz an Parametern und physikalischer Annahmen zu verwenden. Unser Transportmodell wurde ur-

sprünglich zur Beschreibung von Schwerionenkollisionen bei SIS-Energien entwickelt [Tei96, Tei97, Hom99]. Später wurde es erweitert, um pion- [Wei99, Eff99b] sowie photon- und elektroninduzierte Reaktionen [Eff99a, Eff96, Leh99, Leh00] in der Resonanzregion zu beschreiben. Basierend auf frühere Arbeiten zu hochenergetischen Photon-Kern-Reaktionen [Eff99c, Eff00] haben wir das Modell erweitert, um die Reaktionen hochenergetischer Photonen und Elektronen im kinematischen Bereich der Jefferson Lab-, HERMES- und EMC-Experimente zu untersuchen.

Unterhalb invarianter Energien von ungefähr 2 GeV können hadronische Wechselwirkungen durch die Anregung und den Zerfall von Resonanzen beschrieben werden. Bei höheren Energien verschwindet die Resonanzstruktur im Wirkungsquerschnitt, und die Wechselwirkung wird durch den Transfer eines Gluons, Pomerons oder Reggeons dominiert. Die letzteren können als Austausch mehrerer weicher Gluonen und (Anti-) Quarks interpretiert werden. Bei noch höheren Energien gewinnen auch harte Stöße zwischen den Konstituenten der Hadronen an Bedeutung.

Aufgrund der hadronischen Fluktuationen des (virtuellen) Photons weisen photon- und elektroninduzierte Reaktionen signifikante Ähnlichkeiten mit rein hadronischen Wechselwirkungen auf. Abhängig von der Energie und Virtualität des Photons können dieselben Prozesse wie in hochenergetischen Hadron-Hadron-Kollisionen auftreten. Diese beinhalten elastische und diffraktive Streuung sowie harte Stöße zwischen den Konstituenten der hadronischen Fluktuationen und des Targets. Außerdem kann das virtuelle Photon direkt an ein Quark des Targets koppeln. Dieser Prozeß dominiert den Wirkungsquerschnitt in tiefinelastischer Leptonstreuung bei hinreichend großen Werten der Bjorken-Skalenvariable $x \gtrsim 0.2$.

Diverse hochenergetische Reaktionen führen zur Anregung hadronischer Strings. Diese zerfallen durch Quark-Antiquark-Paarerzeugung aus dem Vakuum in Hadronen. Die Fragmentation der Strings kann im Lund-Modell beschrieben werden, auf dem auch die von uns verwendeten Monte-Carlo-Generatoren FRITIOF und PYTHIA basieren. Der Vorteil des Lund-Modells liegt in seiner Möglichkeit, den kompletten Endzustand eines fragmentierenden Strings zu bestimmen, inklusive der Teilchenidentitäten und Impulse. Das Lund-Modell beinhaltet drei Zeitskalen für die Produktion eines Hadrons in der Stringfragmentation: Die ersten beiden Zeiten bestimmen die Produktion des ersten und zweiten Hadronkonstituenten. Die dritte Zeit entspricht der Formationszeit des Hadrons, d.h. dem Zeitpunkt, zu dem sich die hadronische Wellenfunktion aufgebaut hat. Da schon mit der Produktion des zweiten Hadronkonstituenten ein farbneutrales Objekt gebildet wird, bezeichnet man die entsprechende Zeit als Produktionszeit des farbneutralen Prähadrons. Wir haben die Produktionszeiten der Quark-Antiquark-Vertizes in der Stringfragmentation sowie die Formationszeiten der Hadronen im Rahmen des Lund-Modell berechnet. Dabei wurde die endliche Masse des fragmentierenden Strings berücksichtigt, welche die Zahl der Zerfallsprodukte in dem von uns untersuchten Energiebereich auf ca. 3–5 beschränkt. Im Gegensatz zu früheren theoretischen Untersuchungen [Bia87], in denen eine vereinfachte Fragmentationsfunktion verwendet wurde, finden wir eine nichttriviale Massenabhängigkeit der Produktions- und Formationszeiten. Tendenziell beobachtet man ein Ansteigen der Produktions- und Formationszeiten mit der Masse des produzierten Hadrons.

Des weiteren haben wir die Produktions- und Formationszeiten von Hadronen in tiefinelastischer Positron-Nukleon-Streuung im Energiebereich des HERMES-Experi-

ments direkt aus dem Event-Generator PYHTIA extrahiert. Je nach Masse und Energie des produzierten Hadrons liegt die durchschnittliche Produktionseigenzeit des ersten Konstituenten zwischen 0 und 0.8 fm/$c$. Im Gegensatz dazu kann die Produktionseigenzeit des zweiten Konstituenten und die Formationseigenzeit bis zu 1.5–1.7 fm/$c$ betragen.

Wir haben die Ergebnisse des Glauber- und des BUU-Modells für Proton-Kern-Reaktionen bei 100 GeV Einschußenergie untersucht. Die durch das BUU-Modell vorhergesagte Massenabhängigkeit $A^{0.68}$ des totalen Wirkungsquerschnitts ist in hervorragender Übereinstimmung mit den experimentellen Daten. Dagegen liefert das Glauber-Modell einen zu großen Skalierungsexponenten. Der Grund liegt möglicherweise in der Vernachlässigung von diffraktiv angeregten Zwischenzuständen in der Glauber-Mehrfachstreureihe.

Laut AGK-Theorem bewirken Interferenzeffekte, daß der Wirkungsquerschnitt für inklusive Mesonproduktion am Kern proportional zur Massenzahl $A$ ist. Diese $A$-Abhängigkeit wird von unserem Transportmodell reproduziert, wenn wir die Wechselwirkung der Projektil- und Targetbruchstücke während der Formationszeit berücksichtigen. In unserem Standardzugang setzen wir daher die Produktionszeit aller Prähadronen auf null und skalieren ihren Wirkungsquerschnitt während der Formationszeit gemäß einem einfachen Konstituentenquarkmodell. Letzteres bestimmt den Wirkungsquerschnitt eines Prähadrons aus der Anzahl der Konstituenten, die aus dem Projektil oder Target stammen. Allerdings ermöglichen es uns die experimentellen Daten zur Pion- und Kaonproduktion in Proton-Kern-Reaktionen nicht, zwischen einem Szenario mit und ohne prähadronischen Endzustandswechselwirkungen zu unterscheiden.

Eine aussichtsreichere Methode zur Bestimmung des raumzeitlichen Ablaufs des Hadronisierungsprozesses stellt die Untersuchung von photon- und elektroninduzierten Kernreaktionen dar. Allerdings führen die Interferenzen in der Mehrfachstreuung der hadronischen Photonkomponenten zu Komplikationen. Im Glauber-Modell ist die Berücksichtigung dieser Interferenzeffekte kein Problem. Dagegen ist es nicht offensichtlich, wie man ihnen in unserem semiklassischen Transportmodell Rechnung trägt.

Im Rahmen dieser Arbeit haben wir eine mögliche Implementierung des Abschattungseffekt in Transportmodelle vorgestellt und gezeigt, daß sie die von der HERMES-Kollaboration in exklusiver $\rho^0$-Elektroproduktion beobachteten Kohärenzlängeneffekte richtig beschreibt. Außerdem haben wir untersucht, wie die gekoppelten Kanäle das Signal von Farbtransparenz in der $\rho^0$-Photo- und Elektroproduktion beeinflussen und diskutiert, welche kinematischen Schnitte Rechnungen im Glauber-Modell zulassen. Unsere Analyse der HERMES-Daten ergaben kein Anzeichen für Farbtransparenzeffekte während der Formationszeit des $\rho^0$-Mesons. Stattdessen sind unsere Resultate mit der Annahme verträglich, daß das $\rho^0$-Meson im kinematischen Bereich des HERMES-Experiments sofort mit seinem vollen hadronischen Wirkungsquerschnitt wechselwirkt.

In unserem Modell haben wir ebenfalls die semi-inklusive Photoproduktion von geladenen Pionen, Kaonen und $D$-Mesonen im Energiebereich von 1–30 GeV untersucht. In diesen Reaktionen führen die Endzustandswechselwirkungen zu einer starken Erhöhung der Teilchenmultiplizitäten, die im Rahmen des Glauber-Modells nicht zu verstehen ist. Insbesondere finden wir schon bei relativ kleinen Photonenergien eine erhöhte Produktion von $K^+$-Mesonen, da diese aufgrund ihres Quarkinhalts nicht im Kernmedium absorbiert werden können.

Ein Großteil dieser Arbeit hat sich mit der Produktion von Hadronen in tiefinelastischer Lepton-Kern-Streuung bei HERMES-, EMC- und Jefferson Lab-Energien befaßt. Für den raumzeitlichen Ablauf des Hadronisierungsprozesses wurden hierbei im wesentlichen zwei verschiedene Szenarien betrachtet: Im ersten Fall haben wir das gleiche Kontituentenquarkmodell wie in der Beschreibung von Proton-Kern-Reaktionen verwendet. Im zweiten Zugang haben wir die Produktions- und Formationszeiten aus dem Lund-Modell angesetzt. Unsere transporttheoretische Beschreibung ermöglicht es uns, die Produktion von Teilchen in den Endzustandswechselwirkungen der primären Reaktionsprodukte zu berücksichtigen. Wir haben herausgefunden, daß diese sekundären Teilchen einen starken Einfluß auf den Niederenergieanteil der experimentell gemessenen Teilchenmultiplizitäten haben.

Im Zusammenhang mit dem HERMES-Experiment wurden die Auswirkungen der kinematischen Schnitte sowie der geometrischen Akzeptanz des Detektors auf die Teilchenspektren untersucht. Unseren Resultaten zufolge ist eine Berücksichtigung dieser Effekte für eine eindeutige Interpretation der Daten unerläßlich.

Zusätzlich wurden die Produktionsquerschnitte für Pionen, Kaonen, Protonen und Antiprotonen als Funktion ihrer Energie, ihres Transversalimpulses sowie der Energie des Photons betrachtet. Zudem wurde gezielt die Wechselwirkung der beiden energiereichsten Hadronen untersucht. Es scheint, daß sich die meisten der im HERMES Energiebereich beobachteten Phänomene auf prähadronische Endzustandswechselwirkungen zurückführen lassen. Allerdings weist unser Modell Defizite bei der Erklärung der EMC-Spektren sowie der verstärkten Produktion von Teilchen mit hohen Transversalimpulsen auf. Letzteres deutet auf einen partonischen Ursprung des Cronin Effekts in Elektron-Kern-Reaktionen hin.

Motiviert durch unsere erfolgreiche Beschreibung der experimentellen HERMES-Daten haben wir Vorhersagen für die Teilchenmultiplizitäten in jetzigen und zukünftigen Jefferson Lab-Experimenten gemacht. Aufgrund der wesentlich kleineren Photonenergien beobachten wir hier einen starken Einfluß der Fermibewegung. Außerdem führen in diesem Energiebereich schon allein die (prä-)hadronischen Endzustandswechselwirkungen zu einer Erhöhung der Teilchenmultiplizitäten bei hohen Transversalimpulsen.

# Danksagung

An dieser Stelle möchte ich all den Menschen danksagen, die diese Arbeit möglich gemacht haben und die mir in den letzten Jahren unterstützend zur Seite standen.

Mein Dank gilt vor allem Prof. Dr. Ulrich Mosel für die Aufnahme an sein Institut und seine überaus engagierte Betreuung. Sein stetes Interesse an diesem Thema sowie unzählige gemeinsame Diskussionen haben sehr zum Fortgang dieser Arbeit beigetragen. Insbesondere möchte ich mich bei ihm für den großzügig gewährten Freiraum bedanken, der es mir ermöglichte, immer wieder eigene Ideen in diese Arbeit einfließen zu lassen. Weiterhin konnte ich aufgrund seiner wohlwollenden Förderung meine Arbeit auf zahlreichen internationalen Konferenzen vorstellen und dadurch wertvolles Feedback von anderen Wissenschaftlern erhalten.

Besonderer Dank gilt auch Dr. Kai Gallmeister ohne dessen profunde PYTHIA-Kenntnisse ein erfolgreiches Gelingen dieser Arbeit nicht möglich gewesen wäre. Sein kritisches Hinterfragen so manchen Ergebnisses sowie viele Diskussionen haben sich stets positiv auf diese Arbeit ausgewirkt. Gleichermaßen möchte ich mich bei meinem langjährigen Zimmerkollegen und BUU-Kammeraden Dr. Jürgen Lehr für die überaus angenehme und unterhaltsame Arbeitsatmosphäre bedanken. Das gemeinsame Enträtseln einiger Aspekte des BUU-Codes sowie unsere langen Gespräche über physikalische und weniger physikalische Fragestellungen haben mir die Arbeit sehr erleichtert. Zudem danke ich beiden für die sorgfältige Durchsicht großer Teile des Manuskripts.

Ein großes Dankeschön geht auch an Prof. Dr. Dr. Wolfgang Cassing und Prof. Dr. Carsten Greiner von denen ich in zahlreichen gemeinsamen Diskussionen viel gelernt habe und die durch ihre Ideen und Anregungen den Fortgang dieser Arbeit maßgeblich beeinflußt haben. Vor allem danke ich Carsten für seine vielen aufmunternden Worte, die mich in den vergangenen Jahren aus so manchem vorübergehenden Tief geholt haben.

Dr. Gregor Penner und Dr. Marcus Post danke ich für viele erheiternde Gespräche. Gerade an langen Arbeitstagen ist ihr Büro zu einem meiner beliebtesten Ausflugsziele geworden. Bei der Computer-Crew Frank Frömel und Christoph Keil bedanke ich mich für die geduldige und kompetente Lösung aller angefallenen Computerprobleme. Gerade Frank hat seinen Job mit einem Eifer ausgeübt, der seinesgleichen sucht.

Dem gesamten Institut danke ich für die produktive Stimmung und die vielen gemeinsamen sommerlichen BBQs. Besonders hervorheben möchte ich neben den schon erwähnten Personen Dr. Stefan „Öll" Leupold (dem ich immer noch eine Version meiner Diplomarbeit schulde) und Gunnar Martens, Präsident des Institutes BBQ Club. Elke Jung hat mir darüber hinaus mit administrativer Hilfe häufig und gerne zur Seite gestanden.

I also acknowledge valuable discussions with Prof. Dr. Nicola Bianchi, Dr. Pasquale Di Nezza and Dr. Valeria Muccifora and thank them for providing me with lots of essential information on the HERMES experiment.

Der größte Dank geht an meine Eltern und meine Frau Christina für ihr Verständnis und ihre Geduld während der vergangenen Jahre. Ihre permanente moralische Unterstützung war für ein Gelingen dieser Arbeit unerläßlich.